Advances in Civil Engineering

Multi-Field Coupling and Deep Engineering Safety: New Theories and Methods

Lead Guest Editor: Guang-Liang Feng
Guest Editors: Quan Jiang and Jun Xiong

Multi-Field Coupling and Deep Engineering Safety: New Theories and Methods

Advances in Civil Engineering

Multi-Field Coupling and Deep Engineering Safety: New Theories and Methods

Lead Guest Editor: Guang-Liang Feng
Guest Editors: Quan Jiang and Jun Xiong

Contents

Hindawi
Advances in Civil Engineering
Volume 2021, Article ID 1979353, 11 pages
https://doi.org/10.1155/2021/1979353

Research Article

Do Environmental Regulations Improve Industrial Efficiency?

Peng Li [1,2] **and Li-Li Shi** [1]

[1] *International Business School of Shaanxi Normal University, Xi'an 710119, China*
[2] *School of Economics and Management, Northwest A&F University, Yangling 712110, China*

Correspondence should be addressed to Peng Li; hau_lipeng@snnu.edu.cn

Received 29 June 2021; Accepted 25 September 2021; Published 13 November 2021

Academic Editor: Guang-Liang Feng

This study was based on research on the impact of environmental regulation on industrial efficiency in 30 provinces from 2005 to 2017 in China. For the explained variables, the industrial efficiency of the DEA-Malmquist method was utilized for the decomposition and measurement of overall factor productivity, and government environmental governance variables were added as instrumental variables for two-stage least-squares regression. In addition, environmental regulatory intensity and year were utilized as threshold variables for the threshold test. In the benchmark regression, environmental regulation harms regional industrial efficiency. However, according to the IV estimation of government environmental governance variables, environmental regulation has a positive effect on the transformation of regional industrial efficiency. The influence of environmental regulation on industrial efficiency will be first suppressed and then promoted with the gradual increase of regulatory intensity. Furthermore, there is significant spatial heterogeneity in the impact of environmental regulations.

1. Introduction

Whether environmental regulation impedes industrial efficiency is somewhat controversial in academic circles. On the one hand, neoclassical research argues that environmental regulation raises production costs, raises unemployment, and reduces the competitiveness of economies. On the other hand, environmentalists and others argue that stronger environmental regulation policies can force firms to increase research and development of clean technologies, thereby reducing costs and environmental pollution. There are three theories in these mentioned studies. In the first place, there is the "Porter hypothesis-innovation compensation" effect, in which environmental regulation promotes innovation, which is generally based on overall factor productivity or its subtechnological progression. Second, there is the "double dividend" theory, in which environmental taxation will cause a "green dividend" of curbing pollution, improving the environment a "blue dividend" of increasing social employment, and promoting economic growth. Third, there is the "pollution sanctuary" effect, in which economic activities are relocated to areas with lax environmental regulations, resulting in the increased environmental pollution in the area in exchange for economic growth. The first two theories illustrate the positive effect of environmental regulation on industrial efficiency, while the last theory illustrates the inhibiting effect of environmental regulation on local green welfare. Since the "Porter hypothesis" [1] was proposed in 1991, a considerable number of scholars have started to verify whether environmental regulation affects firm productivity and innovation activities, but until now, the "Porter hypothesis" has not reached a consensus. Chakraborty and Chatterjee [2] constructed a nonequilibrium panel DID model using the German ban on azo dyes enacted in July 1994 as a quasi-natural experiment and found that the German dye ban had a significant effect on the innovation expenditure of upstream fuel manufacturing firms (upstream firms) in India. Trevlopoulos et al., Yang et al., and Zhang et al. explored the positive impact of environmental regulation on enterprise innovation and industrial structure upgrading [3–5]. Yu and Wang explained the economic benefit of environmental control policies in the process of industrial upgrading [6]. A considerable number of studies focus on the existence of the "pollution sanctuary effect", but

there are some differences in the target population. Shi and Xu studied the impact of environmental regulations on import and export from the perspective of international trade flow [7]. Some scholars employed the flow of international capital as the object to verify whether the "pollution shelter effect" exists. For example, Lu and Wu utilized the Air pollution Prevention and Control Law to verify whether there is a pollution paradise effect [8]. Zhao et al. is the representative literature of studies on the pollution haven effect and the test of the double dividend hypothesis, who proposed the effect of environmental regulation on the spatial layout of industries and its effect through different geographic locations of polluting industries. Their evidence indicated that the water pollution industry migrates upstream after environmental regulation is enhanced [9]. Huang and Lei further studied how environmental regulation affects green investment in enterprises [10], while Stavropoulos et al. discussed the evolutionary relationship between environmental regulation and industrial competitiveness [11]. In addition, Zhang et al. made useful explorations from sustainable development, reusing industrial byproducts, and green construction in civil engineering [12–16], and further expanded the research scope of environmental regulation and industrial development.

In summary, these authors employed scientific research methods and instruments to scientifically determine the direction and extent of the effect of environmental regulation on industrial efficiency. The specific steps are as follows: first, according to the "Porter's hypothesis-innovation compensation" hypothesis, the DEA-Malmquist method is utilized to measure the industrial overall factor productivity (industrial TFP) index and its decomposition terms: efficiency change, technological progress, the industrial TFP index of 30 provinces, autonomous regions, and municipalities directly under the Central and Western regions of China from 2005 to 2017. Next, the commonly utilized composite index method was then employed to construct a comprehensive measurement system for the intensity of environmental regulations in Chinese industry to measure the intensity of environmental regulations. Third, the panel data of 30 Chinese provinces from 2005 to 2017 are selected, and the backward effect of environmental regulations on industrial efficiency is verified by using panel regression with fixed effects and the least-squares instrumental variables method [17]. Ultimately, through threshold regression [18], the threshold characteristics and spatial heterogeneity of environmental regulations are verified. Based on the spatial heterogeneity and related literature studies, foreign direct investment, regional economic development level, and provincial intervention policies are used as control variables to eliminate influencing factors besides the core explanatory variable of environmental regulation.

2. The Measurement of Industrial Overall Factor Productivity

2.1. Research Methodology-Malmquist Index. The Malmquist index has the advantage of further decomposing productivity changes into efficiency changes and technological progress. Among them, efficiency change refers to the change in organizational and managerial efficiency within the industry, which comes from the change in the efficiency of the original technology use and the efficiency change caused by the scale of production. Therefore, it can be further decomposed into pure technical efficiency change and scale efficiency change. Technological progress alludes to the productivity change caused by the introduction or upgrading of technology. This method has the advantages of not requiring factor price information and a specific form of a production function. It is effortless to calculate efficiency and can deal with multiple input and output problems, so it is more favored among scholars. Due to the limitation of space, this study briefly introduces the construction method of the Malmquist productivity index.

The Malmquist productivity index is defined using a distance function and refers to the geometric mean of the Malmquist productivity index in period t versus period $t+1$. Assuming the premise that each provincial district is a decision unit, (x^t, y^t) and (x^{t+1}, y^{t+1}) represent the input-output quantities in period t and period $t+1$, respectively, and the change in the input-output relationship means the change in productivity, denoted by M_i^{t+1}:

$$M_i^{t+1}\left(x^t, y^t, x^{t+1}, y^{t+1}\right) = \sqrt{\frac{D_i^t\left(x^t, y^t\right)}{D_i^t\left(x^{t+1}, y^{t+1}\right)} \times \frac{D_i^{t+1}\left(x^t, y^t\right)}{D_i^{t+1}\left(x^{t+1}, y^{t+1}\right)}}. \tag{1}$$

In equation (1), $D_i^t(x^t, y^t)$ is the hybrid distance function, which is the inverse of the technical efficiency.

Productivity changes do not only come from technological progress but also efficiency changes. When we say efficiency, we mean the efficiency of utilizing the production technology, that is, the distance between the production frontier surface and the actual amount of output, denoted by EFFCH_i^{t+1}; the technological progress is the movement of the production frontier surface, denoted by TECHCH_i^{t+1}:

$$\mathrm{TECHCH}_i^{t+1}\left(x^t, y^t, x^{t+1}, y^{t+1}\right) = \sqrt{\frac{D_i^{t+1}\left(x^{t+1}, y^{t+1}\right)}{D_i^t\left(x^{t+1}, y^{t+1}\right)} \times \frac{D_i^{t+1}\left(x^t, y^t\right)}{D_i^{t+1}\left(x^{t+1}, y^{t+1}\right)}},$$

$$\mathrm{EFFCH}_i^{t+1}\left(x^t, y^t, x^{t+1}, y^{t+1}\right) = \frac{D_i^t\left(x^t, y^t\right)}{D_i^{t+1}\left(x^{t+1}, y^{t+1}\right)}. \tag{2}$$

The Malmquist productivity index can be decomposed as the product of efficiency changes and technical progress:

$$M_i^{t+1}\left(x^t, y^t, x^{t+1}, y^{t+1}\right) = \mathrm{EFFCH}_i^{t+1}\left(x^t, y^t, x^{t+1}, y^{t+1}\right) \times \mathrm{TECHCH}_i^{t+1}\left(x^t, y^t, x^{t+1}, y^{t+1}\right). \tag{3}$$

If $M > 1$, it indicates overall productivity (TFP) growth; otherwise, it indicates a decline. If EFFCH > 1, it represents efficiency improvement, i.e., proper management style and decision-making; if EFFCH < 1, it represents efficiency deterioration, i.e., improper management style and decision-

making. If TECHCH > 1, it indicates an improvement in production technology; if TECHCH < 1, it indicates a decline in production technology.

2.2. Input-Output Variables Selection and Data Sources. Based on the availability of data and the need for empirical research, this study employed industrial enterprises above the scale to represent the whole industrial industry. In the research process, the overall industrial fixed assets of above-scale enterprises were utilized to replace capital input. In addition, the average annual number of all employees of industrial enterprises was utilized to replace labor input, and the industrial value-added of above-scale enterprises was selected as the expected output. The data were obtained from the China Statistical Yearbook and China Environmental Statistical Yearbook from 2005 to 2017.

2.3. Analysis of Measurement Results. This study employed DEAP2.1 software to calculate the industrial data of 30 provinces and regions in China from 2005 to 2017 to derive industrial TFP and its decomposition terms: efficiency change and technological progress.

Overall, China's industrial productivity from 2005 to 2017 generally indicated a slight fluctuation downward trend, which is chiefly due to the decline of the technical change index and is also in line with the current stage of China's economic adjustment into the "new normal" trend (Table 1). Since 2010, China's economic development has entered a period of growth rate shift, ending nearly 20 years of continuous economic growth. This can be seen as an indication that China's economy is being optimized and diversified. International experience indicates that when developing countries are in the development stage of economic start-up, they often pursue rapid economic growth and tend to neglect technological progress and structural optimization, resulting in problems like the imbalance between economic and social and urban and rural income distribution. As a result, the economy stagnates or even declines severely, falling into the "middle-income trap." In addition, a comparative study found that China's industrial overall factor productivity achieved positive growth in 2009–2010 and 2012–2013, which chiefly depended on the growth of the technological progress index.

As can be seen from Table 2, China's regional industrial TFP decreased in 2005–2017, with the eastern and western regions declining more significantly and the central region tending to be stable. Among the more economically developed provinces in the east of China, only Zhejiang Province has significantly improved its efficiency, and only Henan Province and Guizhou Province have improved their overall factor productivity in the central and western regions, but the efficiency of other provinces has not increased or declined. These all reflect that China's industrial enterprises are optimizing their industrial structure and seeking space for industrial upgrading.

3. Selection, Measurement, and Analysis of Environmental Regulation Intensity Indicators

3.1. Environmental Regulation Intensity Indicator (FERI). The implementation of environmental regulations depends on the willingness of local governments, the level of regional economic development, the current situation of environmental pollution, etc. Even if a country formulates a uniform regulatory policy, the intensity of implementation may vary from region to region. This study applied the comprehensive index method commonly utilized by scholars [8] to construct a comprehensive measurement system of the environmental regulation intensity of Chinese industries, including a target layer and four evaluation index layers (wastewater, waste gas, waste residue, and others) and calculate the environmental regulation intensity of individual pollutants and the comprehensive environmental regulation intensity of each province by assigning different weights to different pollutants. Based on the severity of various pollutant emissions in China and the availability of data, three individual indicators of wastewater treatment, waste gas, and solid waste investment in each province are selected to construct a comprehensive measurement system of environmental regulation intensity. This indicator construction method is as follows: in the first place, the three single indicators are linearly standardized; that is, the values of each indicator are converted to within the range of [0, 1] by mathematical transformations to eliminate the incommensurability between indicators and the contradiction between indicators. The calculation formula is as follows:

$$PR_{ij}^{s} = \frac{PR_{ij} - \min\left(PR_j\right)}{\max\left(PR_j\right) - \min\left(PR_j\right)}, \tag{4}$$

where i refers to the province ($i = 1, 2, \ldots 30$) and j refers to all types of pollutants ($j = 1, 2, 3$); PR_{ij} are the original values of each indicator, while $\max(PR_j)$ and $\min(PR_j)$ are the maximum and minimum values of the three individual indicators for each province each year. In addition, PR_{ij}^{s} are the standardized values of each indicator.

The adjustment coefficient (ω_{ij}) and the weight are calculated for each indicator. For different provinces, the proportion of pollution emissions of "three wastes" varies greatly, so their treatment project investment also varies; for a particular province, the degree of treatment of different pollutant emissions also varies. Therefore, different weights are provided to the indicators of wastewater, waste gas, and solid waste in each province, and the weight of each indicator is adjusted to reflect the changes in the treatment of major pollutants in each province. The adjustment coefficients are calculated as follows:

$$\omega_{ij} = \frac{E_{ij}/\sum E_{ij}}{Y_i/\sum Y_i}, \tag{5}$$

where ω_{ij} is the adjustment factor of pollutant j in province i. E_{ij} is the emission of pollutant j in province i, so $\sum E_{ij}$ is the overall emission of the same pollutant in the country.

Table 1: Industrial TFP index and its decomposition index from 2005 to 2017.

Years	TEP changes	Efficiency changes	Technological advances	Pure technical efficiency	Scale efficiency
2006/2005	1.015	1.043	1.000	1.016	1.059
2007/2006	1.002	1.091	0.987	1.015	1.094
2008/2007	0.988	1.184	0.993	0.995	1.170
2009/2008	0.955	0.972	0.965	0.990	0.929
2010/2009	1.112	1.018	1.073	1.037	1.132
2011/2010	0.980	1.158	0.990	0.990	1.135
2012/2011	0.998	0.986	0.992	1.006	0.984
2013/2012	1.009	0.916	1.020	0.988	0.923
2014/2013	0.977	1.013	0.984	0.993	0.989
2015/2014	0.946	0.990	0.964	0.982	0.936
2016/2015	1.001	1.010	0.995	1.006	1.010
2017/2016	0.983	1.099	0.978	1.005	1.081
2005–2017	0.997	1.04	0.995	1.002	1.037

Table 2: Average values of industrial TFP indices and their decomposition indices in the three major regions, 2005–2017.

Province	TEP changes	Efficiency changes	Technological advances	Pure technical efficiency	Scale efficiency
Beijing	0.992	1.022	1.000	0.992	1.015
Tianjin	1.011	1.058	1.001	1.011	1.070
Hebei	1.000	1.037	1.000	1.000	1.037
Liaoning	0.989	1.050	0.983	1.006	1.039
Shanghai	1.011	1.058	1.000	1.011	1.070
Jiangsu	0.988	1.068	0.984	1.005	1.055
Zhejiang	1.025	1.033	1.014	1.011	1.059
Fujian	0.938	1.023	0.953	0.985	0.960
Shandong	0.984	1.073	0.988	0.996	1.056
Guangdong	0.991	1.067	1.000	0.991	1.057
Hainan	1.006	1.041	1.008	0.998	1.046
Eastern region (mean)	0.990	1.050	0.990	1.000	1.040
Shanxi	1.020	1.031	1.015	1.004	1.051
Jilin	1.002	1.022	1.002	1.000	1.024
Heilongjiang	0.988	1.024	0.988	1.000	1.012
Anhui	0.995	1.054	1.000	0.995	1.048
Jiangxi	0.968	1.028	0.975	0.994	0.996
Henan	1.043	1.041	1.038	1.004	1.085
Hubei	1.007	1.024	1.006	1.002	1.032
Hunan	1.000	1.036	1.000	1.000	1.036
Central region (mean)	1.000	1.030	1.000	1.000	1.040
Neimenggu	0.997	1.024	0.999	0.998	1.021
Guangxi	0.994	1.022	1.000	0.994	1.016
Chongqing	0.983	1.021	0.983	0.999	1.003
Sichuan	0.993	1.027	0.994	1.000	1.020
Guizhou	1.031	1.023	1.018	1.013	1.055
Yunnan	0.959	1.028	0.959	0.999	0.986
Shanxi	1.009	1.028	1.001	1.008	1.037
Gansu	0.955	1.026	0.969	0.986	0.980
Qinghai	1.015	1.071	1.000	1.015	1.088
Ningxia	1.032	1.041	1.000	1.032	1.075
Xinjiang	0.973	1.018	0.966	1.007	0.990
Western region (mean)	0.990	1.030	0.990	1.000	1.020

Moreover, Y_i is the industrial value-added in province i, so $\sum Y_i$ is the national industrial value-added. After calculating the adjustment coefficients of exhaust gas, wastewater, and solid waste for each year, the average value of the adjustment coefficients during 2005–2017 was then calculated as $\overline{\omega}_{ij}$.

Ultimately, the standardized values and average weights of each indicator are utilized to calculate the intensity of environmental regulations in each province as

$$\mathrm{FERI}_i = \frac{1}{3}\sum_{j=1}^{3} \overline{\omega}_{ij} \cdot PR_{ij}^{s}. \tag{6}$$

The higher value indicates the more severe environmental regulation.

3.2. Analysis of Measurement Results. From Table 3, it can be seen that the average intensity of environmental regulations in the western region is significantly higher than that in the central and eastern regions, which laterally reflects that the industrial structure in the western region is significantly lower than that in the eastern and central regions. In the eastern region, the intensity of environmental regulations in Liaoning Province is significantly higher than that in other provinces, which is in line with the current industrial development of Liaoning Province as an old industrial production base whose urgent need is for industrial restructuring. In the central region, the environmental regulation intensity is higher in Anhui Province, and in the western region, the environmental regulation intensity is higher in Guizhou and Gansu Provinces, both of which possess a unique industrial structure and need to upgrade their industrial structures. In terms of years, from 2009, local governments in all provinces increased the intensity of environmental pollution control, which continued to a high-intensity status in 2014. After 2015, the domestic industrial structure was significantly improved, and the intensity of environmental regulations was significantly moderated and improved.

4. The Impact of Environmental Regulation Intensity on Industrial Efficiency: Model Setting and Transmission Mechanism Analysis

4.1. Setting of the Measurement Model

4.1.1. Model Variable Design. To chiefly explore the impact of environmental regulation on industrial efficiency in China, a panel data regression method was utilized for empirical testing, and 30 provincial and urban administrative units across China from 2005 to 2017 were selected as the research objects. Formal environmental regulation indicators were incorporated into the measurement equation as the core explanatory variables, while other factors affecting industrial efficiency were introduced in the form of control variables. To prevent heterosexuality and multidisciplinary, the variables were logarithmically treated, and the specific variable design is shown in Table 4.

4.1.2. Model Setting Test

(1) Model 1. The cross-sectional individual variable coefficient model, or the variable coefficient model, is described in the following way:

$$Y_{it} = \alpha_i + X_{it}\beta_i + \mu_{it}, \quad i = 1, \ldots, n,\ t = 1, \ldots, T, \tag{7}$$

where X_{it} is the $1 \times K$ vector, β_i is the $1 \times K$ vector, and K is the number of explanatory variables.

(2) Model 2. The cross-sectional individual variable-intercept model, or the variable-intercept model, is described as follows:

$$Y_{it} = \alpha_i + X_{it}\beta + \mu_{it}, \quad i = 1, \ldots, n,\ t = 1, \ldots, T. \tag{8}$$

The model indicates that there are individual effects (variable intercepts) but no variation in the economic structure among cross-sectional individuals, so the structural parameters are the same across cross-sectional individuals.

(3) Model 3. The cross-sectional individual intercept, or coefficient invariant model, is described as follows:

$$Y_{\mathrm{it}} = \alpha + X_{\mathrm{it}}\beta + \mu_{\mathrm{it}}, \quad i = 1, \ldots, n,\ t = 1, \ldots, T. \tag{9}$$

The model indicates that there are no individual effects (variable intercepts) and no changes in economic structure among cross section individuals; therefore, both the intercept and structural parameters of the model are the same.

For all three models, it is tested whether the parameters inscribing the explanatory variables are constant at all cross-sectional sample points and at a time; that is, it is tested in which of the previous three cases the problem under study falls to determine the form of the model. The widely utilized test is the covariance analysis test, also known as the F-test, which tests the following two main hypotheses.

Hypothesis 1. The slopes are the same at different cross-sectional sample points and times, but the intercepts are not the same:

$$H_1\colon\ y_{\mathrm{it}} = \alpha_i + X_{\mathrm{it}}\beta + \mu_{\mathrm{it}}. \tag{10}$$

Hypothesis 2. The intercept and slope are the same at different cross-sectional sample points and at a time:

$$H_2\colon\ y_{\mathrm{it}} = \alpha + X_{\mathrm{it}}\beta + \mu_{\mathrm{it}}. \tag{11}$$

To test the parametric constraint of the multiple linear regression model, if Hypothesis 2 is accepted, no further testing is required; if Hypothesis 2 is rejected, Hypothesis 1 should be tested to see if the slopes are all equal. If Hypothesis 1 is rejected, Model 1 should be utilized.

The results show that the hypothesis of "intercept and slope are the same across cross-sectional sample points and time" is rejected at the 5% significance level with $F = 1.273$, while the hypothesis of "the slope is the same across cross-sectional sample points and time, but intercept is different" is accepted at the 5% significance level with $F = 1.293$ with different intercepts. Therefore, the fixed effects model should be chosen:

$$\mathrm{IVA}_{\mathrm{it}} = \alpha_i + \mathrm{FERI}_{\mathrm{it}}\beta + \mathrm{FDI}_{\mathrm{it}}\gamma_1 + \mathrm{GDP}_{\mathrm{it}}\gamma_2 + \mathrm{EP}_{\mathrm{it}}\gamma_3 + \mu_i + t_t + \varepsilon_{\mathrm{it}}. \tag{12}$$

In the previous model, the corresponding parameters β, γ_1, γ_2, and γ_3 vary with cross-sectional individuals, where the explanatory variable is $\mathrm{IVA}_{\mathrm{it}}$ with the industrial value-added of the region i in year t, characterizing industrial efficiency. The core explanatory variable $\mathrm{FERI}_{\mathrm{it}}$ is the

Table 3: Environmental regulation intensity in 30 Chinese provinces, 2005–2017.

Region	2017	2016	2015	2014	2013	2012	2011	2010	2009	2008	2007	2006	2005	Mean
Beijing	0.04	0.04	0.04	0.01	0.02	0.02	0.02	0.02	0.03	0.09	0.07	0.29	0.25	0.07
Tianjin	0.03	0.02	0.23	0.11	0.06	0.09	1.11	0.27	0.31	0.18	0.19	0.27	0.38	0.25
Hebei	0.23	0.08	0.31	0.47	0.47	0.40	0.50	0.22	0.26	0.28	0.27	0.35	0.62	0.34
Liaoning	1.03	0.34	0.72	0.88	2.82	2.27	1.47	3.84	2.80	2.80	1.76	2.51	0.44	1.82
Shanghai	0.57	0.39	0.69	1.34	2.79	0.50	1.19	0.35	0.65	0.30	0.47	0.72	0.05	0.77
Jiangsu	0.06	0.08	0.62	0.09	0.10	0.03	0.07	0.22	0.38	0.10	0.36	0.10	0.12	0.18
Zhejiang	0.04	0.01	0.04	0.03	0.05	0.02	0.11	0.16	0.14	0.06	0.05	0.02	0.06	0.06
Fujian	0.26	0.23	0.16	0.05	0.13	0.03	0.20	0.06	0.15	0.06	0.28	0.02	0.04	0.13
Shandong	6.23	0.69	0.12	0.20	0.05	0.07	0.07	0.05	0.21	0.21	0.24	1.31	0.18	0.74
Guangdong	0.41	0.30	0.28	0.12	0.51	0.43	0.23	0.15	0.21	0.18	0.54	0.26	0.45	0.31
Hainan	0.18	0.24	0.29	0.18	0.30	0.24	0.07	0.07	0.34	0.05	0.06	0.13	0.05	0.17
Eastern region (mean)	0.83	0.22	0.32	0.32	0.66	0.37	0.46	0.49	0.50	0.39	0.39	0.54	0.24	0.44
Shanxi	0.15	0.28	0.10	0.05	0.13	0.18	0.06	0.07	0.15	0.13	0.11	0.12	0.22	0.13
Jilin	0.05	0.31	0.33	0.20	0.35	0.18	0.15	0.31	0.21	0.10	0.11	0.51	0.96	0.29
Heilongjiang	0.46	0.30	0.53	0.23	0.38	0.17	0.25	0.28	0.20	0.21	0.25	0.32	0.25	0.29
Anhui	0.80	0.83	1.29	0.73	0.55	0.92	1.41	0.66	0.68	1.25	0.97	0.78	1.19	0.93
Jiangxi	0.13	0.32	0.17	0.17	0.93	0.07	0.26	0.27	0.27	0.26	0.36	0.53	0.27	0.31
Henan	0.08	3.42	0.05	0.06	0.11	0.10	0.10	1.28	0.98	0.13	0.17	0.52	0.23	0.56
Hubei	0.06	0.05	0.08	0.07	0.20	0.26	0.15	0.53	0.24	0.17	0.39	0.61	0.42	0.25
Hunan	0.06	0.04	0.12	0.04	0.07	0.22	0.06	0.09	0.09	0.02	0.21	0.20	0.19	0.11
Central region (mean)	0.22	0.69	0.33	0.19	0.34	0.26	0.31	0.44	0.35	0.28	0.32	0.45	0.47	0.36
Neimenggu	0.01	0.05	2.02	0.90	0.05	0.11	0.05	1.11	0.15	0.05	1.28	0.06	0.12	0.46
Guangxi	0.06	0.01	0.04	0.04	0.03	0.06	0.05	0.07	0.06	0.02	0.03	0.08	0.00	0.04
Chongqing	0.01	0.01	0.04	0.07	0.04	0.03	0.28	0.15	0.09	0.15	0.23	0.16	0.25	0.12
Sichuan	0.05	0.02	0.04	0.06	0.08	0.08	0.20	0.08	0.13	0.26	0.26	0.45	0.34	0.16
Guizhou	0.02	0.03	0.09	0.10	0.32	0.28	7.79	0.79	6.86	0.73	0.81	1.09	0.25	1.47
Yunnan	0.04	0.15	0.58	5.36	0.86	0.73	0.58	0.99	0.88	1.62	0.37	0.55	0.15	0.99
Shanxi	0.05	0.06	0.10	0.10	0.37	0.46	0.47	1.64	0.56	0.09	0.32	0.18	0.19	0.35
Gansu	0.01	0.22	0.01	0.07	0.16	8.74	0.38	1.50	1.38	0.51	0.67	1.12	0.17	1.15
Qinghai	0.05	0.22	0.59	0.36	0.26	0.04	0.22	0.40	0.23	0.02	0.01	0.01	0.00	0.19
Ningxia	0.51	0.72	0.54	4.98	1.29	0.34	0.31	0.43	0.57	0.33	0.44	0.38	0.03	0.84
Xinjiang	0.05	0.03	0.14	0.20	0.17	0.04	0.20	0.17	0.74	0.03	0.02	0.01	0.00	0.14
Western region (mean)	0.08	0.14	0.38	1.11	0.33	0.99	0.96	0.67	1.06	0.35	0.40	0.37	0.34	0.54
Mean	0.39	0.32	0.35	0.57	0.45	0.57	0.60	0.54	0.66	0.35	0.38	0.46	0.26	

Table 4: Model variable design.

Variable type	Variable Name	Variable indicators	Variable representation
Explained variables	Industrial efficiency	Industrial value-added	IVA
Core explanatory variables	Environmental regulation	Environmental regulation intensity	FERI
	Foreign direct investment	Actual utilization of foreign direct investment (USD million)	FDI
Control variables	Regional economic development level	Overall GDP after deflating by region (billion yuan)	GDP
	Provincial intervention policies	The number of state-owned industrial enterprise units above the scale (a)	EP

intensity of environmental regulations in region i in year t. The control variables FDI_{it}, GDP_{it}, and EP_{it} are the actual amount of foreign direct investment utilized by the region i in year t. The overall GDP of each region, the number of industrial enterprise units above the scale, characterizing foreign direct investment, the GDP of each region, and the intervention policy of each province are shown, respectively, in addition to controlling for individual fixed effects μ_i and time-fixed effects t_t.

Due to the association causality between the explanatory variables and the core explanatory variables, to mitigate their endogeneity, the authors employed a method of Chen and Chen [15] and selected the government environmental governance variable as an instrumental variable to measure the full picture of government environmental governance by the frequency of environment-related terms in provincial government work reports. This indicator not only measures the strength of local government environmental governance but also mitigates the endogeneity problems arising from the use of existing metrics.

To summarize, to quantitatively examine the impact of government environmental governance on industrial

efficiency in China, the two-stage least-squares regression model (2SLS) is set as follows:

$$\begin{aligned} \hat{FERI}_{it} &= \delta_i Z_{it} + FDI_{it}\lambda_{1i} + GDP_{it}\lambda_{2i} + EP_{it}\lambda_{3i} + \upsilon_{it}, \\ IVA_{it} &= \alpha_i + FERI_{it}\beta + FDI_{it}\gamma_1 + GDP_{it}\gamma_2 \\ &\quad + EP_{it}\gamma_3 + \mu_i + t_t + \varepsilon_{it}. \end{aligned} \tag{13}$$

Z_{it} is the number of environment-related terms, "environmental protection," "environmental protection," "pollution," "energy consumption," "emission reduction," "sewage," "ecology," "green," and the sum of the word frequencies of "low carbon." The previous 2SLS model is able not only to assess the impact of government environmental governance on environmental regulation but also to further screen the resulting impact on industrial efficiency.

4.2. Analysis of the Impact of Environmental Regulation Intensity on Industrial Efficiency and Its Transmission Mechanism

4.2.1. Fixed Effects Model Regression. The results of the fixed effects model estimation indicate that the coefficient of the environmental regulation variable is significantly negative, indicating that the increase in the intensity of environmental regulation has a significant negative impact on regional industrial efficiency. In other words, the more stringent government environmental protection measures and the higher demands on industrial enterprises will increase the operational pressure on enterprises, therefore reducing industrial efficiency. In contrast, the regression coefficients for foreign direct investment, gross regional product, and provincial intervention policies are all significantly positive and passed the 1% significance test, suggesting that these three factors contribute significantly to improving industrial efficiency (Table 5).

4.2.2. Regression Analysis of Instrumental Variables. Considering that the regression results of the baseline model are likely to have endogeneity problems, the frequency of words about environmental vocabulary in government work reports was utilized as an instrumental variable for environmental regulation, drawing on the approach of Chen Shiyi's scholar [6]. This indicator not only measures the strength of local government environmental governance but also mitigates the endogeneity problem of the model.

The parametric results of the instrumental variables regression indicate that the F-test values of the first stage regression, although small, are large enough to reject the initial hypothesis due to the large enough sample size, indicating that the selected instrumental variables are highly correlated with the endogenous variables. In the two-stage least-squares estimation model, the core explanatory variables of both Model 1 and Model 3 passed the 1% significance test with positive coefficients, indicating that environmental regulation has a significant positive impact on industrial efficiency when instrumental variables are added for correction. The increased environmental protection efforts by the government have forced local industrial enterprises to transform and upgrade using technology, eliminating end-use industries and "screening" them, which greatly increases the proportion of green and high-tech enterprises and improves the industrial productivity of the whole region. Compared with the baseline regression, GDP and provincial intervention policies have a significant positive effect on the improvement of industrial efficiency. The higher the GDP is, the more favorable the construction of infrastructure and the introduction of a labor force is. Therefore, the more favorable the increase in industrial efficiency is, the higher the provincial intervention policy is. In other words, the higher the number of state-owned industrial units above the regional scale, the more conducive it is to uploading orders and implementing local government policies related to environmental protection. In the process of implementing environmental protection policies, subsidies will be provided for R&D technology, which is more conducive to industrial efficiency (Table 6).

Table 5: Baseline model (fixed effects) estimation results.

Explanatory variables	Explained variable: industrial efficiency			
	FE (1)	FE (2)	FE (3)	FE (4)
Environmental regulation	−95.45	−146.58	−90.06	−85.62
Foreign direct investment		0.0029***	0.0009***	0.0007***
Gross regional product			1.144***	1.154***
Provincial intervention policies				0.085***
Individual fixed effects	Yes	Yes	Yes	Yes
Time-fixed effects	Yes	Yes	Yes	Yes
Observations	390	390	390	390
Modified R-square	0.90	0.92	0.97	0.97

4.3. Spatial Heterogeneity of Environmental Regulation and Industrial Efficiency

4.3.1. Setting of the Panel Threshold Model. Empirical studies indicate that the backward effect of environmental regulation on industrial efficiency does exist, but the stronger the environmental regulation is, the more significant the backward effect on industrial efficiency is. When questioning the Porter hypothesis, Xu [19] pointed out that the Porter hypothesis is based on the premise of "properly designed environmental regulations." In a certain period, a country or region can withstand the impact of how many enterprises are eliminated at a certain limit. If more than a certain limit, such regulatory intensity and standards are not feasible. Too harsh or too relaxed regulatory intensity may not be conducive to the improvement of industrial efficiency. Therefore, there may be several "thresholds" for environmental regulations to affect industrial efficiency, and the impact on industrial efficiency may differ significantly depending on whether the relevant variables in each province cross the corresponding threshold. At the same time, considering the differences in the level of economic development, foreign investment, and the number of state-owned enterprises in each province, the relationship

Table 6: Estimation results of instrumental variables (2SLS).

Explanatory variables	Explained variable: industrial efficiency			
	IV_2SLS (1)	IV_2SLS (2)	IV_2SLS (3)	IV_2SLS (4)
Environmental regulation	14580.75***	−34490.77	1605.082***	363.87
Foreign direct investment		0.0073	0.0003***	0.0006
Gross regional product			1.312***	1.163***
Provincial intervention policies				0.086***
Phase I F-statistic	3.16	3.10	3.04	2.96
Phase II F-statistic	76.77	173.50	288.66	298.53
Observations	390	390	390	390
Modified R-square	0.28	0.32	0.74	0.97

between the two may be spatial, indicating there may be spatial heterogeneity in the relationship between the two.

To empirically test this hypothesis, this study drew on Hansen [18], Wang [20], and other scholars to first endogenously group 30 Chinese provinces through threshold tests, followed by estimation and significance tests of the threshold characteristics of the environmental regulation effect for each subsample, which not only ensures the reliability of the threshold value but also enables examining the relationship between environmental regulation intensity and industrial efficiency in China "threshold effect." On this basis, a panel threshold regression was conducted to quantitatively analyze the spatial heterogeneity in the relationship between the two. The panel threshold regression model was set as follows:

$$\begin{aligned} \mathrm{IVA}_{it} = {} & \alpha_i + \mathrm{FERI}_{it}\beta_1 \times d(q \le \omega_i) + \mathrm{FDI}_{it}\gamma_1 \times d(q > \omega_i) \\ & + \mathrm{GDP}_{it}\gamma_2 + \mathrm{EP}_{it}\gamma_3 + \mu_i + t_t + \varepsilon_{it}, \end{aligned} \tag{14}$$

where $d(*)$ is the equation sex function, q denotes the threshold variable, and ω_i is the specific threshold value; β_1 and β_2 denote the elasticity coefficients of the backward industrial efficiency of environmental regulation intensity at $q \le \omega_i$ and $q > \omega_i$, respectively. The sign or estimates of β_1 and β_2 should be significantly different if the threshold choice is reasonable and the threshold estimates passed the significance.

4.3.2. Selection and Testing of Threshold Variables. According to the principle of the threshold regression model, it is known that the threshold variables can be either explanatory variables or other independent variables in the model. The intensity of environmental regulation and the level of economic development differ greatly among provinces, so the intensity of environmental regulation and its lag period, as well as the GDP of each province and its lag period, were selected as alternative threshold variables (Table 7).

Based on the threshold value, the 30 provinces are divided into three groups: "weakly regulated," "moderately regulated," and "strongly regulated" (Table 8). For the "weakly regulated" and "medium regulated" groups, they include the major economically developed provinces in China, like Guangdong, Zhejiang, Shanghai, Jiangsu, Beijing, and other eastern provinces, which not only have a higher degree of marketization by their location advantages and economic policy inclination but also have a higher degree of their location advantages and economic policies. These provinces not only have a higher degree of marketization but also can optimize resource allocation and guide industrial restructuring with the help of market forces, therefore improving industrial efficiency. Moreover, the higher level of economic development makes these provinces more capable of introducing advanced foreign technology, high-end equipment, and advanced management experience. Consequently, the improvement of industrial efficiency relies more on the adjustment of factor input structure, upgrading, and technology than on environmental regulation. On the other hand, the implementation of environmental regulations is bound to cause increased costs for enterprises and at a given stage of economic development. There is always a limit to the ability of enterprises to bear rising costs, so the intensity of environmental regulations should be increased within a certain limit. Therefore, we cannot blindly increase regulation without causing the extinguishing of many enterprises, especially small- and medium-sized ones, because too much regulation leads to too a few enterprises.

"Strong regulation" has a positive backward elasticity coefficient; that is to say, the intensity of environmental regulation has a significant positive driving effect on industrial efficiency. In this group, typical industrial and resource-based provinces, like Jilin, Anhui, and Yunnan, are dominant. Based on the unique natural resource endowments of these provinces, primary industries like extractive industries, raw material processing industries, and traditional heavy industries with high energy consumption and pollution occupy an important position in economic development, forming a path to dependence on the "environment-for-growth" development model and an energy-driven development model. As the implementation and intensity of environmental regulations increase, severe environmental constraints are imposed on the existing industrial pattern of this group of provinces to establish an effective push-back mechanism, which not only helps this group of provinces prevent the dilemma of "resource curse" but also provides a strong driving force to break away from the established industrial structure and industrial pattern.

According to the threshold regression results, the backward effect of environmental regulation intensity on

Table 7: Threshold variable selection and self-sampling test.

Threshold variable	Single threshold		Double threshold		Triple threshold	
	F-statistic	*P* value	*F*-statistic	*P* value	*F*-statistic	*P* value
Feri	14.25	0.0233*	6.95	0.2833	8.27	0.4267
Feri(-1)	52.34	0.0033**	41.15	0.0467**	34.13	0.6267
GDP	213.13	0.2400	7.34	0.2400	7.32	0.4367
GDP(-1)	211.13	0.0001***	5.24	0.4267	3.49	0.7933

Table 8: Results of sample grouping based on threshold values.

Subgroups	Threshold variable values	Provinces included in each group	Sample size
Weak regulation	$\text{Feri}(-1) \le 0.69$	Beijing, Hebei, Zhejiang, Liaoning, Fujian, Henan, Guangdong, Shanxi, Heilongjiang, Hubei, Hunan, Guangxi, Chongqing, Sichuan, Qinghai, Xinjiang, Shaanxi	17
Medium regulation	$0.69 < \text{Feri}(-1) \le 1.38$	Shanghai, Inner Mongolia, Tianjin, Jiangsu, Hainan	5
Strongly regulated	$\text{Feri}(-1) > 1.38$	Anhui, Jiangxi, Ningxia, Gansu, Yunnan, Guizhou, Jilin, Shandong	8

Table 9: Panel threshold regression results.

Explanatory variables	Parameter estimates	OLS standard error	*t* value
Foreign direct investment	−0.309**	−0.136	−2.27
Regional economic development level	0.309	0.304	1.02
Provincial intervention policies	−0.201	−0.165	−1.22
$\text{Feri}\ (-1) \le 0.69$	−3.567	1.388**	−2.57
$0.69 < \text{Feri}\ (-1) \le 1.38$	−0.112	0.048**	−2.32
$1.38 \le \text{Feri}\ (-1)$	1.362	1.221	−1.12

industrial efficiency is neither monotonically increasing nor decreasing, and the backward elasticity coefficient of environmental regulation intensity varies significantly across provinces. That is to say, as the intensity of regulation changes from weak to strong, it will have an impact on industrial efficiency that is first inhibited and then promoted. When the industrial value-added is higher than 1.38 units, each unit increase in environmental regulation intensity will promote the regional industrial value-added to 1.362 units. When the environmental regulation intensity crosses the second threshold value of 0.69, the backward elasticity coefficient decreases from 1.362 to −0.112 and passes the 5% significance test. As the threshold variable crosses the threshold value of 0.69, the backward elasticity coefficient decreases further, from −0.112 to −3.567, and this result still passes the 5% significance test (Table 9).

5. Discussion and Conclusion

At present, China's economic development has shifted toward a "new normal," the goal of which is to establish sustainable economic growth through establishing a symmetrical economic structure emphasizing the structure of economic growth rather than the overall economy, such as greening industrial efficiency adjustment. Using panel data of 30 Chinese provinces from 2005 to 2017, this study employed panel regression of fixed effects and the least-squares instrumental variables method to test whether environmental regulation can promote industrial efficiency and the push-back mechanism and verified the threshold characteristics and spatial heterogeneity of environmental regulation through threshold regression. This study indicated environmental regulation would effectively improve industrial production efficiency. As different industries have different marginal cost functions when environmental regulations impose severe environmental constraints on emitting enterprises, enterprises with lower marginal costs gain comparative advantages in "green" development, while enterprises with higher marginal costs will gradually shrink in size due to their poor ability to bear rising costs. Severe formal environmental regulations enable the elimination of pollution-intensive backward and overcapacity, therefore creating a driving force for industrial efficiency improvement. Next, this study discovered 30 Chinese provinces could be classified into "strong," "medium," and "weak" regulations according to whether the intensity of environmental regulations crosses the corresponding threshold. It was found that the majority of Chinese provinces fall into the "weak regulation" group. Further threshold regressions indicated that the impact of environmental regulation on industrial efficiency shows a significant threshold characteristic. That is to say, as the intensity of regulation gradually increases, it will have a suppressive and then promotional impact on industrial efficiency, as well as producing significant spatial heterogeneity.

With the findings of related studies, the following policy insights are obtained. On the one hand, differentiated environmental regulation policies should be developed. To fully exploit and utilize the potential of environmental regulation to improve industrial efficiency, it is necessary to consider the pollution characteristics of different provinces and the spatial heterogeneity of environmental regulation to push-back industrial efficiency and to develop differentiated regulatory policies and intensity. It is not appropriate to raise environmental regulations in provinces where they do not facilitate industrial restructuring. Environmental controls should also be relaxed, relying more on the innovation of industrial policies and the resource allocation and competitive functions of the market, deepening the reform of market mechanisms, and taking full advantage of the market's power to promote dynamic industrial restructuring. For provinces where environmental regulation can effectively improve industrial efficiency, environmental regulation should be utilized as a driving force to establish a long-term mechanism by using higher flexibility of pushback. Local governments should appropriately increase the intensity of existing regulations, set stricter environmental standards, and improve the exit mechanism of enterprises to fundamentally curb resource-depleting production patterns and traditional path dependence, therefore contributing to a sustainable and clean industrial structure. Within a certain period, the increase in the intensity of environmental regulations must be limited to what enterprises can afford because promoting industrial efficiency through environmental constraints is a long-term process that cannot be achieved overnight but should be designed gradually and on a rolling basis based on what enterprises can afford.

On the other hand, we should promote reliance on technology and optimize resource allocation through the market. With the gradual increase of environmental awareness in the public mind, people now have a conscious preference for "technology," "clean," and "environmental protection" products. Therefore, as a producer of industrial enterprises, it should also be time to seize the public's favorite taste, production of environmentally friendly products, and then use technology to differentiate production. This is also a reverse behavior to guide consumers to green consumption. When designing environmental regulation policies, the government should not only restrict the production and emission behavior of producers but also consider consumer behavior and influence resource allocation by guiding and encouraging "green" consumption, thereby forming a new path for industrial transformation.

Data Availability

The data used to support the findings of this study are all included within the article.

Conflicts of Interest

The authors declare that they have no conflicts of interest.

Acknowledgments

This work was supported by the National Natural Science Foundation of China Youth Project (71703082), Postdoctoral Fund (2017M613233), and Shaanxi Normal University Central University Basic Scientific Research Business Fund Special Fund Project (20200347). The authors thank TopEdit (https://www.topeditsci.com) for its linguistic assistance during the preparation of this manuscript.

References

[1] M. E. Porter and C. V. D. Linde, "Toward a new conception of the environment-competitiveness relationship," *The Journal of Economic Perspectives*, vol. 9, no. 4, pp. 97–118, 1995.

[2] P. Chakraborty and C. Chatterjee, "Does environmental regulation indirectly induce upstream innovation? New evidence from India," *Research Policy*, vol. 46, no. 5, pp. 935–955, 2017.

[3] N. S. Trevlopoulos, T. A. Tsalis, K. I. Evangelinos, K. P. Tsagarakis, K. I. Vatalis, and I. E. Nikolaou, "The influence of environmental regulations on business innovation, intellectual capital, environmental and economic performance," *Environment Systems and Decisions*, vol. 41, no. 1, pp. 163–178, 2021.

[4] L. Yang, J. Zhang, and Y. Zhang, "Environmental regulations and corporate green innovation in China: the role of city leaders' promotion pressure," *International Journal of Environmental Research and Public Health*, vol. 18, no. 15, 2021.

[5] G. Zhang, P. Zhang, Z. G. Zhang, and J. Li, "Impact of environmental regulations on industrial structure upgrading: an empirical study on the Beijing-Tianjin-Hebei region in China," *Journal of Cleaner Production*, vol. 238, Article ID 117848, 2019.

[6] X. Yu and P. Wang, "Economic effects analysis of environmental regulation policy in the process of industrial structure upgrading: evidence from Chinese provincial panel data," *The Science of the Total Environment*, vol. 753, Article ID 142004, 2021.

[7] X. Shi and Z. Xu, "Environmental regulation and firm exports: evidence from the eleventh five-year plan in China," *Journal of Environmental Economics and Management*, vol. 89, no. 89, pp. 187–200, 2018.

[8] Y. Lu and L. Wu, *Is There a Pollution Haven Effect? Evidence from a Natural Experiment in China*, Mimeo, N Y. USA, 2012.

[9] C. Zhao, E. Kahn, Y. Liu et al., "The consequences of spatially differentiated water pollution regulation in China," *Journal of Environmental Economics and Management*, vol. 88, pp. 468–485, 2018.

[10] L. Huang and Z. Lei, "How environmental regulation affect corporate green investment: evidence from China," *Journal of Cleaner Production*, vol. 279, Article ID 123560, 2021.

[11] S. Stavropoulos, R. Wall, and Y. Xu, "Environmental regulations and industrial competitiveness: evidence from China," *Applied Economics*, vol. 50, no. 12, pp. 1378–1394, 2018.

[12] T. Zhang, Y. L. Yang, and S. Y. Liu, "Application of biomass by-product lignin stabilized soils as sustainable Geomaterials: a review," *The Science of the Total Environment*, vol. 728, Article ID 138830, 2020.

[13] T. Zhang, G. Cai, and S. Liu, "Application of lignin-based by-product stabilized silty soil in highway subgrade: a field investigation," *Journal of Cleaner Production*, vol. 142, pp. 4243–4257, 2017.

[14] G. L. Feng, B. R. Chen, Q. Jiang, Y. X. Xiao, W. J. Niu, and P. X. Li, "Excavation-induced microseismicity and rockburst occurrence: similarities and differences between deep parallel tunnels with alternating soft-hard strata," *Journal of Central South University*, vol. 28, no. 2, pp. 582–594, 2021.

[15] T. Zhang, G.-J. Cai, and S.-Yu Liu, "Application of lignin-stabilized silty soil in highway subgrade: a macroscale laboratory study," *Journal of Materials in Civil Engineering*, vol. 30, no. 4, Article ID 04018034, 2018.

[16] G. L. Feng, X. T. Feng, B. R. Chen, Y. X. Xiao, and Y. Yu, "A microseismic method for dynamic warning of rockburst development processes in tunnels," *Rock Mechanics and Rock Engineering*, vol. 48, no. 5, pp. 2061–2076, 2015.

[17] S. Xu, "Environmental regulation and firm competitiveness: a challenge based on Porter's hypothesis," *Journal of International Trade*, vol. 32, no. 5, pp. 78–83, 2010.

[18] B. E. Hansen, "Sample splitting and threshold estimation," *Econometrica*, vol. 68, no. 3, pp. 575–603, 2000.

[19] S. Chen and D. Chen, "Haze pollution, government governance, and high-quality economic development," *Economic Research*, vol. 53, no. 02, pp. 20–34, 2018.

[20] Q. Wang, "Fixed-effect panel threshold model using s," *STATA Journal: Promoting communications on statistics and Stata*, vol. 15, no. 1, pp. 121–134, 2015.

Hindawi
Advances in Civil Engineering
Volume 2021, Article ID 9959498, 15 pages
https://doi.org/10.1155/2021/9959498

Research Article

Strength and Expansion and Deformation Characteristics of Modified Expansive Soil by Octadecylamine

Jun-Hua Wu,[1,2,3] **Wei-Chao Ao**,[1] **Mao-Sheng Wang**,[1] **Jia-Ming Liu**,[1] **and Fang-Yuan Fu**[1]

[1]*College of Civil Engineering and Architecture, Nanchang Hangkong University, Nanchang, JiangXi, China*
[2]*Key Laboratory of Hydraulic and Waterway Engineering of the Ministry of Education, Chongqing Jiaotong University, ChongQing, China*
[3]*Key Laboratory of Failure Mechanism and Safety Control Techniques of Earth-Rock Dam of the Ministry of Water Resources, Nanjing, JiangSu, China*

Correspondence should be addressed to Jun-Hua Wu; wjh0796@nchu.edu.cn

Received 28 June 2021; Accepted 17 August 2021; Published 30 August 2021

Academic Editor: Guang-Liang Feng

Octadecylamine was used as a primary water repellent and mixed into the remodeled expansive soil, and modified expansive soils with different water contents and octadecylamine contents were configured. The water repellency level of the modified expansive soil was determined by the drip penetration time method, the corresponding free, unloaded, and loaded swelling rate tests were carried out, and the law of the influence of octadecylamine content and water content on the expansion and deformation of expansive soil was obtained. It can be shown that the modified expansive soil with an octadecylamine content of 0.8% (mass fraction) had an extreme water repellent grade, and the water repellency remained stable. The more the water content and octadecylamine content, the lower the free swelling rate, and the unloaded swelling rate and loaded swelling rate of modified expansive soil tended to be stable. When the octadecylamine content was 0.5% and 0.8%, the free expansion rate was significantly reduced, and the maximum drop was 42%. When the octadecylamine content was increased from 0% to 0.8%, the uncharged expansion stability duration was shortened from 97 h to 47 h, and the expansion rate was reduced from 12.9% to 9.4%. When the mass fraction of octadecylamine was 0.8%, the modified expansive soil with a water content of 20% would decrease its load expansion rate from 2.14% at 50 kPa to 0.01% at 400 kPa. When the load was small, the octadecylamine content and initial water content had a greater impact on the loaded expansion rate; when the load was large, the load became the main factor affecting the loaded expansion rate. Under the same overburden pressure, the more the octadecylamine content was, the lower the soil shear strength was and the more it tended to be stable.

1. Introduction

With the gradual implementation of the strategic goal of "One Belt and One Road" in China, many expansive soil areas will encounter geological and climatic challenges, which may lead to engineering safety problems, such as slope instability, pipe gushing, ground deformation, ground subsidence [1–7]. Expansive soils are rich in hydrophilic clay minerals such as montmorillonite [8], and their engineering properties are more complex than those of general clay soils: effects of water will lead to rapid deterioration of engineering properties of expansive soil, causing long-term serious damage to projects in expansive soil areas, resulting in huge economic losses and human casualties [9]. Therefore, it is of great significance to reasonably solve the engineering problems of expansive soil [10].

There are many research studies on the modification of expansive soil. As early as 1966, Ring [11] studied the problem of soil shrinkage swelling potential and analyzed the basic physical properties of different soils. In 1993, Koyluoglu [12] mentioned that expansive soil had great expansion and contraction property. In addition to its internal structure, the external water mainly entered into it, which provided guidance for the research of expansive soil. In recent years, Gao et al. [13] carried out a series of modification on expansive soil, including physical

modification [14–16], biological modification [17–19], and chemical modification [20–22], and carried out corresponding tests to evaluate these three modification methods. In 2014, Malekzadeh and Bilsel [23] studied the application and influence of crabapple ash in the stability of expansive soil. In 2018, Moghal et al. [24], in the case of lime stabilization, proposed synthetic fiber as an alternative to solve the problem of shrinkage and expansion in expansive soil. Jahangir khazaei et al. [25] improved soft expansive soil by environmental waste and lime. In 2020, Blayi et al. [26] proposed to use waste glass powder (WGP) to improve expansive soil, and Wang et al. [27] conducted a systematic study on the modification of expansive soil with cement. Meng et al. [28] studied the influence of cementing fluid concentration on mechanical properties, microstructure, and hydrological characteristics of expansive soil. Some scholars [29, 30] have adopted materials such as lime [31, 32], cement [33], rubber particles [34], natural sand and gravel [35], rock fiber [36], blast furnace water slag [37], and even vegetation root system [38] to improve the expansion and shrinkage properties of expansive soil. After studying the swelling properties of the expansive soil after chemical modification, it was found that the expansive soil itself still had strong hydrophilicity, and the modification effect is not obvious, but it is realized that waterproofing is of great importance in the protection of expansive soil engineering [39]. The current commonly used waterproofing measures only isolate part of the soil from water, without changing the intrinsic nature of soil hydrophilicity, and the long-term impermeability cannot be guaranteed. Once water enters the soil and acts repeatedly for a long time, the seemingly stable slope may still be unstable again [40].

If expansive soil particles can be treated by technical means to make them change from hydrophilic to hydrophobic and, at the same time, if their expansive deformation characteristics can be improved, then the swelling and shrinkage deformation problems caused by the change of moisture in expansive soil can be effectively avoided, and the corresponding engineering problems can be solved [41]. Therefore, in this paper, octadecylamine was used as the water repellent. By configuring expansive soil samples with different initial water contents and different octadecylamine contents, the water repellency level determination tests and swelling rate tests were carried out, and the influence law of different octadecylamine contents and initial water contents on the water repellency and swelling deformation of modified expansive soil was obtained, which provided new ideas for effectively solving expansive soil engineering problems.

2. Test Materials and Methods

2.1. Experiment Materials. The soil for the test was taken from an area of Kunming City, dried and ground, and then passed through a 2 mm sieve for reserve. Based on the provisions in Highway Geotechnical Test Rules (JTG E40-2007), the basic parameters were as follows: relative density was 2.71 g/cm^3, maximum dry density was 1.56 g/cm^3, optimal water content was 27.2%, liquid limit was 63.5%, plastic limit was 30.8%, plastic index was 32.7, and free expansion rate was 52%. The free expansion rate of this expansive soil was less than 60%, and it belonged to weakly expansive soil. The BT-9300Z laser particle size analyzer produced by Dandong Baxter Instrument Co., Ltd., was used to determine the particle size distribution curve, as shown in Figure 1, and the proportions of soil particle mass with particle size <0.002 mm, 0.002–0.02 mm, and 0.02–2 mm were 6.72%, 56.32%, and 36.96%, respectively. According to the International Triangle Classification of Soil Texture, the test soil was silty loam.

2.2. Experiment Method

2.2.1. Test of Water Repulsion Grade. The water repellent grade of modified expansive soil was determined by the dripping penetration time method, and the classification standard is shown in Table 1. After mixing 0%, 0.2%, 0.3%, 0.5%, and 0.8% octadecylamine with expansive soil, it was placed in an oven with 75°C. It was taken out per two hours and put into the oven after mixing. The modified expansive soil was obtained by mixing four times. Octadecylamine is a surfactant with extreme water repellency. Its chemical properties are as follows: melting point—50–52°C and freezing point—53.1°C. Therefore, when the temperature is between 75°C and 80°C, octadecylamine can be liquified and then encapsulated outside the soil particles, as shown in Figure 2 (the white matter outside the soil is octadecylamine). In order to reduce the influence of sample preparation nonuniformity, the dripping penetration time was measured at three places (regular triangle distribution and spacing of 4 cm) on the sample surface, and the amount of dripping water at each place was 80 μL. We take the average as the final result. The temperature was controlled at 24°C during the whole test (±1°C), and humidity was controlled at 64% ± 2%.

2.2.2. Free Expansion Rate Experiment. Five kinds of modified expansive soils with octadecylamine content of 0%, 0.2%, 0.3%, 0.5%, and 0.8% were selected in the experiment. According to the standard for soil test methods (by GB/T50123-2019), the free expansion rate tests of five kinds of modified expansive soils with octadecylamine content of 0%, 0.2%, 0.3%, 0.5%, and 0.8% were carried out.

2.2.3. Unloaded Expansion Rate Test. According to the test results of water repellent grade, 20 groups of samples with octadecylamine content of 0%, 0.2%, 0.3%, 0.5%, and 0.8% and initial water content of 5%, 10%, 15%, and 20% were selected. After sealing for 24 hours, the jack (Figure 3(a)) was used for sampling. According to the standard for soil test methods (GB/T50123-2019), the unloaded expansion rate test was carried out by using WG-1B triple medium pressure consolidometer (Figure 3(b)).

2.2.4. Loaded Expansion Rate Test. According to the standard for soil test methods (GB/T50123-2019), the loaded expansion test was carried out. According to the test results of

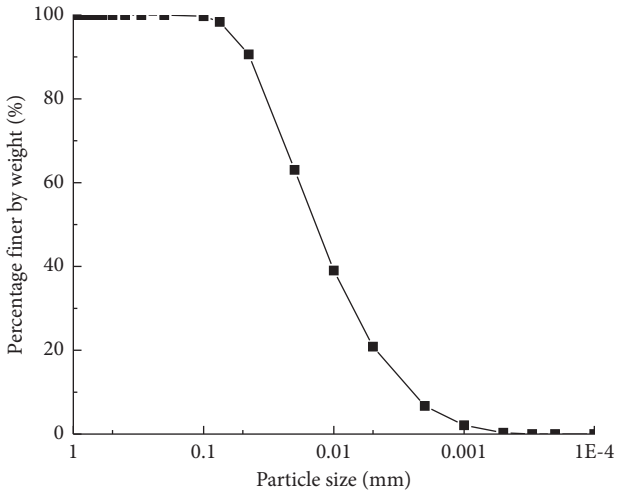

Figure 1: Gradation curve of expansive soil particle size.

Table 1: Classification standard of WDPT

Infiltration time (s)	<5	5~60	60~600	600~3600	>3600
Water repellent grade	Wettable	Slight	Secondary	Serious	Extreme

water repellent grade, 20 groups of samples with content of octadecylamine of 0%, 0.2%, 0.3%, 0.5%, and 0.8% and initial water content of 5%, 10%, 15%, and 20% were selected. After sealing for 24 hours, the jack was used to take samples. The soil samples were placed in the consolidometer, and the vertical loads were applied to 50, 100, 200, and 400 kPa, respectively. The readings were recorded after the predetermined load was stable. After that, pure water was injected to make the pure water 5 mm higher than the sample. The meter was read every 2 hours, and the stable reading was recorded. After the experiment, the water content after expansion was calculated by drying and weighing.

2.2.5. Direct Shear Tests. According to the test results of water repellent grade of eighteen amine modified expansive soils, 0%, 0.2%, 0.3%, 0.5%, and 0.8% of the eighteen amine contents correspond to the modified expansive soil with different water repellent grades. The direct shear test was carried out according to the initial dry density 1.56 g/cm^3. According to the standard for soil test methods (GB/T50123-2019), the unconsolidated undrained direct shear tests of unsaturated water repellent expansive soils with different octadecylamine contents were carried out by using lever type direct shear apparatus (Figure 4).

3. Test Results and Analysis

3.1. Water Repellent Grade of Modified Expansive Soil. The water repellent effect diagram is shown in Figure 5, the contact angle diagram is shown in Figure 6, and the measurement results of water repellent grade of expansive soil modified with different octadecylamine contents are listed in Table 2. It can be seen from Figure 5 that the water droplets on the hydrophilic expansive soil had been completely absorbed by the soil, and the water droplets on the surface of the water repellent expansive soil with 0.8% octadecylamine content still remain full, showing extreme water repellency. The contact angle of hydrophilic expansive soil with 0% octadecylamine content was 12.114° and that of water repellent expansive soil with 0.8% octadecylamine content was 65.441°, respectively. When octadecylamine content was increased from 0% to 0.8%, the contact angle increases by 54.327° and the greater the contact angle was, the higher the water repellency of soil was, which indicated that adding octadecylamine to expansive soil could effectively increase the water repellent effect of soil. It can be seen from Table 2 that the water repellent grade of modified expansive soil was wettable without octadecylamine and slight with 0.2% octadecylamine. Due to the low content of octadecylamine, most of the soil particles were not covered by octadecylamine, and the water repellent grade was still wettable; when octadecylamine content was 0.3% and 0.5%, the water repellency grade was moderate and severe, and the sample had good water repellency; when octadecylamine content was 0.8%, the water repellent grade of the sample was extreme. It can be shown that the more the octadecylamine content was, the stronger the water repellency of expansive soil was. Because the water repellent grade of modified expansive soil was extreme when octadecylamine content was 0.8%, the modification tests of expansive soil with higher content of octadecylamine are not carried out.

3.2. Free Expansion Rate of Modified Expansive Soil. The test results of free expansion rate of expansive soil modified by different octadecylamine contents are shown in Table 3, and the corresponding free expansion rate change rule is shown in Figure 7. It can be seen that the slope, intercept, and R^2 of modified expansive soil with different octadecylamine contents was −27.74, 53.39, and 0.969, respectively. The more the octadecylamine content, the lower the free expansion rate, and there was a negative correlation between them. When octadecylamine content was 0%, the free expansion rate was 52%. According to the corresponding index, the sample soil was weak expansive soil. When octadecylamine content was 0.2%, the free expansion rate was 49%, which had little change compared with that when octadecylamine content was 0%. When octadecylamine content was 0.3%, the free expansion rate was 45%, showing weak expansion potential. When octadecylamine content was 0.5%, the free expansion rate was 41%, and it would lose its weak expansion potential. When octadecylamine content was 0.8%, the free expansion rate was 30%, which was lower than 40% of the corresponding index standard. The expansive property of the sample was too small, and it could not be defined as weak expansive soil.

The main reason for the decrease of free expansion rate of expansive soil with the increase of octadecylamine content was that octadecylamine was dissolved and bound to the surface of soil particles when preparing different octadecylamine

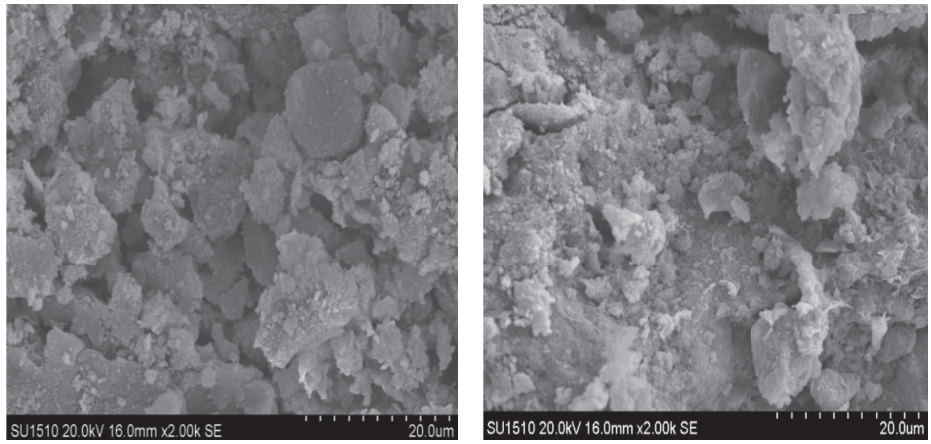

(a) (b)

Figure 2: (a) Soil surface without octadecylamine, 2000x. (b) Soil surface with 0.8% octadecylamine, 2000x.

(a) (b)

Figure 3: Hydraulic jack (a). WG-1B triple medium pressure consolidometer (b).

Figure 4: Unsaturated direct shear apparatus.

modified expansive soils. In the process of free expansion rate test, the ability of water absorption and expansion of expansive soil was reduced, and the free expansive soil decreases with the increase of octadecylamine content. In this experiment, the free expansion rate of 0.2% and 0.3% octadecylamine had little change compared with that of no octadecylamine. When

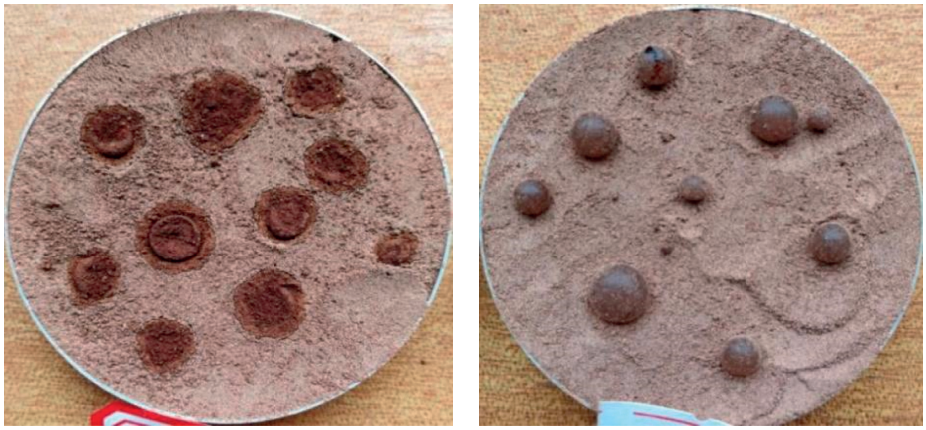

(a) (b)

Figure 5: Hydrophilic expansive soil (a). Water repellent expansive soil (b).

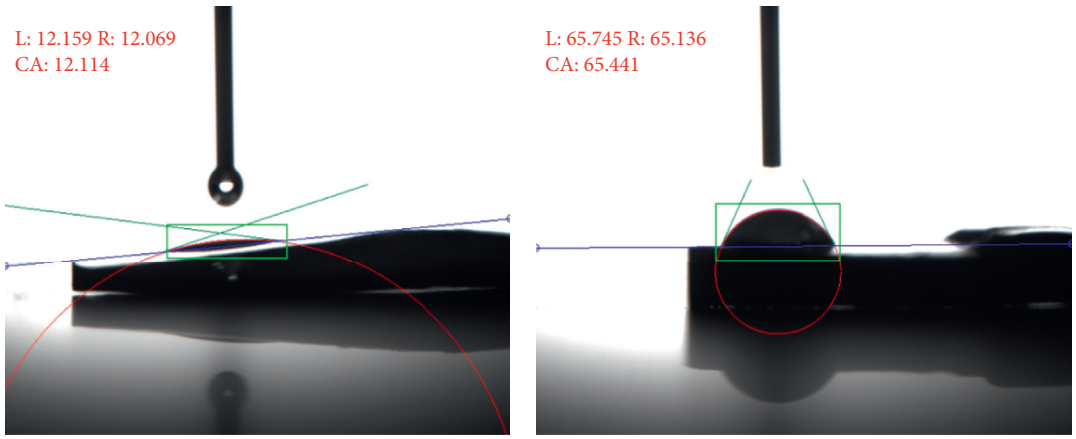

(a) (b)

Figure 6: Contact angle of hydrophilic expansive soil (a). Contact angle with hydrophobic expansive soil (b).

Table 2: Water repellent grade of modified expansive soil.

Octadecylamine content (%)	0	0.2	0.3	0.5	0.8
Water repellent grade	Wettable	Slight	Secondary	Serious	Extreme

Table 3: Free swelling rate of modified expansive soil with different octadecylamine contents.

Octadecylamine content (%)	First free expansion rate (%)	Second free expansion rate (%)	Average value (%)
0.0	51	53	52
0.2	50	48	49
0.3	46	44	45
0.5	43	39	41
0.8	32	28	30

octadecylamine content was 0.5% and 0.8%, the free expansion rate decreased significantly, and the maximum decrease was 42%. It was directly related to the different grades of octadecylamine water repellent expansive soil. The higher the grade of water repellent expansive soil was, the greater the decrease of free expansion rate was.

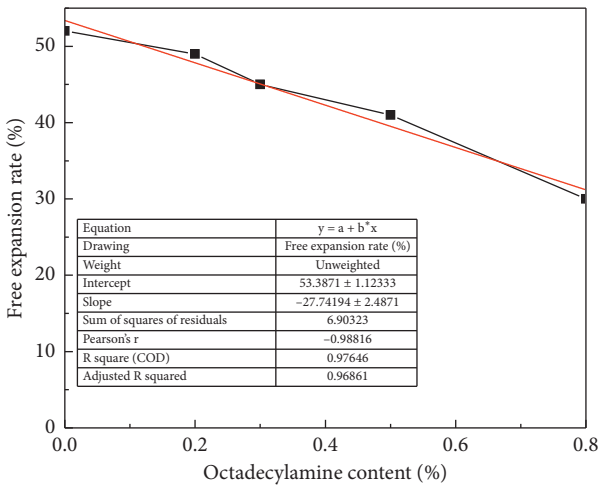

Figure 7: Variation of free swelling rate of expansive soil with different octadecylamine contents.

3.3. Unloaded Expansion Rate of Modified Expansive Soil

3.3.1. Effect of Octadecylamine and Water Content on Unloaded Expansion. The influence of different octadecylamine contents and sample water contents on the unloaded expansion rate of modified expansive soil is shown in Figure 8. It can be seen from Figure 8(a) that under the same octadecylamine content, the more the water content, the lower the unloaded expansion rate of expansive soil, the larger the area filled with water in the internal pores of the sample, the lower the water absorption capacity, and the less the expansion deformation of the sample. It can be seen from Figure 8(b) that the more octadecylamine content the sample contains, the lower the no-load swelling ratio under the same water content. The more the octadecylamine content was, the larger the area covered by octadecylamine on the surface of expansive soil particles was, the more difficult it was for external water to penetrate into the sample, and the lower the unloaded expansion rate was. When octadecylamine content was increased from 0% to 0.2%, the unloaded expansion of the sample with 15% water content decreased from 12.1% to 9.9%, with a decrease of about 20%. When the octadecylamine content was increased to 0.5%, the rate of unloaded expansion decreased slowly, and the unloaded expansion rate was about 5.6%. When octadecylamine content was increased to 0.8%, the unloaded expansion rate remained almost unchanged. It can be shown that octadecylamine could reduce the expansibility of expansive soil to a certain extent, but it could not reduce the expansibility indefinitely, and there was a critical range. According to the experimental results in this paper, when octadecylamine content was 0.8%, its water repellent performance reached the extreme, and the unloaded expansion rate could also be effectively reduced.

3.3.2. Influence of Octadecylamine and Water Content on Expansion Time History. Taking the curves of the time-free expansion rate of octadecylamine content of 0%, 0.2%, 0.5%, and 0.8%, the influence of different octadecylamine contents and water contents on the expansion time course of expansive soil was studied. The results are shown in Figure 9. It can be seen that ①when the octadecylamine content was the same, the smaller the initial water content of the sample was, the larger the expansion was when the expansion was stable because when the octadecylamine content was the same, the smaller the initial water content was, the more the water infiltrated into the pores of the sample, and the greater the expansion was when the expansion deformation was stable. ② When octadecylamine was not added, with the passage of time, the amount of expansion of the unloaded expansion rate first increased faster and then stabilized after 4 days. After adding octadecylamine, the expansion time history curve presented an inverted "s" shape: at the initial stage of expansion, the sample absorbed water slowly, and after a certain period of time, the expansion rate increased obviously; after reaching a certain value, the expansion rate slowed down obviously and finally tended to be stable. The presence of octadecylamine would reduce the water infiltration channel to a certain extent and delay the process of water infiltration. The more the octadecylamine content, the more obvious the delay. However, water could still slowly penetrate into the internal pores, but the infiltration time was relatively longer, so the initial expansion rate was smaller, and the curve showed a slow rising type. When the water infiltrated for a certain period of time, the water connectivity in the pores of the sample increased gradually. At this time, the amount of water infiltration increased significantly, and the expansion rate also increased significantly. When the internal pore channels were completely penetrated by water, the expansion rate would be significantly reduced, and the presence of octadecylamine had little effect on water infiltration. ③When the water content of the sample was the same, the more the octadecylamine content was, the shorter the time for the unloaded expansion rate to reach stability, and the lower the corresponding unloaded expansion rate was. When the water content was 20% and when octadecylamine content was 0%, the expansion stability time was about 4000 min, and the unloaded expansion rate was 11.18%. When octadecylamine content was 0.8%, the expansion time was about 2000 min, the unloaded expansion rate was 8.16%, and the decrease rate was about 30%.

3.4. Loaded Expansion Rate of Modified Expansive Soil

3.4.1. Influence of Initial Water Content on Loaded Expansion Rate. The variation curve of the loaded expansion rate of the sample with different initial water contents is shown in Figure 10. It can be seen that ①when the octadecylamine content was the same, the more the initial water content was, the lower the charged expansion rate was, which was similar to the test result of unloaded expansion rate; ②the more the vertical load was, the lower the loaded expansion rate was. When the vertical load was small, octadecylamine content and initial water content had great influence on the loaded expansion rate. With the increase of vertical load, the amplitude gradually decreased, and the load became the main factor affecting the expansion rate.

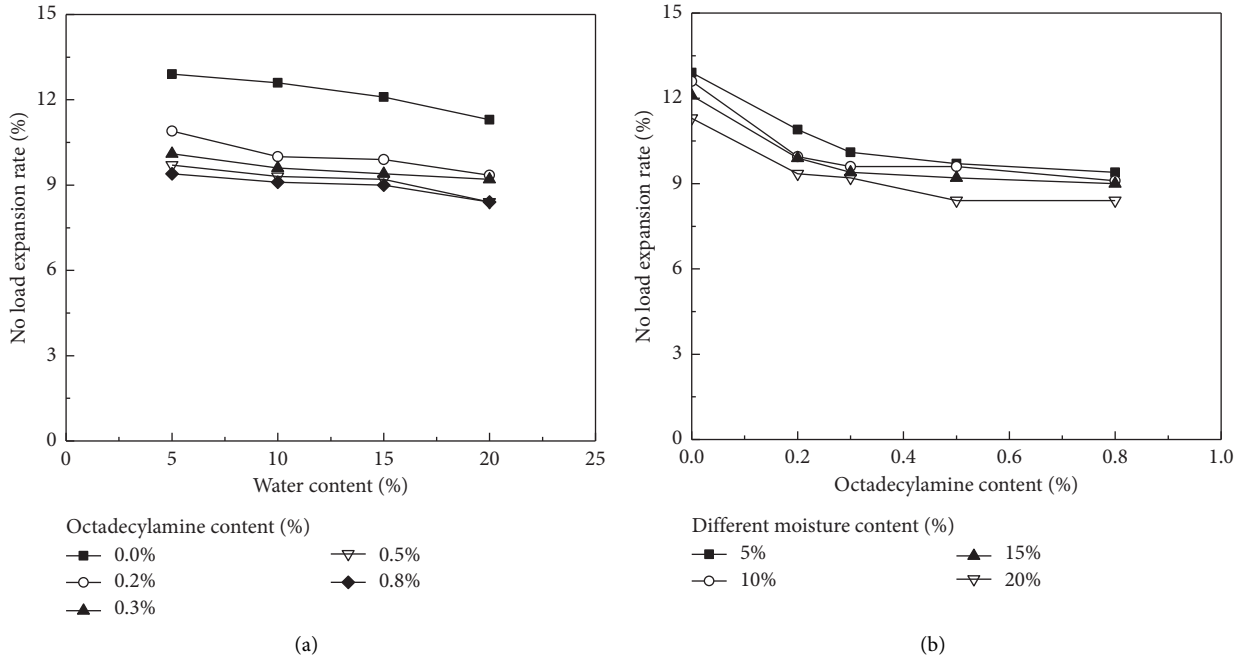

(a) (b)

Figure 8: Relationship between unloaded expansion rate and water content and octadecylamine content. (a) Curve of unloaded expansion with water content. (b) Curve of unloaded expansion with octadecylamine content.

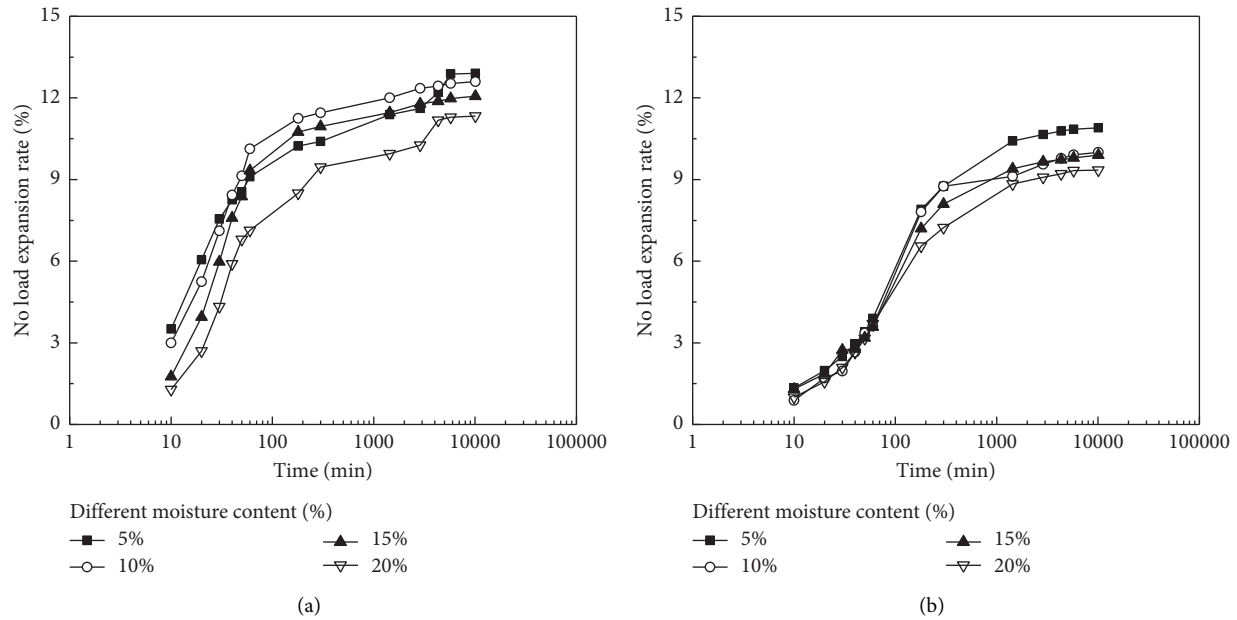

(a) (b)

Figure 9: Continued.

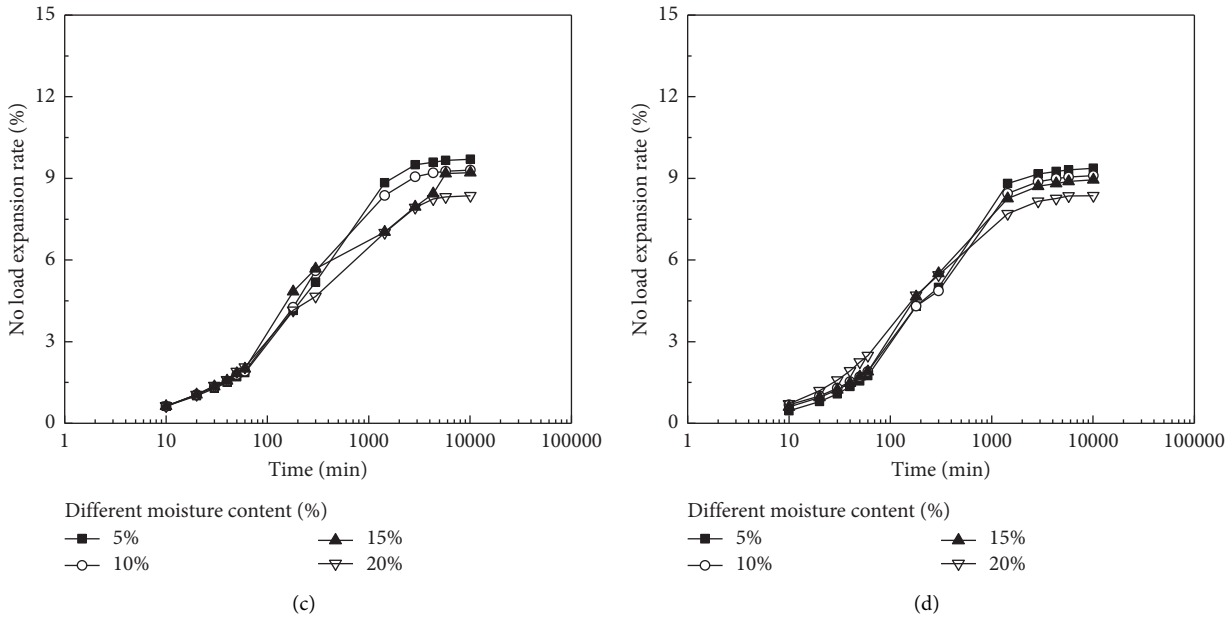

Figure 9: Time history curves of unloaded expansion for different octadecylamine contents. (a) Octadecylamine content of 0%. (b) Octadecylamine content of 0.2%. (c) Octadecylamine content of 0.5%. (d) Octadecylamine content of 0.8%.

3.4.2. Influence of Octadecylamine Content on Charged Expansion Rate. The relation curve of load expansion rate with different octadecylamine contents is shown in Figure 11. It can be seen that when the vertical load was the same, the more the octadecylamine content was, the lower the load expansion rate of the sample was. When octadecylamine content was 0.8%, the charged expansion rate was the smallest. When the water content of the sample was 20% and the vertical load was 50 kPa, octadecylamine content was decreased from 0% to 0.8%, and the load expansion rate decreased from 4.89% to 2.14%, a decrease of about 57%. It can be shown that the presence of octadecylamine could also effectively reduce the swelling property of expansive soil, which was beneficial to engineering.

3.5. Direct Shear Tests. The relationship between horizontal stress and displacement of samples with different octadecylamine contents is shown in Figure 12. It can be seen that ①the more the vertical load was, the more the maximum horizontal load of hydrophilic expansive soil and water repellent expansive soil were. ②Under the same vertical load, the more the octadecylamine content was, the stronger the water repellency was and the smaller the maximum horizontal load was. Under the vertical load of 300 kPa, the maximum horizontal load of hydrophilic expansive soil was 1300 N. When octadecylamine content was 0.8%, the maximum horizontal load of water repellent expansive soil was 900 N, which was 400 N less than that of hydrophilic expansive soil. It can be shown that there was a negative correlation between the maximum horizontal load and octadecylamine content.

The relationship between peak shear stress (shear strength) and overlying pressure under different octadecylamine contents is shown in Figure 13. It can be seen that there was a positive correlation between the shear strength and the vertical pressure. The correlation could be described by Mohr-Coulomb strength criterion, and the fitting results are shown in Table 4. It can be seen that under the same vertical load, the more the octadecylamine content was, the lower the shear strength was. When octadecylamine content was higher, the impact on shear strength changed more obviously, and the decline was greater. It can be seen from Table 4 that when the octadecylamine content was 0%, 0.2%, and 0.3%, f was 44.12°, 43.15°, and 39.70°, respectively, and it can be shown that octadecylamine content had little effect on the shear strength of expansive soil. When the octadecylamine content was 0.5% and 0.8%, f was 34.459° and 33.09°, respectively, and the shear strength varied greatly. When octadecylamine content was increased from 0% to 0.2%, 0.3%, 0.5%, and 0.8%, the cohesive force of expansive soil decreased gradually, from 132.6 kPa to 109.69 kPa, 105.6 kPa, 96.25 kPa, and 83.4 kPa. It can be seen that the more the water repellent grade of soil samples was, the more the effect of the shear strength was and the lower the shear strength was.

In order to analyze the influence of octadecylamine content and vertical pressure on the shear strength of expansive soil, the envelope diagram of octadecylamine modified expansive soil and octadecylamine content was drawn, as shown in Figure 13.

It can be seen from Figure 14 that ① when the vertical pressure was 100 kPa, the more the octadecylamine content was, the lower the shear strength was. When the vertical pressure was 200 kPa, with the increase of octadecylamine content, the shear strength first decreased slowly, then decreased rapidly, and finally tended to be stable. When the vertical pressure was 300 kPa, the change law was similar to

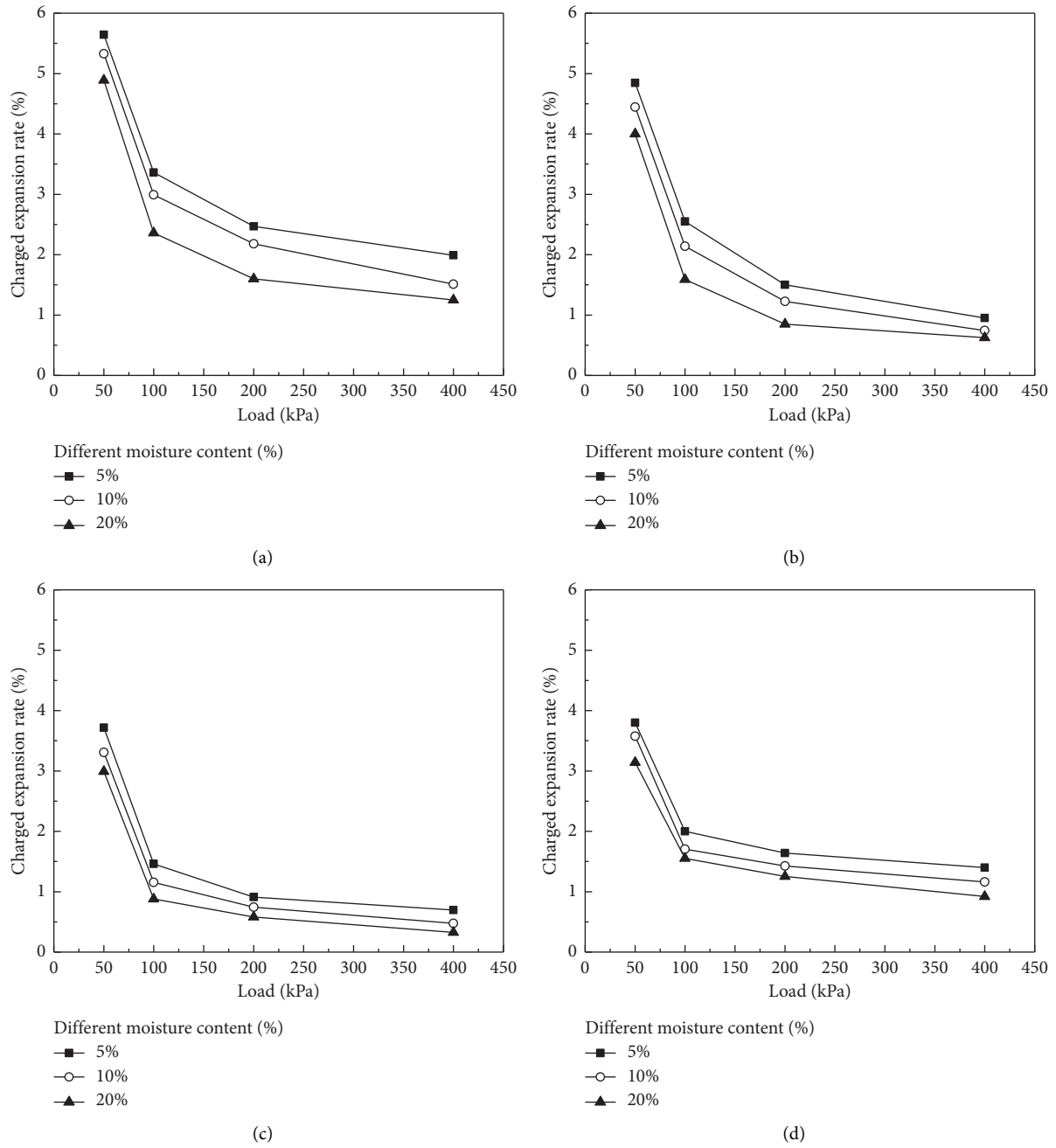

Figure 10: Relation curve of loaded expansion rate under different water contents. (a) Octadecylamine content of 0%. (b) Octadecylamine content of 0.2%. (c) Octadecylamine content of 0.5%. (d) Octadecylamine content of 0.8%.

that when the vertical pressure was 200 kPa. When the vertical pressure was 400 kPa, the shear strength decreased with the increase of octadecylamine content. ② Under different vertical pressures, the shear strength and octadecylamine content were linear. When octadecylamine content was less than 0.3%, the shear strength decreased slowly. When octadecylamine content exceeded 0.3%, the shear strength decreased greatly. When octadecylamine content was 0.5%–0.8%, it tended to be stable. In general, with the increase of octadecylamine content, the shear strength first decreased slightly, then decreased greatly, and finally tended to be stable.

The relationship between the octadecylamine content and total internal friction angle is shown in Figure 15. It can be seen that with the increase of octadecylamine content, the internal friction angle decreased, and the decrease range was slightly reduced. The negative exponential equation (1) could be used for fitting.

$$\varphi = ae^{-bx} + c, \tag{1}$$

where f was the angle of internal friction, X was the octadecylamine content, a was the extent to which the direction was stretched, b was the degree of stretching in the X

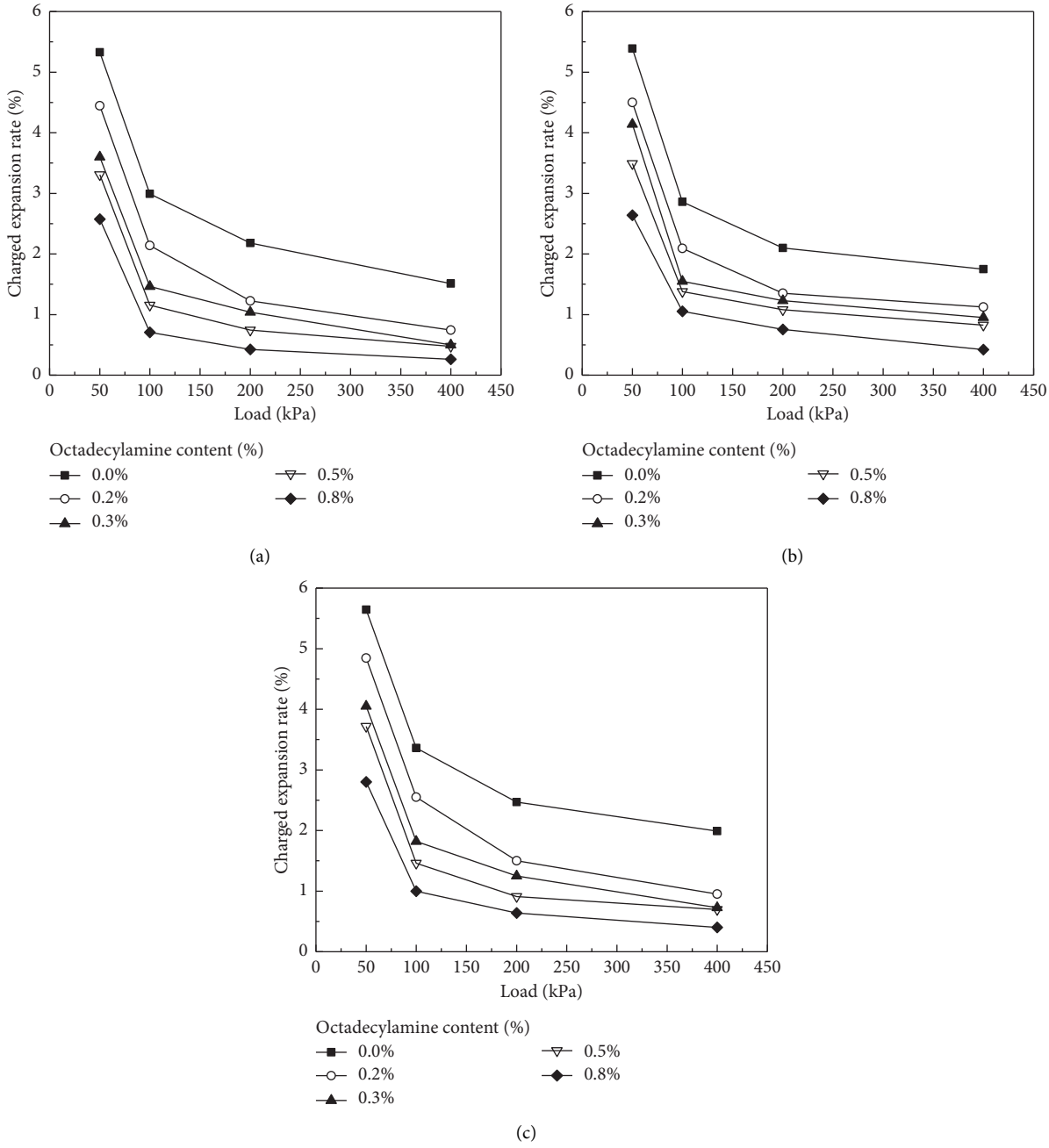

Figure 11: Relation between expansion rate and load under different octadecylamine contents. (a) Water content of 5%. (b) Water content of 10%. (c) Water content of 20%.

direction, and c was the intercept; a, b, and c could reflect the relationship between internal friction angle and octadecylamine content to a certain extent. The fitting results are shown in Table 5.

The relationship between octadecylamine content and total cohesion is shown in Figure 16. It can be seen that with the increase of octadecylamine content, the total cohesion presented a linear downward trend, which could be fitted by the first-order (2). On the whole, the shear strength tended to weaken with the increase of octadecylamine content, but the overall decline could still be accepted by the engineering.

$$c = dx + f, \tag{2}$$

where c was the cohesion, x was the octadecylamine content, d was the slope, and f was the intercept, which could reflect the relationship between cohesion and octadecylamine content to a certain degree. The fitting results are shown in Table 5.

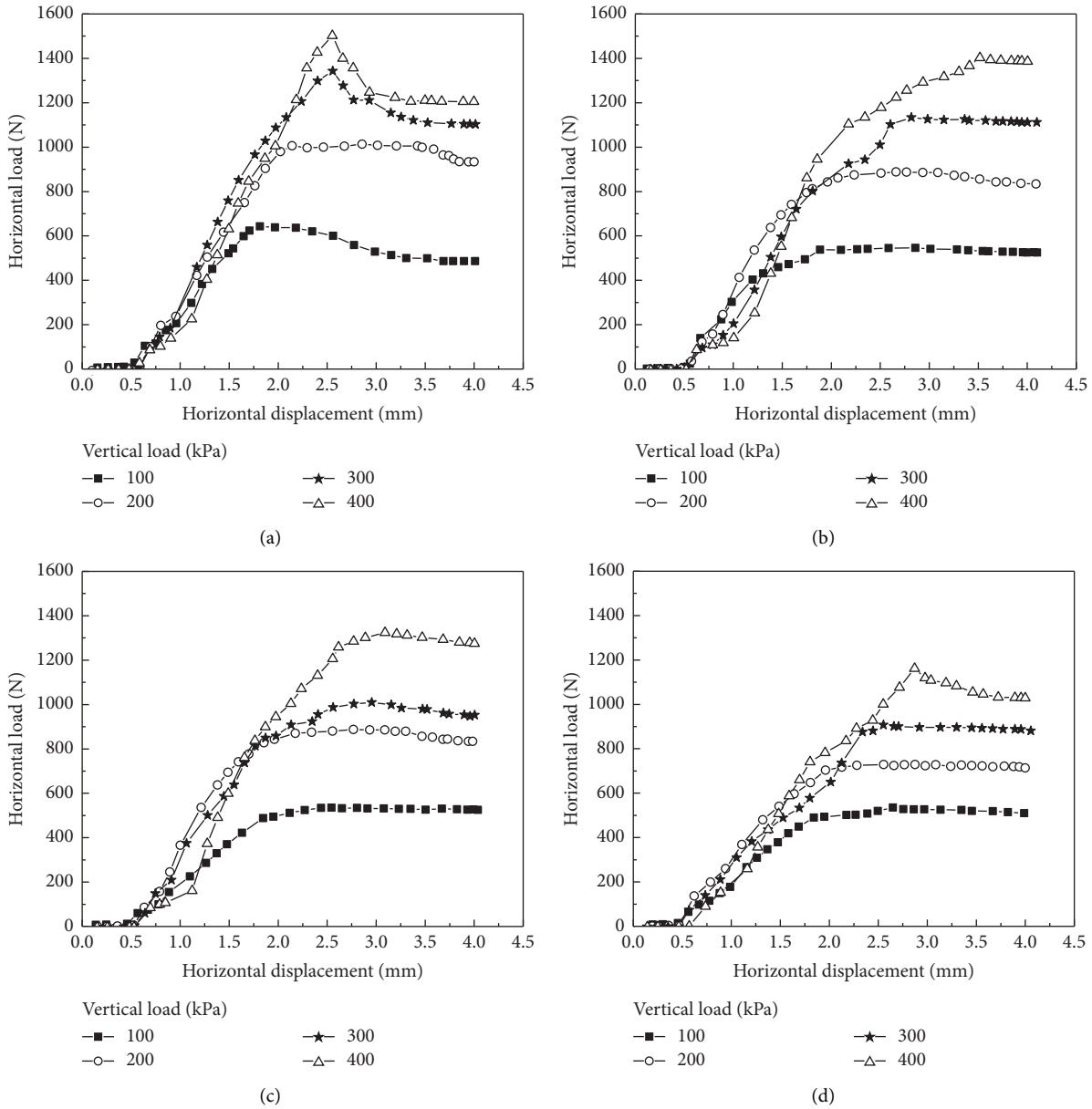

Figure 12: Continued.

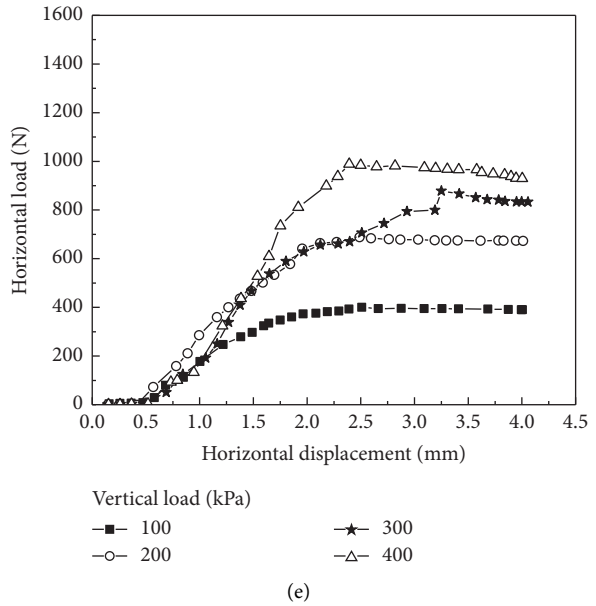

Figure 12: Relationship between horizontal load and horizontal displacement of expansive soil with different octadecylamine contents. (a) Octadecylamine content of 0%. (b) Octadecylamine content of 0.2%. (c) Octadecylamine content of 0.3%. (d) Octadecylamine content of 0.5%. (e) Octadecylamine content of 0.8%.

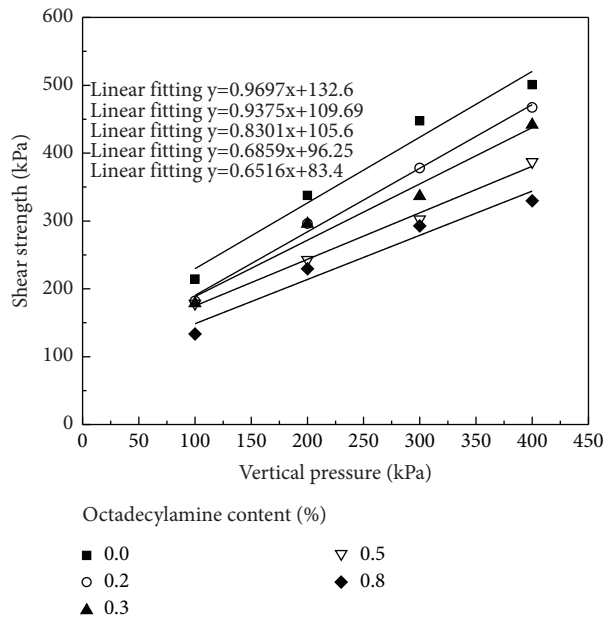

Figure 13: Relationship between shear strength and vertical pressure under different octadecylamine contents.

Table 4: Fitting results of internal friction angle and cohesion of modified expansive soil with different octadecylamine contents.

Octadecylamine content (%)	Φ (°)	C (kPa)
0	44.12	132.6
0.2	43.15	109.69
0.3	39.70	105.6
0.5	34.45	96.25
0.8	33.09	83.4

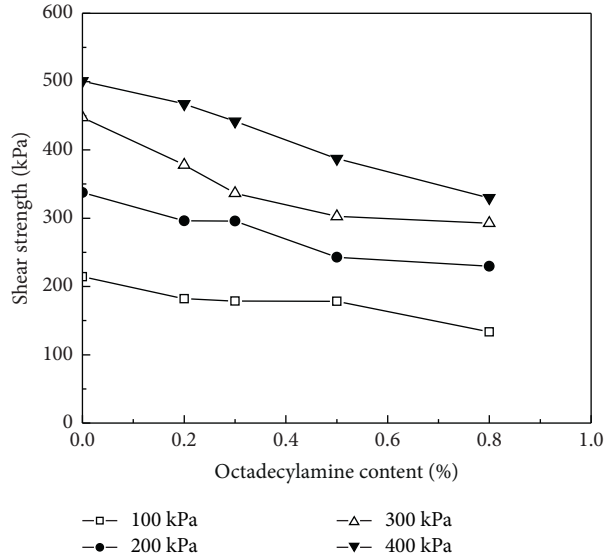

Figure 14: Envelope diagram of shear strength and octadecylamine content under different octadecylamine contents.

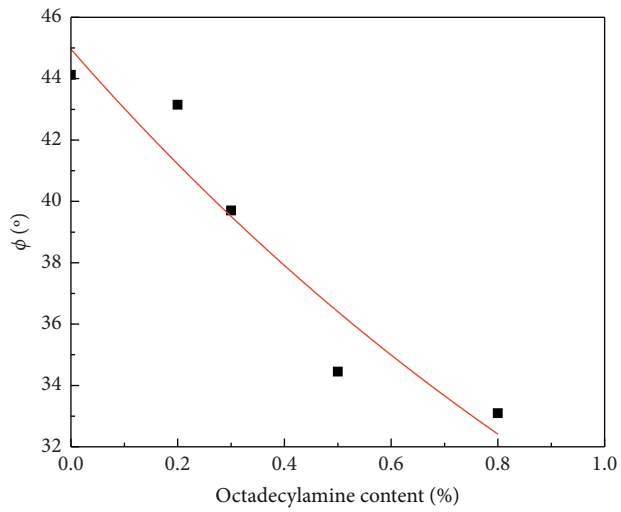

Figure 15: Relationship between internal friction angle and octadecylamine content.

Table 5: Fitting results.

Function	Value	Correlation coefficient
Internal friction angle	$a = 32$	0.999
$\varphi = 32e^{-0.62x} + 12.96$	$b = 0.62$	0.996
	$c = 12.96$	0.999
Cohesion	$d = -57067$	0.932
$c = -56.67x + 126.27$	$f = 126.27$	

x is octadecylamine content.

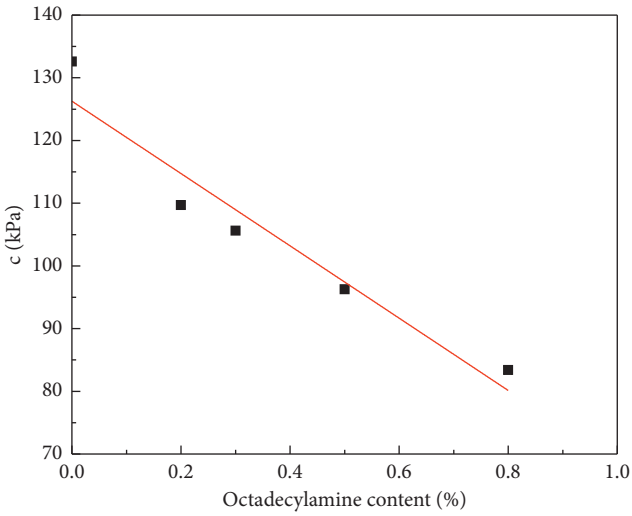

Figure 16: Relationship between cohesion and octadecylamine content.

4. Conclusions

(1) Water repellent with different octadecylamine contents could reduce the free expansion rate of expansive soil. The more the octadecylamine content is, the lower the free expansion rate is.

(2) The octadecylamine content and initial water content are important factors affecting the expansibility of expansive soil. When octadecylamine content is the same, the more the initial water content is, the lower the unloaded expansion rate and the loaded expansion rate are. The more water content the expansive soil contains, the more obviously the unloaded expansion rate of undisturbed soil decreases. When the water content of the sample is the same, the more octadecylamine content the expansive soil contains, the lower the unloaded expansion rate is and the more it tends to be stable. The existence of octadecylamine could effectively reduce the expansibility of expansive soil.

(3) Under the same octadecylamine content, the more the vertical load is, the lower the loaded expansion rate is. When the vertical load was small, octadecylamine content and initial water content had great influence on the loaded expansion rate. When the vertical load was large, the load was an important factor affecting the expansibility of expansive soil. When the vertical load was constant, the more the octadecylamine content is, the lower the loaded expansion rate is.

(4) The existence of octadecylamine can effectively inhibit the swelling characteristics of expansive soil. When the octadecylamine content is greater than or equal to 0.8%, the water repellent grade is extreme, which can inhibit the water swelling of expansive soil to a great extent, and the water repellent effect is good, which can provide a reference for solving the related problems in the expansive soil area. The more the vertical pressure, the more the shear strength of hydrophilic expansive soil and water repellent expansive soil.

(5) Under the same vertical pressure, the more the octadecylamine content is, the lower the shear strength is, and when octadecylamine content is increased, the influence of the shear strength was greater. The shear strength is negatively correlated with the water repellent grade. It has been shown that the influence of the shear strength is greater with the increase of the water repellent grade. Under different vertical pressures, the shear strength has a linear relationship with octadecylamine content, which conformed to the Mohr–Coulomb shear strength criterion.

Data Availability

The data used to support the findings of this study are included within the article.

Disclosure

All opinions, findings, and conclusions in this work represent the views of the authors only.

Conflicts of Interest

The authors declare that they have no conflicts of interest.

Acknowledgments

This study was supported by Project (51869013) of the National Natural Science Foundation of China, Project (SLK2021A05) of Open Research Fund of Key Laboratory of Hydraulic and Waterway Engineering of the Ministry of Education, Project (YK321013) of Open Research Fund of Key Laboratory of Failure Mechanism and Safety Control Techniques of Earth-Rock Dam of the Ministry of Water Resources, and Project (YC2020-094) of Innovation Fund of Nanchang Hangkong University for Graduate Students.

References

[1] W. Yang, "Significance of seepage prevention of water conservancy project channel and its technical measures," *Henan water conservancy and south to North Water Diversion*, vol. 4, pp. 18-19, 2015.

[2] D. G. Toll, "Briefing: r," *Proceedings of the Institution of Civil Engineers - Geotechnical Engineering*, vol. 149, no. 4, pp. 211–216, 2001.

[3] L. Chengyan, X. Hewei, L. Ya et al., "Discussion on slope piping phenomenon and slope safety," *Value Engineering*, vol. 37, no. 25, pp. 107–109, 2018.

[4] C. Liang, "Investigation and evaluation method of ground deformation geological disaster," *Science and technology and enterprise*, vol. 15, p. 115, 2011.

[5] F. Guangliang, B. Chen, Q. Jiang et al., "Excavation-induced microseismicity and rockburst occurrence: similarities and differences between deep parallel tunnels with alternating soft-hard strata," *Journal of Central South University*, vol. 28, pp. 582–594, 2021.

[6] J. Chen, L. Kong, Y. Zhao et al., "Analysis of influence factors of suction and deformation of unsaturated soil under evaporation," *Geotechnical mechanics*, vol. 28, no. 9, pp. 1967–1773, 2007.

[7] F. Guangliang, X. Feng, B. Chen et al., "A microseismic method for dynamic warning of rockburst development processes in tunnels," *Rock Mechanics and Rock Engineering*, vol. 48, no. 5, pp. 2061–2076, 2015.

[8] Y. Zhang, C. Guo, Y. Qu et al., "Discovery of expansive diatomite in Tengchong, Yunnan Province and its engineering geological significance," *Acta Geologica Sinica*, vol. 20, no. 2, pp. 266–275, 2012.

[9] S. Li and H. Chen, "The effect of quicklime on reducing the expansive soil disaster -- Taking Shandong (an) - lai (Wu) first class highway as an example," *Journal of geological disasters of China*, no. 1, pp. 67–74, 1992.

[10] S. Fang and H. Yao, "Effect of K + on swelling rate of expansive soil," *Journal of Anhui Jianzhu University*, vol. 27, pp. 23–28, 2019.

[11] W. E. Ring, "Shrink-swell Potentials of Soil," *Highway Research Record No. 119*, pp. 17–21, National Academy of SciencesNational Council publication, Washington, DC, USA, 1966.

[12] U. Koyluoglu, *Soil Mechanics for Unsaturated Soils: D. G. Fredlund & H. Rahardjo*, John Wiley & Sons, Hoboken, NJ, USA, pp. 449-450, 1993.

[13] L. Gao, S. Ding, H. Du et al., "Research progress of modified treatment methods of expansive land in China," *Exploration and mining engineering in the west*, vol. 7, pp. 41–44, 2006.

[14] H. Li, X. Yu, L. Lu et al., "Experimental study on lime modification of expansive soil in highway engineering," *Journal of Shandong University of Technology*, vol. 1, pp. 92–96, 2002.

[15] Z. Qiu and M. Yang, "Experimental study on mechanical properties of lime modified expansive soil," *Subgrade engineering*, vol. 3, pp. 32–35, 2000.

[16] W. Lee, M.-K. Jin, W.-C. Yoo, and J.-K. Lee, "Nanostructuring of a polymeric substrate with well-defined nanometer-scale topography and tailored surface wettability," *Langmuir*, vol. 20, no. 18, pp. 7665–7669, 2004.

[17] J. Zeng, C. Wen, J. Bao et al., "Laboratory triaxial test of enzyme modified expansive soil," *Chinese scientific paper*, vol. 12, no. 6, pp. 660–665, 2017.

[18] M. M. Roper, "The isolation and characterisation of bacteria with the potential to degrade waxes that cause water repellency in sandy soils," *Soil Research*, vol. 42, no. 4, pp. 427–434, 2004.

[19] C. Franco, M. Tate, and J. Oades, "Studies on non-wetting sands .1. The role of intrinsic particulate organic-matter in the development of water-repellency in non-wetting sands," *Soil Research*, vol. 33, no. 2, pp. 253–263, 1995.

[20] S. Qu and Y. Tang, "Experimental study on chemical improvement of expansive soil," *Jiangxi building materials*, vol. 22, pp. 5-6, 2017.

[21] J. Wu, X. Zhou, L. Hui et al., "Determination and variation of soil water repellency under different water repellents," *Journal of agricultural engineering*, vol. 34, no. 17, pp. 109–115, 2018.

[22] J. Wu and L. Hui, "Determination of shear strength of unsaturated soil under the action of water repellent and its changing law," *Journal of agricultural engineering*, vol. 35, no. 6, pp. 123–129, 2019.

[23] M. Malekzadeh and H. Bilsel, "Use of posidonia oceanica ash in stabilization of expansive soils," *Marine Georesources & Geotechnology*, vol. 32, no. 2, 2014.

[24] J. Khazaei and H. Moayedi, "Soft expansive soil improvement by eco-friendly waste and quick lime," *Arabian Journal for Science and Engineering*, vol. 44, no. 10, 2019.

[25] C. Moghal and A.-M. Basha, "Effect of polypropylene fibre reinforcement on the consolidation, swell and shrinkage behaviour of lime-blended expansive soil," *International Journal of Geotechnical Engineering*, vol. 12, no. 5, 2018.

[26] R. A. Blayi, A. F. H. Sherwani, H. H. Ibrahim et al., "Strength Improvement of Expansive Soil by Utilizing Waste Glass Powder," *Case Studies in Construction Materials*, vol. 13, 2020.

[27] P. Wang, X. Song, H. Xu, and W. Zhou, "Experiment on basic properties of cement modified expansive soil," *Progress of water conservancy and hydropower technology*, vol. 41, no. 3, pp. 56–60, 2021.

[28] Yu Meng, J. Zhang, Y. Zhou, and F. Sun, "Experimental study on modified expansive soil by micp technology," *Journal of Yangtze River academy of Sciences*, vol. 38, no. 5, pp. 103–108+122, 2021.

[29] H. Miao, *Experimental Study on Chemical Modification and Mechanical Properties of Expansive Soil*, Dalian University of technology, Dalian, China, 2007.

[30] Q. Wang, *Experimental Study on Physical and Mechanical Properties and Chemical Modification of Expansive Soil in Ankang Area*, Chang'an University, Xi'an, China, 2011.

[31] M. Wang, S. Qin, L. Jian et al., "Experimental study on unsaturated strength of lime modified expansive soil in Hefei," *Journal of rock mechanics and engineering*, vol. 33, no. S2, pp. 4233–4238, 2014.

[32] Yu Jin, H. Wang, C. Zheng et al., "Surface adsorption test and water absorption verification of lime mixed expansive soil," *Geotechnical mechanics*, vol. 33, no. 1, pp. 73–77, 2012.

[33] M. Liu, J. Song, J. Liu et al., "Experimental study on construction uniformity of cement modified expansive soil," *Journal of geotechnical engineering*, vol. 39, no. S1, pp. 59–63, 2017.

[34] W. Zou, P. Xie, Q. Ma et al., "Experimental study on expansive soil modified by waste tire rubber particles," *Journal of Sichuan University (Engineering Science Edition)*, vol. 43, no. 3, pp. 44–48, 2011.

[35] X. Zhang, S. Sun, W. Yongyao et al., "Laboratory test study of expansive soil modified by adding green sand," *Geotechnical mechanics*, vol. 33, no. S2, pp. 209–212, 2012.

[36] X. Zhuang and X. Yu, "Experimental study on strength characteristics of lime basalt fiber modified expansive soil," *Journal of Civil Engineering*, vol. 48, no. S1, pp. 116–120, 2015.

[37] S. Sun, J. Tang, Q. Zheng et al., "Experimental study on improvement of expansive soil mixed with blast furnace slag," *Geotechnical mechanics*, vol. 33, no. 7, pp. 1940–1944, 2012.

[38] T. H. Wu, C. M. Kokesh, and B. R. Trenner, "Use of live poles for stabilization of a shallow slope failure," *Journal of Geotechnical and GeoEnvironmental Engineering*, vol. 140, no. 10, pp. 1–13, 2014.

[39] H. Yao, S. Zheng, and S. Chen, "Stability analysis of expansive soil slope considering crack and rainwater infiltration," *Chinese Journal of Geotechnical Engineering*, vol. 23, no. 5, pp. 606–609, 2001.

[40] Ma Jia, "Experimental study on fracture evolution process of fractured soil," *Geotechnical mechanics*, vol. 28, no. 10, pp. 2203–2208, 2007.

[41] J. Wu, L. Hui, J. Liu et al., "Study on water repellency and infiltration properties of loam modified by octadecylamine," *Acta Agriculturae engi neering Sinica*, vol. 35, no. 13, pp. 122–128, 2019.

Hindawi
Advances in Civil Engineering
Volume 2021, Article ID 8949846, 16 pages
https://doi.org/10.1155/2021/8949846

Research Article

Mechanism and Stability Analysis of Deformation Failure of a Slope

Yingfa Lu,[1] **Gan Liu**,[1] **Kai Cui**,[2] **and Jie Zheng**[3]

[1]*School of Civil Engineering and Resource Environment, Hubei University of Technology, Wuhan, Hubei, China*
[2]*Key Laboratory of High-Speed Railway Engineering of the Ministry of Education, Southwest Jiaotong University, Chengdu, Sichuan, China*
[3]*Zhengzhou Highway Development Center, Zhengzhou, Henan, China*

Correspondence should be addressed to Yingfa Lu; 20121063@hbut.edu.cn

Received 19 May 2021; Revised 19 June 2021; Accepted 31 July 2021; Published 27 August 2021

Academic Editor: Guang-Liang Feng

Force distribution during progressive slope failure is an important element in slope stability analysis. In this study, five mechanical failure modes are proposed for thrust- and pull-type slopes, respectively, and five field forms of thrust-type slopes are described. The properties of progressive failure are evaluated quantitatively: the failure mode of slope obeys the geo-material rule under the peak stress state, and the instability range is gradually developed. The critical stress state zone is in the process of dynamic change with the development of deformation. It appears that the driving sliding force is greater than the frictional resistance along the sliding surface. When rock or soil stabilizing stresses are at maximum, the vector sum of the driving sliding stress and stabilizing stress is equal to zero at the critical state. The frictional resistance is equal to the driving sliding force in the stable and less-stable regions, and the normal pressure is wherever equal to the counterpressure. Rigid, flexible, and rigid-flexible design theories are proposed for slope control. New terms are defined and used to evaluate the stability. The conventional local and surplus stability factors of slopes and their calculation are explained. The force distribution rule is analyzed during progressive failure, and the conventional stability factor definition is discussed. The geological settings and monitoring data of landslides are used to analyse changes in the critical stress state. An example is given to illustrate the failure process analysis. The results show that progressive failure can be well represented and the safety factor can be well described by the main thrust method (MTM), comprehensive displacement method (CDM), and surplus displacement method (SDM), which can be used to feasibly evaluate slope stability.

1. Introduction

The slope failure mechanism and stability analysis are traditional topics in geotechnical engineering. Geotechnical disasters such as landslide, collapse, rockburst, and water inrush have occurred frequently in recent years [1, 2]. More than ten sort of limit equilibrium stability calculation methods for slope were given in previous studies, such as the Fellenius method [3], the simplified Bishop method [4], the Spencer method [5], the Janbu method [6], the Sarma method [7], the wedge method, and the finite element strength reduction method (SRM) [8–11]. In traditional slope stability analyses, the limit equilibrium slice method is the most often used [12–18]. For the slope with a given slip surface to be statically analyzed, different limit equilibrium slice methods have different assumptions about the action point of the force on the bottom edge of the slice and the direction and action line of thrust between the slices. With the development of numerical analysis, more and more scholars have begun to try other calculation methods, such as chart-based slope stability assessment using the generalized Hoek–Brown criterion and extremum solutions to the limit equilibrium method subjected to physical admissibility [19–31]. Other researchers established a three-dimensional strict equilibrium equation based on certain assumptions and proposed four criteria: potential sliding surface minimum parameter value criterion, slope active reinforcement force upper limit criterion, lower limit criterion for

sliding surface, and sliding and upper bound criterion for potential sliding surface selection [32].

The finite element method is the most widely used numerical analysis method in geotechnical engineering. In the field of slope analysis, the main software packages with strong functionality and wide application are ABAQUS, ANASYS, GeoStudio, rational infiltration analysis, etc. The corresponding analysis method is based on small deformation assumption and is usually applied to continuum mechanics media. Other numerical methods such as the fast Lagrangian analysis of continua (FLAC) method, discrete element method, discontinuous deformation analysis (DDA) method, and popular element method have been increasingly applied to landslide stability analysis.

The above landslide stability analysis is based on the limit equilibrium state. However, landslide damage is a process of gradual development [33–40]. That is, some zones are in the postfailure stress state, some zones are in the critical stress state, some zones are in the prepeak stress state [41, 42], and some zones are in the small deformation state, and this evolution process changes with changes in the environment. However, the traditional method does not consider the nonuniform distribution of the driving force along the sliding surface; different numerical analysis methods have certain difficulties in dealing with the discontinuous surface. Therefore, this paper proposes a new analytical method to solve the above problems.

In this paper, the sliding surface is divided into an unstable zone, a critical zone, a less-stable zone, and a stable zone. The transfer law of the landslide force is analyzed, and the characteristics of the critical block (or unit) force of the slope are proposed. The failure mechanisms, natures, and destruction control standards of thrust-type, pull-type, and mixed landslides are described. Based on the deformation and stress analysis, combined with the possible failure modes of slope, the following methods are defined: comprehensive sliding-resistance, main thrust, comprehensive displacement, and surplus displacement methods. The above analysis methods can be used to analyse slope progressive failure stability and provide a new idea for the study of landslide stability.

2. Failure Modes

Landslides occur due to long-term geological processes, environmental factors, human engineering, etc. Few studies have focused on the progressive deformation process from the initiation crack to the failure of landslide. In this paper, the whole failure process of the landslide can be described by the different stress distribution characteristics of sliding surface points. Only one point along the sliding surface is in the critical state when the sliding force is equal to the sliding resistance for a 2D landslide, and this stress distribution is defined as the critical state. The remaining points are in the postfailure stress state, and their sliding force is greater than the antisliding force; the landslide is in a state of "mechanical failure" at this moment. In the following, the deformation mechanism, failure modes, and destruction control standards are analyzed from a mechanical viewpoint.

2.1. Thrust-Type Landslide. The deformation and force transfer of landslides are established based on the fundamental mechanical behaviours of geomaterials. The load-displacement characteristics of rock and soil can be presented as types I and III curves (Figure 1); any point on the sliding surface experiences elastic stress, elastoplastic stress, critical stress, postfailure stress, and residual stress states from the initiation to the mechanical failure of the slope. At a certain moment, points a_1, a_2, a_3, and a_4 correspond to the postfailure stress state; point a_4 to the critical stress; points a_5 and a_6 to the elastoplastic stress state; and point a_7 to the elastic stress state in a 2D landslide problem. The postfailure stress state can be defined as an unstable zone, the critical stress state as a critical zone, the elastoplastic stress state as a less-stable zone, and the elastic stress state as a stable zone (Figure 1).

The failure occurs along the soft interlayer $(a_1, \ldots, a_5, \ldots, a_8)$, which is defined as mode I. In the rear part, the failure occurs along the weak intercalation $(a_1, \ldots, a_5)$ and along the sliding body (a_5, a_9) in the front part of the landslide, which is classified as mode II. The failure modes are controlled by the mechanical behaviours of soils/rocks.

2.2. Pull-Type Landslide. At a certain moment, points (b_1, b_2) correspond to the postfailure stress state and point (b_3) corresponds to the critical stress state. Points $(b_4, b_5, b_6$ or $b_7, b_8, b_9)$ are before the peak stress, and the whole sliding surface can be classified into unstable, critical, less-stable, and stable zones (Figure 2). The failure occurs along the soft interlayer $(b_1, \ldots, b_6)$, which is defined as mode I. In the front part, the failure occurs along the weak intercalation (b_1, b_2, b_3) and failure occurs along the sliding body (b_7, b_8, b_9) in the rear part of the landslide, which is classified as mode II. In the front part, failure occurs along the weak intercalation (b_1, b_2, b_3) and along the section of the sliding body (b_3, b_{12}) as traction strength control, which is defined as mode III. The failure modes are also controlled by the mechanical behaviours of soils/rocks.

2.3. Mixed Failure Mode. The thrust- and pull-types are the main failure modes during the progressive deformation process of landslides. However, a mixed failure mode of thrust- and pull-types can take place. For instance, tensile-shear failure occurs at depth (see Figure 3, point c_4), while the tensile stress increases to its strength. Traction failure (σ_n) occurs along section (c_4c_8). The first scarp is formed. If the tensile strength does not reach its strength, this scarp does not develop, and a pull-type landslide is certainly produced in zone $(c_4c_8c_9c_1c_2c_3c_4)$. When the tensile stress reaches the tensile strength value, the second scarp (c_9c_3) forms; the segment $(c_5c_4c_3)$ is in a postfailure stress state, and a corresponding unbalanced (or driving sliding) force is shown. The sliding body $(c_3c_4c_5c_6c_7c_8c_9c_3)$ exhibits thrust-type characteristics, and the driving sliding force impels the sliding body ahead. Two unstable, critical, less-stable, and stable zones appear during this period of landslide deformation. When the critical state disappears in the $c_9c_1c_2c_3c_9$ zone, the thrust-type feature is shown for the whole landslide (Figure 3).

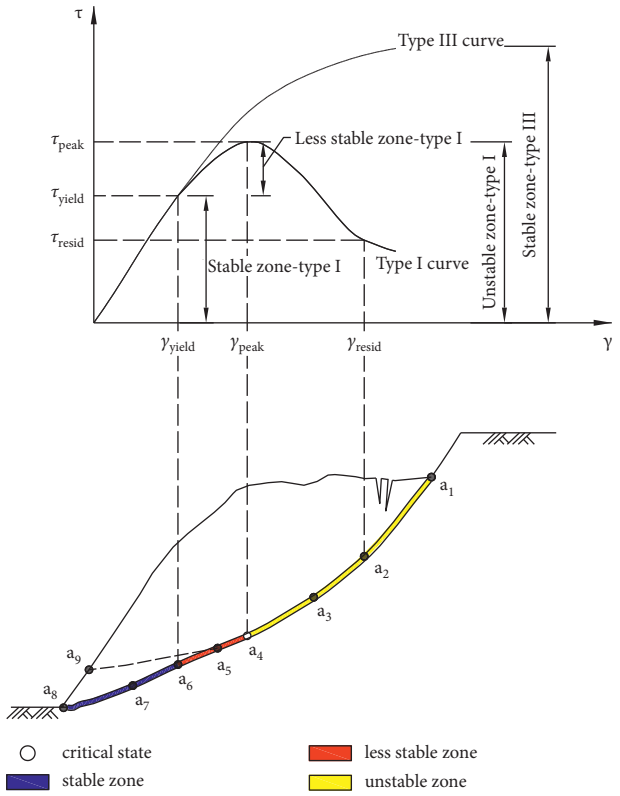

Figure 1: Failure modes of thrust-type landslides.

At a certain moment, points (b_1, b_2) correspond to the postfailure stress state and point (b_3) corresponds to the critical stress state; points $(b_4, b_5, b_6$ or $b_7, b_8, b_9)$ are before the peak stress, and the whole sliding face can be classified into unstable, critical, less-stable, and stable zones (Figure 2). The failure occurs along the soft interlayer $(b_1, \ldots, b_6)$, which is defined as mode I. In the front part, failure occurs along the weak intercalation (b_1, b_2, b_3), and failure occurs along the sliding body (b_7, b_8, b_9) in the rear.

The second mixed failure mode is often involved in a landslide with progressive deformation. At first, the landslide initiates in the rear and front parts of the landslide body along the sliding face, and the postfailure stress state corresponds to the rear and front parts. A thrust- ($d_1 d_2$ zone) and pull- ($d_6 d_5$ zone) type landslide are present in the rear and front parts on the sliding surface, respectively. An antisliding feature takes place in the middle part ($d_2 d_3 d_4 d_5$ zone). Two unstable, critical, less-stable, and stable zones appear during the progressive deformation process (Figure 4). With time and the development of deformation, the antisliding area decreases and the failure area increases. Finally, only one point corresponds to the critical state, and the whole landslide is at the point of "mechanical failure." The landslide initiates at the front, rear, or middle part of the landslide along the sliding face, which can be defined the "mixed failure mode."

3. Failure Process Analysis

The failure mode of the slope on the sliding surface point obeys the mechanical rule of rock and soil mass during the development of progressive deformation, and the mechanical failure properties of the two different types of slopes are analyzed.

3.1. Characteristics of the Thrust-Type Slope. A continuous shear failure occurs from the rear (see Figure 5, point *A*) to the front (see Figure 5, point *C*) (or from point *G* to *Q* of the soft interlayer) regions of a thrust-type slope during the development of progressive deformation. The stress at the failure point is in the peak state; the elastoplastic stress state is located in front of the failure point; and the postfailure stress state is behind the failure point (Figure 5). This failure mode is defined as mode I, and a shear failure occurs along the entire sliding surface. Tensile or tensile-shear failure occurs in the rear zone (see Figure 5, *DB*), and shear failure occurs in the front zone (see Figure 5, *BC*). Then, possible shear failure occurs in the *ABD* triangular area, which can be defined as mode II. In mode III, shear failure occurs in the rear zone (see Figure 5, *ABE*) and tensile (or tensile-shear) failure occurs in the front zone (see Figure 5, *EF*). Mode IV is a combination of modes II and III, in which failure occurs in the rear zone by tensile (or tensile-shear) failure, in the middle zone by shear failure, and in the front zone by tensile (or tensile-shear) failure (see Figure 5, DBEF). Mode V corresponds to a rock mass with distributed joints (or fissures), and shear, tensile, and tensile-shear failures occur along the soft interlayer and joints (or fissures) (see Figure 5, *GHIJ*. . .*KLMP*) alternately. The stability classification (stable zone, less-stable zone, critical zone, and unstable zone; Figure 1) along the entire sliding surface applies for the five failure modes of a thrust-type slope.

3.2. Characteristics of a Pull-Type Slope. Shear failure occurs from the front (see Figure 6, point *B*) to the rear (see Figure 6, point *A*) regions of a pull-type slope during the development of progressive deformation. The stress at the failure point is in the peak state; the elastoplastic stress state is behind the failure point; and the postfailure stress state is in front of the failure point. This failure mode is defined as mode I. Tensile or tensile-shear failure occurs in the rear zone (see Figure 6, *DC*), and shear failure occurs in the front zone (see Figure 6, *CB*). Then, possible shear failure occurs in the *ACD* triangular area, which can be defined as mode II. In mode III, shear failure occurs in the front zone and tensile failure occurs in the rear zone of the sliding body (see Figure 6, *EF*). Mode IV corresponds to a rock mass with distributed joints (or fissures): shear, tensile, and shear failures occur along the soft interlayer and joints (or fissures) alternately (see Figure 6, *GHIJ*. . .*KLMP*). Mode V corresponds to a combination of mode IV and a shear failure (or tensile-shear or tensile failure (see Figure 6, *ET*, or *ES*, or *EF*)) of the sliding body. The previous peak stress state is behind the zone, and the postfailure state is in front of the zone corresponding to a critical state for the five mechanical failure modes of the pull-type slope.

3.3. Characteristics of Deformation. Generally, a slope consists of a sliding body, sliding surface, and landslip bed.

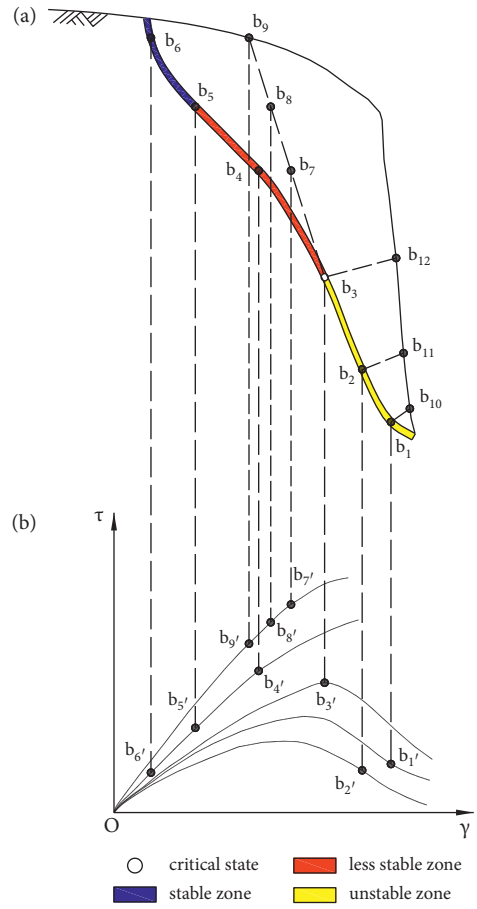

Figure 2: Failure modes of pull-type landslides.

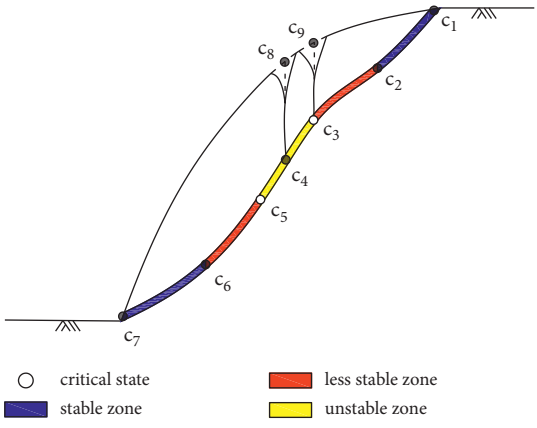

Figure 3: Failure mode of initiation in the middle part of the sliding face.

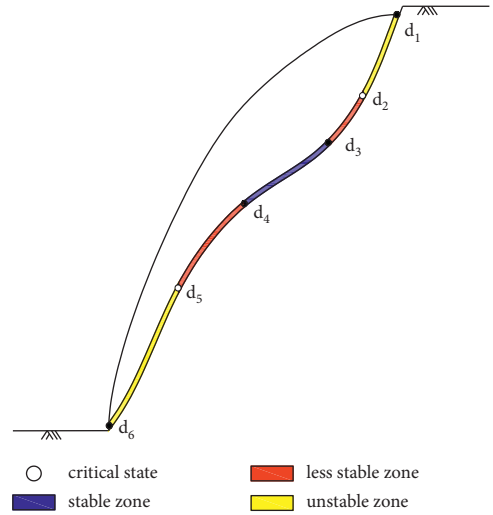

Figure 4: Failure of initiation on the front and rear part of the sliding face.

The values of the shear and tensile strengths of the sliding surface, sliding body, and landslip bed follow a small, moderate, and large pattern. At first, the failure of the sliding surface occurs and the deformation of the sliding body produces a sliding surface. The stress state of the sliding surface changes with the development of deformation. The characteristics of the complete stress-strain process are presented by each point on the sliding surface. The elastic, elastoplastic, peak, postfailure, and residual stress states are shown by each point on the sliding surface during the progressive failure process. The five different stress states may be represented by the points on the sliding surface at the same time. The driving sliding force on the sliding surface is

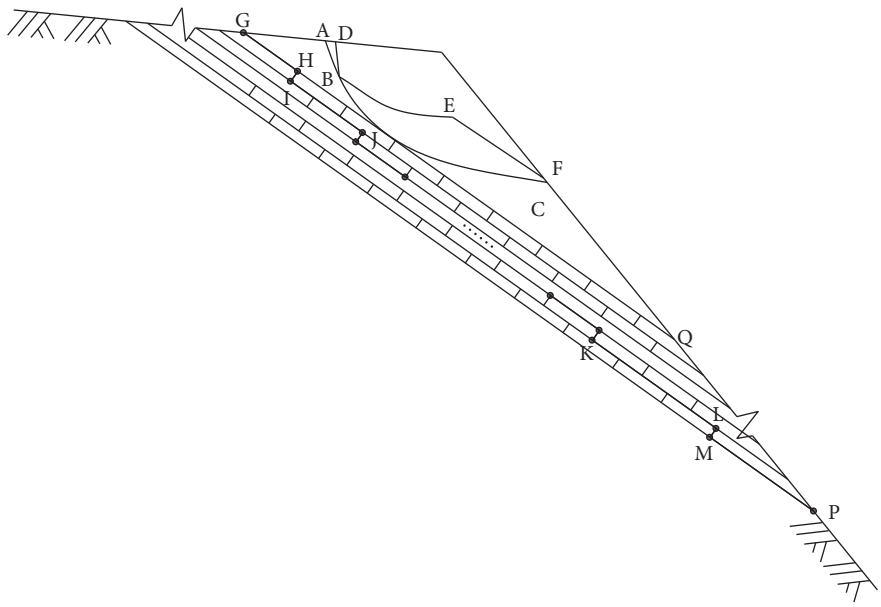

Figure 5: The five failure modes of a thrust-type slope.

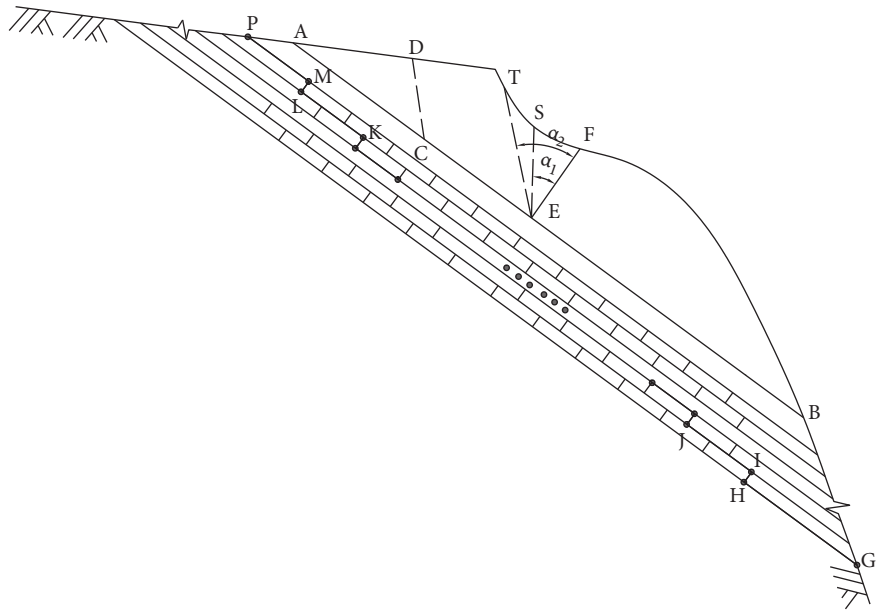

Figure 6: The five failure modes of a pull-type slope.

greater than the frictional resistance in the postfailure zone. Certainly, an unbalanced thrust exists for a slope along the sliding surface. In the front zone of the sliding surface, the driving sliding force is equal to the frictional resistance on the sliding surface and a surplus frictional resistance corresponding to the strength existing for the thrust-type slope. Thrust-type slopes in the field exhibit five forms. In form I, the elastic stress state covers the entire sliding surface. In form II, the whole sliding surface is in the stress state before the peak stress. In form III, a zone of the sliding surface is in the previous peak stress state, another zone is in the critical stress state, and the remainder of the sliding surface is in the postfailure and residual stress states. In form IV, the entire sliding surface is in the postfailure and residual stress states. In form V, only the residual stress state is present for the entire sliding surface (Figure 7). Form I cannot significantly perform slope control without additional reinforcement. The critical state is often the peak stress state for form II, and whether the slope controls are performed depends on the human influence. The critical state does not necessarily correspond to the peak stress for forms III, IV, and V, but the critical state exists for thrust-type slopes. Large deformation is produced for these three slopes. The geometric shape after deformation may possibly be favourable to thrust-type slope

stability, but performing slope control is necessary if the effects on humans are important.

4. Force Distribution on the Sliding Surface

In this section, the different failure modes are introduced during the progressive deformation process and the force distribution properties on the sliding surface are explained taking the thrust-type slope as an example.

An element (Figure 8) considered to represent the stress state of the sliding surface, where $\sigma_n^u, \sigma_\tau^u$, and σ_θ^u are the stresses from the sliding force of the sliding body and ${\sigma_n}^b, {\sigma_\tau}^b$, and ${\sigma_\theta}^b$ are the frictional stresses from the landslip bed. The driving shear stresses are greater than the frictional shear stresses in the postfailure zone along the sliding surface. The frictional shear stress reaches a maximum, and the driving shear stresses are equal to the frictional shear stresses at the critical state. The frictional shear stresses are equal to the driving shear stress in the front zone, corresponding to the critical state. But, the frictional shear stresses do not reach their maximum; the normal stress is equal to the counterstress in the whole sliding surface. The shear displacement is discontinuous in the postfailure zone; both shear stress and shear strain in the postfailure zone on the sliding surface are clearly discontinuous and present a challenge for numerical analysis. Certainly, the driving sliding force (P_i) and pressure (N_i) result from the sliding bed; the frictional force (F_i) and counterpressure (N_i^f) proceed from the landslip bed (Figure 9) for a two-dimensional thrust-type slope. The driving sliding force is greater than the frictional resistance in the postfailure zone on the sliding surface, and the driving sliding force is equal to the frictional resistance in the other zones. However, the maximum frictional resistance is reached at the critical state, when the pressure is equal to the counterpressure on the whole sliding surface.

5. Critical State

The slope stability is related to the critical state. The critical state is an obstacle to unstable zone development. Three stress balance equations exist at the critical state for numerical analysis on the sliding surface:

$$\begin{aligned} \left|\sigma_\theta^u\right| &= \left|\sigma_\theta^b\right|, \\ \left|\sigma_\tau^u\right| &= \left|\sigma_\tau^b\right|, \\ \left|\sigma_n^u\right| &= \left|\sigma_n^b\right|. \end{aligned} \tag{1}$$

The force balance equations in the X-, Y-, and Z-axial directions at the critical state must be satisfied for the slice block method under the shear failure condition:

$$\begin{aligned} \sum F_x &= 0, \\ \sum F_y &= 0, \\ \sum F_z &= 0. \end{aligned} \tag{2}$$

The moment balance equations in the XY-, YZ-, and ZX-planes of the critical state must exist for the slice block method under failure conditions:

$$\begin{aligned} \sum M_{xy} &= 0, \\ \sum M_{yz} &= 0, \\ \sum M_{zx} &= 0. \end{aligned} \tag{3}$$

By considering the field state, the combination of equations (2) and (3) may be chosen for the slice block method. For instance, the moment balance equation is satisfied in the XY-plane and the force balance equations exist in the X-, Y-, and Z-axial directions at the critical state for the slice block method:

$$\begin{aligned} XY-\text{plane}: \sum M_{xy} &= 0, \\ X-\text{axial direction}: \sum F_x &= 0, \\ Y-\text{axial direction}: \sum F_y &= 0, \\ Z-\text{axial direction}: \sum F_z &= 0. \end{aligned} \tag{4}$$

When tensile and shear failures occur for the same slice block, the tensile and shear stresses must be equal to their strength values. However, the shear failure has been studied only for widely used methods, such as the simplified Bishop method, Janbu method, Sarma method, Morgenstern method, and SRM. The tensile failure is negative.

The failure development of a slope can be prevented by an antislide tie, which can be explained by the critical state based on equations (1)~(3), and the slope control position and safety factor can be redefined as follows.

The first method: the position of slope control is chosen at the critical state for thrust- and pull-type slopes and at the yield limit stress state for the foundation pit; a rigid design is used with a safety factor, and a small deformation is permitted for this rigid design. The second method: the position of slope control is chosen at the yield limit stress state for thrust- and pull-type slopes and at the peak stress state for the foundation pit; a flexible design is applied with a safety factor, and a large deformation is allowable for this flexible design. The third method: the position of slope control is chosen between the first and the second positions, and this design can be called a "rigid-flexible" design. The force and moment balance in equations (1)~(4) must be satisfied at the design position with a safety factor, the antisliding force is the vector sum of the unbalanced thrust from the postfailure zone, and the displacement of the slope control can be calculated.

6. Shear Stress-Strain Model

The complete process shear-strain model (CPSM) must necessarily be employed to describe the progressive failure process of a slope. A stress-strain equation with four parameters is a part of the CPSM. The equation can be described by taking a shear stress and strain as an example in the following form:

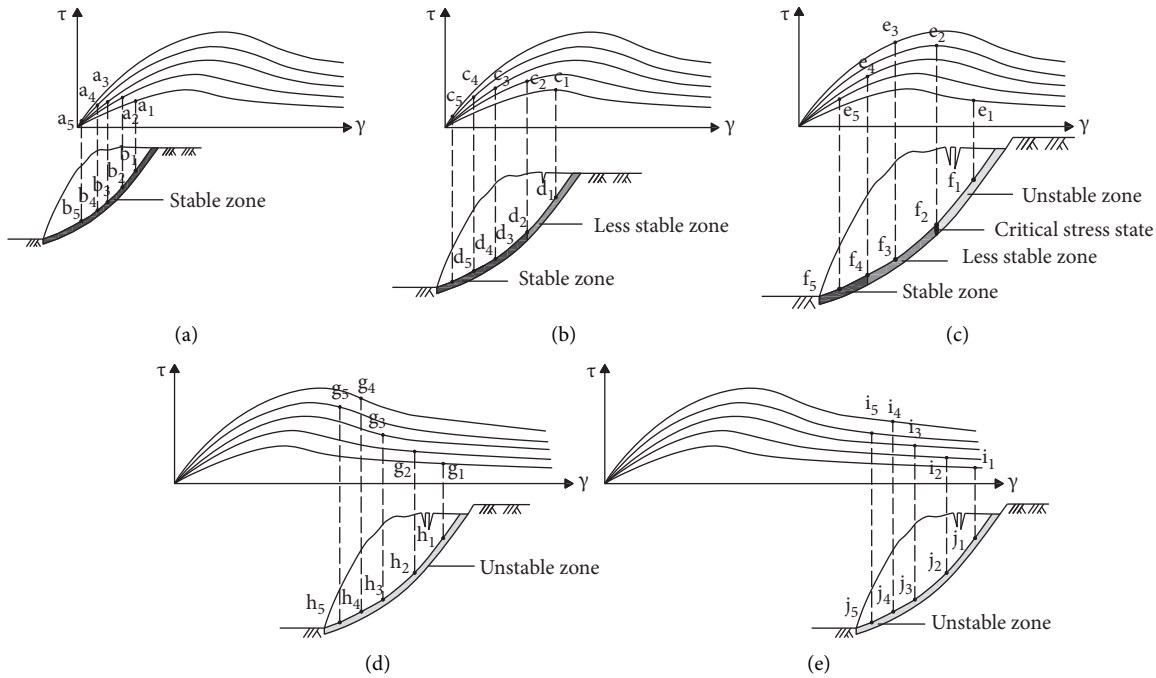

Figure 7: Five forms of the slope existing in the field.

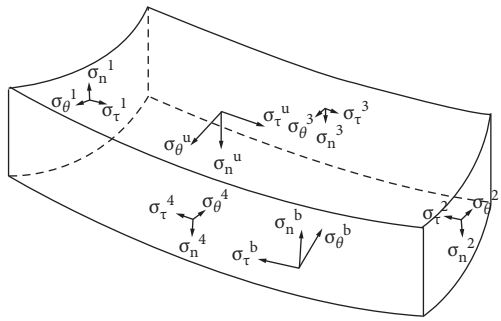

Figure 8: Schematic of a sliding surface element.

$$\tau = G\gamma\left(\frac{1+\gamma^q}{p}\right)^{\xi}, \tag{5}$$

where τ and γ are the shear stress and shear strain, respectively; G is the shear modulus dependent on the normal stress; and p, q, and ξ are the constant coefficients dependent on the normal stress. The units of τ and G are kPa.

The following conditions are needed for the rock or soil with softening mechanical behaviours:

$$\begin{aligned} 1 + q\xi &\neq 0, \\ -1 < \xi &\leq 0. \end{aligned} \tag{6}$$

The critical shear strain (defined as the shear strain corresponding to the peak shear stress) is satisfied in the following form:

$$p + (1 + q\xi)\gamma_{\text{peak}}^{q} = 0, \tag{7}$$

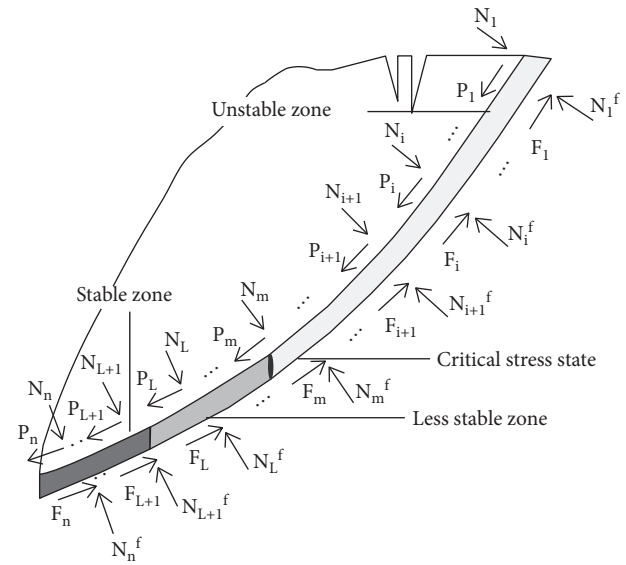

Figure 9: Distribution characteristics of force along the sliding surface of a 2D thrust-type slope.

where γ_{peak} is the critical shear strain corresponding to the critical shear stress.

The Mohr–Coulomb criterion is assumed to describe the critical shear stress (τ_{peak}) (note: other criteria can also describe the critical shear stress):

$$\tau_{\text{peak}} = C + \sigma_n \tan\varphi, \tag{8}$$

where C is the cohesion, σ_n is the normal stress, and φ is the frictional angle. The units of σ_n and C are kPa.

The critical shear strain is assumed to be related only to normal stress, and the critical shear strain (γ_{peak}) can be described as follows:

$$\left(\frac{\gamma_{\text{peak}}}{a_3}\right)^2 + \left(\frac{(\sigma_n - a_2)}{a_1}\right)^{\zeta_N} = 1, \tag{9}$$

where a_1, a_2, a_3, and ζ_N are the constant coefficients which are dependent on the normal stress; the units of a_1 and a_2 are kPa, and a_3 and ζ_N are the constant coefficients without units.

Finally,

$$G = G_0 + b_1\sigma_n + b_2\sigma_n^2, \tag{10}$$

where G_0 is the initial shear modulus when the normal stress (σ_n) is equal to zero, b_1 is a constant coefficient without units, and $b_2 = -b_1/(2a_2)$.

The softening coefficient (ξ) can be presented in the following form:

$$\xi = \frac{\xi_0}{\left(1 + (\xi_0/\xi_c - 1)(\sigma_n/\sigma_n^c)^{\varsigma}\right)}, \tag{11}$$

where ξ_0 is the value of ξ when σ_n is equal to zero, ξ_c is the value of ξ when σ_n is equal to ${\sigma_n}^c$, and ς is a constant coefficient without units. The softening coefficient can be obtained by the shear stress and shear strain complete process tests with different normal stresses.

Regarding the physical significance, it is not necessary to explain the parameters related to the Mohr–Coulomb criterion: a_2 is the critical normal stress ($a_2 = \sigma_n^{\text{crit}}$), a_3 is the critical shear strain ($a_3 = \gamma_{\text{peak}}^{\text{crit}}$) when the normal stress is equal to the critical normal stress ($a_2 = \sigma_n^{\text{crit}}$), a_1 is relative to the critical shear strain ($\gamma_{\text{peak}}^0 = a_3\sqrt{1 - (a_2/a_1)^2}$) when the normal stress is equal to zero, $a_1 > a_2\xi$ represents the softening degree of rock or soil under different normal stresses, and p and q are the representative parameters between the critical shear stress and shear strain.

7. Stability Analysis

In stability analysis, the mechanical behaviours of weak intercalated strata are key factors for the sliding body and different safety factors are proposed to describe the slope stability.

7.1. Stability Analysis of an Ideal Elastoplastic Model

7.1.1. Comprehensive Sliding-Resistance Method (CSRM). The stress fields of the landslide body along the slip surface (see Figure 10, dashed line *ABDEC* represents the sliding surface) can be obtained by the current calculation method, and the vector sums of sliding force can be obtained in the directions of *X*-, *Y*-, and *Z*-axes (see Figure 10):

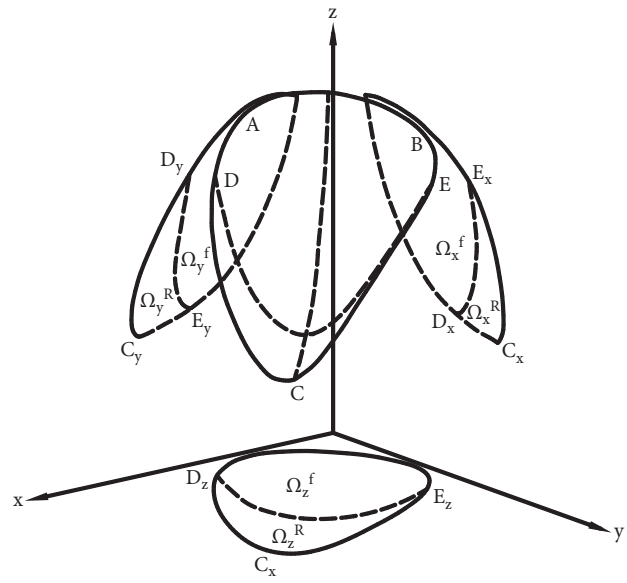

Figure 10: Distribution of failure zones and projections along the *X*-, *Y*-, and *Z*-axes.

$$\begin{aligned} P_{xs} &= \iint_{\Omega_x^f + \Omega_x^R} (\sigma_\theta^u + \sigma_\tau^u)\mathrm{d}y\mathrm{d}z, \\ P_{ys} &= \iint_{\Omega_y^f + \Omega_y^R} (\sigma_\theta^u + \sigma_\tau^u)\mathrm{d}x\mathrm{d}z, \\ P_{zs} &= \iint_{\Omega_z^f + \Omega_z^R} (\sigma_\theta^u + \sigma_\tau^u)\mathrm{d}x\mathrm{d}y, \end{aligned} \tag{12}$$

where P_{xs}, P_{ys}, and P_{zs} are the vector sums of the sliding forces in the directions of the *X*-, *Y*-, and *Z*-axes, Ω is the area of the whole integration, Ω^f is the destroyed region, and Ω^R is the nondestroyed region.

The vector sum (P_s) of P_{xs}, P_{ys}, and P_{zs} is

$$P_s = \sqrt{(P_{xs})^2 + (P_{ys})^2 + (P_{zs})^2}. \tag{13}$$

The direction cosines of P_s with Cartesian coordinate axes are α_s, β_s, and γ_s. The failure mode can be analyzed, the distribution of skid-resistance stresses ($\sigma_n^{p,b}, \sigma_\theta^{p,b}$, and $\sigma_\tau^{p,b}$) under the possible failure mode can be obtained, and the vector sums of the antislip force under the possible failure modes can be calculated in the directions of *X*-, *Y*-, and *Z*-axes:

$$\begin{aligned} T^{xT} &= \iint_{\Omega_x^f + \Omega_x^R} \left(\sigma_n^{p,b} + \sigma_\theta^{p,b} + \sigma_z^{p,b}\right)\mathrm{d}y\mathrm{d}z, \\ T^{yT} &= \iint_{\Omega_y^f + \Omega_y^R} \left(\sigma_n^{p,b} + \sigma_\theta^{p,b} + \sigma_z^{p,b}\right)\mathrm{d}x\mathrm{d}z, \\ T^{zT} &= \iint_{\Omega_y^f + \Omega_y^R} \left(\sigma_n^{p,b} + \sigma_\theta^{p,b} + \sigma_z^{p,b}\right)\mathrm{d}x\mathrm{d}y, \end{aligned} \tag{14}$$

where T^{xT}, T^{yT}, and T^{zT} are the vector sums of the stabilizing forces in the directions of the *X*-, *Y*-, and *Z*-axes under the possible failure modes.

The vector sum (T^T) of T^{xT}, T^{yT}, and T^{zT} is

$$T^T = \sqrt{\left(T^{xT}\right)^2 + \left(T^{yT}\right)^2 + \left(T^{zT}\right)^2}. \tag{15}$$

The direction cosines of T^T with Cartesian coordinate axes are α_T, β_T, and γ_T.

The vector angle (φ_c) between P_s and T^T can be described in the following form (see Figure 11):

$$\varphi_c = \arccos\left(\alpha_s\alpha_T + \beta_s\beta_T + \gamma_s\gamma_T\right). \tag{16}$$

The stable coefficient in the X-axis direction is

$$F^x_{\mathrm{CSRM}} = \frac{T^{xT}}{P_{xs}}. \tag{17}$$

The stable coefficient in the Y-axis direction is

$$F^y_{\mathrm{CSRM}} = \frac{T^{yT}}{P_{ys}}. \tag{18}$$

The stable coefficient in the Z-axis direction is

$$F^z_{\mathrm{CSRM}} = \frac{T^{zT}}{P_{zs}}. \tag{19}$$

The stable coefficient in the sliding force direction is defined as

$$F^s_{\mathrm{CRSM}} = \frac{T^T \cos\phi_c}{P_s}. \tag{20}$$

7.1.2. Main Thrust Method (MTM). The main thrust method is used only to evaluate the stability of a thrust-type landslide. The critical state curves (see Figure 10, dashed line DE) can be obtained, and the residual thrust force from the posterior region to the critical state curve (DE) can be calculated (see Figure 10):

$$\begin{aligned} P_{xp} &= \iint_{\Omega^f_x}\left(\sigma^u_\theta + \sigma^u_\tau - \sigma^b_\theta - \sigma^b_\tau\right)\mathrm{d}y\mathrm{d}z, \\ P_{yp} &= \iint_{\Omega^f_x}\left(\sigma^u_\theta + \sigma^u_\tau - \sigma^b_\theta - \sigma^b_\tau\right)\mathrm{d}x\mathrm{d}z, \\ P_{zp} &= \iint_{\Omega^f_x}\left(\sigma^u_\theta + \sigma^u_\tau - \sigma^b_\theta - \sigma^b_\tau\right)\mathrm{d}x\mathrm{d}y. \end{aligned} \tag{21}$$

The vector sum (P^p) of P_{xp}, P_{yp}, and P_{zp} is

$$P^p = \sqrt{\left(P_{xp}\right)^2 + \left(P_{yp}\right)^2 + \left(P_{zp}\right)^2}. \tag{22}$$

The direction cosines of P^p with Cartesian coordinate axes are α_p, β_p, and γ_p.

The differential value (or residual frictional force) between the frictional force $(\sigma^{p,b}_n, \sigma^{p,b}_\theta$, and $\sigma^{p,b}_\tau)$ under the possible failure mode and the antislip force $(\sigma^b_n, \sigma^b_\theta$, and $\sigma^b_\tau)$ under the current situation can be obtained as follows:

$$\begin{aligned} T^{xp} &= \iint_{\Omega^R_x}\left(\sigma^{p,b}_n + \sigma^{p,b}_\theta + \sigma^{p,b}_\tau - \sigma^b_n - \sigma^b_\theta - \sigma^b_\tau\right)\mathrm{d}y\mathrm{d}z, \\ T^{yp} &= \iint_{\Omega^R_y}\left(\sigma^{p,b}_n + \sigma^{p,b}_\theta + \sigma^{p,b}_\tau - \sigma^b_n - \sigma^b_\theta - \sigma^b_\tau\right)\mathrm{d}x\mathrm{d}z, \\ T^{zp} &= \iint_{\Omega^R_z}\left(\sigma^{p,b}_n + \sigma^{p,b}_\theta + \sigma^{p,b}_\tau - \sigma^b_n - \sigma^b_\theta - \sigma^b_\tau\right)\mathrm{d}y\mathrm{d}x. \end{aligned} \tag{23}$$

The vector sum (T^p) of $F_p{}^x, F_p{}^y$, and $F_p{}^z$ is

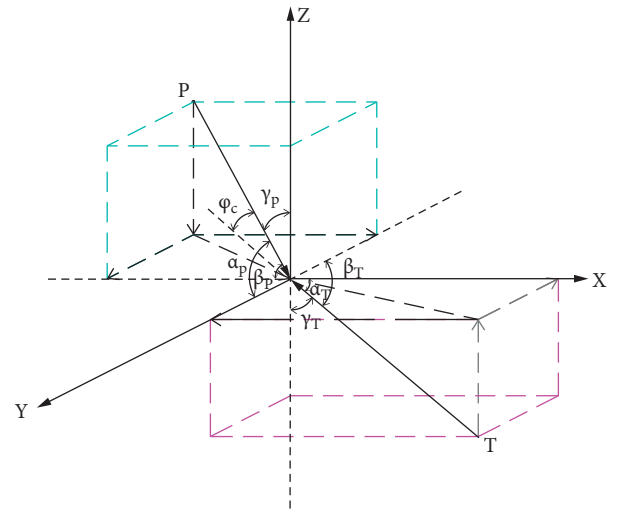

Figure 11: Vector and relation diagram of glide force and antislip force in potentially destructive mode.

$$T^p = \sqrt{\left(T_{xp}\right)^2 + \left(T_{yp}\right)^2 + \left(T_{zp}\right)^2}. \tag{24}$$

The direction cosines of T^p with Cartesian coordinate axes are α_r, β_r, and γ_r.

The vector angle (φ_m) between P^p and $F_{sf} = \mathrm{TSF} - F_{lf}$ can be described in the following form:

$$\alpha_m = \arccos\left(\alpha_p\alpha_r + \beta_p\beta_r + \gamma_p\gamma_r\right). \tag{25}$$

The stable coefficient in the X-axis direction is

$$F^x_{\mathrm{MTM}} = \frac{T^{xp}}{P_{xp}}. \tag{26}$$

The stable coefficient in the Y-axis direction is

$$F^y_{\mathrm{MTM}} = \frac{T^{yp}}{P_{yp}}. \tag{27}$$

The stable coefficient in the Z-axis direction is

$$F^z_{\mathrm{MTM}} = \frac{T^{zp}}{P_{zp}}. \tag{28}$$

The stable coefficient in the main slip force direction is

$$F^s_{\mathrm{MTM}} = \frac{T^p \cos\phi_m}{P^p}. \tag{29}$$

7.1.3. Comprehensive Displacement Method (CDM). The deformation from the present strain states $(\varepsilon^u_\theta$ and $\varepsilon^u_\tau)$ is calculated and is projected onto X-, Y-, and Z-axes:

$$\begin{aligned} S_{xd} &= \iint_{\Omega^f_x+\Omega^R_x}\left(\varepsilon^u_\theta + \varepsilon^u_\tau\right)\mathrm{d}y\mathrm{d}z, \\ S_{yd} &= \iint_{\Omega^f_y+\Omega^R_y}\left(\varepsilon^u_\theta + \varepsilon^u_\tau\right)\mathrm{d}x\mathrm{d}z, \\ S_{zd} &= \iint_{\Omega^f_z+\Omega^R_z}\left(\varepsilon^u_\theta + \varepsilon^u_\tau\right)\mathrm{d}x\mathrm{d}y. \end{aligned} \tag{30}$$

The vector sum (α_i) of c_i is

$$S_d = \sqrt{(S_{x\,d})^2 + (S_{y\,d})^2 + (S_{z\,d})^2}. \tag{31}$$

The direction cosines of F with Cartesian coordinate axes are σ_n^i. The possible failure mode is analyzed, the distribution of the strain ($\varepsilon_n^{p,b}$, $\varepsilon_\theta^{p,b}$, and $\varepsilon_\tau^{p,b}$) under the possible failure mode can be calculated, and the vector sums of displacement under the possible failure mode can be obtained in the directions of X-, Y-, and Z-axes:

$$\begin{aligned} S^{xd} &= \iint_{\Omega_x^f + \Omega_x^R} \left(\varepsilon_n^{p,b} + \varepsilon_\theta^{p,b} + \varepsilon_\tau^{p,b}\right) \mathrm{d}y\mathrm{d}z. \\ S^{yd} &= \iint_{\Omega_y^f + \Omega_y^R} \left(\varepsilon_n^{p,b} + \varepsilon_\theta^{p,b} + \varepsilon_\tau^{p,b}\right) \mathrm{d}x\mathrm{d}z, \\ S^{zd} &= \iint_{\Omega_z^f + \Omega_z^R} \left(\varepsilon_n^{p,b} + \varepsilon_\theta^{p,b} + \varepsilon_\tau^{p,b}\right) \mathrm{d}y\mathrm{d}x. \end{aligned} \tag{32}$$

The vector sum (S^d) of $S^{x\,d}, S^{y\,d}$, and $S^{z\,d}$ is

$$S^d = \sqrt{\left(S^{x\,d}\right)^2 + \left(S^{y\,d}\right)^2 + \left(S^{z\,d}\right)^2}. \tag{33}$$

The direction cosines of S^d with Cartesian coordinate axes are α^d, β^d, and γ^d. The vector angle (φ_d) between the vectors S^d and S_d can be calculated as follows:

$$\varphi_d = \arccos\left(\alpha^d \alpha_d + \beta^d \beta_d + \gamma^d \gamma_d\right). \tag{34}$$

The stable coefficient in the X-axis direction is

$$F_{C\,DM}^x = \frac{S^{xd}}{S_{xd}}. \tag{35}$$

The stable coefficient in the Y-axis direction is

$$F_{C\,DM}^y = \frac{S^{yd}}{S_{yd}}. \tag{36}$$

The stable coefficient in the Z-axis direction is

$$F_{\mathrm{CDM}}^z = \frac{S^{zd}}{S_{zd}}. \tag{37}$$

The stable coefficient in the slip displacement direction is

$$F_{C\,DM}^s = S^d \cos\,\phi_d / S^d. \tag{38}$$

7.1.4. Surplus Displacement Method (SDM). The strains (ε_θ^u and ε_τ^u) from the posterior region to the critical stress state (see Figure 10, DE (dashed line)) in the present status are calculated and are projected onto X-, Y-, and Z-axes:

$$\begin{aligned} S_{xs} &= \iint_{\Omega_x^f} \left(\varepsilon_\theta^u + \varepsilon_\tau^u\right) \mathrm{d}y\mathrm{d}z, \\ S_{ys} &= \iint_{\Omega_y^f} \left(\varepsilon_\theta^u + \varepsilon_\tau^u\right) \mathrm{d}x\mathrm{d}z, \\ S_{zs} &= \iint_{\Omega_z^f} \left(\varepsilon_\theta^u + \varepsilon_\tau^u\right) \mathrm{d}x\mathrm{d}y, \end{aligned} \tag{39}$$

where S_{xs}, S_{ys}, and S_{zs} are the vector sums of the displacements in the directions of the X-, Y-, and Z-axes, respectively, and the vector sum (S_s) of S_{xs}, S_{ys}, and S_{zs} is

$$S_s = \sqrt{\left(S_{xs}\right)^2 + \left(S_{ys}\right)^2 + \left(S_{zs}\right)^2}. \tag{40}$$

The direction cosines of S_s with Cartesian coordinate axes are α_s, β_s, and γ_s. The possible failure mode is analyzed, and the distribution of the strain ($\varepsilon_n^{p.b}$, $\varepsilon_\theta^{p.b}$, and $\varepsilon_\tau^{p.b}$) under the possible failure mode can be calculated. The differences between $\varepsilon_n^{p.b}$, $\varepsilon_\theta^{p.b}$, and $\varepsilon_\tau^{p.b}$ and $\varepsilon_n^b, \varepsilon_\theta^b$, and ε_τ^b can be obtained and projected in the directions of the X-, Y-, and Z-axes:

$$\begin{aligned} S^{xs} &= \iint_{\Omega_x^k} \left(\varepsilon_n^{p,b} + \varepsilon_\theta^{p,b} + \varepsilon_\tau^{p,b} - \varepsilon_n^b - \varepsilon_\theta^b - \varepsilon_\tau^b\right) \mathrm{d}y\mathrm{d}z, \\ S^{ys} &= \iint_{\Omega_y^k} \left(\varepsilon_n^{p,b} + \varepsilon_\theta^{p,b} + \varepsilon_\tau^{p,b} - \varepsilon_n^b - \varepsilon_\theta^b - \varepsilon_\tau^b\right) \mathrm{d}x\mathrm{d}z, \\ S^{zs} &= \iint_{\Omega_z^k} \left(\varepsilon_n^{p,b} + \varepsilon_\theta^{p,b} + \varepsilon_\tau^{p,b} - \varepsilon_n^b - \varepsilon_\theta^b - \varepsilon_\tau^b\right) \mathrm{d}y\mathrm{d}x, \end{aligned} \tag{41}$$

where S^{xs}, S^{ys}, and S^{zs} are the vector sums of the displacement differences in the directions of the X-, Y-, and Z-axes between the possible failure mode and present status, respectively. The vector sum (S^s) of S^{xs}, S^{ys}, and S^{zs} is

$$S^s = \sqrt{\left(S^{xs}\right)^2 + \left(S^{ys}\right)^2 + \left(S^{zs}\right)^2}. \tag{42}$$

The direction cosines of S^s with Cartesian coordinate axes are α^s, β^s, and γ^s. The vector angle (φ_s) between the vectors S^s and S_s can be calculated:

$$\varphi_s = \arccos\left(\alpha^s \alpha_s + \beta^s \beta_s + \gamma^s \gamma_s\right). \tag{43}$$

The stable coefficient in the X-axis direction is

$$F_{S\,DM}^x = \frac{S^{xs}}{S_s}. \tag{44}$$

The stable coefficient in the Y-axis direction is

$$F_{S\,DM}^y = \frac{S^{ys}}{S_s}. \tag{45}$$

The stable coefficient in the Z-axis direction is

$$F_{S\,DM}^z = \frac{S^{zs}}{S_s}. \tag{46}$$

The stable coefficient in the main slip displacement direction is

$$F_{S\,DM}^s = \frac{S^s \cos\,\phi_s}{S_s}. \tag{47}$$

7.2. Stability Analysis of a New Shear Stress Constitutive Model. According to the stability analysis method of the ideal elastoplastic constitutive model in Section 7.1, the stability coefficient of the new shear stress constitutive models, such as the *CSRM*, the *MTM*, and the surplus displacement method (*SDM*), can be obtained.

7.3. Stability Coefficient Study

7.3.1. Some Term Definitions. Some terms are first defined. The failure ratio (f_r) is the value of the driving stress of rock or soil divided by its strength; when the value is greater than 1, the f_r is equal to 1. The failure percentage (f_p) is the value of the sum of the failure ratio multiplied by its area and divided by the total area. The failure area percentage (f_s) is the value of the area sum corresponding to the failure ratio ($f_r = 1$) divided by the total area.

The frictional resistance variation coefficient (F_f) is the vector sum of the frictional resistance of the entire sliding body failure divided by the frictional resistance vector sum during the progressive deformation and includes the X-, Y-, and Z-axial (F_f^x, F_f^y, and F_y^z) and vector sum (F_f) directions. The variation coefficient of the driving sliding force (F_p) is the vector sum of the driving sliding force of the entire sliding surface failure divided by the driving sliding force vector sum during the progressive deformation and includes the X-, Y-, and Z-axial (F_p^x, F_p^y, and F_p^z) and vector sum (F_p) directions.

7.3.2. Comparison of Safety Factors. A partial strength reduction method is proposed, and its result is used to compare with the progressive failure analysis. The steps of the partial strength reduction method are as follows.

First, the traditional safety factor (TSF) of the entire sliding body is calculated by the traditional slice block method. Then, the local safety factor (F_{lf}) from the rear zone to the critical state (Figure 12, where the m-th slice block is assumed to be in a critical stress state under $F_{lf} = 1$) is obtained by the same method. The surplus safety factor ($F_{sf} = \text{TSF} - F_{lf}$) is equal to the safety factor of the entire sliding body minus the local safety factor. This factor is used to compare with that of the MTM during the progressive failure process.

7.3.3. Unbalanced Thrust Method. The unbalanced thrust method (UTM) is taken as an example to calculate the safety factor, and its formula is derived (Figure 13).

The fundamental assumptions are as follows:

(1) The slice block is assumed to have strong deformation capacity and is classified by a vertical interval

(2) The former slice block force from the posterior slice block is parallel to the bottom side of the posterior slice block

(3) The rotation of the slice block is not considered

(4) The frictional stress is satisfied with the new shear stress-strain model

The relationship between the shear strain of two slice blocks can be described in the failure zone as follows:

$$\gamma_i = \frac{\gamma_{i+1}}{\cos\left(\alpha_i - \alpha_{i+1}\right)}. \tag{48}$$

In the i-th slice block, we have the following.

Normal pressure N_i is

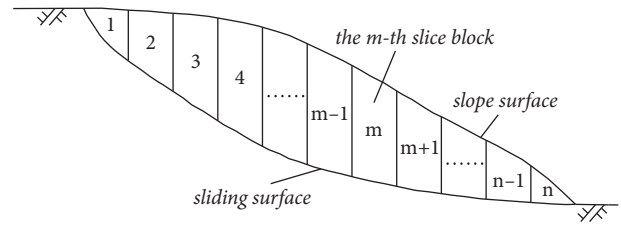

Figure 12: Schematic of the partial strength reduction method.

$$N_i = W_i \cos\alpha_i + P_{i-1}\sin\left(\alpha_{i-1} - \alpha_i\right) + \frac{1}{2}\gamma_w h_{i,u}^2 \sin\alpha_i - \frac{1}{2}\gamma h_{i,b}^2 \sin\alpha_i - \frac{1}{2}\left(\gamma_i h_{i,u} + \gamma_i h_{i,b}\right) l_i. \tag{49}$$

Normal stress σ_n^i is

$$\sigma_n^i = \frac{N_i}{l_i}. \tag{50}$$

Critical frictional stress τ_{peak}^i is

$$\tau_{\text{peak}}^i = c_i + \sigma_n^i \tan\varphi_i. \tag{51}$$

Critical frictional resistance T_{peak}^i is

$$T_{\text{peak}}^i = c_i l_i + N_i \tan\varphi_i. \tag{52}$$

Frictional force after strength reduction $T_{\text{peak},F}^i$ is

$$T_{\text{peak},F}^i = \frac{T_{\text{peak}}^i}{F}. \tag{53}$$

Driving sliding force P_i^S ($P_0 = 0$) is

$$P_i^S = W_i \sin\alpha_i + P_{i-1}\cos\left(\alpha_{i-1} - \alpha_i\right) + \frac{1}{2}\gamma_w h_{i,u}^2 \cos\alpha_i - \frac{1}{2}\gamma_w h_{i,b}^2 \cos\alpha_i. \tag{54}$$

Unbalanced thrust force P_i is

$$P_i = P_i^S - T_{\text{peak},F}^i, \tag{55}$$

where W_i is the weight of the i-th slice block, l_i is the length of the i-th slice block bottom, α_i is the angle between the bottom and the horizontal axis of the i-th slice block, c_i is the cohesion of the bottom of the i-th slice block, φ_i is the frictional angle of the i-th slice block, F is the stability factor, σ_n^i is the normal stress of the i-th slice block, γ_w is the specific gravity of water, $h_{i,u}$ is the height of water at the left of the slice block, and $h_{i,b}$ is the height of water level at the right of the slice block.

8. Case Study

The progressive failure process is presented for the Kaziwan landslide in the Three Gorges Reservoir.

8.1. Geological Survey. The Kaziwan landslide is situated in Zigui County, and its geographic coordinates are as follows:

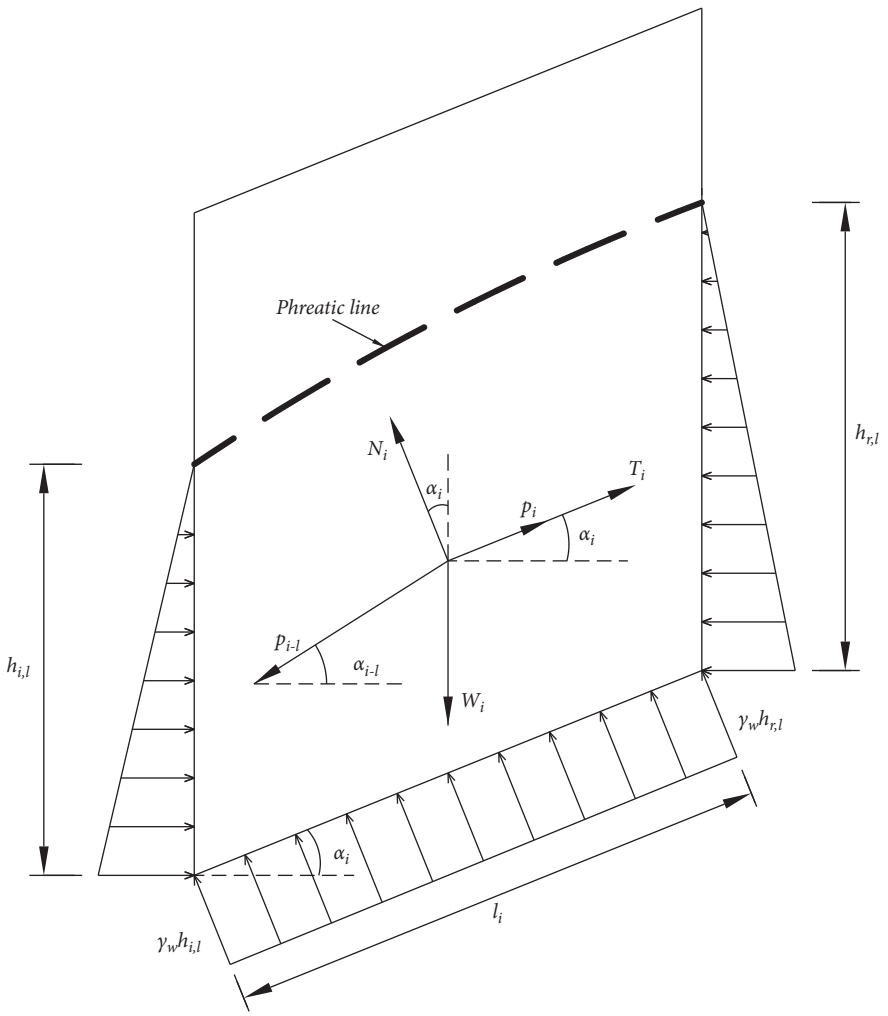

Figure 13: The force distribution of the i-th soil slice block.

(X: 3432550, Y: 37471500), longitude: 110°41′37″E, and latitude: 31° 0′48″N. The Kaziwan landslide is located on the left bank of the Guizou River, 1.9 km from the mouth and 44 km from the Three Gorges Dam. Its basic characteristics are as follows. The trailing edge elevation is 720 m, the leading edge elevation is 85 m, the slope aspect is 296°, the slope length is 1270 m, the slope height is 635 m, and the slope degree is 15°~40° (Figure 14).

Quaternary deposits are distributed across the slope. The deposits consist of broken stone and silty clay. Most stone is located at the toe of the slope; boulders can be seen in the front, the particle sizes range from 0.4 m to 1.0 m, and the largest is more than 1.0 m. The stratigraphic lithology is interbedded sandstone and mudstone of the Upper Jurassic Suining Formation. The purple-red silty mudstone, siltstone, and feldspar sandstone crop out the northeast of the slope. The occurrence of bedrock is 280°~320°∠26°~39°, and the occurrences of fissures are 180°∠82° and 240~250°∠46~79°. Cracks are filled with mudstone. The lateral bedrock crops out to the southwest, and its occurrence is 65°∠66°. The Kaziwan slope is downward.

The Guizhou River is an open face of the Kaziwan landslide. Its left boundary direction is 340°, and its length is 1000 m; the terrain gradient at the boundary is gentle, and the gradient is approximately 20°. Its right boundary direction is 210°, and its length is 1000 m. The landslide is composed of sandstone and mudstone, which are easily softened by water immersion to form a weak layer. The sliding zone between the sandstone and mudstone is formed naturally.

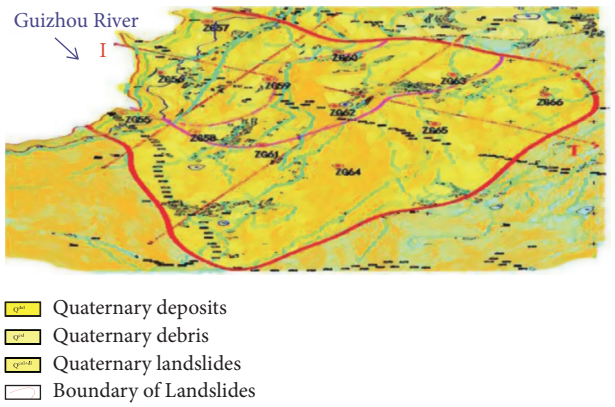

Figure 14: Plan view of the Kaziwan landslide.

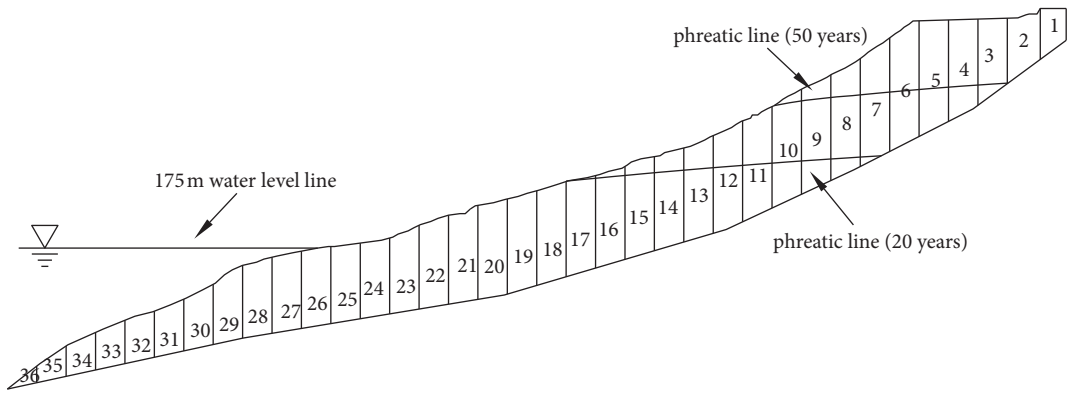

Figure 15: Block division map of the Kaziwan landslide.

Table 1: Safety factor of progressive failure under the rainfall with a recurrence interval of 20 years.

CSB	25	26	27	28	29	30
TSF	1.317	1.349	1.399	1.410	1.428	1.484
F^x_{CSRM}	0.746	0.704	0.655	0.607	0.559	0.510
F^y_{CSRM}	2.925	2.808	2.667	2.526	2.385	2.244
F^s_{CSRM}	1.718	1.558	1.540	1.523	1.475	1.410
F^x_{MTM}	0.202	0.193	0.175	0.157	0.124	0.108
F^y_{MTM}	0.205	0.197	0.186	0.172	0.147	0.121
F^s_{MTM}	0.203	0.195	0.189	0.166	0.135	0.111
F^x_{CDM}	1.152	1.141	1.133	1.117	1.102	1.088
F^y_{CDM}	1.238	1.206	1.193	1.181	1.172	1.162
F^s_{CDM}	1.188	1.175	1.161	1.157	1.144	1.133
F^x_{SDM}	0.284	0.268	0.256	0.211	0.185	0.163
F^y_{SDM}	0.402	0.392	0.342	0.319	0.288	0.267
F^s_{SDM}	0.344	0.333	0.326	0.300	0.282	0.236
CSB	31	32	33	34	35	36
TSF	1.495	1.508	1.519	1.544	1.559	1.587
F^x_{CSRM}	0.462	0.414	0.365	0.317	0.269	0.220
F^y_{CSRM}	2.103	1.962	1.821	1.680	1.539	1.398
F^s_{CSRM}	1.320	1.290	1.214	1.117	1.049	1.011
F^x_{MTM}	0.097	0.075	0.043	0.024	0.018	0.00
F^y_{MTM}	0.101	0.092	0.067	0.043	0.037	0.00
F^s_{MTM}	0.099	0.084	0.046	0.029	0.021	0.00
F^x_{CDM}	1.064	1.053	1.042	1.035	1.025	1.00
F^y_{CDM}	1.142	1.121	1.101	1.090	1.070	1.00
F^s_{CDM}	1.120	1.110	1.075	1.055	1.020	1.00
F^x_{SDM}	0.142	0.109	0.081	0.048	0.026	0.00
F^y_{SDM}	0.253	0.218	0.173	0.127	0.071	0.00
F^s_{SDM}	0.215	0.193	0.122	0.101	0.054	0.00

The normal deformation is neglected.

8.2. Calculation and Analysis. The calculated slice block scheme (Figure 15) can be obtained along the profile I-I' (Figure 14). The specific weight of the sliding body is 20 kN/m^3, and the angle and length of the bottom margin of the slice block can be seen in Figure 15.

The parameters of the model are listed as follows:

$$c = 24\,\mathrm{kPa},$$

$$\phi = 23^{\circ},$$

$$G = 2850\,\mathrm{kPa},$$

$$\begin{aligned}
\rho_{i,0} &= -0.9999,\\
\rho_{i,c} &= -0.51,\\
\sigma_i^{n,c} &= 900\,\mathrm{kPa},\\
\varsigma_i &= 1.28,\\
a_{i,3} &= 0.0129,\\
a_{i,2} &= 1500\,\mathrm{kPa},\\
a_{i,1} &= 2000\,\mathrm{kPa},\\
b_1 &= 50,\\
b_2 &= 0\left(\frac{1}{\mathrm{kPa}}\right).
\end{aligned} \tag{56}$$

The rainfall with a recurrence interval of 20 years is researched, and the seepage curve can be obtained by numerical analysis. The TSF is 1.587.

The critical stress state is located in the 25th slice block, when the partial strength reduction method proposed in this paper is used and the safety factor is equal to 1. When the critical state block (CSB) moves forward step by step, the different safety factors are presented (Table 1) under the rainfall with a recurrence interval of 20 years.

The rainfall once in 50 years is also researched, and the TSF is 1.462. The critical stress state is located at the 30th slice block, when the partial strength reduction method proposed in this paper is used and the safety factor is equal to 1. When the CSB moves forward step by step, the different safety factors are presented (see Table 2) under the rainfall once in 50 years.

The TSFs (1.587 and 1.462) are obtained under the rainfall once in 20 and 50 years, respectively. The surplus safety factors are 0.587 and 0.462, respectively, but the safety factors obtained by the MTM are 0.202, 0.203, 0.203 and 0.097, 0.101, 0.099 in the X-axial, Y-axial, and main sliding directions, respectively. These results show that the surplus safety factors (0.587, 0.462) obtained by the traditional method are greater than those (0.203, 0.099) of the new method (MTM) proposed in this paper.

Tables 1 and 2 show that the safety factor decreases while the critical stress state moves forward step by step. Finally, when the 36th slice block is in the critical stress state, the safety factors of MTM and SDM are equal to 0 and the safety

Table 2: Safety factor of progressive failure under once in 50 years of heavy rain.

CSB	30	31	32	33	34	35	36
TSF	1.21	1.344	1.407	1.415	1.433	1.447	1.462
F^x_{CSRM}	0.595	0.527	0.469	0.394	0.340	0.264	0.210
F^y_{CSRM}	2.645	2.454	2.246	2.073	1.845	1.665	1.456
F^s_{CSRM}	1.743	1.643	1.439	1.350	1.156	1.076	0.976
F^x_{MTM}	0.100	0.071	0.048	0.035	0.028	0.017	0.00
F^y_{MTM}	0.197	0.131	0.107	0.086	0.054	0.031	0.00
F^s_{MTM}	0.120	0.085	0.068	0.052	0.034	0.019	0.00
F^x_{CDM}	1.210	1.193	1.114	1.094	1.055	1.024	1.00
F^y_{CDM}	1.310	1.258	1.200	1.177	1.126	1.069	1.00
F^s_{CDM}	1.227	1.199	1.120	1.108	1.069	1.019	1.00
F^x_{SDM}	0.140	0.107	0.079	0.067	0.041	0.033	0.00
F^y_{SDM}	0.271	0.217	0.171	0.128	0.077	0.039	0.00
F^s_{SDM}	0.191	0.161	0.129	0.080	0.055	0.036	0.00

The normal deformation is neglected.

factor of CDM is equal to 1; thus, the entire Kaziwan landslide maintains the critical state. The physical significance of the MTM, SDM, and CDM are very clear.

9. Conclusion

The failure rule for a slope is investigated, and several results are obtained in this paper. The failure development direction is defined, and the mechanical failure mode can be deduced from the cracking trajectories of the slope.

Five failure modes are proposed for thrust-type slopes. In mode I, shear failure occurs. In mode II, tensile (or tensile-shear) failure occurs in the rear zone and shear failure occurs in the other zones. In mode III, tensile (or tensile-shear) failure occurs in the front zone and shear failure occurs in the other zones. In mode IV, the mechanical failure mode is a combination of modes II and III. In mode V, mechanical failure occurs by alternating shear-tensile-shear modes. That the failure occurs is defined along the sliding surface.

For pull-type slopes, in mode I, shear failure occurs along the whole sliding surface. In mode II, shear failure occurs in the front zone and tensile (or tensile-shear) failure occurs in the rear zone. In mode III, shear failure occurs in the front zone and tensile failure occurs in the rear zone of the sliding body. Mode IV corresponds to a rock mass with distributed joints (or fissures): shear, tensile, and shear failures occur alternately along the soft interlayer and joints (or fissures). Mode V is a combination of mode IV and a shear failure (or tensile-shear or tensile failure).

Five existing forms in the field are proposed for slopes. In form I, the stress distribution is within the yield limit stress state. In form II, the various states of elastic, elastoplastic, and peak stresses are distributed in different zones. In form III, the states of previous peak, peak, postfailure, and residual stresses are distributed. In form IV, the postfailure and residual stress states are present. In form V, the entire sliding surface is in the residual stress state. The stress distribution is designated to follow the sliding surface.

The force distribution characteristics are analyzed along the sliding surface; the driving sliding force is greater than the frictional resistance in the postfailure zone, and the pressure is equal to the counterpressure corresponding to the critical state. The driving sliding force and pressure are equal to the frictional resistance and counterpressure, respectively, in the stable and less-stable zones and at the critical state, but the frictional resistance reaches its maximum at the critical state and both shear stress and shear strain are discontinuous in the failure zone.

The stability of the slope is directly related to the critical state. The force and moment balance corresponding to the material strength are used to describe the critical state for the slice method. Design methods for slope control are proposed according to the failure characteristics. In method I, a rigid design is suggested; the slope control position is selected at the critical state for the thrust- and pull-type slopes and at the yield limit stress state for the foundation pit with a safety factor. In method II, a flexible design is proposed; the slope control position is selected at the yield limit stress state for the thrust- and pull-type slopes and at the peak limit stress state for the foundation pit with a safety factor. In method III, a rigid-flexible design is proposed, and the slope control position is selected between those of methods I and II with a safety factor.

Some terms (failure ratio, etc.) are defined, and they are used for mechanical analysis and probability theory application to slope engineering. The definition of the TSF (the maximum frictional resistance divided by the driving sliding force) is worth discussing, and it is possible for the TSF to evaluate an element (or a slice block). The research results show that the MTM, CDM, and SDM are feasible for evaluating the stability of a slope with regressive failure.

Data Availability

The data used to support the findings of this study are included within the article.

Conflicts of Interest

The authors declare that they have no conflicts of interest.

Acknowledgments

This work was supported by the National Natural Science Foundation of China (Grant nos. 42071264 and 41372363). This work was also supported by the Sichuan Science and Technology Program (Grant no. 2019JDJQ0018) and supported by the Fundamental Research Funds for the Central Universities (Grant no. 2682018GJ02).

References

[1] G.-L. Feng, X.-T. Feng, B.-r. Chen, Y.-X. Xiao, and Y. Yu, "A microseismic method for dynamic warning of rockburst development processes in tunnels," *Rock Mechanics and Rock Engineering*, vol. 48, no. 5, pp. 2061–2076, 2015.

[2] G.-l. Feng, B.-r. Chen, Q. Jiang, Y.-x. Xiao, W.-j. Niu, and P.-x. Li, "Excavation-induced microseismicity and rockburst occurrence: similarities and differences between deep parallel tunnels with alternating soft-hard strata," *Journal of Central South University*, vol. 28, no. 2, pp. 582–594, 2021.

[3] W. Fellenius, "Calculation of stability of earth dam," in *Proceedings of the Transactions. 2nd congress large dams*, vol. 4, pp. 445–462, Washington, DC, USA, September 1936.
[4] A. W. Bishop, "The use of the slip circle in the stability analysis of slopes," *Géotechnique*, vol. 5, no. 1, pp. 7–17, 1955.
[5] E. Spencer, "A method of analysis of the stability of embankments assuming parallel inter-slice forces," *Géotechnique*, vol. 17, no. 1, pp. 11–26, 1967.
[6] N. Janbu, "Slope stability computations," *International Journal of Rock Mechanics and Mining Science & Geomechanics Abstracts*, vol. 12, no. 4, p. 67, 1975.
[7] S. K. Sarma and D. Tan, "Determination of critical slip surface in slope analysis," *Géotechnique*, vol. 56, no. 8, pp. 539–550, 2006.
[8] M. K. Kelesoglu, "The evaluation of three-dimensional effects on slope stability by the strength reduction method," *KSCE Journal of Civil Engineering*, vol. 20, no. 1, pp. 229–242, 2016.
[9] T.-K. Nian, R.-Q. Huang, S.-S. Wan, and G.-Q. Chen, "Three-dimensional strength-reduction finite element analysis of slopes: geometric effects," *Canadian Geotechnical Journal*, vol. 49, no. 5, pp. 574–588, 2012.
[10] H. N. Gharti, D. Komatitsch, V. Oye, R. Martin, and J. Tromp, "Application of an elastoplastic spectral-element method to 3D slope stability analysis," *International Journal for Numerical Methods in Engineering*, vol. 91, no. 1, pp. 1–26, 2012.
[11] R. C. Tiwari, N. P. Bhandary, and R. Yatabe, "3D SEM Approach to evaluate the stability of large-scale landslides in Nepal Himalaya," *Geotechnical & Geological Engineering*, vol. 33, no. 4, pp. 773–793, 2015.
[12] D. Y. Zhu and C. F. Lee, "Explicit limit equilibrium solution for slope stability," *International Journal for Numerical and Analytical Methods in Geomechanics*, vol. 26, no. 15, pp. 1573–1590, 2002.
[13] R. Baker, "Nonlinear Mohr envelopes based on triaxial data," *Journal of Geotechnical and Geoenvironmental Engineering*, vol. 130, no. 5, pp. 498–506, 2004.
[14] W. B. Wei, Y. M. Cheng, and L. Li, "Three-dimensional slope failure analysis by the strength reduction and limit equilibrium methods," *Computers and Geotechnics*, vol. 36, no. 1-2, pp. 70–80, 2009.
[15] C. Matthews, Z. Farook, and P. Helm, "Slope stability analysis-limit equilibrium or the finite element method," *Ground Engineering*, vol. 48, no. 5, pp. 22–28, 2014.
[16] X. P. Zhou and H. Cheng, "Stability analysis of three-dimensional seismic landslides using the rigorous limit equilibrium method," *Engineering Geology*, vol. 174, no. 8, pp. 87–102, 2014.
[17] L. Faramarzi, M. Zare, A. Azhari, and M. Tabaei, "Assessment of rock slope stability at cham-shir dam power plant pit using the limit equilibrium method and numerical modeling," *Bulletin of Engineering Geology and the Environment*, vol. 76, no. 2, pp. 783–794, 2016.
[18] G. Sun, Y. Yang, W. Jiang, and H. Zheng, "Effects of an increase in reservoir drawdown rate on bank slope stability: a case study at the Three Gorges Reservoir, China," *Engineering Geology*, vol. 221, pp. 61–69, 2017.
[19] X. P. Zhou and H. Cheng, "Analysis of stability of three-dimensional slopes using the rigorous limit equilibrium method," *Engineering Geology*, vol. 160, pp. 21–33, 2013.
[20] H. Zheng, Z. L. Yang, and G. H. Sun, "Extremum solutions to the limit equilibrium method subjected to physical admissibility," *Natural Hazards*, vol. 65, no. 1, pp. 79–96, 2013.
[21] X. Lü, D. Xue, Q. Chen, X. Zhai, and M. Huang, "Centrifuge model test and limit equilibrium analysis of the stability of municipal solid waste slopes," *Bulletin of Engineering Geology and the Environment*, vol. 78, no. 4, pp. 3011–3021, 2019.
[22] B. Nilsen, "Rock slope stability analysis according to Eurocode 7, discussion of some dilemmas with particular focus on limit equilibrium analysis," *Bulletin of Engineering Geology and the Environment*, vol. 76, no. 4, pp. 1229–1236, 2016.
[23] X. P. Zhou and H. Cheng, "The long-term stability analysis of 3D creeping slopes using the displacement-based rigorous limit equilibrium method," *Engineering Geology*, vol. 195, pp. 292–300, 2015.
[24] A. Su, Z. Zou, Z. Lu, and J. Wang, "The inclination of the interslice resultant force in the limit equilibrium slope stability analysis," *Engineering Geology*, vol. 240, no. 5, pp. 140–148, 2018.
[25] B. Thiebes, R. Bell, T. Glade, S. Jäger, M. Anderson, and L. Holcombe, "A WebGIS decision-support system for slope stability based on limit-equilibrium modelling," *Engineering Geology*, vol. 158, pp. 109–118, 2013.
[26] J. Shen, M. Karakus, and C. Xu, "Chart-based slope stability assessment using the Generalized Hoek-Brown criterion," *International Journal of Rock Mechanics and Mining Sciences*, vol. 64, pp. 210–219, 2013.
[27] A. N. Antão, T. G. Santana, M. Vicente da Silva, and N. M. da Costa Guerra, "Passive earth-pressure coefficients by upper-bound numerical limit analysis," *Canadian Geotechnical Journal*, vol. 48, no. 5, pp. 767–780, 2011.
[28] D. Benmeddour, M. Mellas, R. Frank, and A. Mabrouki, "Numerical study of passive and active earth pressures of sands," *Computers and Geotechnics*, vol. 40, pp. 34–44, 2012.
[29] A. Locat, H. P. Jostad, and S. Leroueil, "Numerical modeling of progressive failure and its implications for spreads in sensitive clays," *Canadian Geotechnical Journal*, vol. 50, no. 9, pp. 961–978, 2013.
[30] Y.-p. Yin, B. Huang, X. Chen, G. Liu, and S. Wang, "Numerical analysis on wave generated by the qianjiangping landslide in three Gorges reservoir, China," *Landslides*, vol. 12, no. 2, pp. 355–364, 2015.
[31] Y. Zheng, C. Chen, T. Liu, H. Zhang, K. Xia, and F. Liu, "Study on the mechanisms of flexural toppling failure in anti-inclined rock slopes using numerical and limit equilibrium models," *Engineering Geology*, vol. 237, pp. 116–128, 2018.
[32] N. Li and Q.-h. Qian, "Four criteria of stability analysis and assessment of high rock slope," *Chinese Journal of Rock Mechanics and Engineering*, vol. 29, no. 9, pp. 1754–1759, 2010.
[33] H. Suwa, T. Mizuno, S. Suzuki, Y. Yamamoto, and K. Ito, "Sequential processes in a landslide hazard at a slate quarry in Okayama, Japan," *Natural Hazards*, vol. 45, no. 2, pp. 321–331, 2008.
[34] B. Leshchinsky, F. Vahedifard, H.-B. Koo, and S.-H. Kim, "Yumokjeong landslide: an investigation of progressive failure of a hillslope using the finite element method," *Landslides*, vol. 12, no. 5, pp. 997–1005, 2015.
[35] V. Gischig, G. Preisig, and E. Eberhardt, "Numerical investigation of seismically induced rock mass fatigue as a mechanism contributing to the progressive failure of deep-seated landslides," *Rock Mechanics and Rock Engineering*, vol. 49, no. 6, pp. 2457–2478, 2016.
[36] G. Prountzopoulos, P. Fortsakis, K. Seferoglou, F. Chrysochoidis, I. Vassilopoulou, and V. Perleros, "Assessment of failure mechanism and rehabilitation of a landslide within marly formations in NW Greece: from the site investigation to the geotechnical design," *Geotechnical & Geological Engineering*, vol. 32, no. 6, pp. 1485–1502, 2014.

[37] V. Kumar, V. Gupta, and I. Jamir, "Hazard evaluation of progressive Pawari landslide zone, Satluj valley, Himachal Pradesh, India," *Natural Hazards*, vol. 93, no. 2, pp. 1029–1047, 2018.

[38] A. Yerro, N. M. Pinyol, and E. E. Alonso, "Internal progressive failure in deep-seated landslides," *Rock Mechanics and Rock Engineering*, vol. 49, no. 6, pp. 2317–2332, 2016.

[39] O.-L. A. Kwok, P.-C. Guan, W.-P. Cheng, and C.-T. Sun, "Semi-Lagrangian reproducing kernel particle method for slope stability analysis and post-failure simulation," *KSCE Journal of Civil Engineering*, vol. 19, no. 1, pp. 107–115, 2015.

[40] F. Miao, Y. Wu, Y. Xie, F. Yu, and L. Peng, "Research on progressive failure process of Baishuihe landslide based on Monte Carlo model," *Stochastic Environmental Research and Risk Assessment*, vol. 31, no. 7, pp. 1683–1696, 2017.

[41] Y. F. Lu, L. P. Yang, and D. F. Liu, "A new joint constitutive model and several new methods of stability coefficient calculation of landslides," *Chinese Journal of Rock Mechanics and Engineering*, vol. 32, no. 12, pp. 2431–2438, 2013.

[42] Y. F. Lu, "Deformation and failure mechanism of slope in three dimensions," *Journal of Rock Mechanics and Geotechnical Engineering*, vol. 7, no. 2, pp. 109–119, 2015.

Hindawi
Advances in Civil Engineering
Volume 2021, Article ID 9650644, 9 pages
https://doi.org/10.1155/2021/9650644

Research Article

Research on the Fault Diagnosis Method of Mine Fan Based on Sound Signal Analysis

Shijie Song,[1] Dandan Qiu ,[1] and Sunwei Qin[2]

[1]*School of Resources and Safety Engineering, Xingfa School of Mining Engineering, Wuhan Institute of Technology, Wuhan 430073, China*
[2]*Chemistry and Environmental Engineering, Wuhan Institute of Technology, Wuhan 430073, China*

Correspondence should be addressed to Dandan Qiu; dada_qdd@163.com

Received 15 July 2021; Revised 8 August 2021; Accepted 13 August 2021; Published 27 August 2021

Academic Editor: Guang-Liang Feng

The underground local fan and auxiliary fan also play a vital role in the underground air quality, compared with the system fan. However, the number of underground local fans and auxiliary fans is large and widely distributed, which is disadvantageous to adopt the same method of online monitoring and fault diagnosis method as the system fan. In order to find a new fault diagnosis method, which is cost-effective and reliable, this paper proposes a fault diagnosis method based on sound signal. It analyzes the source of fan noise and studies the overall scheme of mine fan fault diagnosis expert system based on sound signal. The fault expert system consists of four parts: signal acquisition and noise elimination, feature extraction, state recognition, and fault diagnosis. Its principle is briefly introduced. The denoising method of wavelet is adopted in this paper. Wavelet packet is used to extract the characteristics of sound signal, and the energy size and energy proportion of each frequency component are used as the basis of knowledge acquisition and reasoning. Through the analysis of the measured signals of the fan in the normal operating state, the feature vectors were extracted as the basis for the discrimination of the normal state after noise elimination. At the same time, the audio processing software was used to simulate the sound signals in three fault states. Then, the feature vector of the fault state is extracted, which is obviously different from that of the fan in the normal operation. As the basis of fault state analysis of the expert system, it lays the foundation for the realization of the expert system of mine fan equipment running state diagnosis.

1. Introduction

Mine fan is the core equipment of mine ventilation safety, which provides the necessary power for air flow. The normal operation of the fan is very important for the whole ventilation system. At present, the real-time monitoring and fault diagnosis technology for the operation status of the main fan in the mine are relatively perfect. Compared with the local fan which is used to press in the working face and the auxiliary fan which is used to adjust the air volume in the branch air path of the mine ventilation network, the real-time monitoring of the underground auxiliary fan and the local fan has the characteristics of large number and complex distribution. Therefore, it is necessary to find an accurate and convenient detection method to detect the operation status of the fan in real time, so as to ensure a good working environment in the mine and the health and labor safety of underground workers.

Nowadays, most of the fan monitoring uses vibration signals for online monitoring. There are always one or more inherent vibration frequencies in the operation of the fan. When the fan runs abnormally, it may produce one or more frequency components different from its own natural frequency. Relevant scholars at home and abroad have done relevant research on fan monitoring and fault diagnosis based on vibration signal, temperature, and artificial intelligence. Yao and others proposed a nonlinear autoregressive moving average model to test the sunspot data and then applied the model to fan fault diagnosis, with high prediction accuracy [1]. Hong and Liao proposed a classification method based on Drosophila algorithm to optimize the least squares support vector machine (LSSVM). Based on the

eigenvectors of fan vibration frequency domain as learning samples, the improved LSSVM model is used to identify the energy characteristics of fan vibration signal, which has the characteristics of high recognition rate and fast diagnosis speed [2]. Shu established the mine fan fault monitoring model by extracting the complex number of fault features in the fan vibration signal, combined with the principle and method of weighted support vector machine, and realized the online monitoring of mine fan fault [3]. Xuan and Li designed a set of online monitoring and fault diagnosis system for large-scale mine fan based on LabVIEW, realized real-time acquisition of fan vibration signal, monitored the operation status of equipment, and reached a diagnosis according to the vibration situation through analytic hierarchy process [4]. Zhai, through the combination of temperature change, vibration frequency, auxiliary, and troubleshooting diagnosis method, carried out fault diagnosis on several points of coal mine [5]. Zhao used BP neural network algorithm to predict the temperature of gearbox bearing, verified the feasibility and rationality of the network model, mastered the fan state, and ensured the stable and reliable operation of the unit [6]. Vibration signals need contact sensors to collect signals, and the fan itself is in the complex environment of high voltage and strong electromagnetic field, which affects the monitoring results and is not conducive to installation and maintenance.

In terms of audible sound, based on the analysis of acoustic characteristics, there is no relevant literature on mechanical fault diagnosis of mine fan equipment. Compared with the vibration signal, it is of great significance to introduce the sound signal into the condition monitoring of the fan equipment. The fan will produce different sound signals in different operation states. The sound signal under the normal operation state can be collected and analyzed to extract the detailed features, which can effectively carry out monitoring and fault diagnosis. Condition monitoring is used in fault diagnosis system, which includes two aspects: signal analysis and processing, and fault diagnosis. The purpose of signal analysis and processing is to transform the obtained information through certain methods and extract the most intuitive, sensitive, and useful feature information from different angles [7].

This paper studies the technical scheme of mine fan sound monitoring and diagnosis system. The front-end equipment is used to collect the sound signal of the normal operation of the mine fan. The wavelet denoising processing is used first and is then combined with the recognizable characteristics of the sound signal. Through the fault diagnosis expert system of the mine fan, the operation state of the fan can be effectively judged.

2. New Program for Safety Monitoring of Mine Fan Operation

There is a close relationship between the audio signal of the mine fan and its running state. The sound of the fan in the normal running state has its fixed time-frequency characteristics, which can be used as the basis for fault diagnosis. Therefore, the real-time acquisition of the sound signal from the fan equipment, the use of digital signal processing analysis of the current time-frequency information, can diagnose whether there is a fan failure or hidden danger. Compared with the vibration signal feature analysis, the fault diagnosis method of sound signal is a real noncontact, nonembedded, and 24-hour online monitoring method. Therefore, the real-time acquisition of acoustic signal from mine fan equipment and quantitative analysis of its variation law and mutation characteristics by digital signal processing method can diagnose faults or hidden dangers [8]. At the same time, compared with the vibration sensor, the sound sensor has advantages in price, long service life, and easy replacement. It is suitable for the dispersion of local fan and auxiliary fan in the mine, reflecting the economy based on sound monitoring. The overall block diagram of mine fan fault diagnosis system based on sound is shown in Figure 1.

The whole system is divided into four parts: signal acquisition and denoising, feature extraction, state recognition, and diagnosis decision.

Signal acquisition collects the sound generated by the normal operation of the mine local fan and selects the sound signal that can represent the working state of the equipment for feature extraction, which is used as the basis for diagnosing the equipment fault. After the completion of signal acquisition, the signal feature extraction is carried out. Acoustic signal feature extraction firstly denoises the collected sound signal and then transforms the denoised signal into energy as the signal feature by signal analysis and data processing. After feature extraction, the state recognition is carried out, and the characteristic parameters of acoustic signal obtained after signal processing are compared with the allowed parameters or discriminant parameters in the system knowledge base through the inference engine, so as to diagnose whether there is fault in its operation state and further determine the type of fault. Finally, the diagnosis system decides the measures to be taken according to the status of the diagnosis equipment and then predicts the possible development trend of the equipment according to the current signal, analyzes the trend, and makes a decision.

The monitoring and fault diagnosis of mine local fan can be realized by collecting the sound signal of fan operation, combining with the signal denoising and feature extraction technology, and then using the expert system.

3. Acoustic Signal Acquisition and Processing

Due to the complex environment of underground mining face, a large amount of noise will be mixed when collecting the fan signal, which is a typical nonstationary signal. Fan noise is a by-product of fan operation, but it also contains rich information about the operation process. Experienced operators can often judge the equipment status by listening to the sound changes in the operation process [9].

3.1. Source of Fan Noise

3.1.1. Noise of Blade Rotation. When the blade rotates, it will rub or impact with the air. The noise is sharper when the speed is faster and the frequency of air connection is higher.

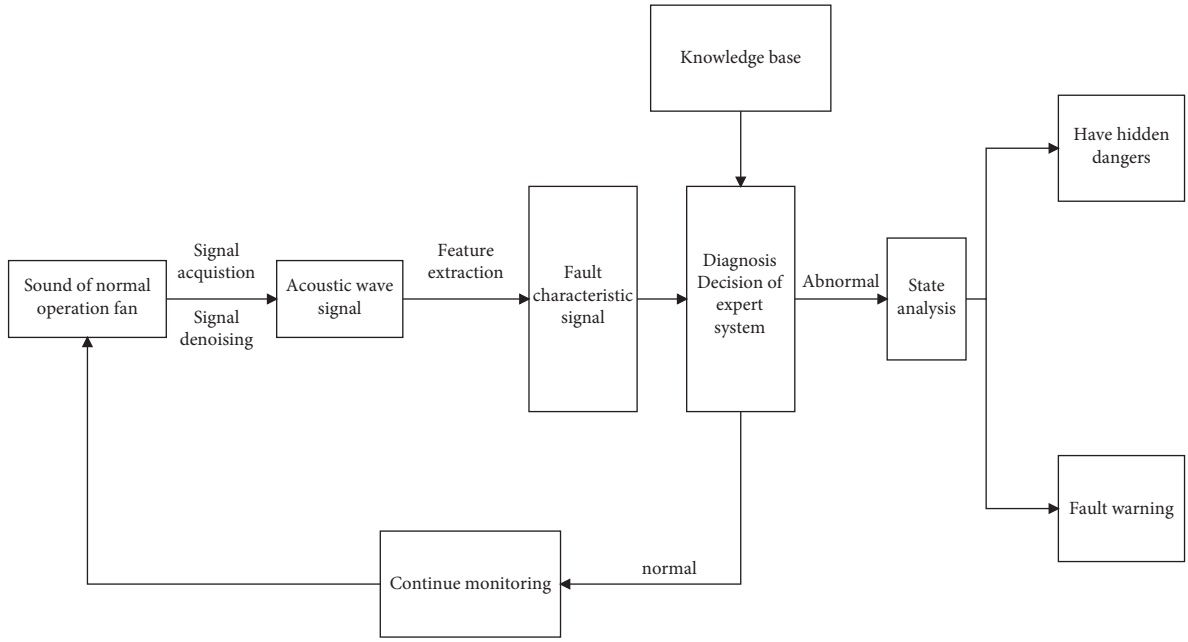

Figure 1: Fault diagnosis system diagram of mine fan.

This phenomenon is more obvious when the width or thickness of the blade increases. The frequency of noise is composed of multiple frequencies, which are related to the speed of the fan.

3.1.2. Noise of Blade Vortex. During the operation of the fan, the vortex will be generated on the back of the moving wing, which will not only reduce the efficiency of the fan, but also produce noise. During the operation of the fan, the vortex will be generated on the back of the moving wing, which will not only reduce the efficiency of the fan, but also produce noise.

3.1.3. Noise of Turbulence. When the air is flowing, if it meets sharp obstacles, it is easy to cause turbulence. Although the turbulence is different from the vortex, it will also produce noise or high-frequency whistling, which will also cause efficiency loss to the fan. Although the turbulence is different from the vortex, it will also produce noise or high-frequency whistling, which will also cause efficiency loss to the fan.

3.1.4. Noise of the Air Duct Housing Resonates. The joint between the air duct and the inner surface of the fan shell shall be smooth to avoid roughness and unevenness, which may cause tearing sound. Moreover, because the connected pipeline will produce resonance, the subtle sound will become larger, resulting in greater noise. In the design, sometimes the air duct can be covered with antisound material to reduce noise.

3.1.5. Noise Outside the Fan. In addition to the fixed noise of the fan itself, there are many noise sources, such as the bearing due to insufficient precision, improper assembly, or poor maintenance, which will cause abnormal noise. The motor also produces noise, some of which is caused by poor design or poor manufacturing quality control, but sometimes by the cooling fans inside and outside the motor. Gears and belts also produce noise due to friction. The noise produced by the resonance of other structures cannot be ignored, which is sometimes caused by the imbalance of the body.

3.2. Signal Acquisition and Analysis. Sound signal carries all kinds of information. The purpose of sound signal processing is to extract these kinds of information. The processing methods can be divided into time-domain analysis and frequency domain analysis. The time-domain analysis is relatively intuitive and simple, while the frequency domain analysis changes the sound signal from the time domain to the frequency domain composed of sine function or cosine function to extract the characteristic parameters.

In this paper, the sound equipment with sampling frequency of 44100 Hz is used to sample the local fan in the mine. The time-domain waveform and frequency spectrum of the fan in normal operation are obtained by processing the audio signal collected from the field. The sampling point is $4.4 * 104$, and the time domain waveform is shown in Figures 2(a) and 2(b), which reflects the image of the sound signal in the time domain, and the relationship between the change of the sound signal with time and the amplitude of the sound signal. The time-domain signal is changed to the frequency domain through Fourier change, and the spectrum components and the intensity of each component of the signal are analyzed. It reflects the relationship between the sound signal frequency (Hz) and the amplitude of the sound signal at this frequency. From the analysis results, it can be seen that the fan audio signal is composed of multiple frequencies, the main frequency components are within 8000 Hz, and the

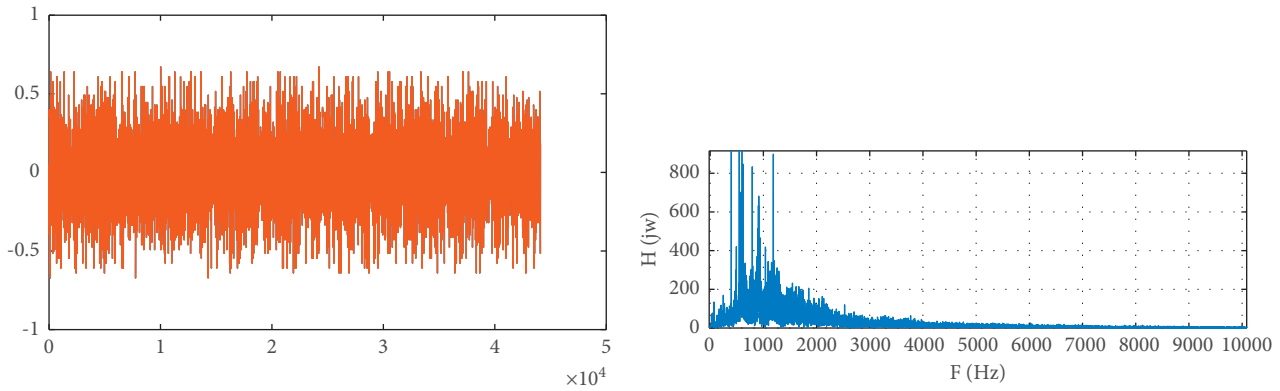

(a) (b)

Figure 2: (a) Time-domain waveform of signal. (b) Spectrum of signal.

200 Hz, 300 Hz, and 600 Hz frequency points in the power spectrum show obvious current spectrum.

3.3. Wavelet Denoising. Because the fault signal is a transient signal, the traditional Fourier transform analysis method cannot be distinguished. This is because the use of Fourier transform analysis will be able to reflect the fault characteristics of the local signal in the entire frequency domain smoothed out, thus losing the useful information used to analyze the fault, resulting in large errors. The wavelet analysis has good time-frequency localization, using different scales, in different widths of the time window for analysis, especially suitable for the processing of odd signals [10, 11]. The principle of wavelet threshold denoising is to generate a threshold value by estimating the noise intensity and use the threshold function to process the wavelet coefficients to remove part of the noise-related components, so as to increase the proportion of useful signals. There are three main steps: firstly, the noisy signal is decomposed into several layers of wavelet coefficients by wavelet variation, then the noise-related components are removed by processing the wavelet coefficients in each layer using the threshold function, and finally the signal is reconstructed by wavelet inverse transform [12].

(1) Choose a wavelet, determine the number of layers M of wavelet decomposition, find suitable wavelet basis, and then use discrete wavelets to perform M-layer wavelet decomposition on noise-bearing signals [13]. The Harr wavelet function is defined as follows:

$$\psi(x) = \begin{cases} 1, & 0 \le x < \frac{1}{2}, \\ -1, & \frac{1}{2} \le x < 1, \\ 0, & \text{others}. \end{cases} \tag{1}$$

(2) Threshold quantization is performed on the high-frequency coefficients of each layer from the first layer to M. Soft and hard thresholding methods are commonly used [14]. The soft thresholding method sets the wavelet coefficients smaller than the threshold to zero and makes the wavelet coefficients larger than the threshold shrink toward zero, with the following expressions:

$$s = \begin{cases} x, & |x| > T, \\ 0, & |x| \le T. \end{cases} \tag{2}$$

The two methods differ from each other, with the former having continuity and being mathematically easy to handle, and the latter being closer to the implementation case.

The key to threshold processing is the selection of the threshold value. If the threshold value is too small, noise will remain after noise cancellation; if the threshold value is too large, important signals will be filtered out and cause bias.

(3) Wavelet reconstruction of the signal based on the low-frequency coefficients of the Mth layer of the wavelet decomposition and the high-frequency coefficients of the first to Mth layers after quantization is performed with the following expression [15]:

$$c_{j-1}, n = \sum_n c_j, nh_k - 2_n + \sum_n d_j, ng_k - 2_n. \tag{3}$$

$c_{j,n}$ is the scale factor; d_j is the wavelet coefficients; h, g are a pair of orthogonal mirror filter sets; j is the number of decomposition layers; n is discrete sampling points.

Wavelet transform has good time-frequency characteristics. Compared with traditional linear filtering and nonlinear filtering, wavelet denoising has the characteristics of low entropy, multiresolution, decorrelation, and diversity of wavelet base selection. Reduce the entropy of the signal after transformation, and better characterize the nonstationary characteristics of the signal, such as edge, peak, and breakpoint. The noise tends to whiten after transformation. At the same time, wavelet transform can

flexibly select different wavelet bases according to the characteristics of the signal.

3.4. Elimination of Measured Signal Noise. MATLAB software is used to denoise the measured sound signal of 5.5 kW mine press in axial flow local fan. Through the denoising function in the wavelet toolbox, the measured audio signal is decomposed into five layers by using the Harr wavelet in the wavelet toolbox to obtain Figure 3(a), in which s is the original signal, $A5$ is the fifth-order approximation signal, $d1$–$d5$ is the detail signal after wavelet decomposition, and the frequency components are arranged from low to high [16].

Denoise the signal and get the image (the red part is the original signal and the purple part is the denoised signal). It can be seen that the burr in the signal can be eliminated by denoising, and the rich high-frequency information can still be retained, which has obvious denoising effect. The characteristics of wavelet transform multiresolution analysis make it have a strong advantage in noise reduction rate [17].

4. Wavelet Packet-Based Feature Extraction

Feature extraction refers to the identification and separation of faults in the process of extracting the characteristic information related to wind turbine faults from the state signal. The general feature quantity is selected in order to transform the information from the measurement space to the feature space that is built for a substantial reduction in the number of dimensions, thus highlighting the fault characteristics and improving the accuracy for subsequent fault diagnosis. There are usually 3 steps to extract feature quantities [18, 19].

(1) The signal is decomposed by 3 layers of wavelet packets, and the signal features of 8 frequency components from low to high frequencies are extracted in layer 3, respectively. These 8 wavelet packet coefficients summarize the features of the wind turbine audio signal in different frequency bands. Its wavelet packet decomposition tree is shown in Figure 4. The wavelet packet coefficients of each node are obtained as $[S_{3,0}, S_{3,1}, S_{3,2}, S_{3,3}, S_{3,4}, S_{3,5}, S_{3,6}, S_{3,7}]$.

(2) Find the total energy of the signal in each frequency band. Let the energy corresponding to S_{3jbe} E_{3j}, $j = 0, 1, \ldots, 7$; then we have

$$E_{3j} = \left| \int S_{3j}(t) \right|^2 \mathrm{d}t = \sum_{k=1}^{n} \left| x_{jk}^2 \right|, \tag{4}$$

where x_{jk} ($j = 0, 1, \ldots, 7$, $k = 1, 2, \ldots, n$) denotes the amplitude of the discrete points of the reconstructed signal S_{3j}.

(3) Construct the eigenvectors. Construct the eigenvector T with energy as an element: $T = [E30, E31, E32, E33, E34, E35, E36, E37,]$.

In practical engineering, when the energy is relatively large, it can cause inconvenience during data analysis. Therefore, the energy value of the signal is usually normalized, and the ratio of the energy of each node to the total energy is taken as a feature to form the corresponding feature vector [20]. The corresponding equation is

$$T(j,i) = \frac{E(j,i)}{\sum_{k \in (j,i)} E(j,i)}. \tag{5}$$

$T(j,i)$ is the percentage of energy of the corresponding node; $E(j, i)$ is the energy value of the corresponding node. The above calculation results in a new feature vector $T` = [T0, T1, T2, T3, T4, T5, T6, T7,]$ for the wind turbine audio.

Collect the audio signals of five groups of fans under normal operation, which are $G1$, $G2$, $G3$, $G4$, and $G5$, respectively. The duration of the audio signal is 1 s. Each group of audio signals is divided into eight energy nodes ($T0$, $T1$, $T2$, $T3$, $T4$, $T5$, $T6$, $T7$). Use the wavelet packet of db3 of MATLAB wavelet packet tool for three-layer decomposition to obtain the ratio of the energy of each node to the total energy, as shown in Figure 5. After obtaining the total energy of the signal, the energy of each node is obtained (E_{30}, E_{31}, E_{32}, E_{33}, E_{34}, E_{35}, E_{36}, E_{37}), as shown in Table 1. From the energy proportion in Figure 5, it can be seen that the proportion of each node in the total energy has no obvious change. From the output energy of the signal in Table 1, it can be seen that the output energy of each node has a small change. From the two aspects, it can be seen that the test data has good repeatability, so the requirement for the number of tests n is not too much. Finally, according to the feature vector of the signal, through the fault diagnosis expert system for decision-making classification, we can judge whether the mine fan is faulty or not.

By collecting the sound signal of the mine fan, wavelet noise eliminated. Extract the feature vector of the signal to get several groups of data that can characterize the signal information by using MATLAB. This is used as the judgment basis of inference machine [21, 22].

5. Fault Signal Simulation

Due to the low failure rate of mine fan, it is easy to collect the audio signal in the normal operation state, but it is very difficult to study the audio signal in the specific fault type. Therefore, in order to study the fan audio signal under some specific fault conditions, the audio processing software is used for simulation. In this paper, three kinds of fan fault audio signals are simulated. When the fan is running under load, the fan bearing overheats, and the fault sound is "buzzing." When the bearing is abnormal, the fault phenomena are various abnormal sounds, such as sharp sound, whistling sound, or impact sound. When the operation of the belt is abnormal, the fault phenomenon is that the belt jumps out during the operation and makes a "pop" sound, and the speed of the belt pulley decreases. Based on the above audio signal denoising and feature extraction algorithm, five groups of data of three kinds of fault audio signals are analyzed, and their corresponding energy is calculated as shown in Figure 6.

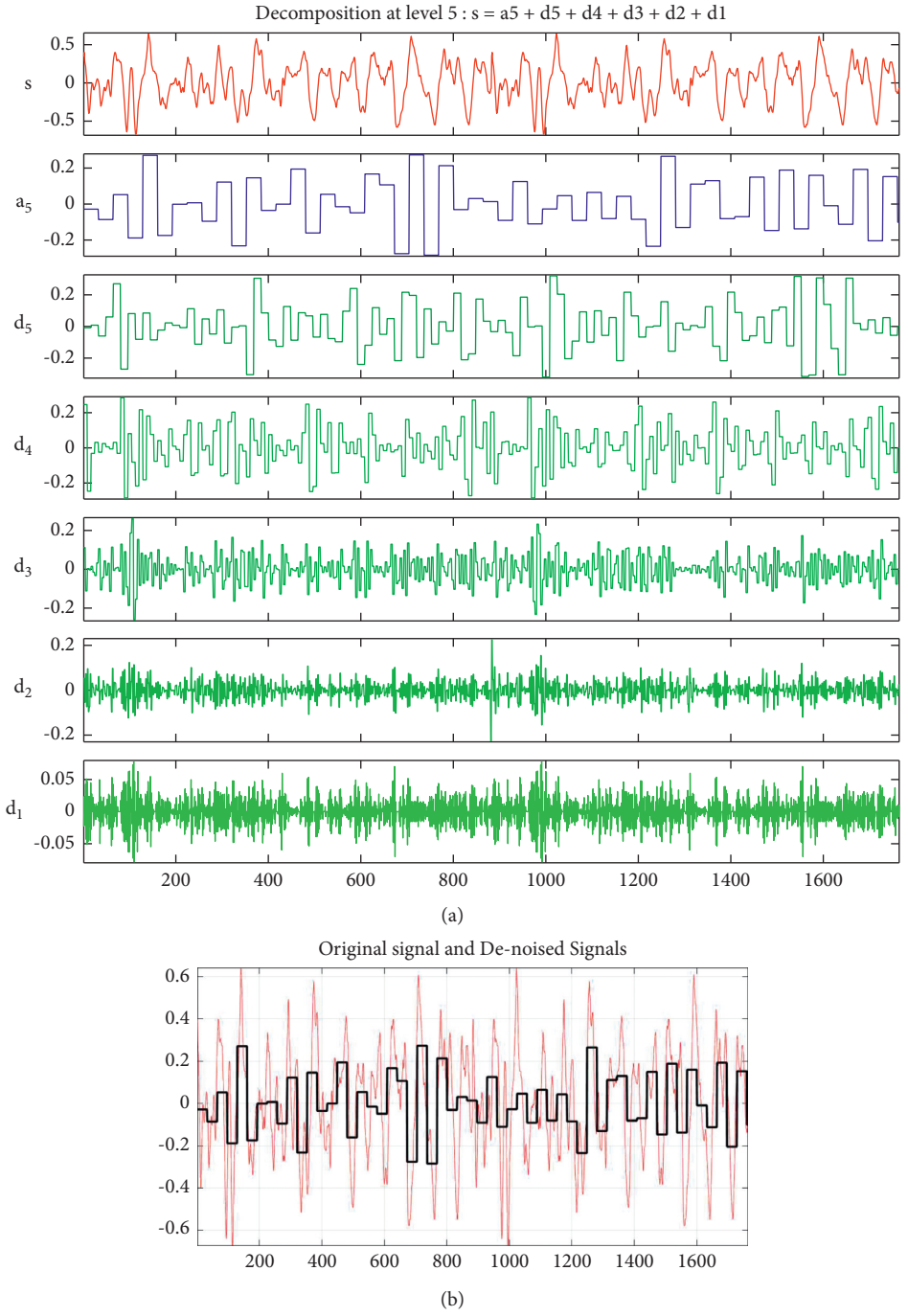

Figure 3: (a) Original signal decomposition diagram. (b) Comparison of original signal and denoised signal.

Figure 6(a) simulates the sound of the fan under load. Simulate five groups of audio signals in this state, namely, *G*1, *G*2, *G*3, *G*4, and *G*5, and calculate the proportion of each node energy to the total energy. Similarly, Figures 6(b) and 6(c) are audio signals under the fault state of fan bearing and the abnormal state of fan belt. Different types of fault audio signals simulate 5 groups of signals and extract characteristic information. It is not difficult to find that the fan has corresponding frequency characteristics under different fault operating states, and the characteristic frequencies of audio signals with the same fault have high similarity. The characteristic frequencies of different fault types change greatly, and these fault characteristic frequencies are also quite different from the frequency of normal operation state, which can be used as the basis of fault reasoning. Once the test audio signal has different characteristic frequencies, the fault can be judged, and the reliability of sound monitoring is verified. However, due to the limited research data, the threshold between different states cannot be accurately determined, which needs further research.

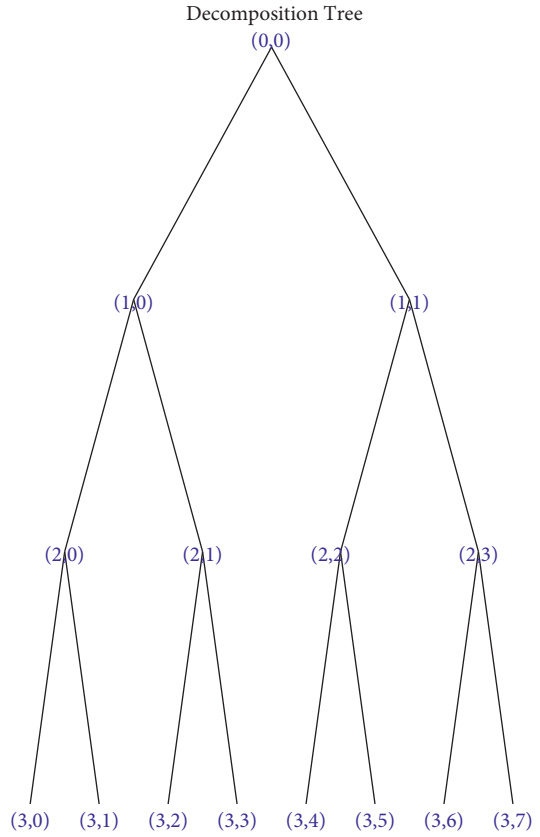

Figure 4: Wavelet decomposition tree.

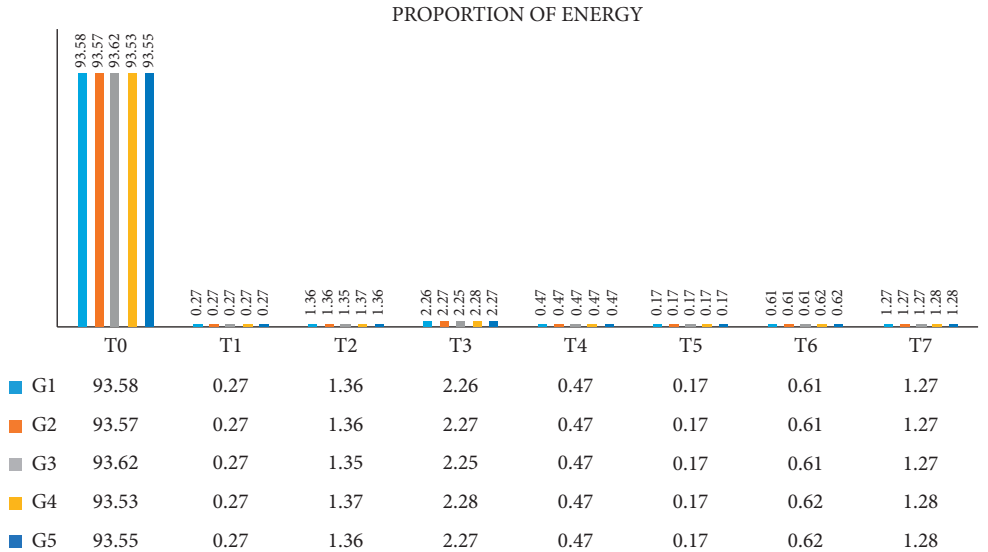

Figure 5: Energy proportion.

Table 1: The output energy of the signal table.

Group	E_{30}	E_{31}	E_{32}	E_{33}	E_{34}	E_{35}	E_{36}	E_{37}
1	12590.25	36.32	182.97	304.06	63.23	22.87	82.06	170.86
2	12268.89	35.4	178.32	297.64	61.62	22.29	79.98	166.52
3	12462.69	35.94	179.71	299.52	62.56	22.63	81.2	169.06
4	12864.11	37.13	188.42	313.59	64.64	23.38	85.27	176.05
5	12794.83	36.92	186	310.46	64.28	23.25	84.79	175.06

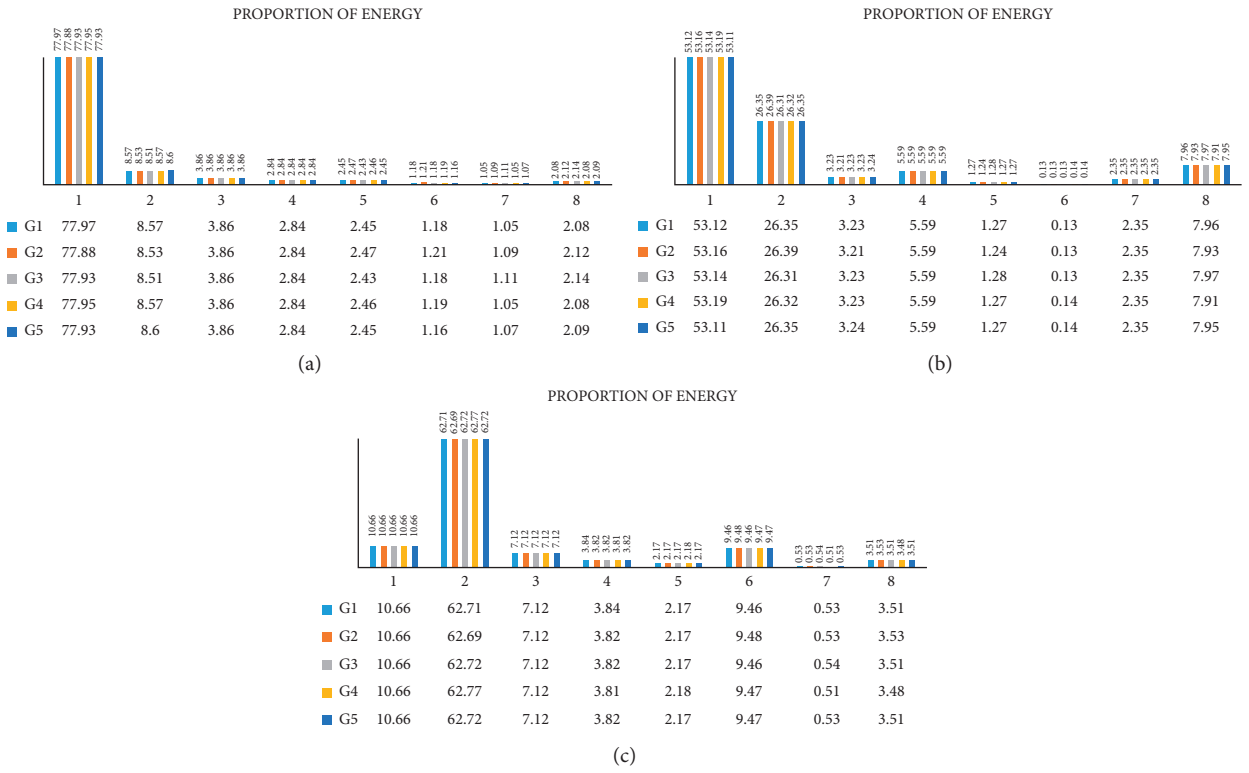

Figure 6: (a) Under fan load condition. (b) Fan bearing fault. (c) Under abnormal condition of fan belt.

6. Conclusion

This paper puts forward a fault diagnosis scheme based on the sound signal of mine fan and analyzes the noise source of mine fan, including the noise generated by blade rotation, the noise generated by blade eddy current, the noise generated by turbulent flow, the noise generated by resonance with the air duct shell, and the noise caused outside the fan. Through the audio data collected by the audio device, the wavelet denoising is used to filter the signal layer by layer, and the noise in the signal is reconstructed to retain its mutation characteristics. The wavelet packet algorithm is used to quantify the time-domain information. According to the output energy and energy proportion of each node, the feature vector is used for the diagnosis and decision-making of reasoning machine. The results show that the method highlights the fault characteristics and can judge whether there are hidden faults in the mine fan. Through the audio processing software to simulate the sound signal of the fan in three fault states, using the above data analysis, the feature vector of the fault state signal is extracted. It is found that different fault states have their corresponding feature frequencies, which are obviously different from the feature vector of the fan in normal operation, which can be used as the basis for the fault signal identification of the expert system.

The fault diagnosis based on sound analysis is a new noncontact online monitoring method, which can accurately reflect the operation status of electrical equipment without affecting the normal operation of electrical equipment. It is more effective for online monitoring and fault diagnosis of mine fan. This method can ensure the normal operation of the mine fan, find the hidden danger of the fan in time, and ensure the life safety of the underground workers, which is of great significance to promote the digital mine.

Data Availability

The sound signal data used to support the findings of this study are included within the article.

Conflicts of Interest

The authors declare that they have no conflicts of interest.

Acknowledgments

The authors acknowledge the support from the Science Research Foundation of Wuhan Institute of Technology (K201854).

References

[1] L. Yao and L. Pan, "The application of nonlinear modeling in the fault diagnosis of fan," *Advanced Materials Research*, vol. 926-930, p. 3181, 2014.

[2] W. P. Hong, M. J. Liao, Application of fruit fly optimization algorithm-least square support vector machine in fault diagnosis of fans," *Advanced Materials Research*, vol. 860-863, p. 2912, 2014.

[3] F. Shu, "Application of improved support vector machine in fault diagnosis of mine fan," *Mining machinery*, vol. 34, no. 3, pp. 39–41, 2006.

[4] Z. Xuan and X. Li, "HHT extraction of vibration signal characteristic components of mine fan," *Journal of Hefei Union University*, vol. 38, no. 1, pp. 34–38, 2016.

[5] R. Zhai ., "Research on fault diagnosis and maintenance technology of coal mine electromechanical equipment," *China Petroleum and chemical industry standard and quality*, vol. 40, no. 16, pp. 21-22, 2020.

[6] H. Zhao, "Fault prediction of key components of wind turbine based on BP neural network," *Power station system engineering*, vol. 37, no. 2, pp. 21-22, 2021.

[7] W. Chang, Xi Peng, Q. Luo, B. Zeng, X. Jin, and L. Hu, "Fault analysis of catalytic main fan based on condition monitoring and fault diagnosis technology," *China Equipment Engineering*, no. 5, pp. 152–154, 2021.

[8] L. Pan, S. Zhao, and B. Li, "A new method for fault diagnosis of electrical equipment based on acoustic signal analysis," *Electric power automation equipment*, vol. 29, no. 8, pp. 87–90, 2009.

[9] J. Chen, *Research on Abrasive belt Wear Condition Monitoring Method Based on Grinding Sound Signal Characteristics*, Shanghai Jiaotong University, Shanghai, China, 2018.

[10] Y. Liu and G. Zhao, "Wavelet fault detection method based on filter preprocessing," *Power automation equipment*, no. 2, pp. 51–55, 2007.

[11] H. Zhao, Da Zhang, J. Yang, fancui Meng, and M. Zhang, "Application of wavelet stratification in laser Doppler velocimetry," *Laser Technology*, vol. 43, no. 1, pp. 103–108, 2019.

[12] J. Zhang, Q. Zhong, and Y. Dai, "Determination of decomposition level and threshold in application of wavelet threshold denoising method," *Chinese Journal of electrical engineering*, vol. 24, no. 2, pp. 119–123, 2004.

[13] X. Wang, J. Lian, S. Fei, and Z. Zhang, "Chaotic multiple regression daily runoff prediction model based on wavelet denoising," *Journal of System Simulation*, no. 15, pp. 3605–3608, 2007.

[14] Y. Qin, S. Huang, and Q. Zhao, "Chaotic time series prediction model based on wavelet denoising and LS-SVM and its application," *Geodesy and geodynamics*, vol. 28, no. 6, pp. 96–100, 2008.

[15] Li Wen, Z. Liu, and Y. Ge, "Several methods of wavelet denoising," *Journal of Hefei University of Technology*, no. 2, pp. 167–172, 2002.

[16] J. Ren, "Research on data analysis method based on wavelet transform," *Science and technology innovation*, no. 16, pp. 39-40, 2019.

[17] yunyun Zheng, S. Chen, and Y. Hu, "Application of wavelet transform and BP neural network model in settlement deformation monitoring," *Surveying and mapping and spatial geographic information*, vol. 42, no. 2, pp. 101–103 + 107, 2019.

[18] D. Xu, "AC sampling signal denoising technology based on wavelet transform," *Electric power automation equipment*, no. 10, pp. 15–17, 2001.

[19] X. Liu, H. Liu, Y. Chen, and dingfang Ke, "Classification method of transient power quality based on optimal wavelet packet basis decomposition," *Power automation equipment*, no. 10, pp. 36–39, 2005.

[20] J. Chen, "Research on fault diagnosis method of traction transformer based on sound signal analysis," *Electrical application*, vol. 39, no. 2, pp. 25–29, 2020.

[21] G.-l. Feng, B.-r. Chen, Q. Jiang, Y.-x. Xiao, W.-j. Niu, and P.-x. Li, "Excavation-induced microseismicity and rockburst occurrence: s," vol. 28, no. 2, , pp. 582–594, Journal of Central South University, 2021.

[22] G.-L. Feng, X.-T. Feng, B.-r. Chen, Y.-X. Xiao, and Y. Yu, "A microseismic method for dynamic warning of rockburst development processes in tunnels," *Rock Mechanics and Rock Engineering*, vol. 48, no. 5, pp. 2061–2076, 2015.

Hindawi
Advances in Civil Engineering
Volume 2021, Article ID 4247027, 14 pages
https://doi.org/10.1155/2021/4247027

Research Article

Research on the Impact of Different Force Directions on the Mechanical Properties and Damage Evolution Law of Sandstone with Different Hole Diameters

Fukun Xiao, Renhe Li, and Le Xing

Heilongjiang Ground Pressure & Gas Control in Deep Mining Key Lab, Heilongjiang University of Science & Technology, Harbin 150022, China

Correspondence should be addressed to Fukun Xiao; xiaofukun@hotmail.com

Received 3 July 2021; Revised 3 August 2021; Accepted 16 August 2021; Published 26 August 2021

Academic Editor: Guang-Liang Feng

In this research, a uniaxial acoustic emission experiment was conducted on rock samples with different positions and diameters of the hole, and an analysis was made on the impact of different hole positions and diameters on the mechanical properties, failure, energy conversion, and acoustic emission-caused damage characteristics and laws of the rock samples. The results reveal as follows: first, due to the existence of holes in rocks, the stress-strain curve changes at each stage, accompanied by multiple stress drops. And the peak strength gradually reduces with the increase in hole diameter. At different hole positions, the duration that the rock sample passes through at each stage of the stress-strain curve varies, and the peak strength of the rock with the vertical hole is greater than that of the rock with the horizontal hole. This indicates that the bearing capacity and stability of the rock sample with the vertical hole are greater than those of the rock sample with the horizontal hole of the same diameter. Second, by making a comparison on the failure characteristics of rock samples, it is found that the intact rock shows brittle failure. For the rock sample with the horizontal hole, symmetrical tensile cracks initially appear in the upper and lower parts of the hole and finally form shear failure. As for the rock sample with the vertical hole, Y-shape failure originally presents and eventually forms N-shape failure with the increase in hole diameter. Over a comparison with the failure pattern of an intact rock sample, it is demonstrated that the final failure pattern and crack expansion trend on the rock sample vary with the change in the hole position and diameter. Third, as obtained by comparing and analyzing the energy conversion of the rock with different diameters of the hole, the energy conversion in the rock is changed due to the existence of holes, and the increase in hole diameter causes a gradual decrease in the elastic energy stored in the rock and gradual increase in the dissipated energy. And by comparing the energy conversion of the rock with different positions of the hole, it is acquired that the elastic energy conversion ratio of the rock with the vertical hole is higher than that of the rock with the horizontal hole. Furthermore, an explanation was made on the difference in the failure processes of the two types of rocks from the perspective of energy conversion.

1. Introduction

There are many causes for the rock failure, and one of the important causes is the existence of natural hole in the rock, mainly for the reason that the size and distribution of the hole in the rock are inseparable from the mechanical properties of the rock [1]. A large number of research studies have demonstrated that rock failure is a process of generation, evolution, and penetration of cracks, and defective hole in the rock is a key factor that leads to rock failure [2].

For this reason, researchers both in China and foreign countries have conducted a large number of theoretical and experimental research studies on the prefabricated rock with holes. First of all, in terms of theories and experiments, Lajtai [3, 4] artificially simulated rocks with the hole by using gypsum and studied the evolution process of cracks around the hole by uniaxial compression. The research results reveal that some primary pulling cracks, positive shear cracks, secondary pulling cracks, and oblique shear cracks appear during the failure process of the rock; Yang et al. [5–7]

conducted uniaxial compression test on sandstone and marble with a single hole. Consequently, crack appeared around the hole, which was caused by the concentration of tensile stress. Later, the crack gradually expanded toward the edge or weak part of the rock along the loading direction which revealed that the heterogeneity of the rock had a huge impact on the expansion of the crack on the rock. Li et al. [8, 9] conducted uniaxial compression and blow tests on slab-like granite and marble with the hole and analyzed the vital role that the splitting tensile damage occurred around the hole played in rock failure, where the elastic-plastic rockburst characteristics of the rock also evolved around the hole. Tang and Xu and Liu et al. [10, 11] established an acoustic emission damage model and conducted uniaxial compression on it, obtaining the equation curve of the damage evolution rule. Li et al. [12–14] found that mechanical parameters and acoustic emission characteristics were affected by the distribution of cracks on the rock containing hole. The research result demonstrates that emission is one of the key means of studying the damage evolution of the rock, and in this evolution process, the rock shows significant crack expansion and acoustic emission characteristics. In the research of Yankui and Nie [15], compression test was conducted on a rock with the hole and crack. Their research results demonstrate that the crack has a greater impact on the mechanical properties of the rock than the hole, different from the acoustic emission characteristics of the rock without the hole and crack.

Feng et al. [16, 17] obtained the discrimination method of tunnel rockburst by abstracting the rock with holes; it is the existence of the hole and crack that change the acoustic emission characteristics of the rock with the hole and crack. As known by analyzing the research studies on the damage failure of the defective coal rock, the current research studies on the impact of the hole on rock failure only focus on analysis from the macrofailure perspective of the rock, and few research studies involve the distribution of stress in the pressurized rock with the hole and the impact of stress distribution on the crack failure of the rock with the hole in the loading process. In addition to the failure caused by the internal defect of the rock, the position of the hole should also be taken into consideration because the direction of the stress acting on the hole at different positions varies, and the impact on the rock failure is also quite different. However, there are few achievements in studying the impact of the hole position on rock failure.

In view of this, from the macroperspective and energy dissipation perspective, this paper analyzes the damage and change of macromechanical behavior of the porous rock by monitoring acoustic emission and simulating the stress distribution of the porous rock during loading. The conclusion obtained is of certain significance for guiding the stability control of the defective surrounding rock, the driving in the well, and the selection of the supporting measure in the face of the surrounding rock with the hole.

2. Materials and Methods

2.1. Materials. The rock samples were black stones collected from a mining area. Considering the influence on mechanical properties of the rock sample with the hole, the processed rocks were bored in two steps. First, high-precision electric drill was used to bore on the rock for the first time due to the difficulty in initial boring. Second, after initial boring, existing hand drill was used to conduct secondary fining-off and finally produce rock samples with the vertical hole and horizontal hole of different diameters (respectively, 5 mm, 10 mm, and 15 mm).

According to regulations relevant to the mechanical test on rocks and considering the test error caused by experimental loading equipment, data acquisition, and a series of manual misoperations, the quantity of rock samples prepared for the experiment was not less than 4 and that actually used in the experiment was not less than 3. The experimental result is the average value of the results obtained. The prepared rock samples are as shown in Figure 1 and numbered as shown in Table 1.

2.2. Experimental Loading Procedures. A digital camera was aligned with the rock sample. Four acoustic emission probes were arranged around the rock sample with the hole to count and acquire the energy emitted by acoustic emission. Then, the evolution rule of the entire rock failure was observed via the camera in combination with the acoustic emission system and electrohydraulic servo press (see Figure 2).

The uniaxial compression device was loaded by displacement at a speed of 0.01 mm/sec.

The camera adopted an acquisition speed of 0.5 s/picture. Moreover, in the experiment, the uniaxial compression device and acoustic emission device were started at the same time in order to ensure the preciseness of the experiment and the consistency in the experimental data. The impact of the external environment on the correctness of the experimental result and personnel walking around were reduced as much as possible, and the door and windows were closed during the experiment.

3. Analysis of Mechanical Properties and Failure Law

3.1. The Impact of Different Hole Diameters on the Mechanical Characteristics of the Rock Sample. As can be seen from Figure 3, stress-strain curves of the intact rock sample show significant brittle failure. Due to the existence of the hole, stress-strain curves of the rock sample in the elastic stage are short compared with those of an intact rock sample, and those in the yield stage are prolonged relatively.

However, the stress concentration around the hole becomes very strong, and this part of the rock is easier to enter the destructive stage. With the increase of hole diameter, the failure will become more obvious.

As presented in Figure 3(a) for the horizontal hole, the stress change of the rock in the compression stage is obvious and in an arc shape. Before reaching the peak point, the stress falls apparently, where sample B05 with Φ5 mm hole shows two stress drops: the stress is dropped by 3.4 MPa for the first time when reaching 39.6 MPa and by 2.6 MPa for the second time when reaching 42 MPa. Sample C10 with

Figure 1: Samples with different hole positions and diameters.

Table 1: Sizes and mass of rock samples with different hole positions and diameters.

Sample no.	Hole diameter, in mm	Hole position	Average mass, in g
A00 (1234)	00	N/A	99
B05 (1234)	05	Horizontal	95
C10 (1234)	10	Horizontal	88
D15 (1234)	15	Horizontal	80
E05 (1234)	05	Vertical	93
F10 (1234)	10	Vertical	88
G15 (1234)	15	Vertical	81

Figure 2: Site of the acoustic emission monitoring experiment under uniaxial compression.

Φ10 mm hole also undergoes two stress drops: the first drop is 3.4 MPa when the stress reaches 26.5 MPa, and the second drop is 3.1 MPa but occurs after the stress reaches the peak point. Sample D15 with Φ15 mm hole only has one stress drop, and the drop is merely 0.75 MPa, while as shown in Figure 3(b) for the vertical hole, only sample C10 with Φ10 mm hole shows one stress drop, which indicates that the rock with the vertical hole has good stability. Compared with the brittle failure characteristics of the intact sample, after the stress on this sample reaches the peak point with the increase in hole diameter, almost all the samples with holes obtain certain bearing capacity and undergo a repetitive process (drop and then rise) in stress after reaching the peak point. This is mainly because of the buckling failure that occurred on the rock sample due to unceasing expansion and penetration of the interior cracks. In the failure stage, the rock sample with the hole shows obvious stress drops. As observed via the high-speed camera, every stress drop is accompanied by the generation, expansion, and penetration of new cracks.

According to Figure 4, the hole diameter has a great impact on peak strength of the rock sample with the hole and is inversely proportional to the peak strength. As for the peak stress on the rock with different diameters of the horizontal hole (Figure 4(a)), the average peak stress on the intact rock in the failure state is 75.1 MPa. If the hole diameter is 5 mm,

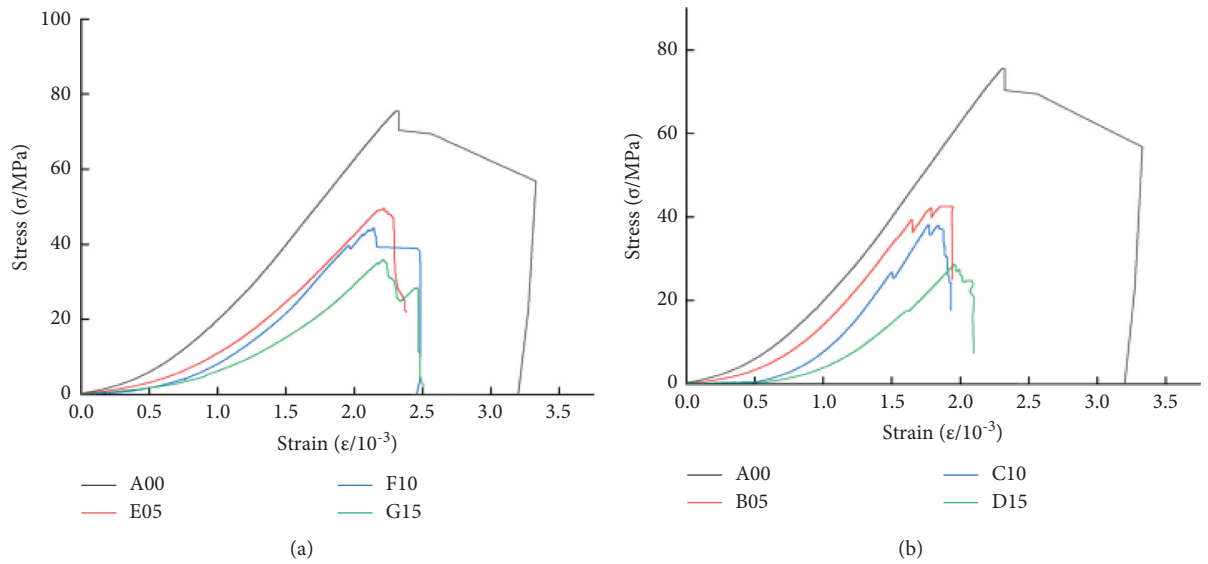

Figure 3: Stress-strain curves of the rock with different diameters of the hole. (a) Stress-strain curves of the rock with different diameters. (b) Stress-strain curves of the rock with different hole orientations.

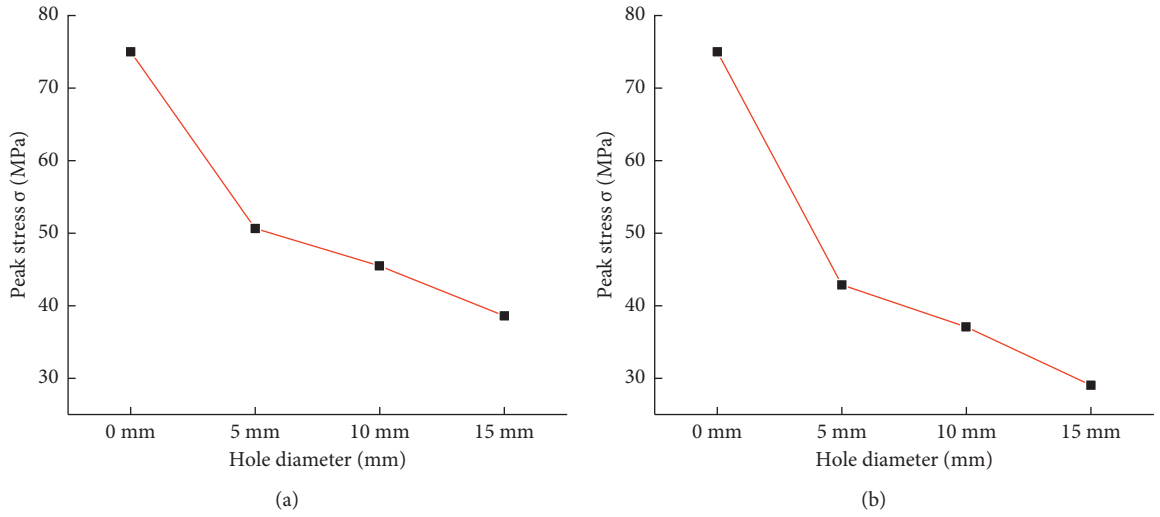

Figure 4: Peak stress on the rock with different diameters of the hole. (a) Peak stress on the rock with different diameters of the horizontal hole. (b) Peak stress on the rock with different diameters of the vertical hole.

the peak stress on the rock in the failure state is 42.7 MPa, reduced by 44.2% compared with the intact rock; if the hole diameter is 10 mm, the average peak stress is 37 MPa, significantly reduced by 51.1%; if the hole diameter is 15 mm, the average peak stress is 28.8 MPa, reduced by 62.2%. In contrast, the peak stress on the rock with the vertical hole is as presented in Figure 4(b), where the peak stresses on rocks with Φ5 mm, Φ10 mm, and Φ15 mm holes are, respectively, 50.6 MPa, 45.5 MPa, and 38.6 MPa, reduced by 33.1%, 40%, and 49%, respectively. In comparison, the rock sample with the horizontal hole has a low level of stress drop.

3.2. The Impact of Different Hole Positions and Diameters on the Failure Pattern of the Rock Sample. As shown in Figure 5(a), the intact rock sample is being damaged, which is the typical characteristic of brittle failure of the intact rock sample and well corresponds to Figure 3, where the bearing capacity of the intact rock sample quickly becomes 0 when the stress-strain curves exceed the peak point. Figure 5(b) presents the failure characteristics of the rock sample with Φ5 mm horizontal hole, where the number represents the order of crack expansion. Under the loading of axial stress, initial cracks 1a and 1b appear in the central part of the hole for the first time. Crack 1b expands upward along with the axial stress on the rock sample and produces tensile crack for the reason that stress concentration occurs above the hole under the action of uniaxial load on the rock sample with the hole. With the continuous loading, newborn wing-shape tensile crack 2 and distant crack 3 appear, where the distant crack is produced when the interior stress exceeds the extreme stress under the action of uniaxial load on the rock

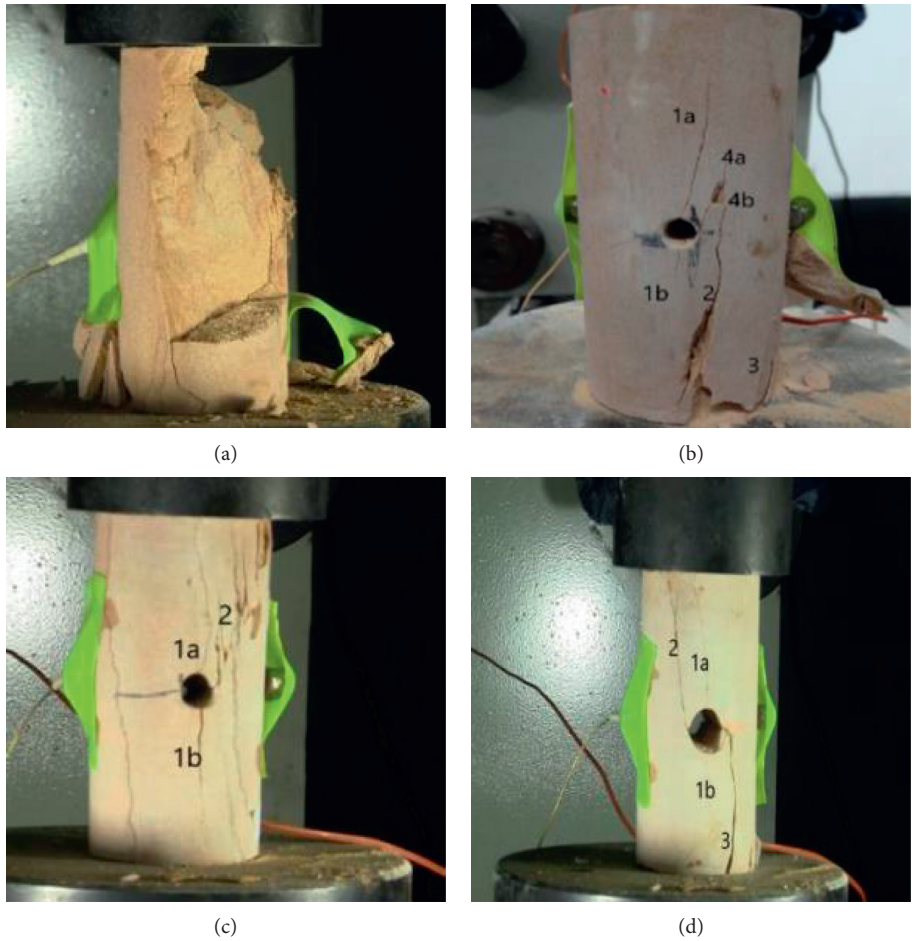

(a) (b) (c) (d)

Figure 5: Failure patterns of the rock sample with different diameters of the horizontal hole. (a) Failure pattern of the intact rock sample. (b) Failure pattern of the rock sample with Φ5 mm hole. (c) Failure pattern of the rock sample with Φ10 mm hole. (d) Failure pattern of the rock sample with Φ15 mm hole.

sample. Later with further loading, tensile crack 4a emerges at the right end of the hole and connects with crack 2. The surface peeling failure at 4b may be caused by the stress concentration in the loading process. Next, crack 2 quickly expands downward and finally penetrates through and connects with crack 3, leading to the final failure of the rock sample.

Figure 5(c) shows the failure pattern of the rock with Φ10 mm hole. As clearly demonstrated in the figure, the characteristic of the crack changes with the change in hole diameter. First, with the loading of axial stress, the crack change is similar to that when the hole diameter is 5 mm, namely, vertical tensile cracks 1a and 1b appear above and below the hole. However, with the continuous increase in axial stress, shear crack 2 comes out at the right end of the hole and extends to the right upper end of the rock. The right compression-shear crack may be caused by the pressure and stress concentration on the right and left of the hole under the action of uniaxial load on the rock with the hole. Followed by this, several secondary cracks appear around the right shear crack, accompanied by "kar kar" noise and falling debris from the rock sample, which well correspond to the two stress drops shown in the stress-strain curves of the rock with the hole. Eventually, the right shear crack expands to the right end of the rock, causing the final failure of the rock.

Figure 5(d) illustrates the failure characteristics of the rock sample with Φ15 mm hole. At the beginning, crack is generated in the same way as the crack on rock samples with Φ5 mm hole and Φ10 mm hole, respectively, namely, tensile cracks 1a and 1b appear in the middle part of the hole. Then, a large amount of broken rocks fall off from the above of the hole to the inside of the hole, which indicates that, with the increase in hole diameter, the action of the hole becomes more and more distinct. With the continuous loading of stress, shear crack 2 appears at the left end of the hole, and then the right lower end of the hole emits a noise of "kar," followed by a stress drop which can be clearly observed in the stress-strain curves. Next, shear crack 3 comes out at the right lower end of the hole and is in bilateral symmetry with shear crack 2 in the initial position. Later, shear crack 2 extends to the left upper end, and crack 3 extends to the right lower end, finally resulting in significant shear failure on the rock sample. For the rock sample with Φ5 mm hole, tensile failure is dominant in the rock failure, while the failure of the rock sample with Φ10 mm hole is dominated by right shear failure and that of the rock sample with Φ15 mm hole is

dominated by shear failure. As observed, for the rock sample with the horizontal hole, under the action of horizontal stress, the rock failure is gradually changed from tensile failure to shear failure with the increase in hole diameter.

In case of the vertical hole, the failure patterns of rock samples with different hole diameters are as shown in Figure 6 and quite different from those of the intact rock sample (Figure 6(a)). Figure 6(b) presents the crack failure characteristics of the rock sample with Φ5 mm vertical hole. In the initial loading stage, the left bottom of the rock sample presents backward tensile crack 1 and then shows pulling crack 2 and shear crack 3. With the continuous loading of stress, crack 3 coincides with crack 2, forming into a Y-shaped crack. Meanwhile, crack 2 extends to the top and bottom of the rock sample, small shear crack 4 occurs at the top, and the left side of crack 2 presents several pulling cracks connected to backward crack 1, resulting in the final failure pattern of the rock sample.

Figure 6(c) demonstrates the crack failure pattern of the rock sample with Φ10 mm vertical hole which is somewhat similar to that of the rock sample with Φ5 mm vertical hole. First, the rock sample presents pulling crack 1, and then obvious shear crack 2 appears. Followed by this, the two cracks connect with each other and form into a Y-shaped crack. At the same time, pulling crack 3 comes out. With the continuous enlarging of stress, the Y-shaped crack and pulling crack 3, respectively, extend toward the top and bottom of the rock, accompanied with significant peeling of the partial sample piece. The rock failure is mainly caused by the Y-shaped crack extending to the bottom of the rock, compared with that of the rock sample with Φ5 mm vertical hole. Figure 6(d) illustrates the crack failure pattern of the rock sample with Φ15 mm vertical hole which is different from that of the rock samples with Φ5 mm and Φ10 mm vertical holes. The initial crack is backward crack 1 that appeared at the right lower part of the rock sample followed by the peeling of a large piece of rock, which seriously affects the stability of the rock sample. Later, large tensile crack 2 appears, and crack 1 extends upward, accompanied with the derivation of several small cracks around it.

With the peeling of broken rock pieces, crack 1 extends to the extent paralleling with the initial end of tensile crack 2. Accompanied with a drastic sound, shear crack 3 comes out and directly extends to the bottom of the rock sample, resulting in the N-shaped final crack failure. In combination with the Y-shaped crack failures of rock samples with Φ5 mm and Φ10 mm vertical holes, it is revealed that the increase in hole diameter affects the expansion of the crack and the final pattern of failure. Meanwhile, the rock sample with different hole positions also shows completely different crack expansion and failure pattern. This implies that the expansion in the hole position also has a great impact on rock failure.

4. Dissipative Energy Analysis

4.1. Theories of Energy Conversion and Dissipation of the Rock in the Loading Process. In the loading process for the test, the energy continually input into the rock by press was converted into elastic energy and dissipated energy. In ideal conditions, according to the first law of thermodynamics, the total energy, elastic strain energy, and dissipated energy of a rock under uniaxial loading should comply with the following relationship:

$$W = W_s - W_d. \tag{1}$$

In the equation, W is the total energy input by the press, in kJ/m^3; W_s is the elastic strain energy accumulated inside the coal sample, in kJ/m^3; W_d is the energy dissipated in this loading process, in kJ/m^3.

The total energy can be calculated as per the area enclosed by the stress-strain curve, while the elastic strain energy can be calculated as per the unloading area enclosed by the stress-strain curve. The relationship between the two energies is illustrated in Figure 7.

This figure shows the stress-strain curve of the rock in the loading process. W_i^s represents the elastic strain energy, which can be calculated by using the area enclosed by the curve; W_i^d represents the energy dissipated in the loading process, which is irreversible and can be calculated by the difference between the total energy and elastic strain energy; E_i is the elastic modulus. This research is mainly to study the conversion and dissipation of energy in the rock at the loading peak. If the loading condition is not available, E_i cannot be calculated. In this case, E_i can be replaced with the elastic modulus E of the loading curve.

Based on the above discussion, the total energy W and elastic strain energy W_s of the rock under loading by uniaxial compression can be calculated as per the following equation:

$$\begin{aligned} W &= \int \sigma \mathrm{d}\varepsilon = \sum_{i=1}^{n-1} \int_{\varepsilon_i}^{\varepsilon_{i+1}} \sigma_i \mathrm{d}\varepsilon \\ &= \sum_{i=1}^{n-1} \frac{\varepsilon_{i+1} - \varepsilon_i}{2} (\sigma_{i+1} + \sigma_i), \\ W_s &= \frac{1}{2} \sigma_i (\varepsilon_i - \varepsilon_d) \\ &= \frac{\sigma_i^2}{2Ed} \approx \frac{\sigma_i^2}{2E}. \end{aligned} \tag{2}$$

In the equation, ε_i is the strain of the coal sample when the stress is at σ_i; E_d is the elastic modulus of the unloading stress-strain curve; E is the elastic modulus of the loading curve; and ε_d is the strain unrecoverable after being unloaded from σ_i to zero. Then, the dissipated energy W_d in the rock loading process is

$$W_d = W - W_s. \tag{3}$$

4.2. The Impact of Different Hole Positions on the Energy Conversion of the Rock in the Loading Process. According to Figure 8, a comparison was made on the conversion of elastic energy and dissipated energy in rocks with different hole positions and the elastic energy conversion ratios of

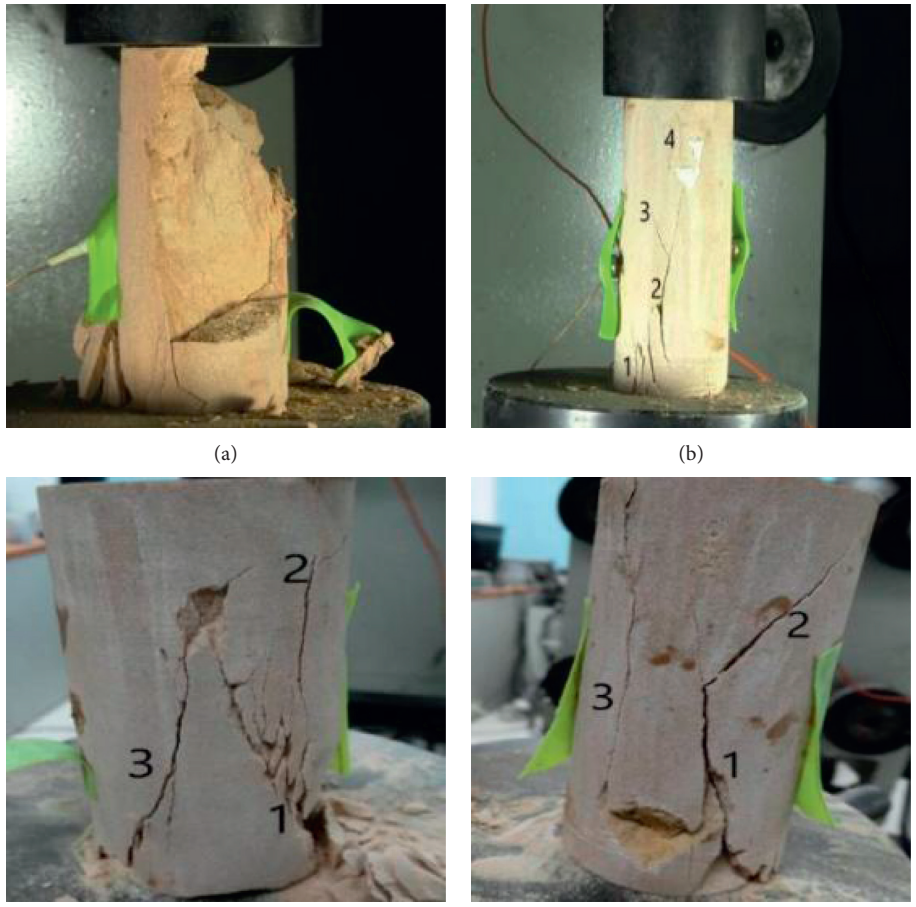

(a) (b) (c) (d)

Figure 6: Failure patterns of the rock sample with different diameters of the vertical hole. (a) Failure pattern of the intact rock sample. (b) Failure pattern of the rock sample with Φ5 mm hole. (c) Failure pattern of the rock sample with Φ10 mm hole. (d) Failure pattern of the rock sample with Φ15 mm hole.

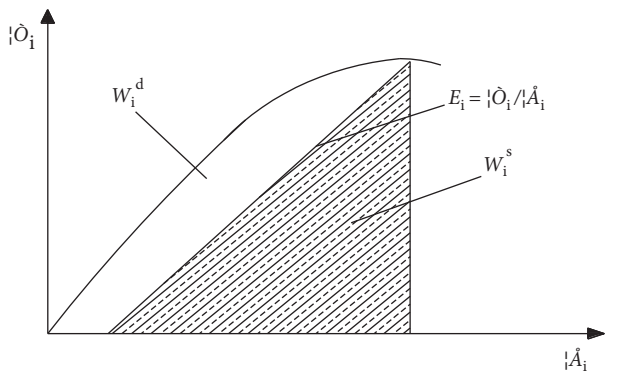

Figure 7: The relationship between elastic strain energy and dissipated energy in the rock unit.

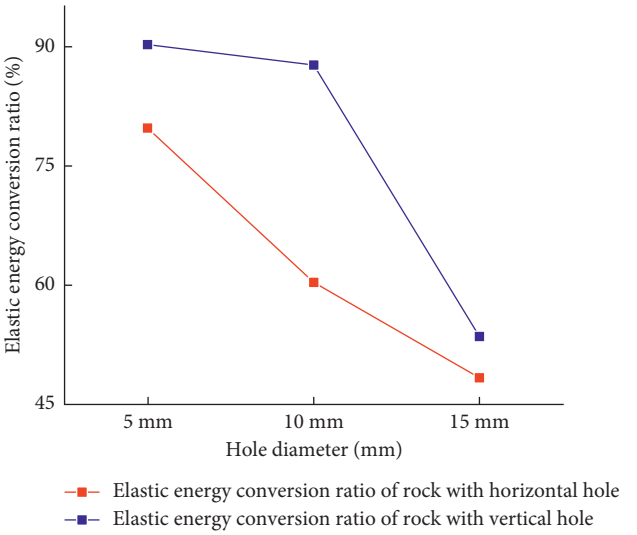

Figure 8: Elastic energy conversion ratio of the rock with different hole positions.

rock samples E05 and B05. The results reveal that 79.68% of the total energy input in rock B05 with the horizontal hole is stored in the rock in the form of elastic energy, while in rock E05 with the vertical hole, 90.19% of the total energy is converted into elastic energy and stored in the rock. The greater the strength, the greater the deformation and the more energy accumulation, which are roughly in direct proportion. Hence, the failure of the rock with the vertical hole is severer than that of the rock with the horizontal hole of the same diameter, which can be

explained from the perspective of energy conversion because the accumulation degree of elastic energy is directly proportional to the intensity of energy released and the failure intensity. The elastic energy conversion ratio of rock C10 with the horizontal hole is smaller than that of rock F10 with the vertical hole. This indicates that the horizontal hole has better pressure relief effect than the vertical hole and explains from the energy conversion point of view that the rock with the horizontal hole often subjects to greater impact from the existence of the hole than the rock with the vertical hole of the same diameter if the mechanical properties inside the rock are affected by the hole. Furthermore, the elastic energy conversion ratio of rock D15 with the horizontal hole is slightly higher than that of rock G15 with the vertical hole, which implies that, for the rock with Φ15 mm hole, there is no too large difference between the impacts of different hole positions on the rock failure. Therefore, from the perspective of energy conversion, it is explained that when the hole diameter is 15 mm, there is no large difference between the impacts of horizontal and vertical holes on the brittleness and elastic modulus of the rock.

5. Experimental Study Based on Acoustic Emission

5.1. The Impact of Different Hole Diameters on the Acoustic Emission Characteristics of the Rock Sample in the Process of Loading. The acoustic emission characteristics of rock samples with the horizontal hole of different diameters are as shown in Figure 9. Figure 9(a) shows the acoustic emission frequency of an intact rock sample, which has larger acoustic emission change characteristics than the rock sample with the hole. This is mainly because the crack and microhole in the intact crack expand fully in the stress loading process, resulting in large accumulation of energy in the rock. When the internal crack is not fully developed, macrocrack expands toward the edge of the rock along the cracking direction of the hole so that failure has appeared before the internal crack is fully developed.

And this phenomenon is more and more obvious with the increase in the hole diameter. At first, as shown in Figure 9(b), the acoustic emission frequency is high when the hole is of 5 mm in diameter and becomes low when the hole diameter is 10 mm (Figure 9(c)). This evolution law is further verified when the hole is of 15 mm in diameter as displayed in Figure 9(d). This also verifies the brittle failure of the intact rock so that the accompanied acoustic emission frequency is high. It is the existence of the hole that causes pulling shear failure.

As a result, the hole diameter is directly proportional to the pressure relief effect and inversely proportional to the acoustic emission characteristics.

The acoustic emission characteristics of rock samples with the vertical hole of different diameters are as shown in Figure 10.

Over a comparison with the acoustic emission frequency of the intact rock sample (Figure 10(a)), it is acknowledged that the vertical hole has a larger impact on the acoustic emission characteristics of the rock, and the acoustic emission characteristics vary greatly with the increase in hole diameter.

At the beginning of loading, the acoustic emission frequency is inversely proportional to the hole diameter, mainly for the reason that the internal crack of the rock is fully expanded with the increase in hole diameter. With the continuous loading of axial stress, different precursory information of acoustic emission, respectively, appeared on rocks with Φ5 mm hole (Figure 10(b)), Φ10 mm hole (Figure 10(c)), and Φ15 mm hole (Figure 10(d)) at 210 s, 225 s, and 185 s. The intact rock sample has no obvious precursory information except for the sudden increase in acoustic emission caused by stress drop. Hence, in this phenomenon, it is the existence of the vertical hole that caused the appearance of precursory information of failure on the rock with the vertical hole. When the stress loaded on the intact rock sample and rock samples with Φ5 mm hole, Φ10 mm hole, and Φ15 mm hole, respectively, reaches 40%, 25%, 22%, and 12.5% of the peak stress, the rock samples enter the plastic stage. In this stage, their acoustic emission signals are greatly different, where the intact rock sample has the strongest acoustic emission signal, followed by rock samples with Φ5 mm hole and Φ10 mm hole, and this signal of the rock sample with Φ15 mm hole is the weakest. However, when entering the subinstability loading stage, this signal of the rock sample with Φ15 mm hole is the strongest, followed by that of rock samples with Φ10 mm hole, Φ5 mm hole, and Φ0 mm hole in turn. The main reason is that the larger the hole diameter is, the more unavailable it is for the internal crack to fully expand so that the rock in the hole still has a certain bearing capacity after failure after loading. Thereby, the bearing capacity of the rock after the loading peak is directly proportional to the hole diameter. It is for this reason that, in the subinstability loading stage, the acoustic emission signal is strong and severe.

Nevertheless, the acoustic emission evolution characteristics of the rock samples with different diameters of holes are similar. Such evolution characteristics are divided into 4 stages and analyzed in detail as follows:

(1) Compaction stage: in the initial compaction stage, the acoustic emission signals of the rock sample are scattered for the reason that the internal of the rock sample is in the compaction period of the original crack. In this stage, the acoustic emission signal is relatively weak.

(2) Elastic stage: with the continuous increase in axial stress, the original crack enters the elastic stage. In this stage, the stress is in direct proportion to the strain. The acoustic emission signal appeared is weak as the applied load is not enough to have the internal crack of the rock sample expanded greatly. However, compared with the previous stage, the acoustic emission signal in this stage is apparently strong and becomes significantly strong in the later period of the elastic stage.

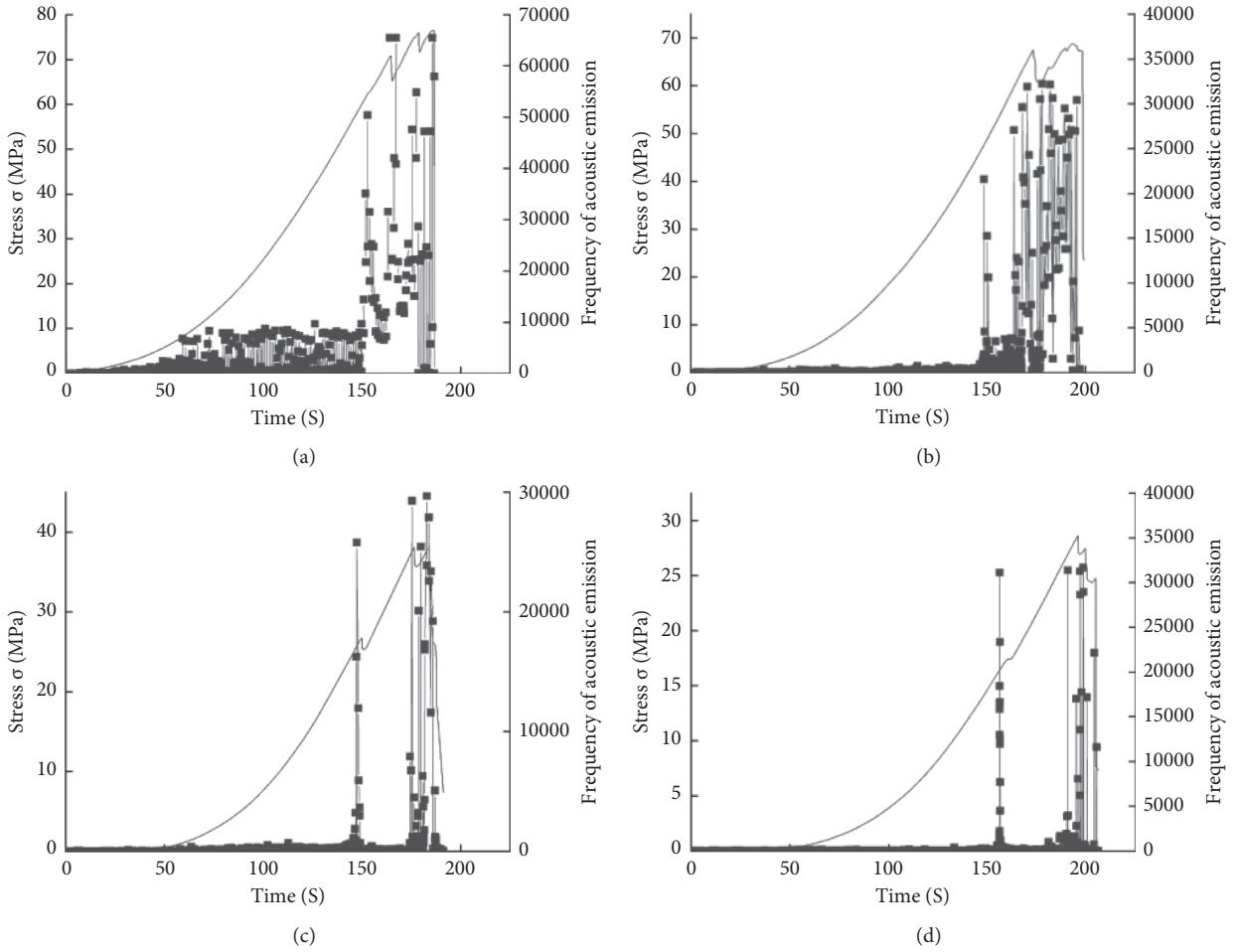

Figure 9: Stress-time-acoustic emission information of the rock sample with the horizontal hole of different diameters. (a) Stress-*N*-time of rock A00. (b) Stress-*N*-time of rock B05. (c) Stress-*N*-time of rock C10. (d) Stress-*N*-time of rock D10.

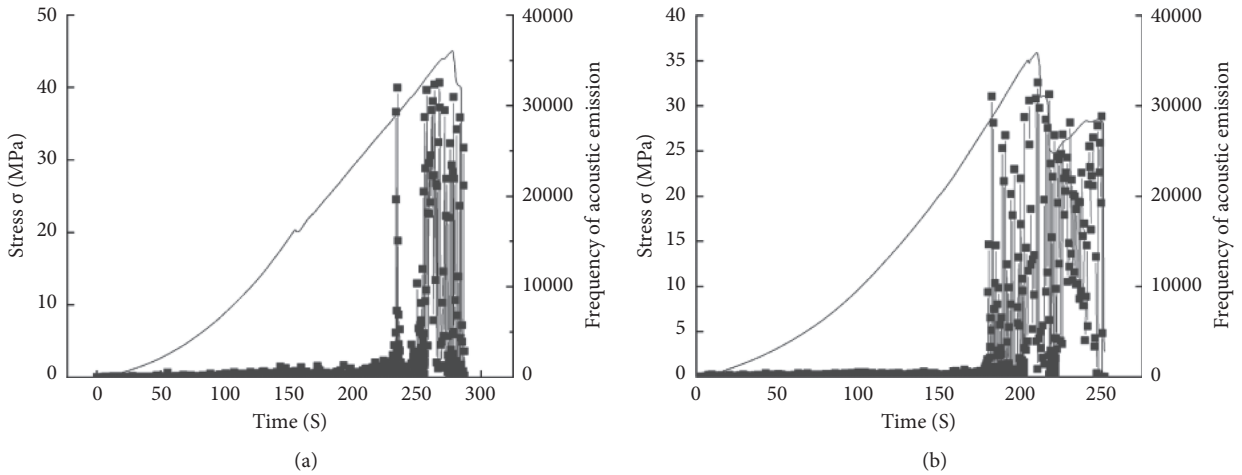

Figure 10: Continued.

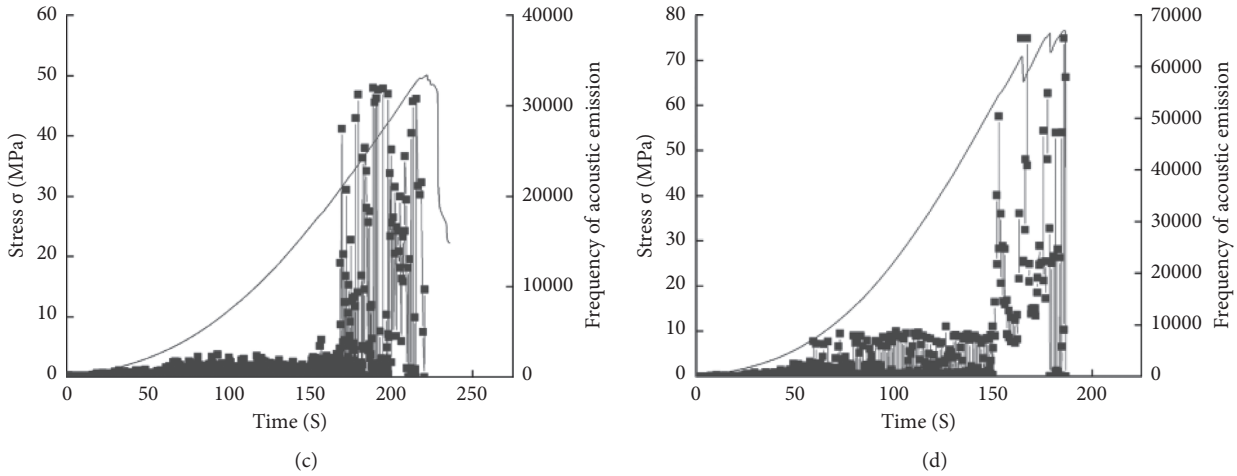

Figure 10: Stress-time-acoustic emission information of the rock sample with the vertical hole of different diameters. (a) Stress-*N*-time of rock A00. (b) Stress-*N*-time of rock E05. (c) Stress-*N*-time of rock F10. (d) Stress-*N*-time of rock G15.

(3) Plastic stage: after the original crack is compacted again, new cracks appear in the rock sample under the loading action so that the cracks expand, extrude, and rub with each other and slip, accompanied with the appearance of a large amount of macrocracks, resulting in a large increase in the acoustic emission frequency and energy.

5.2. Analysis of Acoustic Emission Characteristics of the Rock Sample with Different Hole Positions. According to Figure 11, a detailed analysis was made on the impact of different hole positions on the acoustic emission characteristics of the rock sample. As discovered by comparing the total acoustic emission signals of rock samples with different hole positions, the total acoustic emission signal of the rock sample with the vertical hole is stronger than that of the rock sample with the horizontal hole. This may be mainly caused by the difference in the force direction on the hole so that the internal crack of the rock sample with the vertical hole expands better than that of the rock sample with the horizontal hole. The rock sample with the horizontal hole and that with the vertical hole both undergo four acoustic emission evolution stages but have greatly different acoustic emission characteristics in the four stages. In the initial loading stage, the acoustic emission signal of the rock with the vertical hole is apparently slightly stronger than that of the rock with the horizontal hole. This indicates that, in this stage, the internal crack of the rock with the vertical hole is fully compacted, causing a stronger acoustic emission signal than that of the rock with the horizontal hole, since different positions of the hole are subject to different forces. In the early elastic stage, the position of the hole has little effect on the rock pattern on the acoustic emission signal of the rock sample.

However, in the later elastic stage, the rock sample with Φ10 mm horizontal hole (Figure 11(c)) and that with Φ15 mm horizontal hole (Figure 11(e)) both undergo uprush of the acoustic emission signal. Meanwhile, the rock sample with Φ10 mm vertical hole (Figure 11(d)) and that with Φ15 mm vertical hole (Figure 11(f)) also undergo such uprush, but for different reason. The uprush of the rock sample with the horizontal hole is mainly caused by stress drop, indicating the instable state of the rock sample in this stage, while that of the rock sample with the vertical hole is mainly caused by the expansion of the internal crack. In comparison, the rock sample with the vertical hole has begun the continuous emission of acoustic signals in the later elastic stage, while the acoustic emission signal of the rock sample with the horizontal hole undergoes a small quiet period after stress drop in the later elastic stage, followed by a large amount of acoustic emission signals in the later plastic stage. This further verifies that the uprush of such signal in the later elastic stage is caused by stress drop, and in the elastic stage, the internal crack of the rock sample with the vertical hole expands better than that of the rock sample with the horizontal hole. According to the acoustic emission frequencies of rock samples with different hole positions as generally shown in Figure 11, the density of the rock with the vertical hole is higher than that of the rock with the horizontal hole and maintains this law in the residual strength stage. This demonstrates that different positions of holes are subject to different force directions and thus have a large impact on the acoustic emission characteristics of the rock sample.

6. Characteristic Analysis of the Damage Model

6.1. Establishment and Derivation of the Damage Model. As proved by a large number of experiments, acoustic emission ringing frequency can well reflect the variation in the property of a material and is directly proportional to the expansion and evolution characteristics of the crack inside the material. Therefore, acoustic emission ringing frequency is selected as a characteristic parameter for description in order to discuss the damage evolution law of sandstone. The damage variable is defined by the former Soviet researcher L. M. Kachanov as

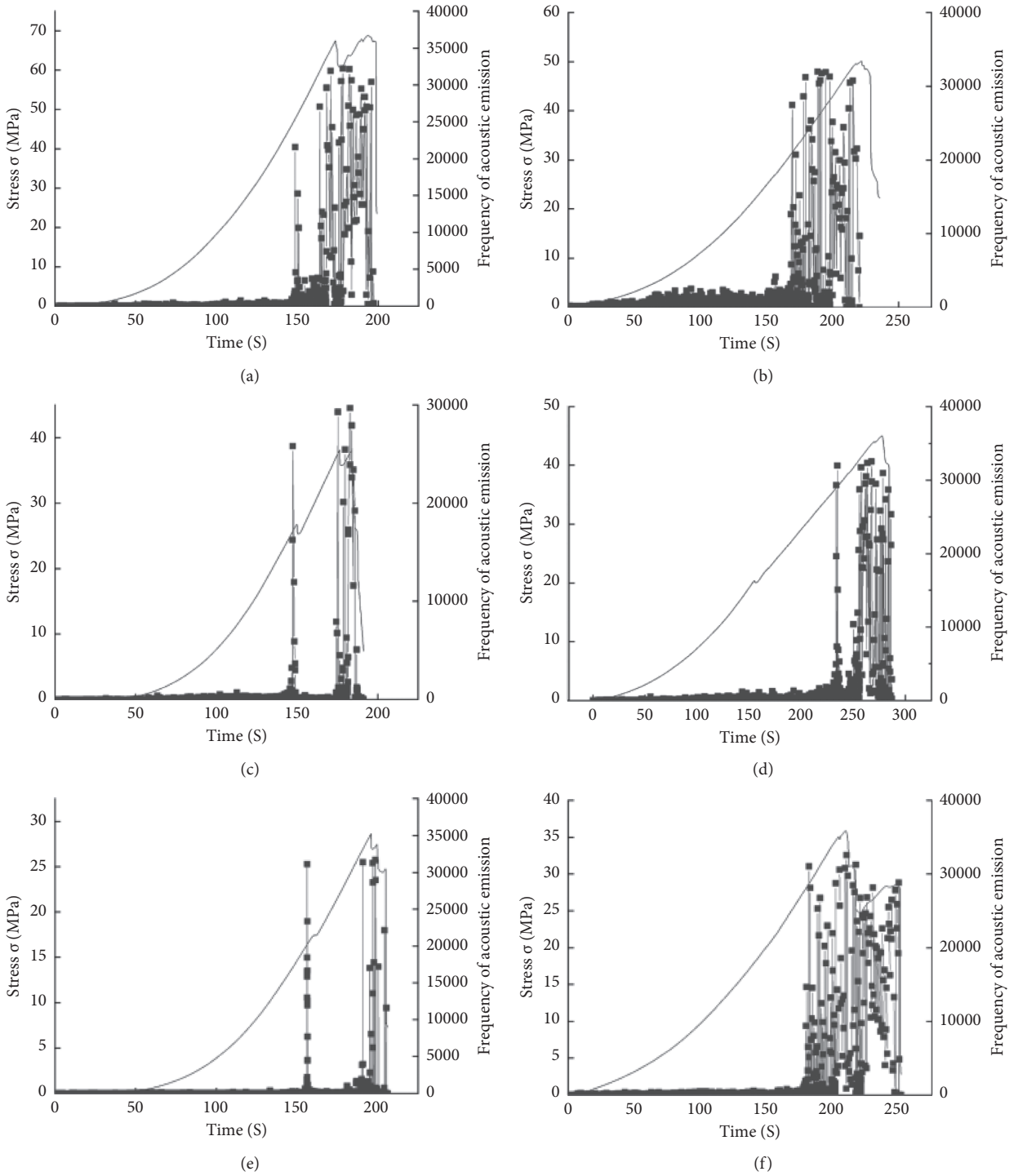

Figure 11: Stress-time-acoustic emission information of the rock sample with different hole positions. (a) Stress-*N*-time of rock B05. (b) Stress-*N*-time of rock E05. (c) Stress-*N*-time of rock C10. (d) Stress-*N*-time of rock F10. (e) Stress-*N*-time of rock D15. (f) Stress-*N*-time of rock G15.

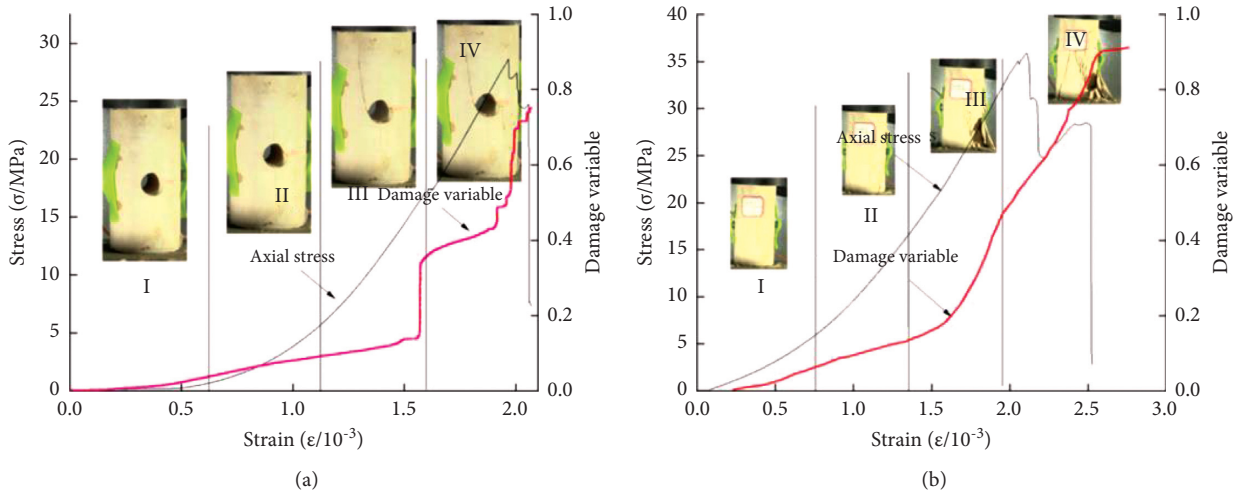

Figure 12: Damage-stress-strain relationship of rock samples with Φ15 mm hole at different positions. (a) Damage-stress-strain relationship of rock D15. (b) Damage-stress-strain relationship of rock G15.

$$D = \frac{A_d}{A}. \tag{4}$$

In the equation, A_d is the damaged cross-sectional area of the rock showing obvious crack under pressure; and A is the undamaged cross-sectional area of the rock under stress loading. Assuming that the cumulative ringing frequency in the evolution process of the undamaged area A from a complete state to a complete damage state is recorded as W_0, the acoustic emission ringing frequency of infinitesimal damage of unit area is recorded as W_C:

$$W_C = \frac{W_O}{A}. \tag{5}$$

Therefore, when the damaged cross-sectional area reaches A_d, the cumulative acoustic emission frequency W_d is calculated as follows:

$$\begin{aligned} W_d &= W_C A_d = \frac{W_o}{A} A_d, \\ D &= \frac{W_d}{W_O}. \end{aligned} \tag{6}$$

The initial damage can be defined by initial porosity, but in the author's opinion, it is more suitable to define the critical point in the compaction stage as initial damage. Therefore, the initial damage value is defined by proposing the critical stress and stress intensity in the initial compaction stage:

$$D_O = \frac{\sigma_m}{\sigma_c}. \tag{7}$$

In the equation, D_O is the initial damage value; σ_m is the critical stress in the initial compaction stage; σ_c is the peak strength of stress on the rock, which can be determined by the stress-strain curve.

Due to different failure conditions of different rocks or the insufficient hardness of the testing machine, it is a common thing that the testing machine has stopped running before the rock sample reaches a complete failure state (namely, the damage does not reach 1). Hence, the critical value of damage is defined as follows:

$$D_c = 1 - \frac{\sigma d}{\sigma c}. \tag{8}$$

In the equation, D_c is the critical damage value; σ_d is the residual strength.

According to the research results of Liu Baoxian et al., the initial damage and critical damage are unified in the normalization method and then corrected, obtaining the damage evolution equation including initial damage:

$$D = D_d + (D_C - D_O)\frac{W_d}{W_O}. \tag{9}$$

Thereby, the damage model based on acoustic emission characteristics of the rock under uniaxial compression is

$$\begin{aligned} \sigma &= (1 - D)E\varepsilon \\ &= \left[1 - D_0 - (D_C - D_0)\frac{W_d}{W_O}\right]E\varepsilon. \end{aligned} \tag{10}$$

Considering the length limit of the paper, only rock samples D15 and G15 are used for an analysis here. Figure 12 simulates the damage evolution process by loading. As the trends of damage relationship curves of the rock samples with different hole positions and diameters are almost the same, the damage evolution process of the rock sample with holes can be roughly divided into 4 stages (Figure 12), which well correspond to the four stages of the acoustic emission evolution characteristics of the rock sample with holes.

6.2. Damage Mechanics Law of the Rock with Holes

(1) Initial damage stage: the damage value at this stage is very low. Because initial compaction is in this stage, the original cracks do not expand. With the

continuous increase of axial stress, only new tiny cracks appear and expand in the rock so that there are few acoustic emission events. And no obvious crack can be seen from the corresponding rock sample.

(2) Damage stabilization and increase stage: for rock samples with the horizontal hole, there are obvious cracks near the hole, while for rock samples with the vertical hole, the cracks appear at the lower right of the rock, and the microdamage tends to concentrate locally, gradually concentrate at the failure part of the rock, and evolve into macrocracks.

(3) Due to the mutual friction and collision of cracks in the rock sample, the parameters of acoustic emission in this stage undergo abnormal increase. At this time, the rock sample is extremely unstable and undergoes significant macrofailure and obviously fast crack expansion regardless of the hole position.

7. Conclusion

(1) As revealed by comparing the stress-strain curves of rock samples with different hole positions, the stages on the stress-strain curve that the rock with the vertical hole undergoes are all longer than those underwent by the rock with the horizontal hole, and the brittleness strength and the like mechanical properties of the rock with the vertical hole are higher than those of the rock with the horizontal hole. This indicates that the rock sample with the vertical hole has higher bearing capacity and stability than the rock sample with the horizontal hole of the same diameter.

(2) As for the failure characteristics of the rock sample with the horizontal hole, symmetric tensile cracks firstly appear in the upper and lower part of the hole, form into initial tensile failure, and finally turn into shear failure. With respect to the failure characteristics of the rock sample with the vertical hole, the final N-shaped failure is formed from the initial Y-shaped failure with the increase in hole diameter. Compared with the failure pattern of the intact rock sample, the final failure pattern and crack expansion direction of the rock sample with holes can be changed with different hole positions and diameters.

(3) It is the existence of holes that changes the energy conversion in the rock. The hole diameter is inversely proportional to the elastic energy stored in the rock and directly proportional to the dissipated energy in the rock. The results of analysis on the energy conversion of the rock with different hole positions demonstrate that the elastic energy conversion ratio of the rock with the vertical hole is higher than that of the rock with the horizontal hole. Furthermore, an explanation was made on the difference between the failure processes of the two types of rocks from the perspective of energy conversion.

Data Availability

All data, models, or codes generated or used during the study are available in a repository or online in accordance with funder data retention policies.

Conflicts of Interest

The authors declare no conflicts of interest.

Authors' Contributions

Xiao Fukun designed research and completed most of the research work, followed by Li Renhe. Xing Le analyzed the data. All authors reviewed the manuscript.

Acknowledgments

This research was supported by the National Natural Science Foundation of China (51774121 and 52074110), Innovative Scientific Research Project for Postgraduates of Heilongjiang University of Science and Technology (YJSCX2020-103HKD), and Joint Guidance Project of the Natural Science Foundation of Heilongjiang Province (LH2019E087 and LH2019E119).

References

[1] S.-q. Yang, H.-w. Jing, and T. Xu, "Mechanical behavior and failure analysis of brittle sandstone specimens containing combined flaws under uniaxial compression," *Journal of Central South University*, vol. 21, no. 5, pp. 2059–2073, 2014.

[2] Metallurgical Industry Press, *Rock Failure Principle and Application*, Metallurgical Industry Press, Beijing, China, 1994, in Chinese.

[3] E. Z. Lajtai and V. N. Lajtai, "The collapse of cavities," *International Journal of Rock Mechanics and Mining Science & Geomechanics Abstracts*, vol. 12, no. 4, pp. 81–86, 1975.

[4] E. Z. Lajtai, "Shear strength of weakness planes in rock," *International Journal of Rock Mechanics and Mining Science & Geomechanics Abstracts*, vol. 6, no. 5, pp. 499–515, 1969.

[5] S. Yang, C. Lv, and T. Qu, "Investigations of crack expansion in marble having a single pre-existing hole: experiment and simulations," *Journal of China University of Mining & Technology*, vol. 38, no. 6, 2009, in Chinese.

[6] L. Cheng, S. Yang, and X. Liu, "Experimental and numerial investigation on crack expansion of sandstone containing flaws," *Journal of Mining & Safety Engineering*, vol. 29, no. 5, pp. 719–724, 2012, in Chinese.

[7] S. Yang, X. Liu, and Y. Li, "Experimental analysis of mechanical behavior of sandstone containing hole and fissure under uniaxial compression," *Chinese Journal of Rock Mechanics and Engineering*, vol. 31, no. 2, pp. 3539–3546, 2012, in Chinese.

[8] D. Li, T. Cheng, T. Zhou et al., "Experimental study of the dynamic strength and fracturing characteristics of marble specimens with a single hole under impact loading," *Chinese Journal of Rock Mechanics and Engineering*, vol. 34, no. 2, pp. 249–260, 2015, in Chinese.

[9] R. Peng, H. Xie, J. Yang et al., "Effect of elastic accumulation energy of testing machine on the mechanical measurement of rocks," *Mechanics in Engineering*, vol. 27, no. 3, pp. 51–55, 2005, in Chinese.

[10] C. Tang and X. Xu, "Evolution and propagation of material defects and Kaiser effect function," *Journal of Seismological Research*, vol. 13, no. 2, pp. 203–313, 1990.

[11] B. Liu, J. Huang, Z. Wang et al., "Study on damage evolution and acoustic emission character of coal-rock under uniaxial compression," *Chinese Journal of Rock Mechanics and Engineering*, vol. 28, no. S1, pp. 3234–3238, 2009, in Chinese.

[12] Y. Li, L. Chen, and Y. Wang, "Experimental research on pre-cracked marble under compression," *International Journal of Solids and Structures*, vol. 42, no. 9, pp. 2505–2516, 2005.

[13] X.-d. Zhao, H.-x. Zhang, and W.-c. Zhu, "Fracture evolution around pre-existing cylindrical cavities in brittle rocks under uniaxial compression," *Transactions of Nonferrous Metals Society of China*, vol. 24, no. 3, pp. 806–815, 2014.

[14] S.-Q. Yang and H.-W. Jing, "Strength failure and crack coalescence behavior of brittle sandstone samples containing a single fissure under uniaxial compression," *International Journal of Fracture*, vol. 168, no. 2, pp. 227–250, 2011.

[15] H. Yankui and X. Nie, "Analysis of mechanical and acoustic emission characteristics of hole-fracture defective rocks," *Geological Survey of China*, vol. 6, no. 3, pp. 63–67, 2019, in Chinese.

[16] G.-l. Feng, B.-r. Chen, Q. Jiang, Y.-x. Xiao, W.-j. Niu, and P.-x. Li, "Excavation-induced microseismicity and rockburst occurrence: s," vol. 28, no. 2, pp. 582–594, Journal of Central South University, 2021.

[17] G.-L. Feng, X.-T. Feng, B.-r. Chen, Y.-X. Xiao, and Y. Yu, "A microseismic method for dynamic warning of rockburst development processes in tunnels," *Rock Mechanics and Rock Engineering*, vol. 48, no. 5, pp. 2061–2076, 2015.

Hindawi
Advances in Civil Engineering
Volume 2021, Article ID 8449905, 12 pages
https://doi.org/10.1155/2021/8449905

Research Article

Techniques for Progressive Failure Simulation of Hard Brittle Surrounding Rockmass: Taking the URL Test Tunnel as an Example

Daning Zhong,[1] **Jianlin Chen**,[1] **Hui Zhou**,[2] **Xiangrong Chen**,[1] **Yali Jiang**,[1] **Liangquan Li**,[1] **and Jun Chen**[1]

[1]*PowerChina Huadong Engineering Corporation, Hangzhou 310014, China*
[2]*State Key Laboratory of Geomechanics and Geotechnical Engineering, Institute of Rock and Soil Mechanics, Chinese Academy of Sciences, Wuhan 430071, China*

Correspondence should be addressed to Daning Zhong; zhong_dn@hdec.com

Received 9 July 2021; Accepted 16 August 2021; Published 25 August 2021

Academic Editor: Wei-yao Guo

Accurate simulation of the failure process of hard brittle surrounding rockmass is very important for the analysis and control of the structural stability in deep underground engineering. In order to simulate the progressive failure process of the hard brittle surrounding rockmass, a continuous discontinuous deformation analysis method that couples the finite element and discrete element is adopted. Taking the URL test tunnel in Canada as an engineering case, the constitutive model of the contact considering the effects of cohesion weakening and friction strengthening is applied, and the 2D approximation to 3D excavation by applying elastic modulus reduction technology is adopted to simulate the range and depth of crack growth of the surrounding rockmass. Then, the comparison between simulated results and on-site monitoring results is performed, which shows good consistency. At the same time, the key factors in the numerical simulation of progressive failure in hard brittle rockmass are identified, including the number of elements, excavation effects, and constitutive models. The results show that the constitutive model determines the basic form of crack propagation, but in order to accurately simulate the progressive propagation of cracks, the number of elements must be sufficient enough and the effects of 3D excavation must be considered. The analysis accurately simulates the progressive failure characteristics of hard brittle surrounding rockmass under high stress, achieving the purpose of reasonably grasping the degree of damage to the surrounding rockmass, and provides technical reference and support on how to accurately simulate the failure of hard brittle surrounding rockmass using the finite discrete element method.

1. Introduction

Under the conditions of deep burial and high stress, the hard brittle rockmass exhibits completely different mechanical behaviors from those under shallow burial and low stress. Spalling and rock burst are the main failure modes of this type of rockmass. Studies have shown that, during the excavation of deep buried tunnels, the stress of surrounding rockmass redistributes and small cracks appear around the tunnel. These cracks continue to expand and penetrate each other under the action of external forces and eventually cause part of the rockmass to separate from the matrix rockmass, forming an excavation damage zone [1]. Tracking this process is helpful to understand the failure mechanism of hard brittle rockmass, so as to formulate corresponding control measures.

In recent years, numerical simulation technology has developed rapidly. When on-site monitoring or in-site observation is insufficient, numerical simulation methods can effectively track the failure process of surrounding rockmass. The methods are mainly divided into the continuous analysis method and discontinuous analysis method. For the failure mode and mechanism study of hard brittle rockmass under high stress, the most representative one is related work carried out by the URL test tunnel of Atomic Energy Canada Limited (AECL). The V-shaped

spalling zone formed during the excavation process is a typical brittle failure of surrounding rockmass under high stress. Martin [2, 3] studied the deformation and failure mechanism of granite through conventional indoor triaxial loading and unloading tests. On the basis of Martin's test, Hajiabdolmajid et al. [4, 5] put forward the CWFS (cohesion weakening and friction strengthening) constitutive model by deeply analyzing the evolution law of strength parameters of the rockmass with damage development. This constitutive model can well describe the brittle failure behavior of granite, and the V-shaped spalling zone is well reproduced through numerical simulation. Diederichs et al. [6, 7] proposed the DISL (damage initiation and spalling limit) model based on the Hoek–Brown constitutive model and also reproduced the formation of the V-shaped failure zone. Many scholars have also made many contributions in simulating hard brittle rock cracking with discontinuous analysis methods such as PFC3D [8–10] and UDEC [11–13], not elaborated one by one here.

In actual situations, we not only focus on the continuous and discontinuous mechanical properties of geological bodies but also often need to obtain the temporal and spatial transition process from the continuous state to discontinuous state. In order to solve this problem, the finite discrete element method that combines continuous and discontinuous analysis methods has been gradually developed to simulate the complex interactive failure process of deformed bodies [14–17]. At present, the method has been successfully used in the simulation of slopes [18, 19], tunnels [20–23], etc. Among them, Vazaios et al. [23] used the self-developed program to realize the progressive failure of the URL test tunnel and compared it with calculated results of the continuous analysis method. In addition, some scholars have combined extended finite element and discrete element [24], peridynamics, and finite element [25–27] for similar research, and the essence is also the coupling of the finite element method and other failure analysis method.

In this paper, the continuum-discontinuum numerical analysis method CDEM is used and the URL test tunnel is taken as an example to analyze the fracture response of the surrounding rockmass and to compare it with on-site monitoring, focusing on the progressive propagation of cracks. In the calculation process, the key effects of number of elements, excavation effects, and constitutive model on simulating crack formation are analyzed, which provide reference on how to correctly simulate the crack propagation of hard and brittle rockmass under high stress.

2. Overview of the URL Test Tunnel

2.1. Rock Characteristics and Mechanical Properties. The URL test tunnel of Canadian Atomic Energy Limited (ACEL) is located about 120 kilometers northeast of Winnipeg, Manitoba, Canada. The lithology is Lac du Bonnet granite. The circular Mine_by test tunnel is located at a depth of 420 m, which was built in 1989 to study the failure process induced by excavation disturbance and the progressive failure process of surrounding rockmass under high stress. The granite near this depth can be classified as hard, massive, and brittle rockmass, which can be assumed to be homogeneous and isotropic. According to indoor test results, the mechanical parameters of surrounding rockmass are shown in Table 1, which will be used to simulate the failure process of the circular test tunnel.

2.2. Failure Characteristics. The circular test tunnel has a length of 46 m and a diameter of 3.5 m. It is excavated by the technology of nonblasting hydraulic rock cracking. The excavation footage is 1 m. The axis of the tunnel is approximately parallel to the direction of the intermediate principal stress, making the ratio of the maximum principal stress to the minimum principal stress as the largest in the plane perpendicular to the tunnel axis, which is beneficial to promote the failure of the rockmass. The displacement, strain, and acoustic emission/microseismic (AE/MS) of the surrounding rockmass are monitored by advanced instruments and equipment.

During the excavation process, flake damage can be observed at the top and bottom of the test tunnel. With the advancement of the tunnel face, the damage develops radially. The spalling process mainly occurs in the range of about 2 times advancing diameters, and finally, a V-shaped notch is formed. The radial depth of the damage zone (measured from the center of the tunnel) is generally 1.3 to 1.5 times the tunnel radius, that is, the depth of the damage zone is between 525 mm and 875 mm, and the range angle is about 70 degrees, as shown in Figure 1.

According to the description of the failure area of the surrounding rockmass by Read [28], the damage is mainly concentrated in the notch area, that is to say, the rockmass outside the notch basically has no serious defects. This is because the progressive damage of the rockmass at the tunnel boundary will lead to spalling and then form a damage zone. With the gradual occurrence of spalling, due to the accumulation of constraints and the restriction of the end of the notch to the rockmass, no more plastic strain or damage will occur in the notch area, and the tunnel will gradually stabilize.

3. Finite Discrete Element Simulation

In order to obtain a better simulation consistent with on-site monitoring, multiple trial and error calculations have been repeated. The paper is introduced based on the final calculations, and then, the effects of some factors such as the number of elements, excavation effects, and constitutive models are discussed, which provides suggestions and directions for simulating the progressive failure of hard brittle surrounding rockmass using the finite discrete element method.

3.1. Method Introduction. The GDEM stress analysis system [29] is a high-performance finite element-discrete element calculation software based on CDEM (continuum discontinuum element method). This method couples the finite element and discrete element, performs finite element calculation inside the block, and performs discrete element

Table 1: Relevant physical and mechanical parameters of Lac du Bonnet granite [23].

The type of rock	Parameters	Values
LdB granite	Compressive strength of intact rock σ_{ci} (MPa)	224
	Tensile strength of intact rock σ_{ti} (MPa)	10
	Hoek–Brown constant m_i	28.11
	Geological strength index GSI	90
	Internal friction angle φ°	48
	Cohesion c (MPa)	25
	Elastic modulus E (GPa)	60
	Poisson's ratio ν	0.2
	Compressive strength of rockmass σ_{cm} (MPa)	128
	Tensile strength of rockmass σ_{tm} (MPa)	3.7

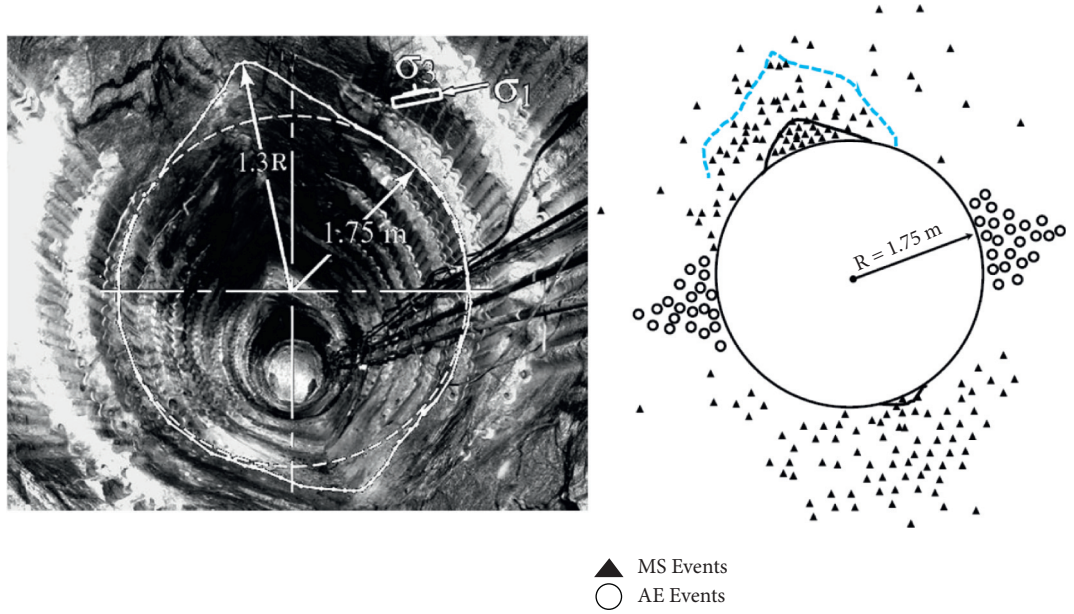

Figure 1: On-site monitoring results of the URL test tunnel [23].

calculation at the block and element interface. By introducing a breakable one-dimensional spring, as shown in Figure 2, and through the rupture of the block interior and the element interface, it cannot only simulate the deformation and movement characteristics of the material in continuous and discontinuous state but also realize the simulation of the progressive failure process of the material from continuous to discontinuous.

The explicit iterative calculations are adopted based on the time-history-based dynamic relaxation technology in CDEM. Therefore, the stress of elements and spring force of nodes at each time step can be obtained, and the strength judgment can be made according to the rupture criterion. The basic iterative process is shown in Figure 3.

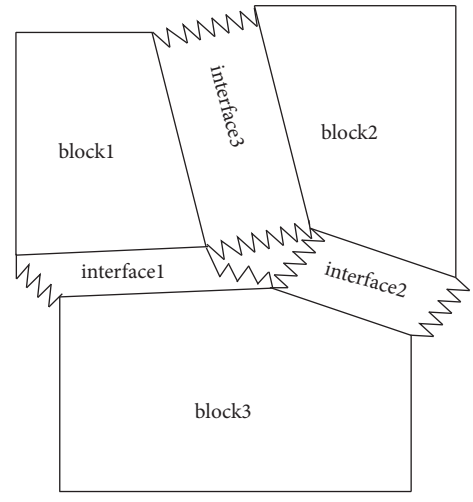

Figure 2: Blocks and interfaces in CDEM.

3.2. Model Description

3.2.1. Geometric Model. Referring to the paper by Vazaios et al. [23], the software Gmsh is adopted to obtain a two-dimensional random mesh. In order to eliminate the boundary effects, the simulation range is about 17 times the excavation diameter, with the section size 60 m × 60 m. The model is divided into four regions, as shown in Figure 4. Among them, region 1 is the circular tunnel to be excavated,

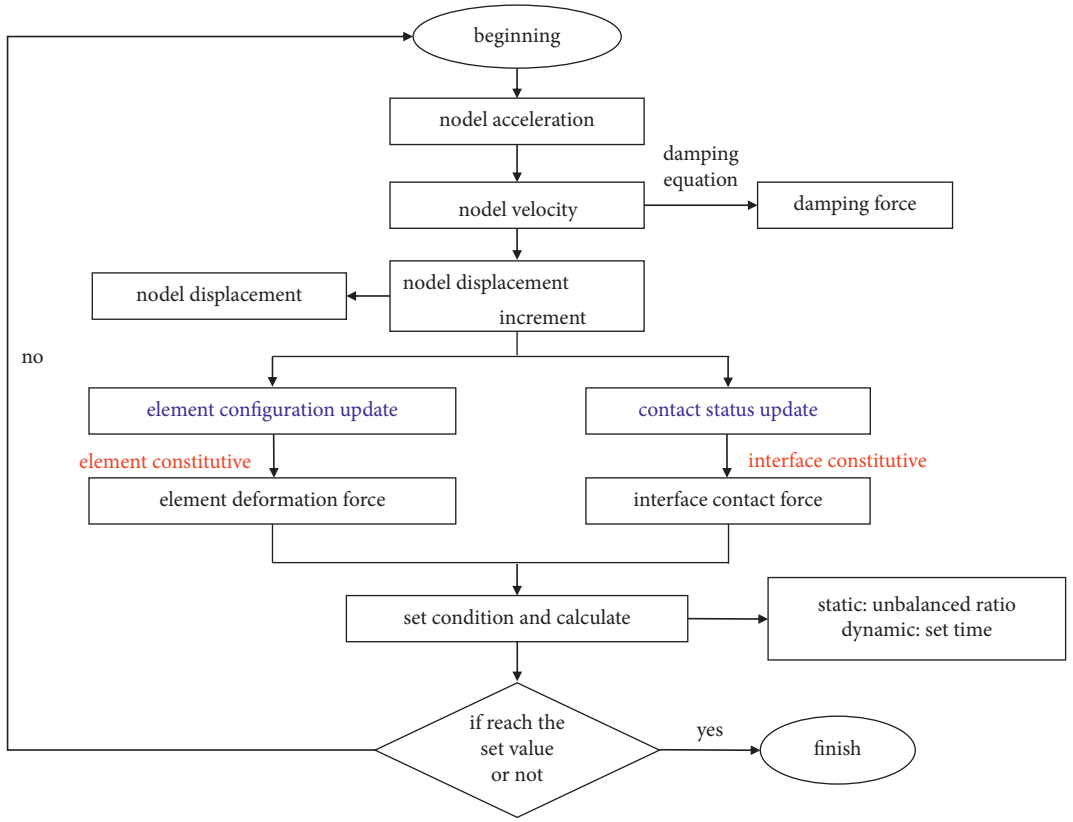

Figure 3: The basic iterative process of CDEM.

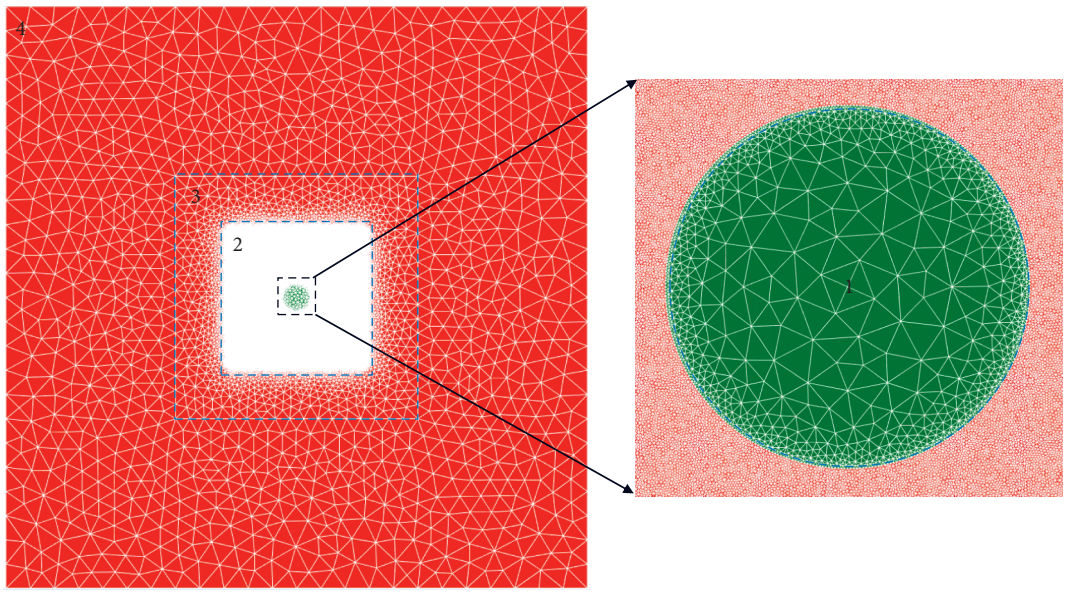

Figure 4: The geometric model of the URL test tunnel.

the element size of which transitions from 0.5 m to 0.03 m. Region 2 is the square area adjacent to the circular tunnel where cracks first appear during the excavation process. So, the element size should be small enough. The area range is 14 m × 14 m, and the element size is 0.03 m. Due to the large range of the entire model, in order to avoid the loss of computational efficiency caused by too many elements, two transition regions are specially set. Among them, the range of region 3 is 25 m × 25 m, and the element size varies from 0.03 m to 1.5 m. The range of region 4 is 60 m × 60 m, and the element size varies from 1.5 m to 2.5 m. The total number of elements is 574,828.

3.2.2. Boundary Conditions and Geostress. The boundary conditions of the model include displacement boundary conditions and stress boundary conditions. The measured in situ stress results show that the maximum principal stress in this area is 60 MPa, the intermediate principal stress is 45 MPa, the minimum principal stress is 11 MPa, the maximum stress ratio of which reaches 6 : 1. Considering the directions and converting the geostress from the principal stress space to the Cartesian space, the magnitudes of the normal stress and shear stress are shown in Table 2.

And, because the tunnel is deeply buried, the gravity-induced stress is not considered. Regarding the far-field boundary conditions, the displacement is fixed at the bottom of the model, and the corresponding normal stress and shear stress are applied to the upper surface and the left and right sides, respectively.

3.2.3. Constitutive Model. In the traditional continuous analysis method, in order to consider the reduction of the postpeak strength of the rockmass, the strain softening model and the CWFS model are commonly used. Among them, the strain softening model claims that both the cohesive force and frictional strength constitute its peak strength before plastic deformation occurs, and then, both begin to lose at the same time and gradually decrease as the strain increases. The CWFS model believes that only the cohesion of the rockmass plays a role at the initial moment, and the cohesion gradually decreases as the damage develops, and then, the friction strength begins to play a role and gradually increases as the damage develops. Hajiabdolmajid et al. [4, 5], Wu [30], and Liu [31] reproduced the V-shaped damage of the URL test tunnel based on the CWFS method, verifying the significance of friction strength strengthening in the postpeak stage.

Inspired by CWFS in continuum, this feature of rockmass is transplanted to the interface of discontinuous elements. The elastic constitutive model is adopted inside the element, and the input parameters include density, elastic modulus, and Poisson's ratio. The fracture energy model is used on the element interface, and the input parameters include normal stiffness, tangential stiffness, cohesion, internal friction angle, tensile strength, tensile fracture energy, and shear fracture energy. The incremental relationship of the elastic constitutive model is

$$\Delta\sigma_{ij} = \left(K - \frac{2}{3}G\right)\Delta\theta\delta_{ij} + 2G\Delta\varepsilon_{ij}, \tag{1}$$

Table 2: The stress component used in numerical simulation.

Stress component	Values (MPa)
σ_{xx}	−58
σ_{yy}	−13
τ_{xy}	−9.2

where $\Delta\sigma_{ij}$ and $\Delta\varepsilon_{ij}$ are the average stress increment and strain increment, $\Delta\theta$ is the volumetric strain increment, and K and G are the bulk modulus and shear modulus of the material, respectively.

The fracture energy model is essentially the maximum tensile stress model and the M-C model, both of which consider a linear softening effect of the tensile strength and shear strength, respectively. The incremental method is used to calculate the normal and tangential force of the next step on the interface:

$$\begin{cases} F_n(t_1) = F_n(t_0) - K_n \times \Delta d_n, \\ F_s(t_1) = F_s(t_0) - K_s \times \Delta d_s, \end{cases} \tag{2}$$

where F_n and $F_s$are the normal and tangential force, K_n and $K_s$are the normal stiffness and tangential stiffness, which are obtained by inheriting form the element stiffness, and Δd_n and Δd_s are the relative displacement increments in normal and tangential directions. Then, following formula (3) is used to judge the tensile failure, and the normal force is corrected. That is, the tensile strength linearly weakens when the normal force exceeds the tensile strength:

$$\begin{cases} \text{if,} & -F_n(t_1) \geq \sigma_t(t_0)A, \\ F_n(t_1) = -\sigma_t(t_0)A, & \sigma_t(t_1) = -\dfrac{\sigma_0^2}{2G_t}d_n + \sigma_0, \end{cases} \tag{3}$$

where σ_0, $\sigma_t(t_0)$, and $\sigma_t(t_1)$ are the tensile strength of the interface at the initial time, this time, and the next time respectively, d_n is the normal relative displacement on the interface at this time, G_t is the tensile fracture energy, and A is the area of the interface.

At the same time, formula (4) is used to judge the shear failure and tangential force is corrected. That is, the shear strength linearly weakens when the tangential force exceeds the shear strength:

$$\begin{cases} \text{if,} & F_s(t_1) \geq F_n(t_1)\tan\varphi + c(t_0)A, \\ F_s(t_1) = F_n(t_1)\tan\varphi + c(t_0)A, & c(t_1) = -\dfrac{c_0^2}{2G_s}d_s + c_0, \end{cases} \tag{4}$$

where c_0, $c(t_0)$, and $c(t_1)$ are the cohesion of the interface at the initial time, this time, and the next time, respectively, d_s is the tangential relative displacement on the interface at this time, and G_t is the shear fracture energy.

In the fracture energy model, the shear strength is composed of both cohesive force and frictional strength. In order to simulate the effects of CWFS, a small friction strength is given at the initial moment. At this time, the friction strength contributes little to the shear strength. Then, when the shear failure criterion is reached, the cohesion starts to lose gradually. At this time, the friction strength of the interface is set to increase by 10 times. Thus, the goal of cohesive weakening and friction strengthening is reached.

3.2.4. Calculation Steps. The first step is to calculate the initial geostress field of the model under the given boundary conditions, 832,800 steps were performed, and the initial result was saved for the following calculation. The next step is to simulate the excavation of the test tunnel, but how to simulate the three-dimensional effect with the two-dimensional model is a very important question. Because the tunnel is generally excavated in stages, the resistance of the surrounding rockmass and the excavation boundary are formed gradually not instantaneously. While in the two-dimensional model, excavation is simulated by emptying the tunnel elements, which means that the tunnel is excavated completely at the same time, resulting in a significant difference from the real situation. So, some measures should be taken to try to eliminate such excavation effects. Vlachopoulos and Diederichs [32] introduced four methods of using two-dimensional analysis to approximate three-dimensional tunnel excavation behavior, as shown in Figure 5. Curran et al. [33] specifically introduced the fourth method, that is, the face replacement method in the support designing in weak rocks. In short, the progressive excavation process is simulated by setting the elastic modulus of the to-be-excavated part to decrease gradually. The face replacement method, (d) in Figure 5, will be used in this paper.

In this paper, the specific performed process is as follows. After the initial elastic calculation is completed, the elastic modulus of the to-be-excavated area will be reduced, with other parameters keeping unchanged. And, the parameters of other areas also remain unchanged; then, 5000 steps are performed to achieve a temporary balance. Repeat the process 5 times until the 3D excavation behavior is almost approximated. The specific settings of elastic modulus are shown in Table 3. Then, the excavation process is performed by emptying the tunnel elements, and 3000 steps are performed to observe the crack growth.

3.2.5. Input Parameters. Due to the lack of experience in the simulation of crack propagation during tunnel excavation, it is difficult to directly solve the problem using the discontinuous analysis method, and the debugging process takes a lot of time. Therefore, the strategy we adopted is to first obtain good results in the category of continuum, then migrate to discontinuous analysis by considering contact elements, and obtain the final result through continuous test calculations.

In the continuous analysis, the strain softening model is adopted. The material parameters adopted are the same with Table 1. The goal is to make the failure state of the surrounding rockmass coincide with the on-site monitoring results. The software Gmsh is used for meshing, and the model region is the same with Figure 4, but the number of elements is 58336. By adjusting the value of tensile strength and dilatancy angle, the results of several schemes are shown in Figure 6. It is indicated that the increase in tensile strength can significantly reduce the number of elements in the tensile failure, and the increase in the dilatancy angle can make the V-shaped notch failure more obvious, and the range and depth of the damage zone are enlarged.

In the end, it is confirmed that the tensile strength of the surrounding rockmass is 10 MPa and the dilatancy angle is 30 degrees, which will be used in following calculations. The final input parameters in the model are shown in Table 4.

4. Simulated Brittle Response

4.1. Simulated Initial Stress Field. Firstly, the geostress field after calculating 832,800 steps is given in Figure 7, taking the first principal stress for example. As shown in the legend, the calculated stress of the whole model is between 53 MPa and 62 MPa, which is almost consistent with the nominal value 60 MPa. The direction of the first principal stress is indicated by the short red line, coinciding with the true direction of the first principal stress. The inclination angle is about 11 degrees. The accurate simulation of the geostress field guarantees the subsequent excavation calculation to be performed successfully.

4.2. Simulated Brittle Failure. After the 3D excavation approximation by repeating the elastic modulus reduction 5 times, the tunnel elements were removed completely, and the evolution process of the cracks of the rockmass is shown in Figure 8. Picture (a) shows the crack state at step 857,900 when there are only small cracks on the top and bottom of the tunnel. Picture (b) shows the crack state at step 858,000. At this time, the range of cracks at the top and bottom expands a little. And, at the same time, small tensile cracks appear in the vertical direction on the left and right sides of the tunnel. Picture (c) shows the crack state at step 858,900. The cracks at the top and bottom gradually extend to the deep part of the tunnel, and the tensile cracks on both sides also extend to the depth of the surrounding rockmass. The area of the tensile cracks has not expanded, being still a long and thin crack. Besides, at this time, the prototype of V-shaped failure has been basically formed. Pictures (d)~(f) show the crack state at 859,400 steps, 859,900 steps, and 860900 steps separately. During these three stages, the cracks at the top and bottom expand to the depth further, the form of the V-shaped failure is more obvious, and the tensile cracks on both sides do not expand in a large area. After calculating 3000 steps, the crack growth has reached a relatively stable state.

The comparison between the failure state of the surrounding rockmass and the on-site monitoring results, when

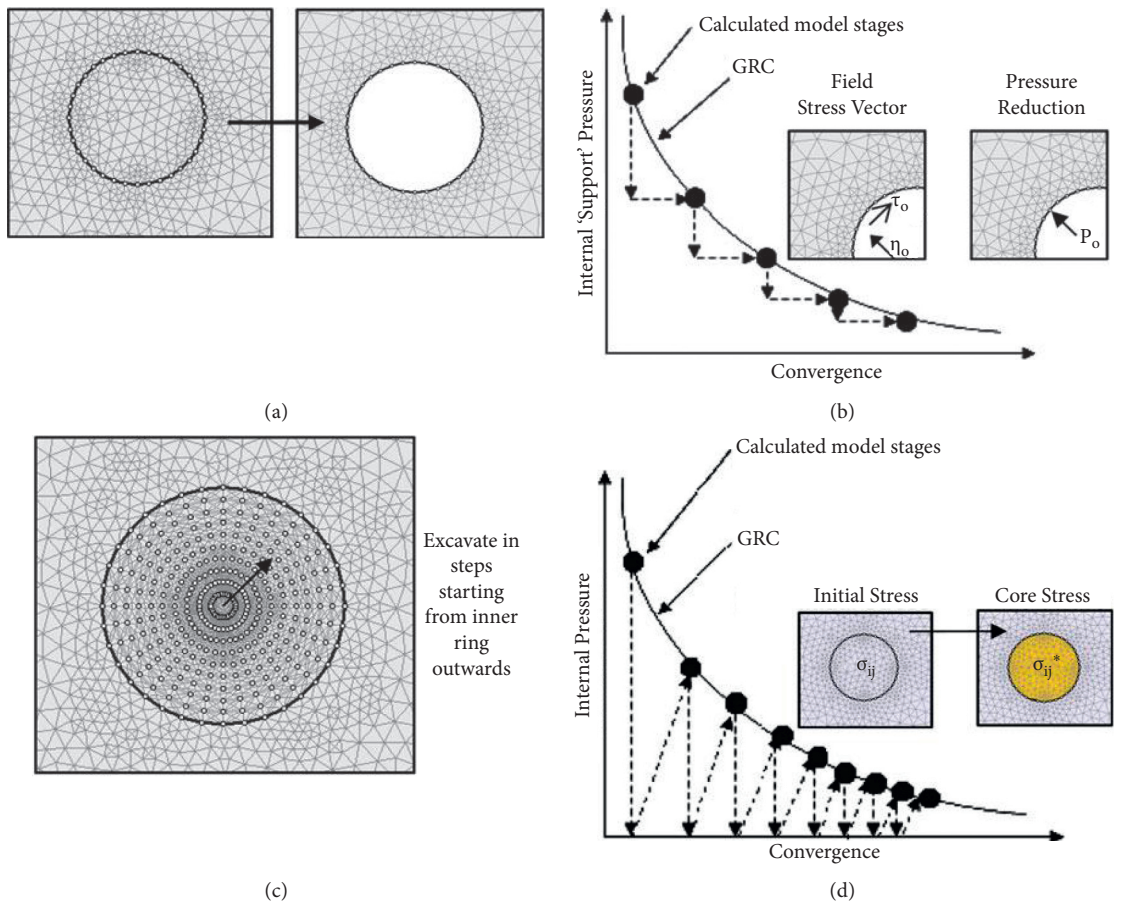

Figure 5: Four strategies used in 2D analysis to approximate the 3D excavation behavior [32].

Table 3: The settings of the elastic modulus to simulate the excavation process.

The stages of simulated excavation	1	2	3	4	5
Elastic modulus (GPa)	50	30	20	10	4

the crack no longer continues to grow, is further performed, as shown in Figure 9. The orientation of the top and bottom cracks is perpendicular to the direction of the first principal stress, and the direction of tensile cracks on both sides coincides with the first principal stress. After measurement, the range and depth of the V-shaped notch are in good agreement with the on-site monitoring results. The angle of the damage zone measured from the center of the tunnel is about 70 degrees. The depth of the relatively broken zone at the top is about 0.3 times the diameter, and the total depth of the cracks is about 0.5 times the diameter. The damage range and depth at the bottom of the tunnel in numerical calculation are similar to those obtained at the top. But in on-site monitoring, the actual damage zone measured at the bottom of the tunnel is smaller than the calculated value. There are probably two reasons, one is that the surrounding rockmass at the top falls off and may cover the ground; the other is that, under the combined function of self-weight stress and tectonic stress, the crack at the bottom is actually weaker than that at the top. But in the calculation, self-weight stress is ignored but symmetrical stress is adopted so that the same calculated results at the top and bottom are obtained.

In addition, compare the acoustic emission signals and the microseismic location around the tunnel with the crack propagation, as shown in Figure 9. It can be seen that, within the area where cracks appear, relatively dense acoustic emission signals and microseismic signals have been monitored, indicating that there is indeed crack appearing and energy releasing, which confirmed the correctness of the calculation results once again.

5. Key Factors Identification

This section mainly focuses on the key factors in accurately simulating the progressive propagation of cracks, which are all concluded from numbers of trials.

5.1. Effects of Number of Elements. Generally speaking, the element size has a great influence on numerical simulations [34]. In this calculation, the mesh and material parameters of the continuous model are used, and the contact is applied to the boundary of the elements to carry out continuous

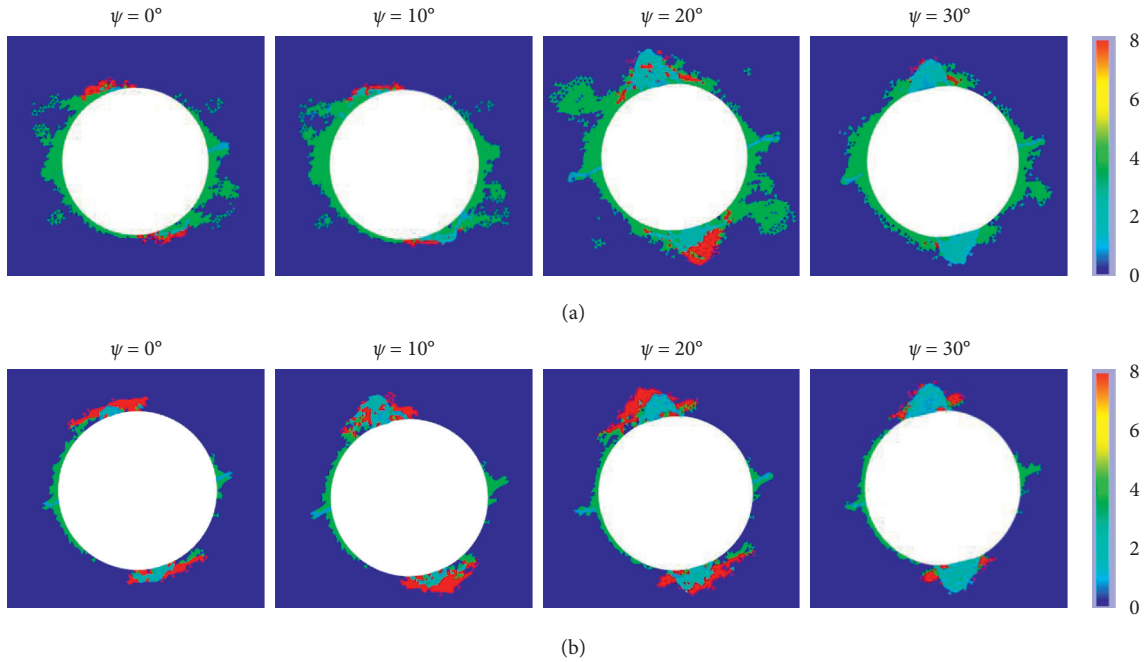

Figure 6: The failure state of several schemes under different dilatancy angles: (a) tensile strength is 3.7 MPa; (b) tensile strength is 10 MPa (0-no failure; 1-tensile failure now; 2-shear failure now; 4-tensile failure past; 8-shear failure past).

Table 4: Finalized input parameters of Lac du Bonnet granite in GDEM.

Parameters	Values
Elastic modulus E (GPa)	60
Poisson's ratio ν	0.2
Cohesion c (MPa)	50
Tensile strength of intact rock σ_{ti} (MPa)	10
Internal friction angle at initial time φ°	5
Internal friction angle after failure φ°	50
Dilatancy angle ψ°	30
Tensile fracture energy (Pa m)	50
Shear fracture energy (Pa m)	500

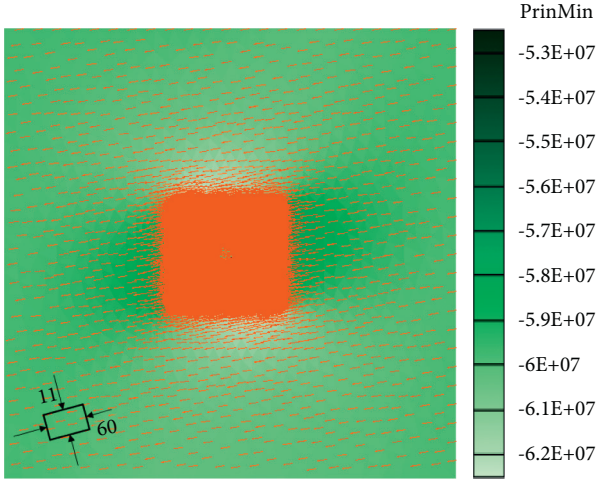

Figure 7: First principal stress after the initial elastic calculation.

discontinuous simulation. The constitutive model of the contact element adopts cohesion weakening and friction strengthening, and the excavation approximation by elastic modulus weakening is considered. Therefore, compared with the final calculation scheme, there is no other variable but the number of elements.

The crack propagation process during 3000 calculation steps is shown in Figure 10, and three results at corresponding steps are chosen and analyzed. Compared with Figure 8, the location of the cracks around the tunnel is roughly right, but the range and depth of cracks extend more widely and deep, especially on the top and bottom. The cracks extend a long distance to both sides, and the V-shaped notch on the top is not completely formed. It can be inferred that more elements are needed to obtain ideal simulation effects.

5.2. Effects of Excavation Method. It can be seen from Section 5.1 that when there are not enough elements, the range and depth of the cracks expand widely although the crack location is roughly the same. The number of elements should be adjusted. At the same time, referring to the literature of Vazaios [23], the number of elements is finally added to 574828. The constitutive model of the contact considers cohesion weakening and friction strengthening, and the excavation effect is not considered but direct excavation is used for this calculation. In this way, compared with the final model, the only variable is the excavation method.

The crack propagation process during 3000 calculation steps is shown in Figure 11. Compared with Figure 8, cracks first appeared in the four corners of the tunnel instead of the top of the tunnel. As the calculation

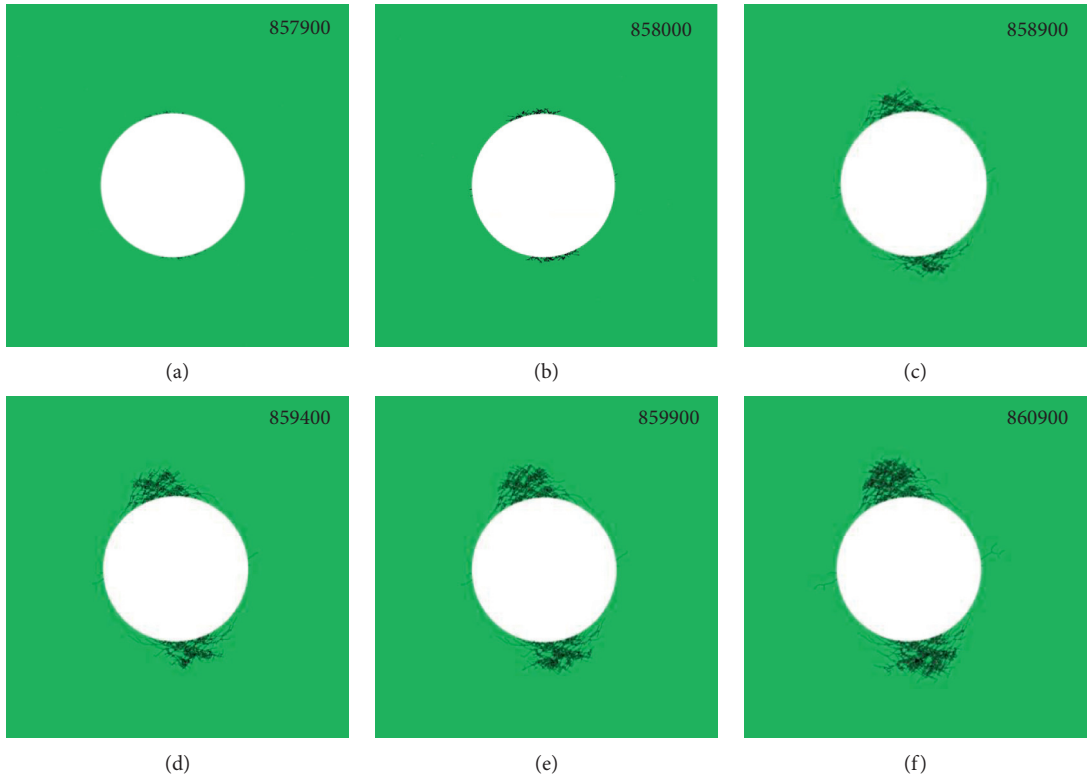

Figure 8: The schematic diagram of fracture evolution during excavation.

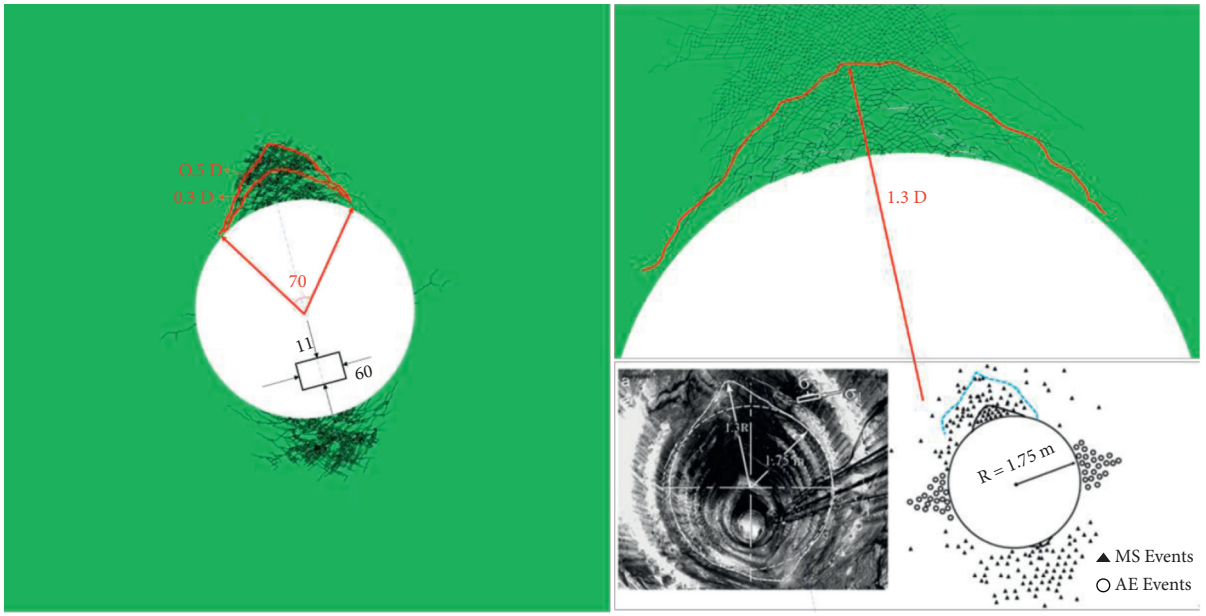

Figure 9: Comparison between simulated and observed results.

progressed, cracks began to appear on the top and bottom, but the cracks in the four corners still exist and get widely. When the crack propagation is almost in the stable state, the V-shaped notch has been roughly formed. At this time, the cracks on the top and bottom intersect with the cracks in the four corners. Compared with Figure 10, the increase of elements restricts the cracks from propagating farther and deeper, but new problems have appeared due

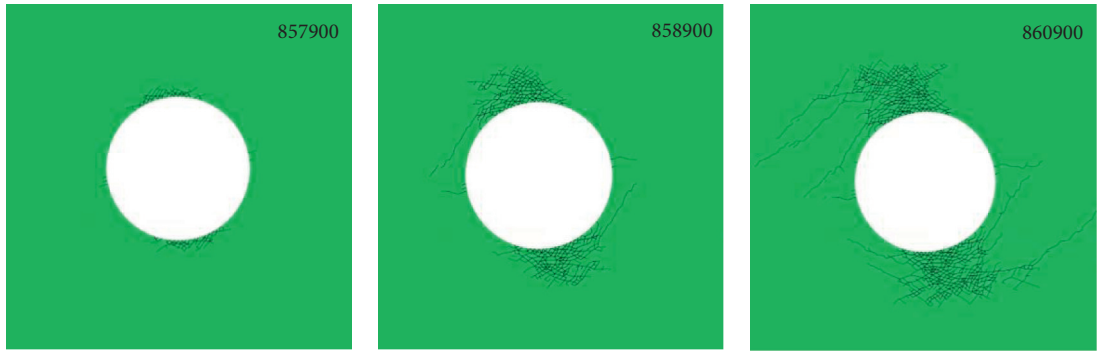

(a) (b) (c)

Figure 10: The simulated crack propagation process in studying size effects.

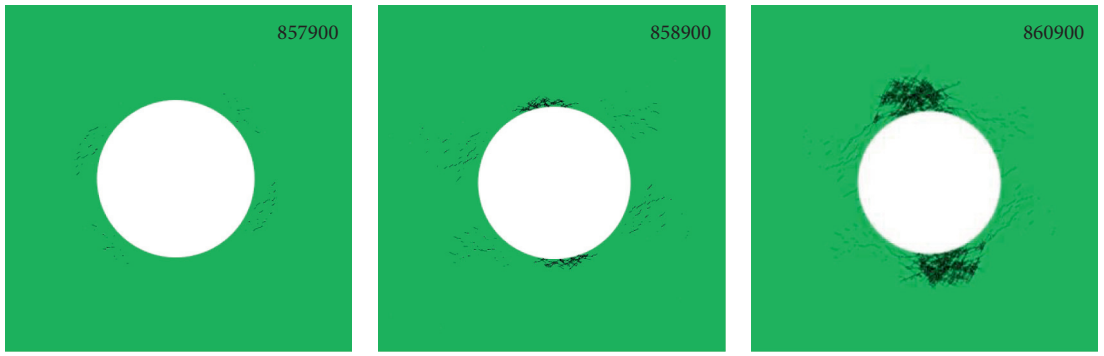

(a) (b) (c)

Figure 11: The simulated crack propagation process in studying excavation effects.

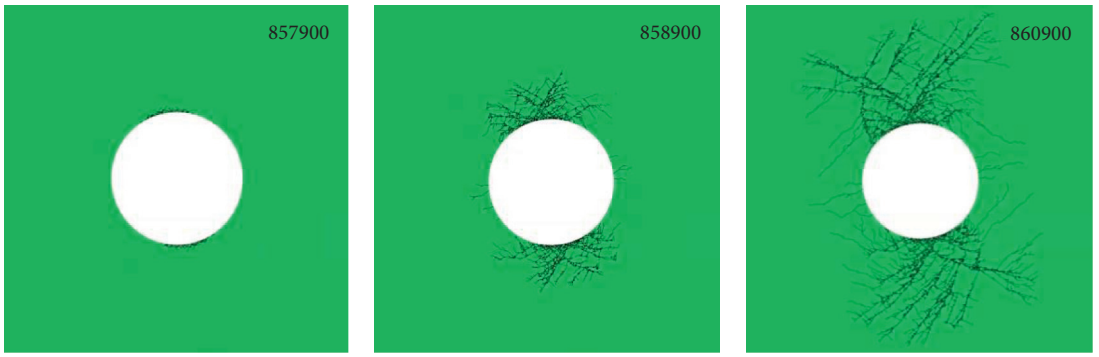

(a) (b) (c)

Figure 12: The simulated crack propagation process in studying the constitutive model.

to ignoring the excavation effects, which need to be further optimized and solved.

5.3. Effects of Constitutive Model. Finally, the influence of the constitutive model is compared. The material parameters used is obtained from the continuous analysis in Section 5.1. The number of elements is 573288, and the constitutive model of the contact element does not consider cohesion weakening and friction strengthening, but the excavation effect is considered. The only variable compared with the final model is the constitutive model.

The crack propagation process during 3000 calculation steps is shown in Figure 12. Compared with Figure 8, cracks initially appeared on the top and bottom of the tunnel. As the calculation progresses, the range of the cracks at the top and bottom expands rapidly and expands

deeper and farther. After 3000 steps is finished, the crack expanding is still continuing, and the range is further expanded. Until this time, no V-shaped notch was formed on the roof of the tunnel and the cracks look messy. The reason could be that when the stress state of the element reaches the rupture criterion, the cohesive force begins to decrease, but the friction strength does not increase, resulting in the load-bearing capacity of the element not meeting the requirements; then, the rapid crack propagation happens. Therefore, choosing a reasonable constitutive model is very critical.

6. Conclusions

The brittle failure of hard brittle surrounding rockmass has always been a problem in engineering and academia. The coupling analysis method of the finite discrete element has therefore been developed rapidly, but how to accurately simulate the progressive propagation of cracks still needs to be studied in depth. In this paper, the URL test tunnel in Canada is taken as an example, the number of elements, excavation effects, and constitutive models are discussed through continuous adjustment of models and trial calculations, and finally, the result that is in good agreement with the on-site monitoring is obtained, and the following are summarized in conclusion:

(1) The constitutive model of the contact element is the key factor that determines the basic form of crack propagation, which is generally obtained through laboratory tests. This paper draws on the experience summarized by the predecessors, applies the model considering cohesion weakening and friction strengthening to the contact, and achieves good results.

(2) When dealing with crack propagation of hard brittle rockmass, the number of elements must be sufficient enough. Due to the element boundary being the contact surface, more elements can make the expansion of the stress path more accurate.

(3) When using two-dimensional simulation to approximate three-dimensional excavation, the actual excavation method must be considered. Then, certain measures must be taken to simulate the real excavation situation as much as possible.

In addition, in this paper, the URL test tunnel is specified. When migrating to other similar projects with hard brittle rockmass, such experience can be copied, but it should be adjusted according to the specific situation. For example, the constitutive equation changes with different kinds of rocks or other methods need to be used to approximate the three-dimensional excavation effects.

Data Availability

The data used to support the findings of this study are available from the corresponding author upon request.

Conflicts of Interest

The authors declare that there are no conflicts of interest regarding the publication of this paper.

Acknowledgments

The work was supported by China Postdoctoral Science Foundation with Grant no. 2021M690999.

References

[1] T.-b. Zhao, M.-l. Xing, W.-y. Guo, C.-w. Wang, and B. Wang, "Anchoring effect and energy-absorbing support mechanism of large deformation bolt," *Journal of Central South University*, vol. 28, no. 2, pp. 572–581, 2021.

[2] C. D. Martin, *The strength of massive lac du bonnet granite around underground openings*, Ph.D. thesis, University of Manitoba, Winnipeg, Canada, 1993.

[3] C. D. Martin, "Seventeenth Canadian geotechnical colloquium: the effect of cohesion loss and stress path on brittle rock strength," *Canadian Geotechnical Journal*, vol. 34, no. 5, pp. 698–725, 1997.

[4] V. Hajiabdolmajid, "Mobilization of strength in brittle failure of rock," Ph. D. Thesis, Queen's University, Kingston, Canada, 2001.

[5] V. Hajiabdolmajid, P. K. Kaiser, and C. D. Martin, "Modelling brittle failure of rock," *International Journal of Rock Mechanics and Mining Sciences*, vol. 39, no. 6, pp. 731–741, 2002.

[6] M. S. Diederichs, P. K. Kaiser, and E. Eberhardt, "Damage initiation and propagation in hard rock during tunnelling and the influence of near-face stress rotation," *International Journal of Rock Mechanics and Mining Sciences*, vol. 41, no. 5, pp. 785–812, 2004.

[7] M. S. Diederichs, "The 2003 Canadian Geotechnical Colloquium: m," *Canadian Geotechnical Journal*, vol. 44, no. 9, pp. 1082–1116, 2007.

[8] A. Fakhimi, F. Carvalho, T. Ishida, and J. F. Labuz, "Simulation of failure around a circular opening in rock," *International Journal of Rock Mechanics and Mining Sciences*, vol. 39, no. 4, pp. 507–515, 2002.

[9] S. Aziznejad, K. Esmaieli, J. Hadjigeorgiou, and D. Labrie, "Responses of jointed rock masses subjected to impact loading," *Journal of Rock Mechanics and Geotechnical Engineering*, vol. 10, no. 4, pp. 624–634, 2018.

[10] D. O. Potyondy and P. A. Cundall, "A bonded-particle model for rock," *International Journal of Rock Mechanics and Mining Sciences*, vol. 41, no. 8, pp. 1329–1364, 2004.

[11] F. Q. Gao, "Simulation of failure mechanisms around underground coal mine openings using discrete element modelling," Ph. D. Thesis, Simon Fraser University, Burnaby, Canada, 2013.

[12] T. Kazerani and J. Zhao, "Micromechanical parameters in bonded particle method for modelling of brittle material failure," *International Journal for Numerical and Analytical Methods in Geomechanics*, vol. 34, no. 18, pp. 1877–1895, 2010.

[13] H. X. Lan, C. D. Martin, and B. Hu, "Effect of heterogeneity of brittle rock on micromechanical extensile behavior during compression loading," *Journal of Geophysical Research*, vol. 115, no. B1, Article ID B01202, 2010.

[14] C. Feng, S. H. Li, and Z. X. Yao, "Study of block-discrete-spring method based on continuum mechanics," *Chinese Journal of Rock Mechanics and Engineering*, vol. 29, no. S1, pp. 2690–2704, 2010, in Chinese.

[15] H. Jiang and D. Meng, "3D numerical modelling of rock fracture with a hybrid finite and cohesive element method," *Engineering Fracture Mechanics*, vol. 199, pp. 280–293, 2018.

[16] O. K. Mahabadi, A. Lisjak, A. Munjiza, and G. Grasselli, "Y-geo: new combined finite-discrete element numerical code for geomechanical applications," *International Journal of Geomechanics*, vol. 12, no. 6, pp. 676–688, 2012.

[17] A. Munjiza, *The Combined Finite-Discrete Element Method*, John Wiley & Sons, Chichester, England, 2004.

[18] C. Feng, S. H. Li, and J. Wang, "Stability analysis method for bedding rock slopes under seismic load," *Chinese Journal of Geotechnical Engineering*, vol. 34, no. 4, pp. 717–724, 2012, in Chinese.

[19] H. Z. Wang, C. H. Bai, C. Feng, K. Xue, and X. G. Zhu, "An efficient CDEM-based method to calculate full-scale fragment field of warhead," *International Journal of Impact Engineering*, vol. 133, pp. 1–15, 2019.

[20] A. Lisjak, B. S. A. Tatone, O. K. Mahabadi et al., "Hybrid finite-discrete element simulation of the EDZ formation and mechanical sealing process around a microtunnel in opalinus clay," *Rock Mechanics and Rock Engineering*, vol. 49, no. 5, pp. 1849–1873, 2016.

[21] I. Vazaios, M. S. Diederichs, and N. Vlachopoulos, "Assessment of strain bursting in deep tunnelling by using the finite-discrete element method," *Journal of Rock Mechanics and Geotechnical Engineering*, vol. 11, no. 1, pp. 12–37, 2019.

[22] I. Vazaios, N. Vlachopoulos, and M. S. Diederichs, "Assessing fracturing mechanisms and evolution of excavation damaged zone of tunnels in interlocked rock masses at high stresses using a finite-discrete element approach," *Journal of Rock Mechanics and Geotechnical Engineering*, vol. 11, no. 4, pp. 701–722, 2019.

[23] I. Vazaios, N. Vlachopoulos, and M. S. Diederichs, "Mechanical analysis and interpretation of excavation damage zone formation around deep tunnels within massive rock masses using hybrid finite-discrete element approach: case of Atomic Energy of Canada Limited (AECL) Underground Research Laboratory (URL) test tunnel," *Canadian Geotechnical Journal*, vol. 56, no. 1, pp. 35–59, 2019.

[24] J. Raisianzadeh, A. A. Mirghasemi, and S. Mohammadi, "2D simulation of breakage of angular particles using combined DEM and XFEM," *Powder Technology*, vol. 336, pp. 282–297, 2018.

[25] W. Sun and J. Fish, "Superposition-based coupling of peridynamics and finite element method," *Computational Mechanics*, vol. 64, no. 1, pp. 213–248, 2019.

[26] W. Sun and J. Fish, "Coupling of non-ordinary state-based peridynamics and finite element method for fracture propagation in saturated porous media," *International Journal for Numerical and Analytical Methods in Geomechanics*, vol. 45, no. 9, pp. 1260–1281, 2021.

[27] W. Sun, G. Zhang, and Z. L. Zhang, "Damage analysis of the cut-off wall in a landslide dam based on centrifuge and numerical modeling," *Computers and Geotechnics*, vol. 130, Article ID 103936, 2021.

[28] R. S. Read, "Characterizing excavation damage in highly stressed granite at AECL's underground research laboratory," in *Proceedings of the International Conference on Deep Geological Disposal of Radioactive Waste*, pp. 35–46, Canadian Nuclear Society, Winnipeg, Canada, September 1996.

[29] S. H. Li, J. G. Wang, B. S. Liu, and D. P. Dong, "Analysis of critical excavation depth for a jointed rock slope using a face-to-face discrete element method," *Rock Mechanics and Rock Engineering*, vol. 40, no. 4, pp. 331–348, 2007.

[30] C. Wu, "Numerical analysis for the excavation failure zone of deep underground opening in hard rock with high geostress," Master Thesis, Hunan University, Hunan, China, 2012, in Chinese.

[31] L. Liu, "Stability analysis for surrounding rockmass based on cwfs model," Master Thesis, Chongqing University, Chongqing, China, 2019.

[32] N. Vlachopoulos and M. S. Diederichs, "Appropriate uses and practical limitations of 2D numerical analysis of tunnels and tunnel support response," *Geotechnical & Geological Engineering*, vol. 32, no. 2, pp. 469–488, 2014.

[33] J. H. Curran, R. E. Hammah, and T. E. Yacoub, "A two-dimensional approach for designing tunnel support in weak rock," in *Proceedings of the 56th Canadian Geotechnology Conference*, Winnipeg, Canada, 2003.

[34] S. Q. Lin, C. Q. Zhang, H. Zhou, and F. Dai, "Numerical analyses of mesh size effects on core discing," *Arabian Journal of Geosciences*, vol. 13, no. 12, Article ID 440, 2020.

Hindawi
Advances in Civil Engineering
Volume 2021, Article ID 9096540, 10 pages
https://doi.org/10.1155/2021/9096540

Research Article

A Simplified Method for Analysis of Laterally Loaded Piles considering Cyclic Soil Degradation

Yuzhe Yang,[1] **Xiaodong Gao**,[1,2] **Wenbing Wu**,[1,3] **and Kangyu Xing**[1]

[1]*Engineering Research Centre of Rock-Soil Drilling and Excavation and Protection, Ministry of Education, China University of Geosciences, Wuhan, Hubei 430074, China*
[2]*Office of the Discipline Inspection Commission, China University of Geosciences, Wuhan, Hubei 430074, China*
[3]*Zhejiang Institute, China University of Geosciences, Hangzhou 311305, China*

Correspondence should be addressed to Xiaodong Gao; gaoxingzi2019@126.com and Wenbing Wu; zjuwwb1126@163.com

Received 12 May 2021; Accepted 16 June 2021; Published 5 July 2021

Academic Editor: Guang-Liang Feng

This paper proposes a simplified method to analyze the bearing behavior of pile undergoing cyclic lateral load. Firstly, a modified strain model is proposed by utilizing the Duncan–Chang model to describe the stress-strain behavior of soils in the strain wedge. Then, a cyclic degradation model of soft clay considering the accumulation of plastic strain and pore water pressure is presented based on the cyclic triaxial test. Combining with the modified strain wedge model and degradation model of soil, a simplified method is established for the cyclic laterally loaded pile. The accuracy of the present method is verified by comparing it with existing model tests. The results show that the pile lateral displacement and strain wedge depth increase with the number of cycles and cyclic load amplitude. It is necessary to consider the effect of cumulative pore water pressure during the analysis of cyclic laterally loaded pile embedded in soft clay.

1. Introduction

Piles supporting offshore engineering structures are mainly subjected to cyclic lateral loads, such as wind, waves, and currents, which may cause large lateral displacements of pile body and attenuation of bearing capacity. The major reason for these phenomena is that the soil strength would be degraded due to the accumulation of plastic strain caused by cyclic loads [1]. Many precious approaches have been proposed to investigate the bearing behavior of pile under cyclic lateral loads, including simplified *p-y* curve methods [2–4] and finite element methods [5–8]. The mentioned simplified *p-y* methods consider soil degradation by scaling down the ultimate lateral resistance of soil or the stiffness of *p-y* curve. However, these *p-y* curve methods may not be applicable to offshore piles under cyclic loads with a large number of cycles, for they are mainly proposed based on the lateral loading tests of small-diameter pile under small cycle numbers, without directly considering the effect of cyclic loading amplitude and cycle number [9]. Based on degradation stiffness model in sand, Achmus et al. [6] and Hu et al. [7] developed finite element methods to study the bearing behavior of pile under cyclic lateral loads. The most important advantage of these finite element methods is that they can determine the stress distribution and degree of soil degradation of pile surrounding soil. However, their calculation process is much more complicated and not conducive to engineering applications. In addition, the above studies have been mostly conducted on sand, which may be not suitable for the piles in soft clay. Compared with rigid pile in sand [6, 7, 10], piles installed in soft clay often behave as flexible soil-pile systems [11], and the accumulation of pore water pressure in soft clay cannot be ignored for it would cause the degradation of soil strength [12].

Unlike the complicated finite element methods, Norris [13] originally proposed the strain wedge model (SW model), which can obtain the stress distribution of pile surrounding soil, to calculate the appropriate reaction modulus of pile surrounding soil from the soil strain in the three-dimensional passive wedge in uniform soil.

Subsequently, Ashour et al. [14] extended Norris's method to deal with layered soil in the strain wedge. However, the used stress-strain relation in Norris's method was developed based on limited experiment data and difficult to be applied in the analysis of pile under cyclic lateral loads [15]. Besides, the assumption of linear displacement of piles in SW model would cause some contradictions with the actual bearing behavior of piles [16].

The objective of this study is to investigate the bearing behavior of laterally loaded piles considering cyclic soil degradation. A modified SW model is introduced to examine the stress distribution of pile surrounding soil. Besides, a cyclic degradation model of soft clay considering the accumulation of plastic strain and pore water pressure is proposed based on cyclic triaxial tests. Then, a simplified method to analyze the bearing behavior of piles under cyclic lateral loads is presented by applying the cyclic degradation model into the modified SW model. Finally, the proposed simplified method is verified by comparing the model predictions with results obtained from model tests.

2. Modified Strain Wedge Model

2.1. Basic Concept of SW Model. The aim of SW model proposed by Ashour et al. [14] is to determine the subgrade reaction modulus in the following differential equation:

$$\mathrm{EI}\frac{\mathrm{d}^4 y}{\mathrm{d}z^4} + k(z)y = 0, \tag{1}$$

where EI and y denote the flexural stiffness and lateral deflection of pile, respectively, and $k(z)$ is the subgrade reaction modulus at a depth of z, which is defined as follows:

$$k = \frac{p}{y}, \tag{2}$$

where p is the soil resistance per unit length of pile and can be calculated by SW model.

As shown in Figure 1, a three-dimensional passive wedge of soil is developed in front of the deflected pile in SW model. The passive soil wedge is described by the base angle β_m, fan angle φ_m, and depth of the passive wedge H. The pile embedded length is L, and the depth of the passive wedge H is equivalent to the depth of first zero-deflection point of pile. The lateral deformation of pile is assumed to vary linearly with depth, and the rotation angle of pile δ is consistent along pile shaft (see Figure 1(b)) [14]. The soil stress condition in the passive wedge can be determined by using triaxial test. The lateral earth pressure coefficient K_0 can be assumed to be 1 owing to pile driving effect. Hence, the major principle stress change in the direction of pile movement $\Delta\sigma_h$ is equal to the deviatoric stress in the triaxial test, and vertical stress σ_v in the subgrade is taken as confining stress in the triaxial test. With the increase of the lateral load acting on the pile head, the size and stress level of passive soil wedge would change accordingly. φ_m also denotes the mobilized internal friction angle of soil. The relationship of β_m, width of the wedge face BC at depth z, and φ_m can be obtained as follows [14]:

$$\begin{aligned} \beta_m &= 45^\circ + \varphi_m, \\ \mathrm{BC} &= D + (H - z)\tan\varphi_m \tan\beta_m, \end{aligned} \tag{3}$$

where D represents the diameter of pile. For square piles, D can be calculated in the form of equal perimeter.

The soil resistance p at depth z is written as follows:

$$p = S_1 \mathrm{BC}\Delta\sigma_h + 2S_2 D\tau\ , \tag{4}$$

where S_1 and S_2 are pile shape factors which equal 0.75 and 0.5 for circular pile, and both equal 1 for square pile, respectively. τ denotes the mobilized pile side shear stress, which can be calculated as follows [14]:

$$\frac{\tau}{\tau_{\mathrm{ult}}} = \begin{cases} 12.9yD - 40.5y^2D^2, & (x < 6\mathrm{m}), \\ 32.3yD - 255D^2, & (x > 6\mathrm{m}), \end{cases} \tag{5}$$

where the units of y and D are centimeter and meter, respectively. τ_{ult} is the ultimate shear stress of surrounding soil acting on pile shaft and given as $\tau_{\mathrm{ult}} = \zeta Su$, in which Su and ζ are undrained shear strength and adhesion factor, respectively. ζ is equal to 0.5, $1 - (S_u - 25)/90$ and 0.5 for $S_u \le 25$ kPa, $25\,\mathrm{kPa} < S_u \le 70\,\mathrm{kPa}$, and $S_u > 70$ kPa, respectively.

2.2. Modifications of SM Model. The modifications of SM model mainly include two aspects: (1) based on the nonlinear deformation assumption of single pile, the relationship between lateral deflection of pile and lateral strain of soil in passive wedge is established; (2) the Duncan–Chang model is introduced to describe the stress-strain relationship of clay.

In the SM model proposed by Norris's group [13, 14], the lateral deformation of pile is assumed to vary linearly with depth, and the rotation angle of pile δ is consistent along pile shaft (see Figure 2(a)). However, the actual rotation angle of the lower part of pile should be less than the assumed one, which would lead to a discrepancy with the actual conditions [15, 16]. Therefore, this work introduces the nonlinear deformation assumption proposed by Xu et al. [16] for laterally loaded pile in sand. As shown in Figure 2(b), the strain wedge-pile system is divided into a series of segments or layers with thickness h. The strain of the ith strain wedge is ε_i, and the displacements at the upper and lower interfaces of the ith pile segments are y_{i-1} and y_i, respectively. The rotation angle of pile is assumed to vary with depth and satisfy the following equation:

$$\begin{aligned} \delta_i &= \left(\frac{\mathrm{d}y}{\mathrm{d}z}\right)_i, \\ &= \frac{y_{i-1} - y_i}{h}. \end{aligned} \tag{6}$$

Meanwhile, the rotation angle also has the following relationship with $\varepsilon_i$and φ_{mi} [13]:

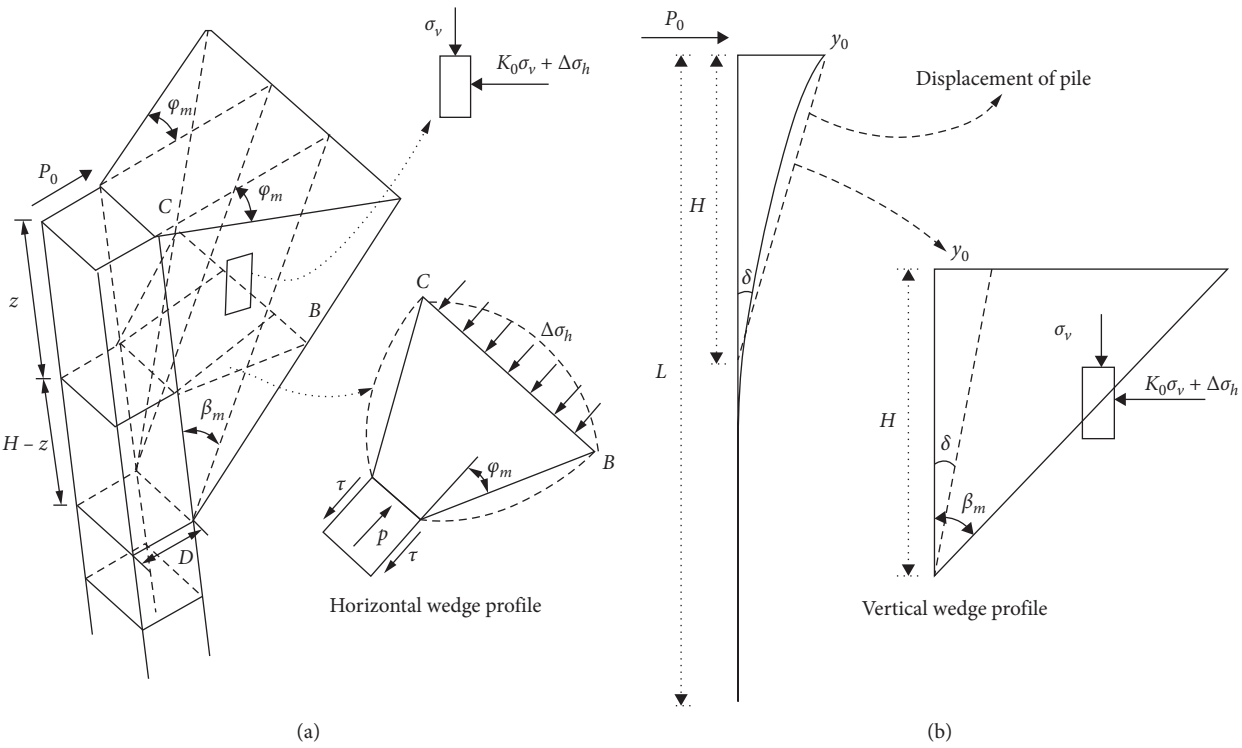

Figure 1: Basic strain wedge model [14]. (a) Three-dimensional wedge in front of pile. (b) Deformation of pile and vertical wedge profile.

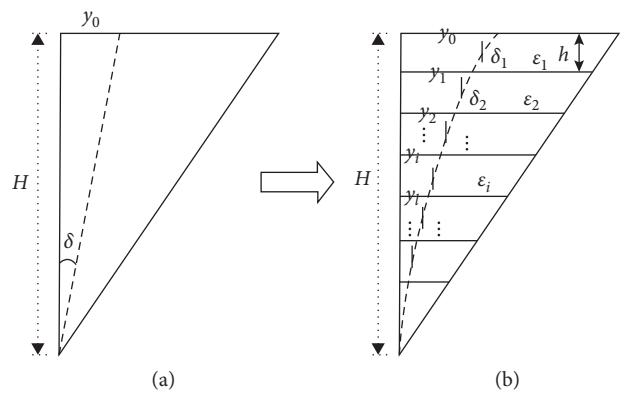

Figure 2: Displacement distribution of pile in SW model. (a) Linear displacement of pile in SWM. (b) Nonlinear displacement of pile in SWM.

$$\delta_i = \frac{\gamma_i}{2} = \frac{(1+\nu_i)\varepsilon_i}{2}\cos\varphi_{mi}, \tag{7}$$

where γ_i and ν_i are the shear strain and Poisson's ratio of the ith soil layer, respectively. φ_{mi} is the fan angle of the ith passive soil wedge.

Then, the Duncan–Chang model [17] is used to obtain the $\Delta\sigma_h \sim \varepsilon$ relationship as follows:

$$\Delta\sigma_{h_i} = \frac{\varepsilon_i}{(1/E_{\text{ini}}) + \left(R_f\varepsilon_i/\Delta\sigma_{\text{hfi}}\right)}, \tag{8}$$

where R_f is the failure ratio within the range of 0.75–1. $E_{\text{ini}} = K_e P_a (\sigma_{vi}^{J}/P_a)^n$ denotes the initial elastic modulus, in which K_e and n are the calculated parameters within the range of 20–200 and 0.5–0.8 for clay [18], respectively. P_a = 101 kPa represents the standard atmospheric pressure. $\Delta\sigma_{\text{hfi}}$ is the deviatoric stress σ_{sfi} at failure and can be expressed as follows:

$$\Delta\sigma_{\text{hfi}} = \sigma_{\text{sfi}}|_{\text{failure}}, = \frac{2c_i\cos j_i + 2\sigma_{vi}\sin j_i}{1-\sigma_{vi}\sin j_i}, \tag{9}$$

where c_i and φ_i are the cohesion and internal friction angle of the ith soil layer, respectively, which can be determined by unconsolidated undrained (UU) triaxial test.

The mobilized internal friction angle φ_{mi} can be determined according to the stress level of soil in strain wedge (see Figure 3):

$$\sin\varphi_{mi} = \frac{\Delta\sigma_{hi}}{\Delta\sigma_{hi} + 2\sigma_{vi} + \left(2c_i/\tan\varphi_i\right)}. \tag{10}$$

With the increase of lateral load, the stress level of soil in strain wedge increases continuously until approaching the ultimate state. Then, the soil reaction at pile side reaches the ultimate soil resistance p_u and can be expressed as follows [19]:

$$p_u = (S_1 10 S_u + S_2 2 S_u) D. \tag{11}$$

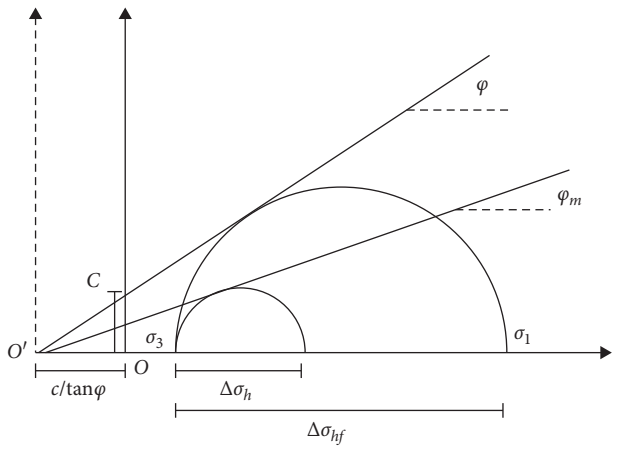

Figure 3: Relationship between friction angle and stress level of soil.

2.3. Calculation of SM Model. The finite difference method is used to solve (1), and the soil-pile system is evenly divided into N_L ($= L/h$) elements or layers with thickness h, and the soil-pile system within strain wedge range is divided into N_H ($= H/h$) segments. Combining with the lateral force and bending moment constraints of pile head and pile end, the differential solution equations of pile-strain wedge system are expressed as follows:

$$[K][Y] = [P], \tag{12}$$

where $[K]$ is the pile stiffness matrix of order $(N+1) \times (N+1)$. $[Y]$ and $[P]$ are the vectors of pile displacement and lateral load of $(N+1)$, respectively. The specific solution of (12) can be referred to in [20, 21].

Combining equation (4) and equations (6) and (7), the subgrade reaction modulus of soil within the depth of strain wedge can be obtained as follows:

$$k_i = \frac{p_i}{(y_{i-1} + y_i)/2}, \quad 1 \le i \le N_H. \tag{13}$$

The subgrade reaction modulus below the strain wedge varies linearly with depth and can be expressed as follows:

$$k_i = \eta_h z, \quad N_H < i \le N_L, \tag{14}$$

where η_h is the coefficient of the subgrade reaction [22].

Figure 4 shows the specific process for solving the static response of laterally loaded pile by utilizing the modified SM model. The corresponding computational program has developed using MATLAB software [23]. Based on the proposed procedure, the stress and strain levels of pile surrounding soil under different load levels can be determined for different depths. To facilitate calculation, the initial displacement value of pile in Figure 4 can be determined according to the solution solving by elastic-plastic analyzing method [24].

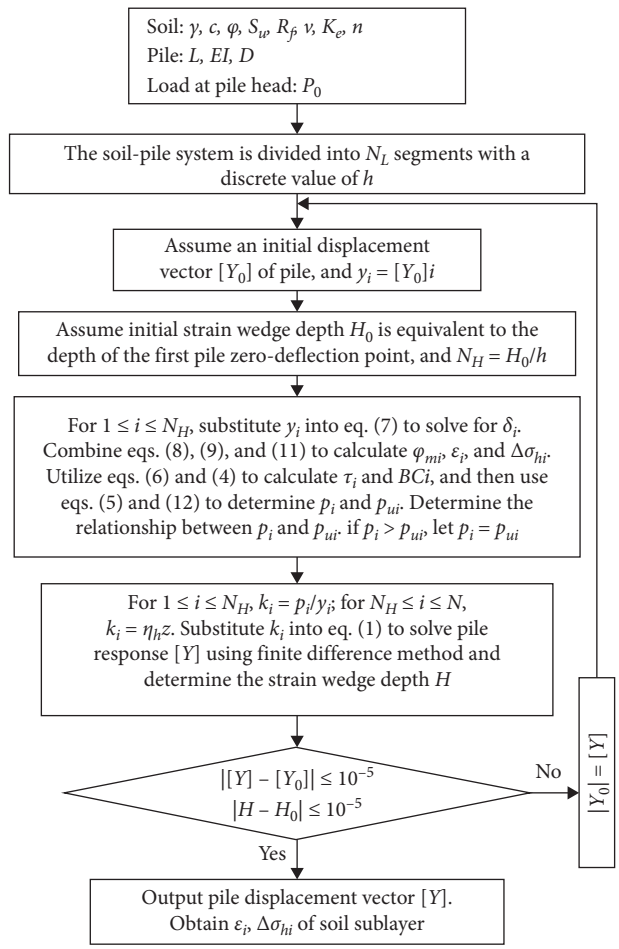

Figure 4: Flowchart for procedure of modified SW model.

3. Degradation Model of Soft Clay under Cyclic Loading

For the lateral loading conditions, the stress states of soil in the strain wedge under static load are similar to the static triaxial test and undrained cyclic triaxial test, respectively. In other words, the vertical stress σ_v is equivalent to confining pressure and lateral stress increment is equivalent to cyclic deviatoric stress σ_{cyc}. During cyclic triaxial test, with the increase of the number of cycles, cumulative plastic strains and pore water pressure would occur in the soil sample, which leads to the decrease of effective stress and further causes the weakening of the secant stiffness of clay and the increase of pile lateral displacement. Assuming that the elastic strain can be negligible, the degradation of secant stiffness after N cycles E_{sN} can be described by the cumulative plastic axial strains and pore water pressure as follows:

$$\begin{aligned} \frac{E_{sN}}{E_{s1}} &= \frac{\left(\sigma_{cyc} - u_N\right)/\varepsilon_N^a}{\sigma_{cyc}/\varepsilon_{N=1}^a}, \\ &\cong \frac{\sigma_{cyc} - u_N}{\sigma_{cyc}} \frac{\varepsilon_{p,N=1}^a}{\varepsilon_{p,N}^a}, \end{aligned} \tag{15}$$

where $\varepsilon^a_{p,N=1}$ and $\varepsilon^a_{p,N}$ are the plastic strains of soil after first cycle and N cycles of cyclic deviatoric stress σ_{cyc}, respectively. $\varepsilon^a_{N=1}$ and ε^a_N are the vertical strains after first cycle and N cycles, respectively. u_N is the pore water pressure after N cycles, and E_{s1} is the secant stiffness after the first cycle.

3.1. Semiempirical Formulas for Cumulative Plastic Strain and Pore Water Pressure of Soft Clay. According to (15), the cumulative plastic strain and pore water pressure are key parameters to determine the degradation degree of clay. Triaxial test results [25, 26] show that $\varepsilon^a_{p,N}$ and u_N of soft clay are related to the amplitude of cyclic deviatoric stress and the number of cycles. Based on triaxial tests, many scholars have fitted the curves of $\varepsilon^a_{p,N} \sim N$ and $u_N \sim N$ to obtain the semiempirical calculation formulas of cumulative plastic strain and pore water pressure of soft clay, which have been widely applied in engineering [27–30]. Here, based on the results of cyclic triaxial test [25] and considering the increase of cumulative pore water pressure, two semiempirical formulas cumulative plastic strain and pore water pressure of soft clay are proposed as follows:

$$\varepsilon^a_{p,N} = \varepsilon^a_{p,N=1} N^{\left(a_\varepsilon \eta_d^{\,b_\varepsilon}\right)}, \tag{16}$$

$$u^r_N = u^r_{N=1} N^{\left(a_u \eta_d^{\,b_u}\right)}, \tag{17}$$

where $\eta_d = \sigma_{\mathrm{cyc}}/\sigma_{sf}$ denotes the cyclic stress ratio of pile surrounding soil, that is, the ratio of cyclic deviatoric stress to ultimate static deviatoric stress which satisfies $\sigma_{sf} = (\sigma_1 - \sigma_3)_f$. $u^r_N = u_N/\sigma_3$ and $u^1_r = u_1/\sigma_3$ denote the ratios of cumulative pore water pressure and initial pore water pressure to minor principal stress σ_3. a_ε, b_ε, a_u, and b_u are corresponding fitting regression parameters, which can be determined by cyclic triaxial test. Then, $\varepsilon^a_{p,N=1}$ can be calculated as follows:

$$\varepsilon^a_{p,N=1} = \frac{\sigma_{\mathrm{cyc}}}{E_{\mathrm{in}}\left(1 - \sigma_{\mathrm{cyc}}/\sigma_{sf}\right)} - \frac{\sigma_{\mathrm{cyc}}}{E_{\mathrm{ur}}}, \tag{18}$$

where E_{ur} is unloading elastic modulus and is 1 to 3 times of the initial elastic modulus E_{in} [17].

3.2. Determination and Validation of Semiempirical Formulas Parameters. Liu et al. [25] conducted a series of undrained cyclic triaxial tests on soft clay and obtained the cumulative plastic strain and pore water pressure curves of soil under different cyclic stress ratios. The parameters of equations (16) and (17) can be obtained by fitting the test results. Typical regression parameters are found for cumulative plastic strain to be $a_\varepsilon = 0.594$ and $b_\varepsilon = 1.908$, and for cumulative pore water pressure to be $a_u = 0.828$ and $b_u = 1.124$. Then, the regression equation of the initial pore water pressure ratio is expressed as follows:

$$u^r_1 = 0.06125\eta_d^{1.6085}. \tag{19}$$

Equations (16) and (17) with the given parameters are used to fit the results of cyclic triaxial tests by Liu et al. [25], and the fitting results are shown in Figure 5. It is found that the two semiempirical formulas presented in this paper have sufficient accuracy and can better reflect the engineering characteristics of soft clay undergoing cyclic loads. Furthermore, substituting equations (16) and (17) into equation (15), the stiffness attenuation of soft clay can be reasonably simulated.

4. Calculation Method of Pile Lateral Displacement under Long-Term Cyclic Loading

In this section, the modified SM model and degradation model of soft clay are used to calculate the pile lateral displacement under long-term cyclic loading with the constant loading amplitude $P_{\max}$ and the number of cycles N. Firstly, based on the quasistatic method, the modified SM model is adopted to calculate the distribution law of stress and strain of pile surrounding soil undergoing the static load $P_{\max}$ along the depth. Based on the stress state determined by the modified SM model, the distribution of cyclic stress ratio of pile surrounding soil can be obtained, and then the attenuation stiffness of soil after N cycles can be calculated according to the degradation model of soft clay. Finally, the attenuation stiffness is introduced into the modified SW model to calculate the lateral displacement of pile. The specific calculation steps are as follows:

(i) *Step 1*. Determine η_{di}. Let $P_0 = P_{\max}$, and input the parameters of pile and soil into flowchart (Figure 4). Based on the modified SW model, the lateral displacement of pile under load P_0 is calculated. Then, the increment of lateral stress $\Delta\sigma_{hi}$ and lateral strain ε_i of the ith soil layer at different depths are obtained. Letting $\sigma_{\mathrm{cyci}} = \Delta\sigma_{hi}$ and taking $\Delta\sigma_{hi}$ as the amplitude of cyclic deviatoric stress, the corresponding cyclic stress ratio of pile surrounding soil $\eta_{di} = \sigma_{\mathrm{cyci}}/\sigma_{\mathrm{sfi}}$ is determined.

(ii) *Step 2*. Determine $\varepsilon^a_{pi,N}$, u_{Ni}, and E_{sNi}. Calculate the cumulative plastic strain $\varepsilon^a_{pi,N}$ and cumulative pore water pressure u_{Ni} of the ith soil layer in strain wedge subjected to different cyclic stress ratios by using equations (16) and (17). Then, substituting $\varepsilon^a_{pi,N}$ and u_{Ni} into equation (15), the attenuation stiffness E_{sNi} of the ith soil layer in strain wedge after N cycles can be obtained.

(iii) *Step 3*. Determine the stress-strain relationship of each soil layer during the Nth loading process. As shown in Figure 6, unlike the static loading process, the soil stiffness is attenuated due to the cumulative plastic strain and pore water pressure in soft clay. If the elastic strain during the reloading process is not considered, the stress-strain relationship of the ith soil layer during the Nth loading process can be approximated as follows:

$$\Delta\sigma_{hi} = \begin{cases} E_{sNi}\varepsilon, & \left(\varepsilon \le \varepsilon^{\mathrm{a}}_{p,Ni}\right), \\ \dfrac{\varepsilon}{\left(1/E_{\mathrm{ini}}\right) + \left(R_f\varepsilon/\Delta\sigma_{\mathrm{hfi}}\right)}, & \left(\varepsilon > \varepsilon^{\mathrm{a}}_{p,Ni}\right). \end{cases} \tag{20}$$

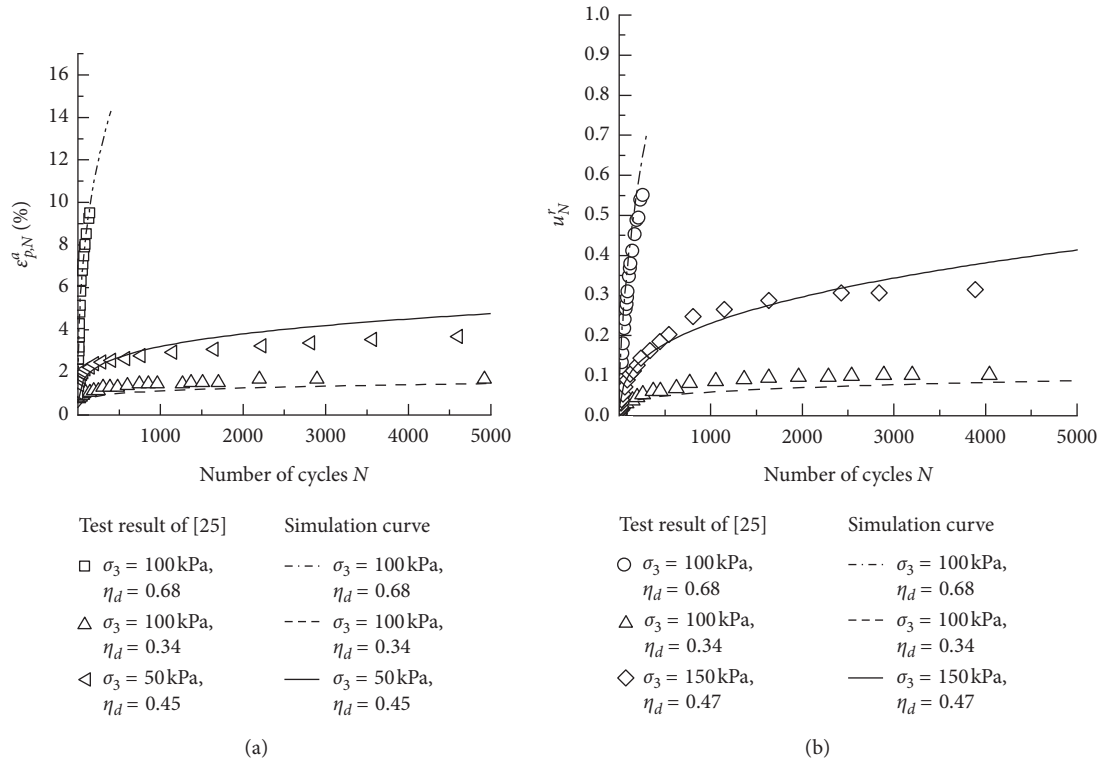

Figure 5: Comparison between the results of prediction and cyclic triaxial test [25]. (a) Simulation of $\varepsilon^a_{p,N} \sim N$curve. (b) Simulation of $u^N_r \sim N$curve.

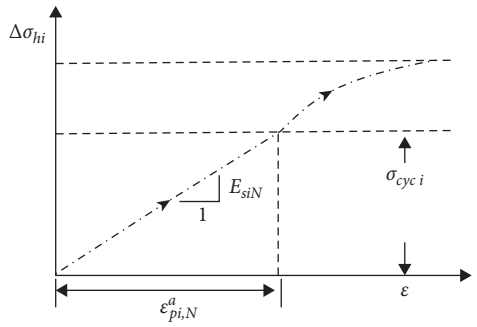

Figure 6: Relations of stress-strain of the soils during the Nthloading process.

(iv) *Step 4*. Letting $P_0 = P_{\max}$, and replacing equation (20) with equation (8) and substituting it into the flowchart of SW model procedure to consider the effect of cyclic load, the lateral displacement and internal force of pile are calculated when there is lateral cyclic load acting on the pile head.

Based on the above four steps, the authors utilize MATLAB [23] to compile a corresponding calculation program for the analysis of laterally loaded piles considering cyclic soil degradation.

5. Verification and Discussion

In this section, a comparison with existing model tests is conducted to verify the proposed method. Liao et al. [11] carried out a series of 1 g model tests to study the response of flexible pile under static and one-way cyclic loading on marine clay. The model pile was a circular PVC tube with a total length of 1000 mm and an embedded length of 700 mm. The outer diameter and wall thickness of the model pile are 50 mm and 5 mm, respectively. The loading position is 100 mm below the pile head. The bending stiffness of model pile is 0.4 kN · m^2, and the unit weight of soil is 17.82 kg/m^3. The undrained shear strength of soil varies linearly with depth and can be expressed as $S_u = 1.2 + 3.24z$. The other selected parameters of soil are given in Table 1.

The present modified SW model is applied to calculate the load-displacement curve at loading position and displacement distribution of pile under different lateral cyclic loads. The comparison between the calculated results and test results are shown in Figure 7. It is noted that the results predicted by the proposed method are almost consistent with those results from tests. It also shows that the modified SW model can effectively simulate the bearing behavior of pile in soft clay under static lateral load.

When the lateral displacement of pile at the loading position is 0.2D, the pile reaches the ultimate bearing state [31]. According to Figure 7, the ultimate static lateral

Table 1: Parameters of soil.

c (kPa)	φ (°)	ν	K_e	n	η_h (kN/m^3)
0.82	17.4	0.49	100	0.68	6000

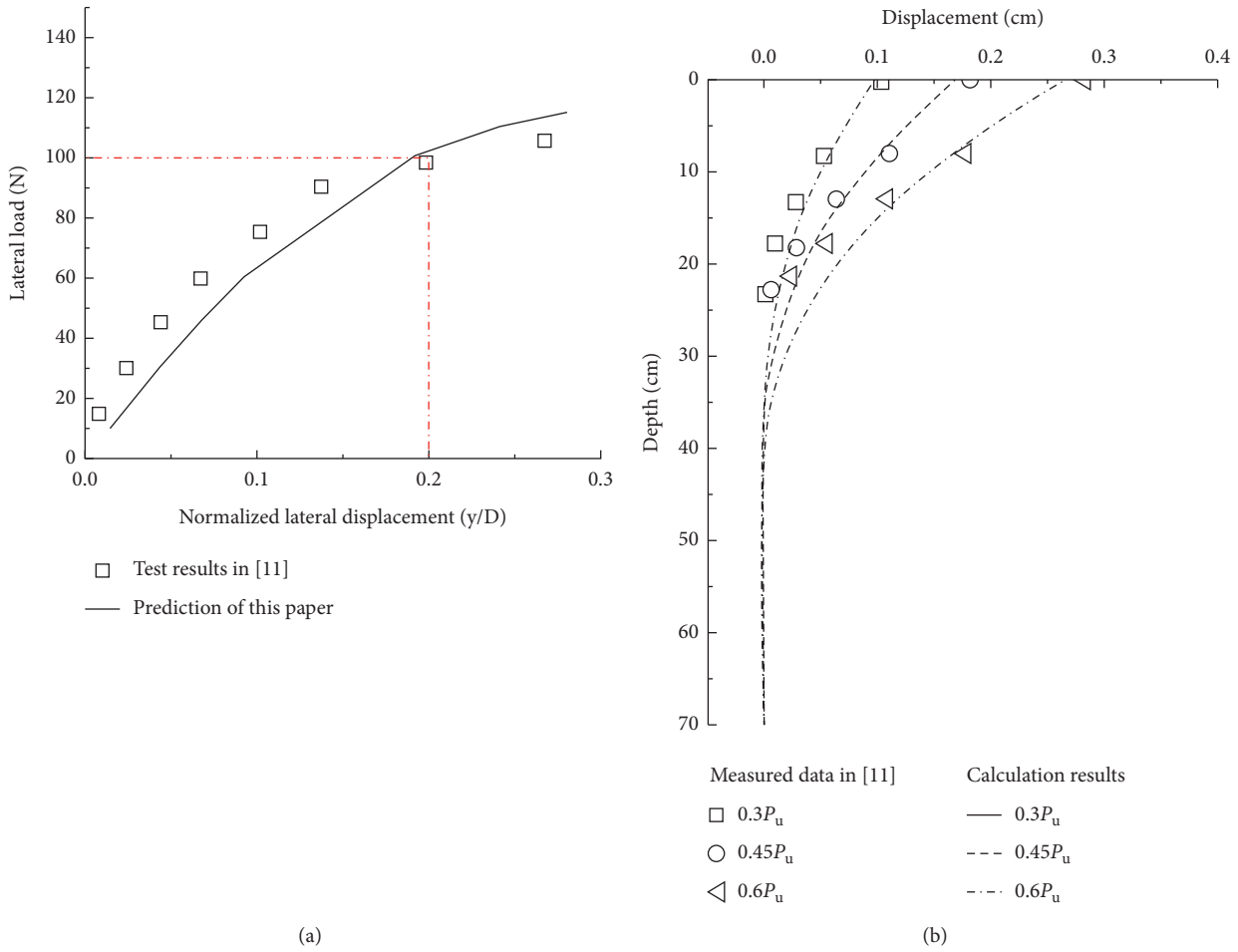

Figure 7: Comparison of measured data [11] with calculated results in static test. (a) Load-displacement curve at loading position. (b) Displacement distribution of pile.

capacity of the model pile P_u is approximately 100 N. In literature [11], three sets of cyclic loading tests with the loading amplitudes of $0.3P_u$, $0.45P_u$, and $0.6P_u$ were also carried out by one-way cyclic loading. The proposed method is applied to fit these tests and validate itself. Since the engineering properties of the test soil are similar to the soil sample of the cyclic triaxial test in literature [25], those fitting parameters in literature [25] are used in this fitting process. As well known, clay in different regions has different cyclic softening characteristics. For specific cases of cyclic laterally loaded pile, the fitting parameters of cyclic degradation model should be obtained by cyclic triaxial test on in-site sample. The proposed fitting parameters are only for reference.

Figure 8 depicts the comparison between the results calculated by the present method and the test results under different cyclic loading amplitudes. As shown in Figure 8, y^1 and y^N are the peak lateral displacement of the pile at loading position after the 1st cycle and the Nth cycle, respectively. y^N/y^1 represents the development degree of displacement and can reflect the softening degree of pile lateral stiffness; that is, $(P_{\max}/y^N)/(P_{\max}/y^1) = y^1/y^N$.

It is found that the results obtained by the present method are in good agreement with the test results. As the number of cycles and the load amplitude increase, the lateral displacement of pile shaft increases, but the pile lateral stiffness decreases. This indicates that the simplified calculation method can reasonably reflect the development of pile lateral displacement and the degradation of pile lateral stiffness when the pile in soft clay is undergone long-term cyclic loading.

Figure 9 shows the influence of cumulative pore water pressure on the lateral displacement of pile. For the cases of cyclic load amplitude of $0.45P_u$ and $0.6P_u$, when the effect of cumulative pore water pressure on the stiffness of pile surround soil is considered, the development degrees of pile

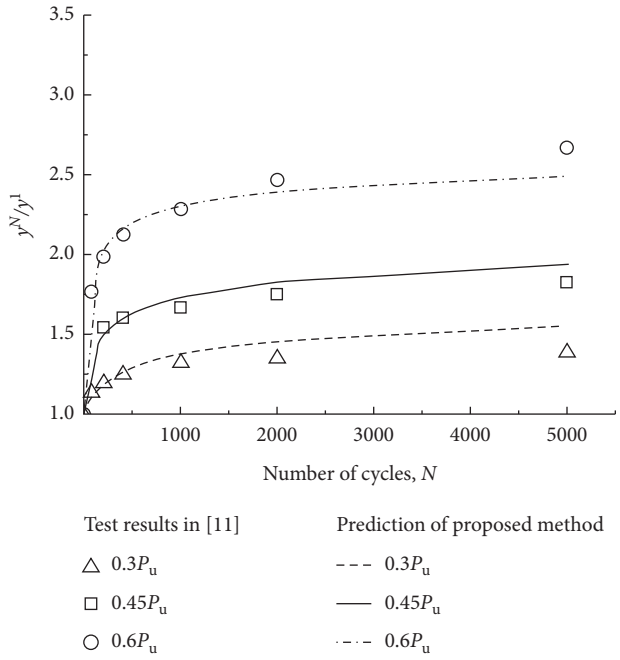

Figure 8: Comparison between results of the proposed method and model test [11].

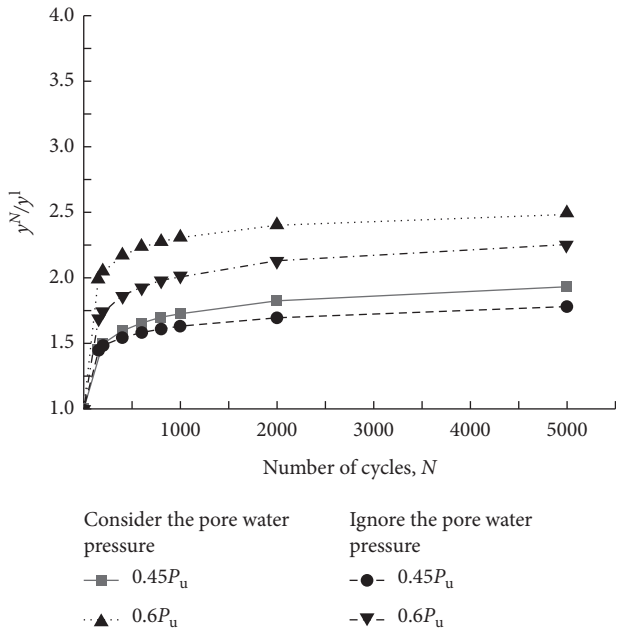

Figure 9: Influence of cumulative pore water pressure on lateral displacement of pile.

displacement are increased by 9% and 13% relative to the method of ignoring the cumulative pore water pressure, respectively. It means that the cumulative pore water pressure has a negative effect on the development of pile displacement in soft clay, and this negative effect increases with the cyclic load amplitude. Therefore, it is necessary to consider the influence of cumulative pore water pressure in the analysis of cyclic laterally loaded pile, in the calculation

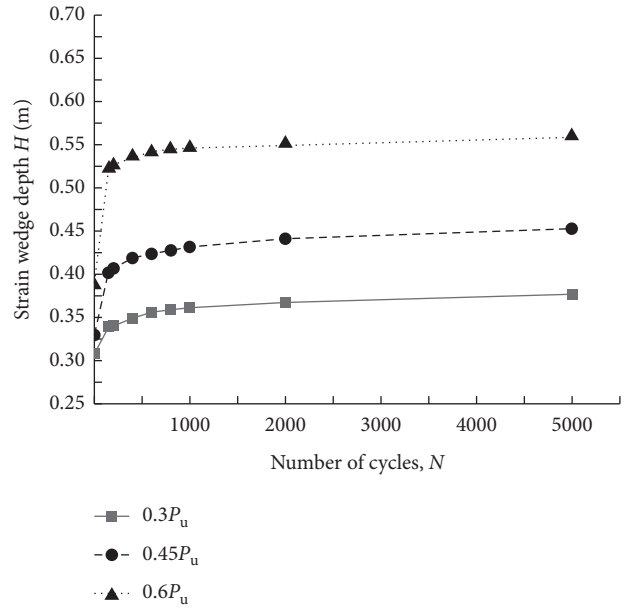

Figure 10: Influence of number of cycles on the depth of strain wedge.

response of pile in clay, which is also one of the main differences between clay subgrade and sandy subgrade under low-frequency cyclic loads.

Figure 10 illustrates the influence of the number of cycles on the depth of strain wedge. The strain wedge depth is an index reflecting the degree of bearing capacity of pile surrounding soil. It is found that the strain wedge depth increases as the number of cycles and cyclic load amplitude increase. This indicates that the degradation of soil in the upper strain wedge depth would lead to the deeper soil layers to participate in resisting lateral movement of pile shaft and exert its bearing capacity, which also reflects the working state of the soil-pile system under cyclic loads.

6. Conclusions

In this paper, a simplified method for the analysis of laterally loaded pile is proposed by combining a modified SW model with degradation model of soft clay. The effectiveness of the proposed method is verified by comparing with the results of 1g model tests by Liao et al. [11]. Moreover, the study on the influence of pore water pressure implies that there is a need to consider the effect of cumulative pore water pressure during the analysis of cyclic laterally loaded pile embedded in soft clay. Finally, it is also found that the strain wedge depth increases as the number of cycles and cyclic load amplitude increase, which can reflect the working state of the soil-pile system under cyclic loads.

Compared with the finite element methods, the present method has a greater advantage in terms of calculation speed. Compared with *p-y* curve method recommended by API, the present method can more effectively reflect the cyclic softening characteristics of pile surrounding and

consider the influence of cyclic load characteristics. However, the research in this paper is currently only applicable to the cyclic loading conditions with constant amplitude. The calculation of pile under cyclic loading cases with variable amplitude still needs to be further studied in the future.

Data Availability

The data that support the findings of this study are available from the corresponding author, Wenbing Wu, upon reasonable request.

Conflicts of Interest

The authors declare that they have no conflicts of interest regarding the publication of this study.

Acknowledgments

This research was supported by the National Natural Science Foundation of China (Grant nos. 51878634, 51678547, 51878185, and 41867034), the Outstanding Youth Project of Natural Science Foundation of Zhejiang Province (Grant no. LR21E080005), the Young Elite Scientists Sponsorship Program by CAST (Grant no. 2018QNRC001), and the Fundamental Research Funds for National University, China University of Geosciences (Wuhan) (Grant nos. 1910491T04 and CUGC09).

References

[1] H. G. Poulos, "Single pile response to cyclic lateral load," *Journal of the Geotechnical Engineering Division, ASCE*, vol. 108, no. 3, pp. 355–375, 1982.

[2] F. Y. Liang, H. B. Chen, and Y. J. Jia, "Quasi-static p-y hysteresis loop for cyclic lateral response of pile foundations in offshore platforms," *Ocean Engineering*, vol. 148, pp. 62–74, 2018.

[3] H. J. Li, L. Y. Tong, and S. Y. Liu, "Effect of excavation unloading on p-y curves for laterally loaded piles," *Computers and Geotechnics*, vol. 104, pp. 131–139, 2018.

[4] Y. P. Zhang, W. B. Wu, G. S. Jiang et al., "A new approach for estimating the vertical elastic settlement of a single pile based on the fictitious soil pile model," *Computers and Geotechnics*, vol. 134, Article ID 104100, 2021.

[5] A. J. Grashuis, H. A. Dietermann, and N. F. Zorn, "Calculation of cyclic response of laterally loaded piles," *Computers and Geotechnics*, vol. 10, no. 4, pp. 287–305, 1990.

[6] M. Achmus, Y. S. Kuo, and K. Abdel-Rahman, "Behavior of monopile foundations under cyclic lateral load," *Computers and Geotechnics*, vol. 36, no. 5, pp. 725–735, 2009.

[7] A. F. Hu, G. J. Zhang, Y. S. Jia, and X. D. Zhang, "Application of degradation stiffness model in analysis of cumulative lateral displacement of monopile foundation," *Journal of Zhejiang University*, vol. 48, no. 4, pp. 721–726, 2014.

[8] Y. P. Zhang, H. Liu, W. B. Wu, L. X. Wang, and G. S. Jiang, "A 3D analytical model for distributed low strain test and parallel seismic test of pipe piles," *Ocean Engineering*, vol. 225, Article ID 108828, 2021.

[9] P. Jeanjean, "Re-assessment of p-y curves for soft clays from centrifuge testing and finite element modeling," in *Proceedings of the Offshore Technology Conference*, pp. 1–23, OTC, Houston, TX, USA, May 2009, Article ID 20158.

[10] C. LeBlanc, G. T. Houlsby, and B. W. Byrne, "Response of stiff piles in sand to long-term cyclic lateral loading," *Géotechnique*, vol. 60, no. 2, pp. 79–90, 2010.

[11] W. M. Liao, J. Zhang, J. B. Wu, and K. Yan, "Response of flexible monopile in marine clay under cyclic lateral load," *Ocean Engineering*, vol. 147, pp. 89–106, 2018.

[12] M. Vucetic and R. Dobry, "Degradation of marine clays under cyclic loading," *Journal of Geotechnical Engineering*, vol. 114, no. 2, pp. 133–149, 1988.

[13] G. Norris, "Theoretically based BEF laterally loaded pile analysis," in *Proceedings of the 3rd international conference on numerical methods in offshore piling*, pp. 361–386, Paris, France, May 1986.

[14] M. Ashour, G. Norris, and P. Pilling, "Lateral loading of a pile in layered soil using the strain wedge model," *Journal of Geotechnical and Geoenvironmental Engineering*, vol. 124, no. 4, pp. 303–315, 1998.

[15] M. Heidari, M. H. El Naggar, M. Jahanandish, and A. Ghahramani, "Generalized cyclic p-y curve model for analysis of laterally loaded piles," *Soil Dynamics and Earthquake Engineering*, vol. 63, pp. 138–149, 2014.

[16] L. Y. Xu, F. Cai, G. X. Wang, and K. Ugai, "Nonlinear analysis of laterally loaded single piles in sand using modified strain wedge model," *Computers and Geotechnics*, vol. 51, pp. 60–71, 2013.

[17] J. M. Duncan and C. Y. Chang, "Nonlinear analysis of stress and strain in soils," *Journal of the Soil Mechanics and Foundations Division*, vol. 96, no. 5, pp. 1629–1653, 1970.

[18] J. H. Qian and Z. Z. Yin, *The Earthwork Principle and Calculation*, Water Power Press, Beijing, China, 1995, in Chinese.

[19] Y. Kim, S. Jeong, and S. Lee, "Wedge failure analysis of soil resistance on laterally loaded piles in clay," *Journal of Geotechnical and Geoenvironmental Engineering*, vol. 137, no. 7, pp. 678–694, 2010.

[20] S. M. Gleser, *Generalized Behavior of Laterally Loaded Vertical Piles. Laterally Loaded Deep Foundations: Analysis And Performance*, ASTM STP, West Conshohocken, PA, USA, 1984.

[21] R. Z. Liang, W. B. Wu, F. Yu, G. S. Jiang, and J. W. Liu, "Simplified method for evaluating shield tunnel deformation due to adjacent excavation," *Tunnelling and Underground Space Technology*, vol. 71, pp. 94–105, 2018.

[22] K. Yang and R. Liang, "Numerical solution for laterally loaded piles in a two-layer soil profile," *Journal of Geotechnical and Geoenvironmental Engineering*, vol. 132, no. 11, pp. 1436–1443, 2006.

[23] Matlab, *Computer Software*, MathWorks, Natick, MA, USA, 2017.

[24] Y. Hsiung, "Theoretical elastic-plastic solution for laterally loaded piles," *Journal of Geotechnical and Geoenvironmental Engineering*, vol. 129, no. 5, pp. 475–480, 2003.

[25] T. J. Liu, X. R. Ge, and G. F. An, "Study of characteristics of saturated soft clay under uniaxial cyclic load," *Chinese Journal of Rock Mechanics and Engineering*, vol. 31, no. A01, pp. 3345–3351, 2012, in Chinese.

[26] G. L. Feng, X. T. Feng, B. R. Chen, Y. X. Xiao, and Y. Yu, "A microseismic method for dynamic warning of rockburst development processes in tunnels," *Rock Mechanics and Rock Engineering*, vol. 48, no. 5, pp. 2061–2076, 2015.

[27] J. C. Chai and N. Miura, "Traffic-load-induced permanent deformation of road on soft subsoil," *Journal of Geotechnical*

and Geoenvironmental Engineering, vol. 128, no. 11, pp. 907–916, 2002.

[28] A. Sakai, L. Samang, and N. Miura, "Partially-drained cyclic behavior and its application to the settlement of a low embankment road on silty-clay," *Soils and Foundations*, vol. 43, no. 1, pp. 33–46, 2003.

[29] G. L. Feng, B. R. Chen, Q. Jiang, Y. X. Xiao, W. J. Niu, and P. X. Li, "Excavation-induced microseismicity and rockburst occurrence: similarities and differences between deep parallel tunnels with alternating soft-hard strata," *Journal of Central South University*, vol. 28, pp. 582–594, 2021.

[30] G. L. Feng, X. T. Feng, and Y. X. Xiao, "Characteristic microseismicity during the development process of intermittent rockburst in a deep railway tunnel," *International Journal of Rock Mechanics and Mining Sciences*, vol. 124, Article ID 104135, 2019.

[31] B. B. Broms, "Lateral resistance of piles in cohesive soils," *Journal of the Soil Mechanics and Foundations Division*, vol. 90, no. 2, pp. 27–64, 1964.

Hindawi
Advances in Civil Engineering
Volume 2021, Article ID 5539628, 17 pages
https://doi.org/10.1155/2021/5539628

Research Article

Seismic Response Analysis of Deep Underground Roadways and Coal Pillars under the Influence of the Adjacent Goaf

Xu Cao, Xiaoshan Cao, and Tielin Han

School of Civil Engineering and Architecture, Xi'an University of Technology, Xi'an, Shaanxi, China

Correspondence should be addressed to Xiaoshan Cao; caoxsh@xaut.edu.cn

Received 12 January 2021; Revised 18 May 2021; Accepted 26 May 2021; Published 11 June 2021

Academic Editor: Guang-Liang Feng

In this work, a numerical study is conducted on the seismic response of deep-buried roadways in coal mines under the influence of goafs, and a 3D numerical model of the seismic response simulation of deep-buried roadways is established using the coupling model of the finite difference method and the distinct element method. This model simulates the seismic response of different coal pillar widths and the seismic conditions of the deep-buried roadways under the influence of the adjacent goafs. The deformation, stress distribution, and plastic area distribution of roadways and coal pillars are systematically studied, and the situations under the static load and the roadways, which are not affected by the goafs, are compared and analyzed. A reasonable width of the coal pillar is proposed on the basis of the stability of the roadway and the coal pillars. In the end, suggestions for the reasonable setting of coal pillars under seismic load are provided.

1. Introduction

The earthquake disaster causes serious damage to ground buildings and brings about serious effects to underground structures [1–3]. The deep underground mining often induces seismic activity, which is called mine earthquake [4–7]. Natural and mine earthquakes are not essentially different [8, 9]. Natural earthquakes have caused different degrees of damage to coal mines [10, 11]. Underground coal mines are gradually affected by mine earthquakes with increased coal mining depth [12, 13]. In the limited deep space, mine earthquakes may cause a series of other coal mine disasters, such as rock explosion, coal and gas outburst [14], and water penetration [15–20]. Therefore, the response of deep underground coal mine structure should be analyzed under the seismic load.

The gob-side entry driving is a long-walled coal mining often used in the form of exploitation [21–25], and the roadway driving with coal pillars can effectively isolate the goaf to prevent water and harmful gases in the goafs into the roadway [26, 27]. Feng et al. [28] established the relationship between microseismicity and the risk of rockburst and then proposed an early warning technique based on it to predict the rockburst in tunnels. By analyzing the monitored microseismic data, this method can provide a real-time early warning of the rockburst risk during excavation of the tunnel. The application of this method in some engineering cases shows that it can well predict the development of rock burst [29, 30]. Li and Chai [31] studied the relationship between the width of coal pillars and the susceptible coal explosion in deep-buried roadways and proposed a reasonable coal pillar width setting to reduce the risk of the coal explosion. Considering that coal pillars play a supporting role in the active coal mining space and are subjected to different forms of dynamic action, the current mining stress of the coal mining face is the main dynamic form. Coal pillars are also affected by the process of isolating the goaf and the overlying rock strata sinking the goaf during the compaction process. Coal pillars are affected by dynamics, which often cause large deformations and bring about difficulties to the coal mining. Zhao et al. [32] and Wang et al. [33] analyzed the stress changes and the damage risks of coal pillars under dynamic and static loads with specific cases and proposed reasonable coal pillars under corresponding geological conditions. In previous studies, underground chambers or roadways often produced a certain

amount of deformation under the action of earthquake loads. Wang et al. [34] analyzed the seismic response of underground gas storage salt caverns, which produce certain deformation and damage in the seismic response. In turn, the seismic response has a certain effect on the safety of gas storage salt caverns. This deformation does not pose a great threat to the roadway in the coal mining space of the coal mine, and the effect of the dynamic stress on the roadway far from the goaf is small [35–37]. However, the deformation of the roadway formed by the gob-side entry driving due to the isolation of coal pillars near the goaf is often severe. In the study of the dynamic response of isolated coal pillars under the action of the goaf, the goaf is often regarded as a continuous medium [38–40], which is often inconsistent with the actual situation of broken rocks in the adjacent goaf.

In this study, the finite difference method (FDM) and the distinct element method (DEM) are coupled, and a continuous medium model of isolated coal pillars and formations is established. A discrete medium model of the adjacent goaf is established using the DEM. The effect of the adjacent goaf under seismic load on the coal pillar and the response of coal pillars with different widths under the seismic load are analyzed. These results should provide suggestions for the reasonable setting of coal pillars under the seismic load.

2. FDM and DEM Constitutive Models

The computational resource required to model coal strata sequence using a distinct element code similar to PFC is enormous, especially in dynamic calculation. The goaf is filled with broken gangue, and the discrete medium in the goaf belongs to unbonded granular materials. Therefore, using PFC to simulate the goaf is reasonable. The Mohr-Coulomb model is widely used in the seismic analysis in the nonlinear dynamic analysis in geotechnical engineering [41–43]. The continuum model is selected for the coal pillar and the adjacent complete stratum, and the Mohr-Coulomb model is selected for the constitutive relationship of the model. The contact connection model is used to simulate the discrete medium in the goaf without considering the internal fragmentation of the particles. The solid element (zone) in the FDM and the wall in the DEM are used for coupling. The coupling of FDM and DEM is required to reduce computation time while ensuring solution accuracy.

A model (Figure 1) is established to verify the feasibility of the coupling scheme. The length, width, and height dimensions of the overall model are 160 m × 5 m × 15 m in the x, y, and z directions in the software. The hollow area of 150 m × 5 m × 10 m is filled with the DEM and the FDM. The mechanical parameters related to the FDM and the DEM are shown in Table 1. FDM parameters are obtained from coal mine strata. The DEM refers to the data in literature [44]. In the coupling model of the FDM and the DEM, the DEM particle size is 0.2–0.5 m. A total of 24,816 particles (balls) are generated, and the number of physical units (zone) is 4,500. The number of solid elements (zone) is 12,000 in the model with only continuum.

After the model is established, the parameters are assigned, and the bottom and all sides of the model are fixed.

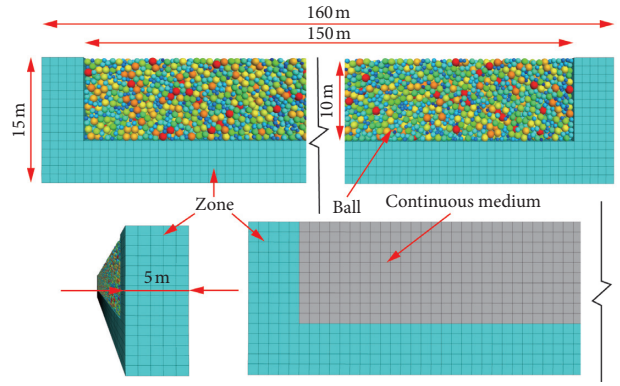

Figure 1: Coupling verification model.

No stress or restriction is observed in the upper part. The self-weight stress balance is calculated, and the model displacement and the velocity are initialized to 0. The acceleration time range (Figure 2) is entered from the bottom of the model and provides artificial waves for the software. The acceleration equation for the wave is

$$u(t) = \frac{1}{2}\left(1 - \cos\left(\frac{\pi}{3}t\right)\right)A \sin(2\pi f t), \tag{1}$$

where A is the amplitude and f is the frequency.

The free-field boundary is applied around the model to reduce the reflection of the acceleration wave. The static boundary conditions are removed, and the dynamic response of the model is verified under the influence of no surrounding stress. The dimensional effects are considered. The distance at the y direction is short, and the free-field boundary is observed at both ends. The acceleration in the y direction is set to 0, and the acceleration in the x and z directions is entered in accordance with the actual size.

The model dynamic calculation time is set to 10 s. The coupling of FDM and DEM under self-weight stress (Figures 3(a) and 3(b)) and dynamic load (Figures 3(c) and 3(d)) conditions and the vertical stress in the left pillar of the continuous medium models (Figures 3(b) and 3(d)) is extracted to verify that the response of the bulk and the continuum media to the cylinder differs. The coordinates of the pillars are x(0–5), y(0–5), and z(0–15), and the stress is extracted from $x = 4.9$ in the x plane. Considering that 5.0 is affected by displacement, some areas cannot be extracted due to stress. As shown in Figure 3, the vertical stress of the continuum (Figure 3(b)) shows a linear change along the z-axis as a whole under the condition of self-weight stress. However, the coupling model of the FDM and the DEM (Figure 3(a)) is affected by the contact stress of the loose body. Moreover, the local area is no longer linear, shows a fluctuation in the whole plane, and does not change uniformly in the direction of the y-axis. These observations show that the DEM and the continuum have completely different forces on adjacent areas. This difference is also evident under the dynamic load conditions. As shown in Figures 3(c) and 3(d), the stress distribution in the continuous medium (Figure 3(d)) shows a certain regularity. For example, at the position of $z = 0$, the vertical stress in the

Table 1: Reference table of FDM and DEM physical mechanical parameters.

Name of coal and rock mass	Bulk modulus (GPa)	Shear modulus (GPa)	Density (kg/m^3)	Cohesion (MPa)	Internal friction angle (°)
Model floor, 5 m	5.9	2.5	2620	1.3	29
Left and right pillars	3.1	1.5	1420	0.5	22
Mechanical parameters in the DEM model					
Contact modulus E_c (GPa)	Stiffness ratio k_n/k_s	Frictional coefficient μ	Normal strength/σ_c (MPa)	Tangential strength/τ_c (MPa)	
10	1.0	0.5	10	10	

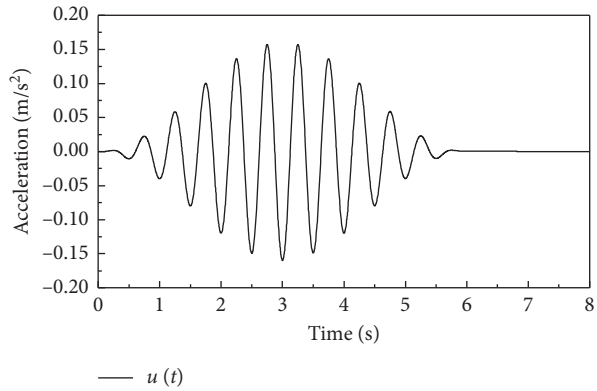

Figure 2: Input acceleration time history.

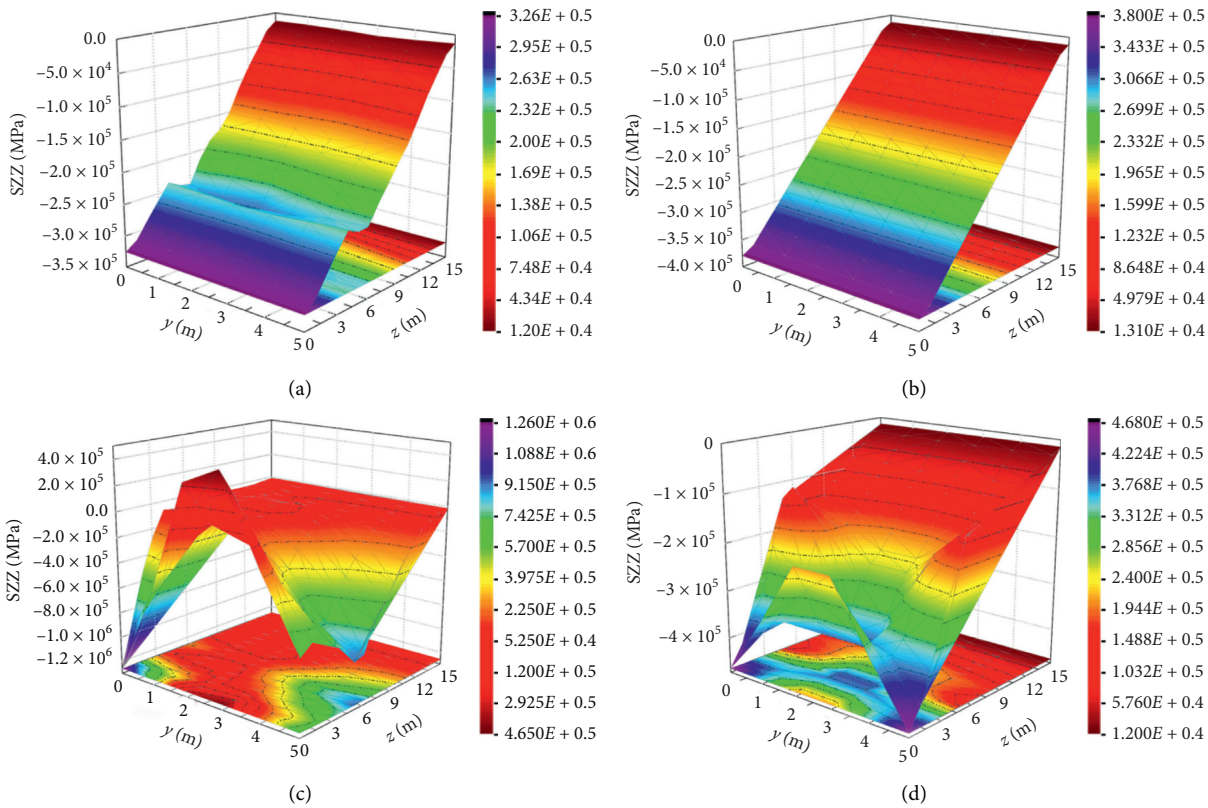

Figure 3: Vertical stress distribution of the left column under the self-weight and the dynamic load.

y direction is low at both ends, high in the middle, linear, and gradually stable from both ends to the middle. At the position of $y = 2.5$, the stress in the z direction increases first and then decreases. In the FDM and the DEM coupling model (Figure 3(c)), an irregularity between the self-weight stress and the continuous medium is observed. Therefore,

the dynamic load response of coal pillars under this discrete medium, which is different from the continuous medium, should be studied.

3. Establishment of the Numerical Model

3.1. Geological Background and Site Details. The Kongzhuang Coal Mine in Xuzhou, China, was selected as a numerical example. The longwall panels (7433 panels and 7435 panels) with width of 200 m and length of 100 m are selected. The coal seam thickness of the working face is 4.20 m~5.10 m, and the average thickness is 4.60 m.

The immediate roof of the coal seam is sandy mudstone, with a thickness of 0.60~11.19 m, an average thickness of 3.90 m, gray-black, thin-layered, uneven sand content, and more plant fossils. The main roof is composed of siltstone and medium-grained sandstone. The thickness of siltstone is 1.87~3.21 m with an average thickness of 1.50 m. The thickness of medium-grained sandstone is 5.23~9.81 m with an average thickness of 6.66 m. The siltstone is gray-white; the main components are quartz, feldspar, calcareous cement, compact, fine-grained sand-like structure, and nearly horizontal bedding; for details, see Figure 4.

3.2. Modeling and Solutions. The numerical model is established on the basis of the tail entry of the 7435 working face of the Kongzhuang Coal Mine. The 7435 working face is the first working face buried more than 1000 m deep in Kongzhuang Coal Mine. The plane relationship between 7433 and 7435 working faces is shown in Figure 5. During mining at the 7433 working face, if the 7435 working face is excavated, then an isolated coal pillar should be set between two working faces. The length along the dip of the two working faces is 150 m. Thus, the length along the dip of the 7433 goaf is 150 m, and the tail entry of the 7435 working face is shown in Figure 5. The width and the height of the roadway section are 5 and 4 m, respectively. The 3D sizes of the comprehensive strata histogram and model are shown in Figure 4. The size of the model in the x direction is 350 m, and the sizes in the z and y directions are 200 and 5 m, respectively. The layout of monitoring points around the roadway is shown in Figure 4 to monitor the displacement and the stress of the roadway and the coal pillars. The height dimension of the goaf, that is, the caving zone, uses statistical theoretical analysis to arrive at the regression formula of the fall zone on the basis of the highly measured data of the caving zone of a large number of goafs in China and the United States made by Bai et al. [45].

$$H_c = \frac{100h}{c_1 h + c_2}, \tag{2}$$

where H_c is the height of the caving zone (m), h is the height mining (m), and c_1 and c_2 are the strata strength parameters. The values of c_1 and c_2 can be determined on the basis of literature [45]. The 7433 working face has a mining height of 4.5 m, and the calculated caving zone height is approximately 11.2 m and is regarded as 11 m. The working face has a length of 150 m. Therefore, the size of the goaf is (i) $X \times Y \times Z$, 150 m × 5 m × 11 m by using the DEM for modeling. The DEM model (Figure 6) is built. The randomly generated geometric model is imported from the external software to simulate the broken rocks in the goaf realistically, and the spherical particles are filled into the geometric model to make the surface of the model as close to the actual one as possible under stable model conditions. For the physical and mechanical parameters of the two models, the FDM parameters are determined in accordance with the geological conditions of field engineering and the mechanical properties of the rock formations. The DEM model parameters are determined in reference to literature [44], and the physical mechanical parameters are presented in Table 2.

The total numbers of model units and DEM are 124 250 and 3866, respectively. The size of broken rock mass is 0.3–2 m, and the particles of the broken rock mass are randomly generated in this range. The porosity of the model is 0.3. In this discussion, the effect of particle breakage and size is ignored. The position of the 7435 tail entry in the model moves to the left in the dashed box of Figure 4 to change the widths of the coal pillar to 5, 7, 9, 11, 13, 15, 20, 25, 30, 35, and 40 m, which indicates the construction of 11 models. The grid size of the model is dense around the adjacent roadway and the goaf. The grid size is far from the roadway, and the goaf is appropriately enlarged to improve the accuracy of the calculation without affecting the calculation results.

The 7435 working face of the Kongzhuang Coal Mine has an elevation of −1017.50 m to −883.80 m. This study ignores the effects of the stratigraphic dip. The working face is arranged horizontally. The working face and the roadway are arranged at 1000 m. The rock mass density and the upper vertical stress are valued at 2500 kg/m^3 and 25 MPa, respectively, and the horizontal stress ratio is 1.5 during the static calculation of the model. The front, rear left, right, and the bottom are fixed at the model static calculation boundary conditions. The dynamic boundary condition of the model is the free-field boundary condition to reduce the reflection of waves.

The mechanical parameters of coal and rock can be found in Table 2, and the DEM mechanical parameters are the same as those in Table 1. The two sides of the 7435 return airway are supported by bolts, with length, diameter, and spacing of 2.4 m, 20 mm, and 1 m × 1 m, respectively. Four anchors are present on each section with the yield load and pretightening force of 150 and 80 kN, respectively. The roof is supported by bolts and cables with spacing of 1 m × 1 m. The anchor cables are arranged in the middle of the bolts near the middle point of the bolster and the roof of the roadway with anchor cable diameter, length, yield load, and pretightening force of 17.8 mm, 8.2, 600 kN, and 150 kN, respectively.

3.3. Input and Processing of Seismic Waves. In the calculation process, the Northridge, Loma, Kobe, and artificial seismic waves are used [46]. The first 20 of the four seismic waves are extracted as input dynamic loads, and the four seismic waves

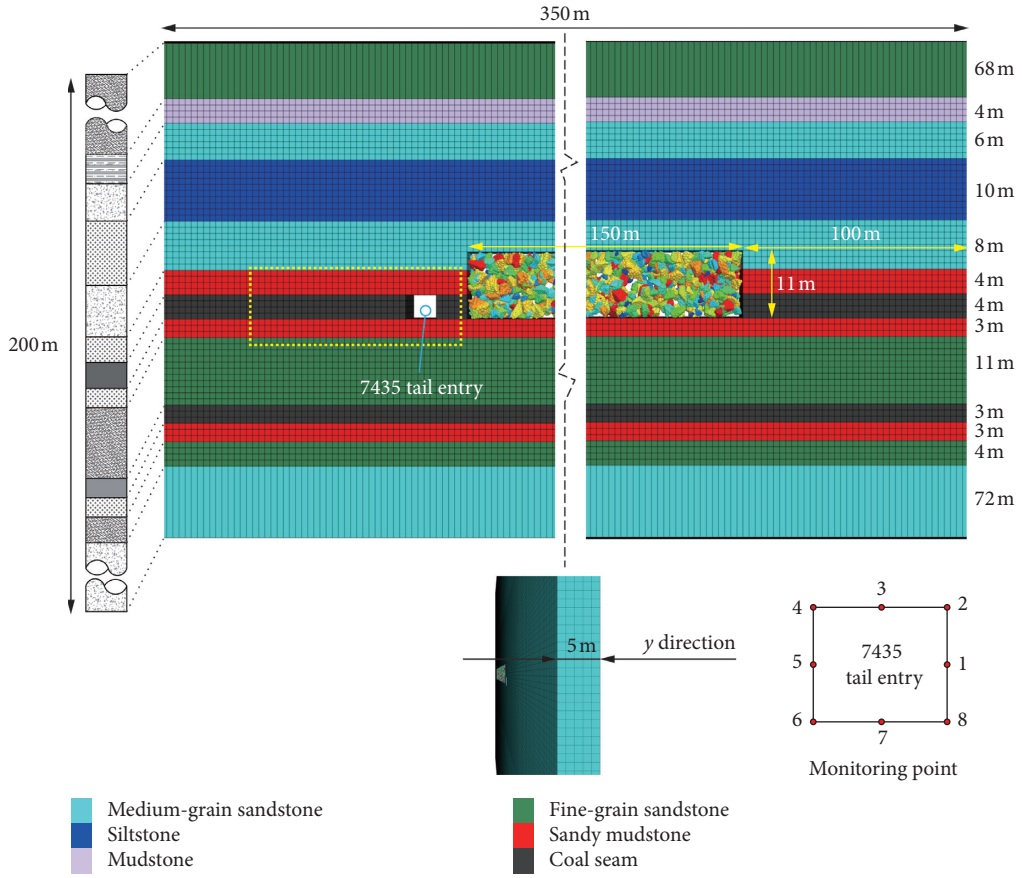

Figure 4: 3D size of the numerical model and integrated stratigraphic histogram.

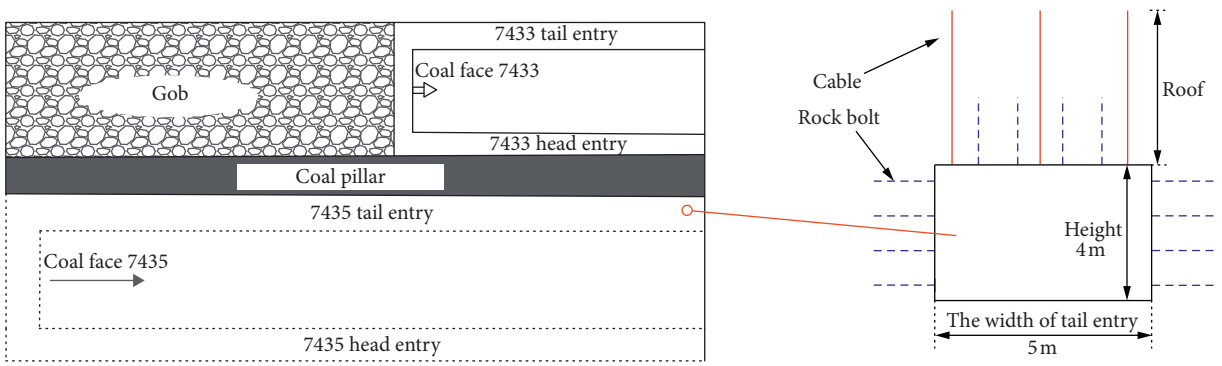

Figure 5: Plane position relationship of the model and the support form of the 7435 return airway.

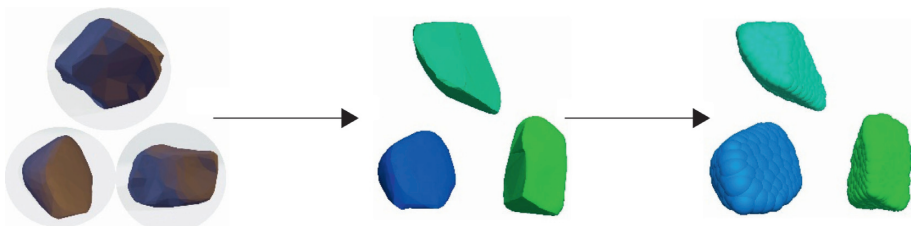

Figure 6: Establishment of the DEM model.

Table 2: Physical and mechanical parameters used in the model.

Name of coal and rock mass	Bulk modulus (GPa)	Shear modulus (GPa)	Density (kg/m^3)	Cohesion (MPa)	Internal friction angle (°)
Siltstone	9.1	3.8	2500	16	37
Mudstone	6.6	2.2	2550	10	35
Fine sandstone	9.2	4.0	2700	20	43
Coal	3.1	1.5	1420	5	22
SDSH	5.9	2.5	2620	13	29
Medium-grain sandstone	8.7	4.1	2500	18	40

are filtered and baseline-corrected using the SeismoSignal [47] software. This procedure eliminates a small number of high-frequency waves in the seismic waves, reduces the number of meshes, and ensures that the displacement and velocity of the model grid points after the power calculation are 0. The acceleration of the four seismic waves is shown in Figures 7(a)–7(d). Considering the effect of the model size, the acceleration of the seismic wave in the y direction is set to 0 due to the small size of the y direction, and the acceleration in the x and z directions is entered in accordance with the original size.

4. Deformation Characteristics of Roadway

4.1. Horizontal Deformation. Figure 8 shows a change curve in the horizontal displacement of 56 study cases, including 11 different coal pillar widths under static load conditions and four seismic wave conditions. Figures 8(a), 8(c), 8(e), 8(g), and 8(h) show the horizontal displacement of monitoring point 1, which reveals the maximum horizontal displacement change on the side of the coal pillar of the roadway. Figures 8(b), 8(d), 8(f), 8(h), and 8(j) show the horizontal displacement of monitoring point 5, which reveals the maximum horizontal displacement change curve of the solid coal side of the 7435 return air lane, where a and b are the horizontal displacement curves under the static load.

(1) Under the static load, the influence of width is not great within the range of 5–15 m, and the coal pillar side of roadway total of horizontal displacement is between 0.4 and 0.5 m. The horizontal displacement of the coal pillar with width of 5 m is smaller than that of the coal pillar with width of 7–15 m, and this finding is similar to that observed in previous research. The displacement change in the solid coal side of roadway between 5 and 15 m has also a minimal effect, that is, 0.2–0.3 m. However, the effect on the roadway deformation is small under the coal column width of 5–9 m. Therefore, in recent years, the narrow coal roadway has been chosen to improve the coal extraction rate. The stability of the roadway and coal pillars can be maintained and the coal output can be improved under the condition of improving and strengthening the support.

(2) Within the coal pillar width range of 15–40 m, the coal pillar side of roadway total of horizontal displacement gradually decreases with the increase in coal pillar width. The overall displacement is less than 0.3 m. In particular, the deformation of coal pillar side of roadway reduced to 0.2 m when the width of coal pillar was greater than 25 m.

(3) For the seismic reaction of a single roadway not affected by the goaf, the displacement curve is represented by no gob in Figure 8 for comparative analysis. As shown in Figure 8, the horizontal displacement change of the single-roadway deep underground, which is relatively safe for coal mining, is not affected by the goaf. This finding has also been confirmed by previous studies and surveys. However, the horizontal displacement deformations of coal pillars and roadways in adjacent goafs under the influence of frequent or continuous dynamic loads differ, and the width of the coal pillars remarkably affects the changes in displacement. Figures 8(c), 8(e), 8(g), and 8(i) represent the deformation of the coal pillar side of the roadway under the influence of four kinds of seismic waves. At the beginning of the ground motion, the displacement under the 5–15 m wide coal pillars increases significantly, and the displacement under the 5 m wide coal pillars increases to more than 0.3 m within 1 s of the ground motion. The difference from the static load condition is that the displacement under the coal pillar with width of 5 m no longer shows an insignificant change from that under the coal pillars with width of 7–15 m but continues to increase as the earthquake time continues. Under the coal pillar with width of 7–15 m, the displacement is less than that of the coal pillar with width of 5 m, but the effect is insignificant. When the width of the coal pillars reaches 20 m, the trend of the lane displacement change in the pre-seismic period is approximately linear and gradually slows down. Figures 8(d), 8(f), 8(h), and 8(j) show the displacement curves of the solid coal side of the roadway. Considering the long distance from the goaf and the support of solid coal, the displacement is smaller than the deformation of the coal pillar side, and the overall trend of the displacement is similar to that of the solid coal side. Similarly, the displacement changes in coal pillars with width of 5–15 m are evident, and the coal pillars are gradually eased when their width reaches 20 m.

(4) Different displacements are observed under four seismic conditions. The displacement under the Loma seismic wave is the largest. The maximum

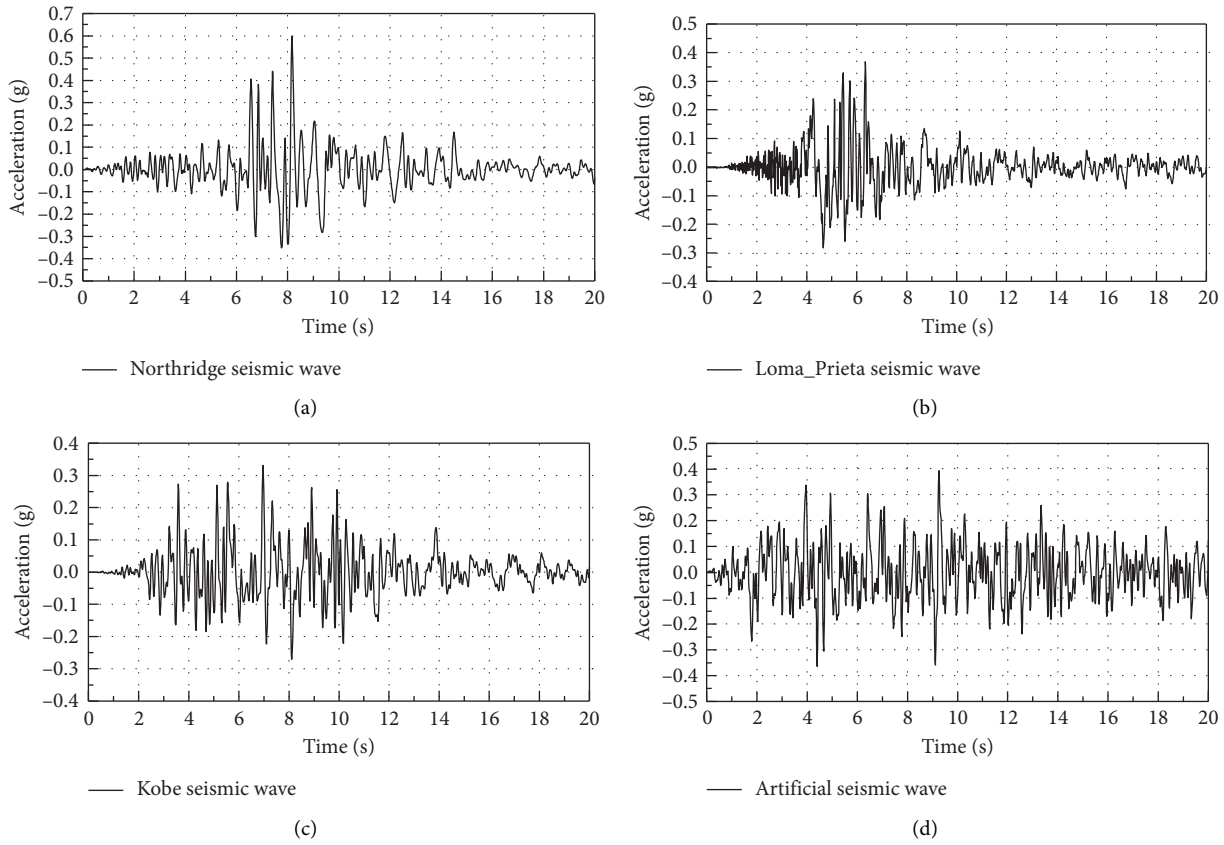

Figure 7: Acceleration records used in the filtered and corrected analysis. (a) Northridge seismic wave. (b) Loma seismic wave. (c) Kobe seismic wave. (d) Artificial seismic wave.

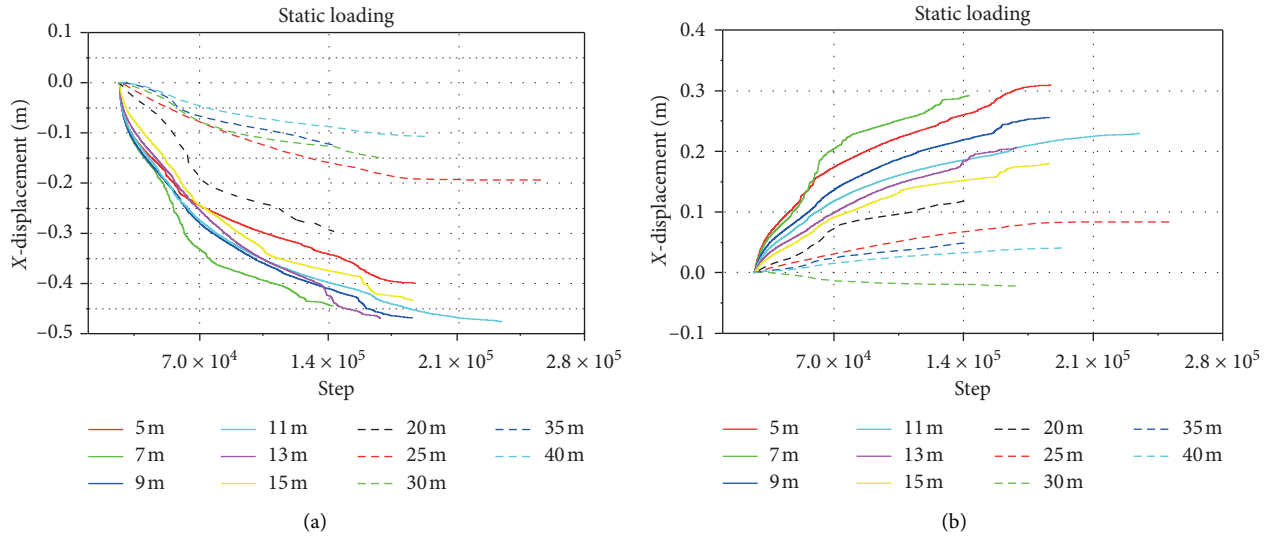

Figure 8: Continued.

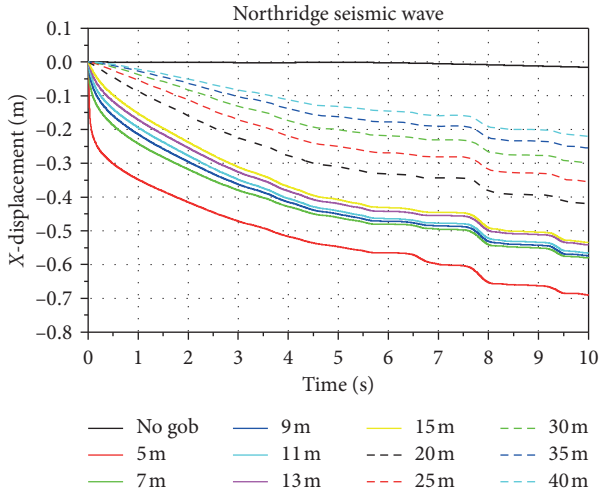

(c)

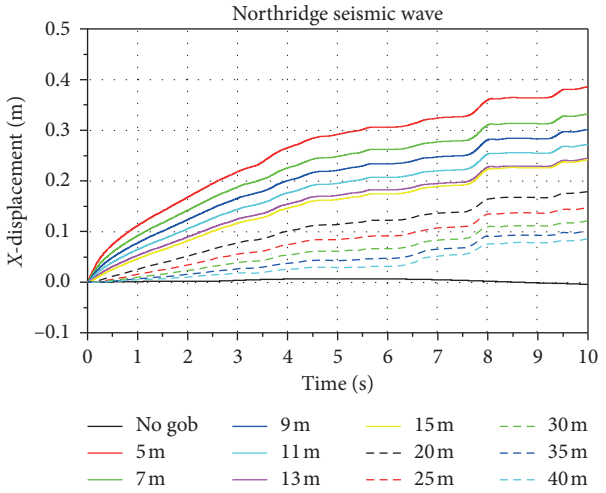

(d)

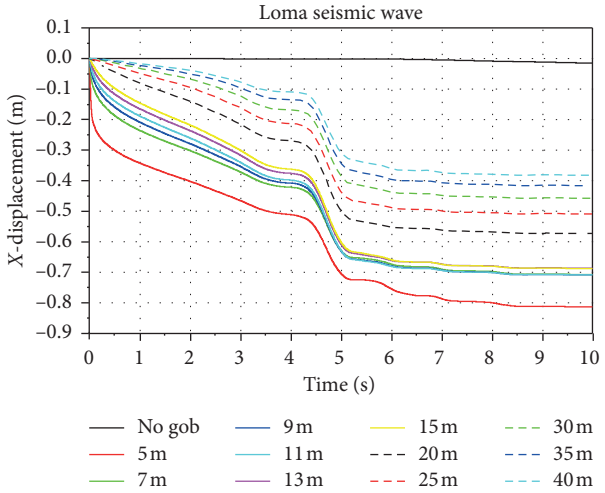

(e)

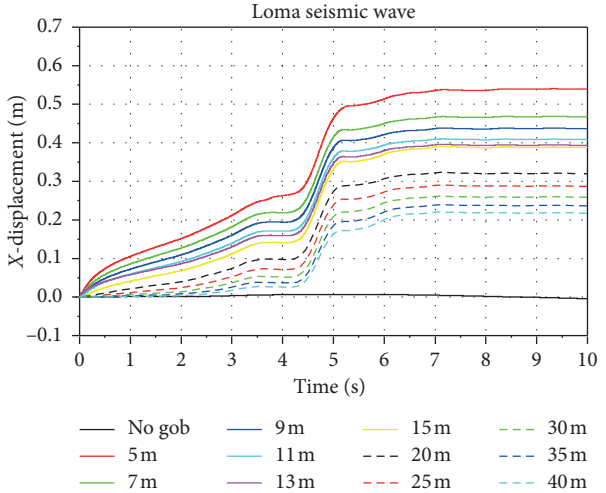

(f)

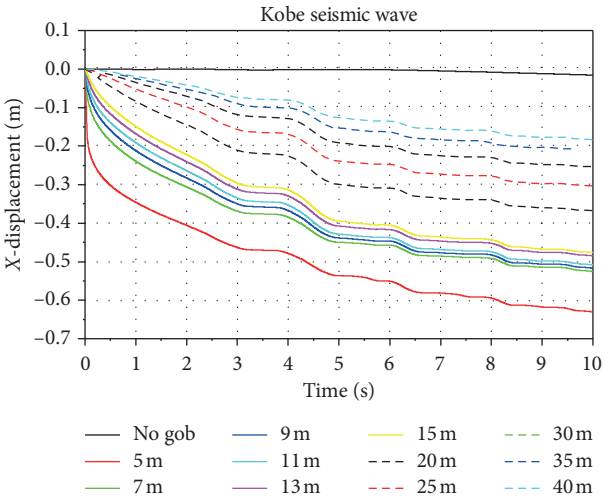

(g)

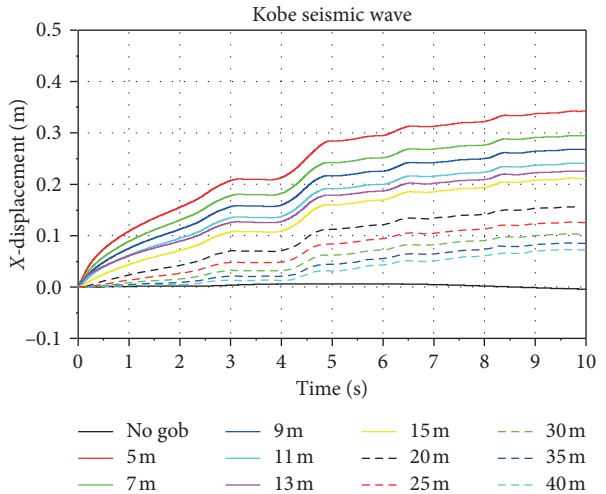

(h)

Figure 8: Continued.

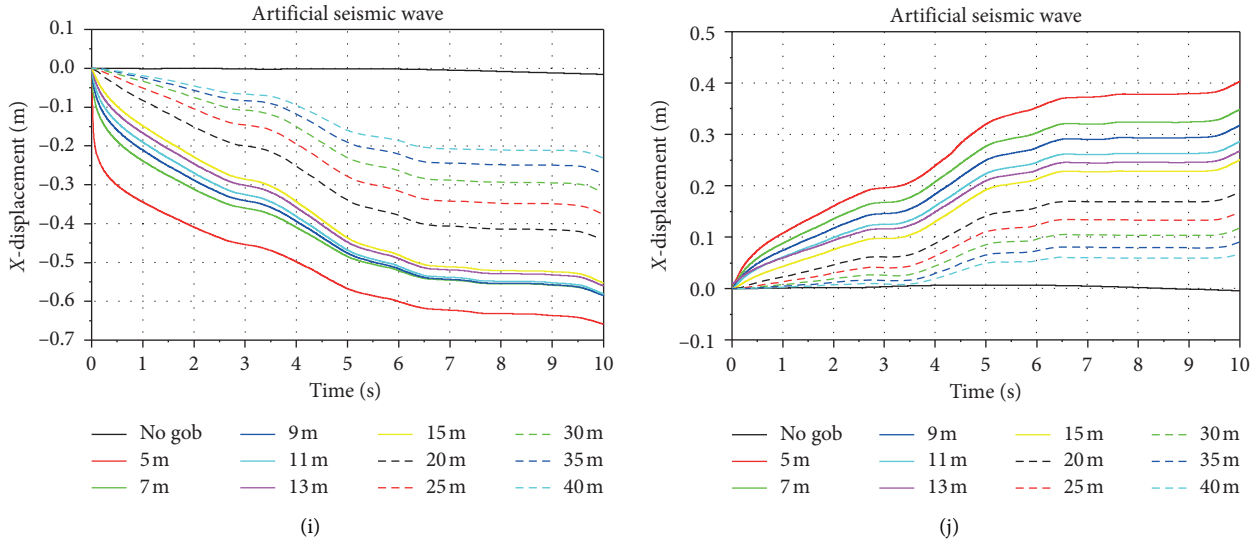

Figure 8: Horizontal displacement curve of monitoring points: (a, c, e, g, i) horizontal displacement of monitoring point 1, m, and (b, d, f, h, j) horizontal displacement of monitoring point 5, m.

displacement of the coal pillar side reaches 0.81 m at the width of 5 m, and the maximum displacement of the solid coal side reaches 0.54 m. The amount of continuous displacement continues to increase with the seismic motions. Therefore, setting the width of the coal pillar to 20 m or greater is appropriate for the risk of instability in accordance with the narrow coal pillar design in the adjacent goafs under the influence of frequent or sustained dynamic load.

4.2. Vertical Deformation. Figure 9 shows the vertical displacement change curve of monitoring points 3 and 7, which is the largest displacement change of all monitoring points:

(1) Figures 9(a) and 9(b) show the lane roof and floor displacement curves, respectively, under static load. The displacement of the roof under the static load is between 5 and 15 m coal pillar width, and the sinking volume is between 0.225 and 0.3 m. The effect of changing the coal pillar width within this width interval on the roof sinking is insignificant. The displacement of the floor under the static load is small in coal pillars with width of 5–40 m, and the total displacement of the floor is between −0.03 and 0.03 m. Therefore, the effect of static load on the displacement of the floor is less under such geological conditions.

(2) Figures 9(c)–9(j) show that the displacements of the roof of the roadway and the floor under the condition of four seismic waves are the displacement curves of the floor. Similarly, no gob is the displacement response of a single roadway under the influence of no goaf. The research shows that the displacement of the roof of the roadway not affected by the goafs is small, and the roadway is relatively safe. The displacement change of the roof is influenced by the displacement of the goafs, and the general change trend of displacement increases slowly as the seismic time progresses. The maximum displacement of the coal pillar is 5 m wide under the Northridge and the Loma seismic waves, and the maximum roof sinking volume is close to 0.4 m. At coal pillar width of 5–15 m, increasing the width of coal pillar only slightly reduces the amount of deformation. The displacement of the floor is accompanied by the continuous seismic movement, which shows a trend of fluctuation. The final displacement is smaller than the displacement of the roof, and the displacement of the floor is relatively safe for the stability of the roadway. Therefore, setting the width of the coal pillar to approximately 20 m or more under frequent or continuous dynamic conditions is reasonable in accordance with the displacement change of the top and the floors.

5. Stress Analysis

Figures 10 and 11 show the maximum main stress wave cloud diagrams of the roadway and coal pillars under the static load and Northridge seismic waves. More models of four seismic waves exist, and only the Northridge seismic wave is selected for comparative analysis because of space limitation. As shown in Figures 10 and 11, a low stress zone is formed around the roadway under static and dynamic conditions, and this result is due to the deformation of the excavated chamber to unload the pressure. These findings are similar to those of previous studies.

Under the static load, the stress concentration in coal pillars with width of 5 and 7 m is low. This case is conducive to the stability of the coal pillars. When the width is increased from 9 m to 20 m, the stress concentration in the coal pillar gradually increases. The stress value gradually increases from −10 MPa at 9 m coal column to −35 MPa when

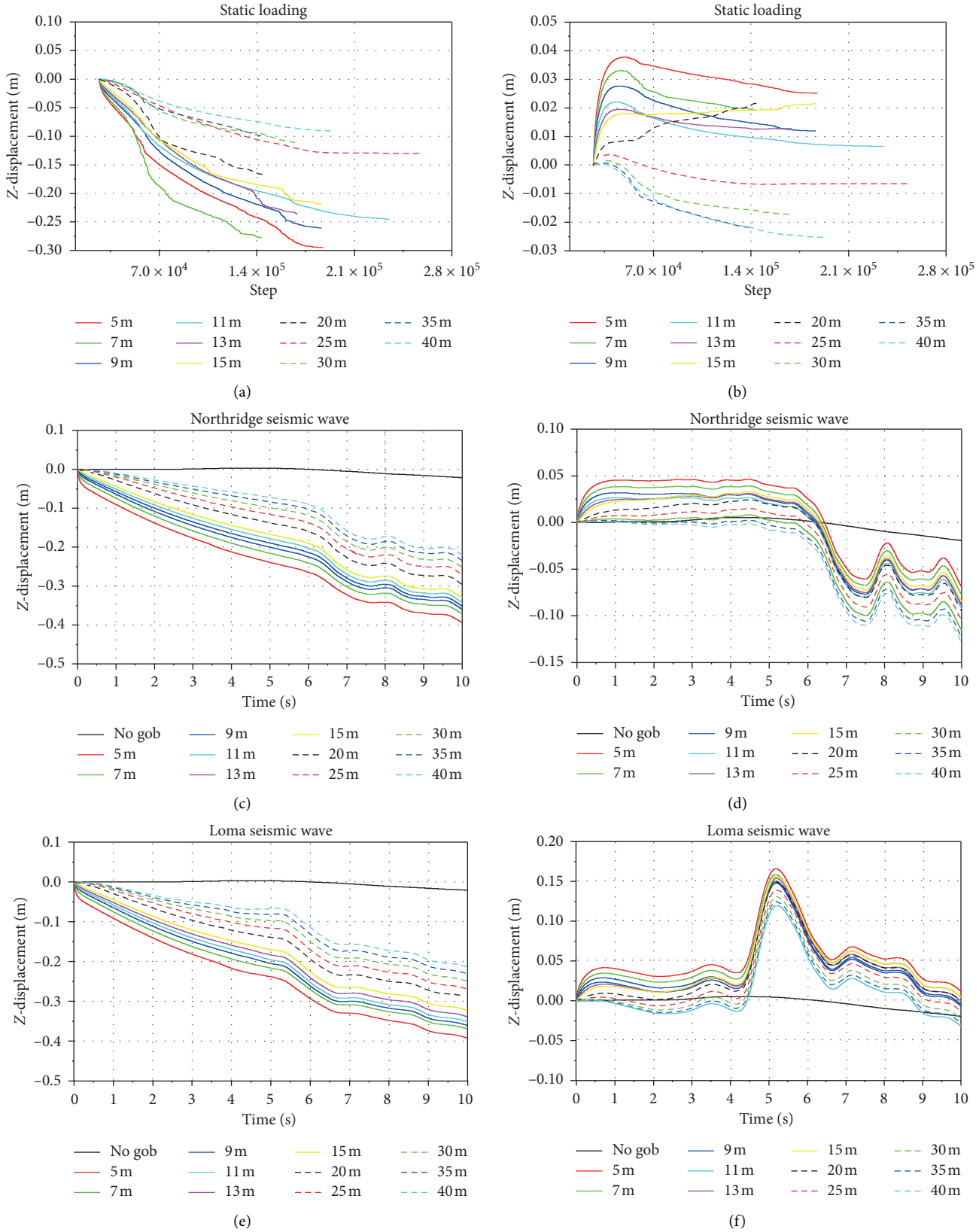

Figure 9: Continued.

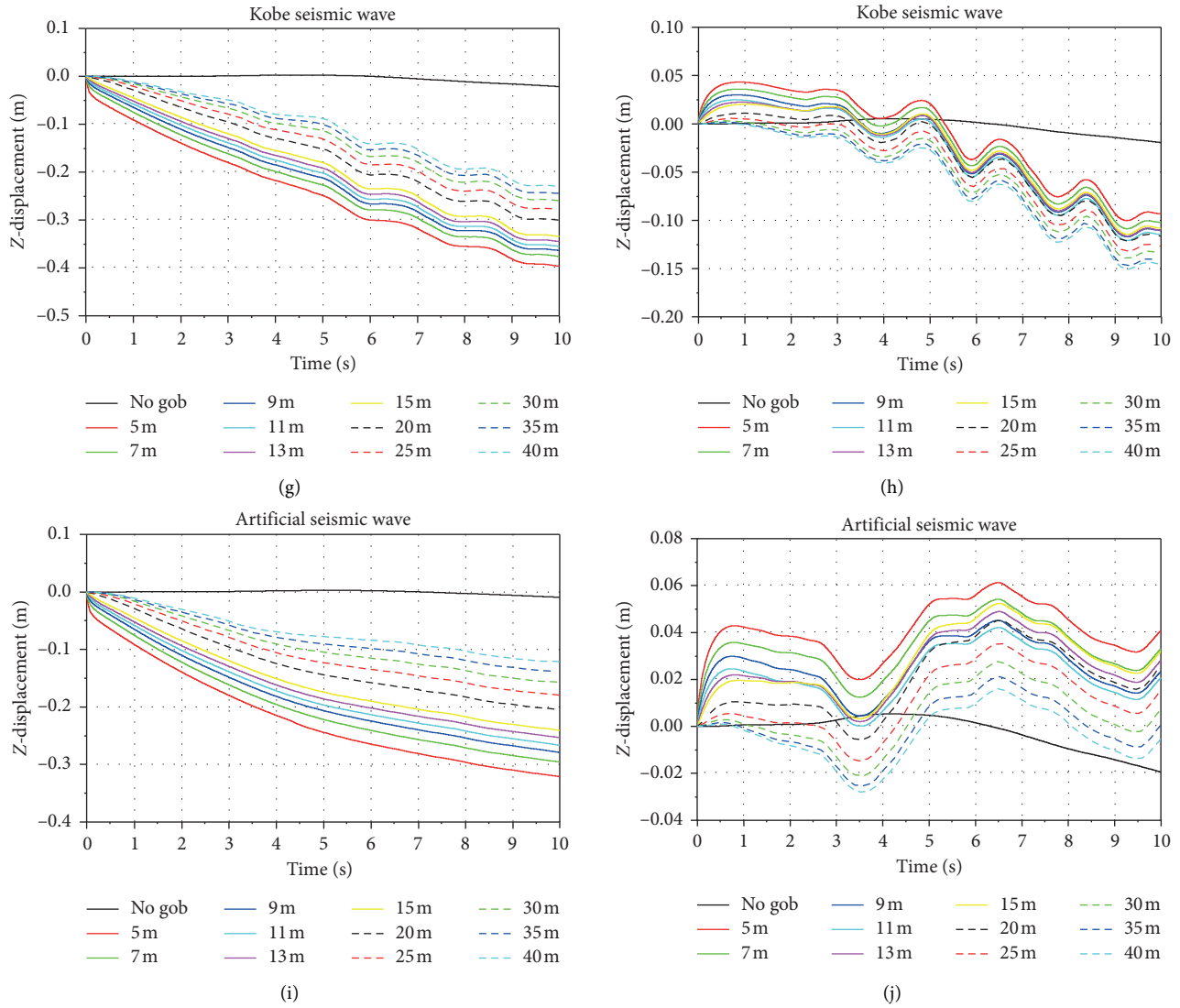

Figure 9: Vertical displacement curve of monitoring points: (a, c, e, g, i) vertical displacement of monitoring point 3, m, and (b, d, f, h, j) vertical displacement of monitoring point 7, m.

the width of the coal pillar is increased. The symbol here is opposite to the axis direction when the model is built; thus, this stress distribution is negative. In the range of 9–20 m, the high-stress areas formed on the sides of the goafs and the side of the roadway gradually converge, and this condition forms a stress core with a high value, which is extremely detrimental to the stability of the coal pillars, especially in the process of mining. No convergence occurs between the stress on the side of the roadway under the coal pillars with width of 20–40 m and the stress on the sides of the goafs due to the distance, which is beneficial to the stability of the coal pillars. However, the wide coal pillars reduce the rate of resource extraction especially for the scarce types of coal to improve the recovery rate. The use of narrow coal pillars entry protection is relatively economical.

Under the action of the Northridge seismic wave, the stress value of the whole model is lower than that of the static load. This condition indicates that the stress concentration in the coal pillars is not evident under the dynamic action. However, the stress concentration area of the whole coal pillars is still distributed on the solid coal side of the roadway and inside the coal pillars but may gradually spread to the top and the bottom. The high value of local stress is at most around 20 MPa, which is relatively safe for the stability of coal pillars. However, as mentioned earlier, the displacement of the coal pillar side of the roadway increases as the earthquake continues, and this condition may cause the risk of instability for coal pillars that are subject to continuous or frequent movement. Therefore, the narrow coal pillars cannot ensure the safety of the coal pillars and roadway under the dynamic action and should be increased to 20 m or more to ensure safety.

Figure 12 shows the vertical stress distribution within the coal pillars in the adjacent goafs under 5 and 20 m wide coal pillars and the action of the Loma seismic wave. The distances of *a*, *b*, *c*, and *d* to the goafs are 0.5, 1.5, 2.5, and 3.5 m,

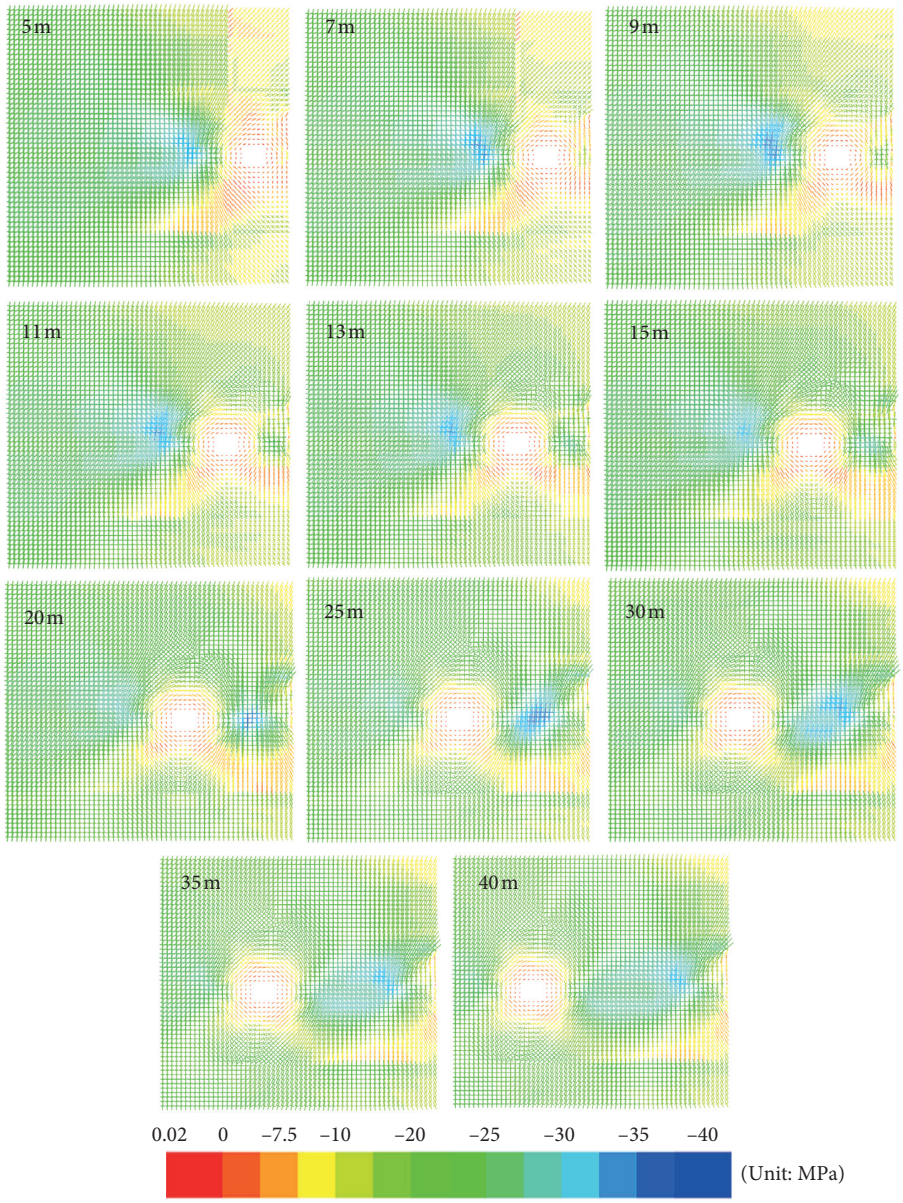

Figure 10: Cloud diagram of the maximum principal stress tensor of different coal pillar widths under the static load.

respectively. As shown in Figure 12, the vertical stress is higher than the vertical stress under 5 m wide coal pillars and is roughly distributed in the range of −25 MPa to −40 MPa. Under the 5 m wide coal pillar, the vertical stress in the coal pillars ranges from 10 MPa to −15 MPa. Given the plastic damage to the 5 m wide coal pillar, the overlying strata and roof can no longer be supported, and this condition shifts the stress. Figure 12 shows that the vertical stresses in the 5 and 20 m wide coal pillars are unevenly distributed in areas closer to the goaf. Evident unevenness is observed when the coal pillar is close to the goaf. With the increased distance from the goaf, the stress gradually becomes uniform, which indicates that the loose medium of the goaf causes uneven stress of the coal pillar in the close range from the goaf, and the influence of the position of the distance is gradually reduced.

6. Distribution Analysis of the Plastic Zone

Figures 13 and 14 show the distribution of plastic regions under the static load and Kobe seismic waves, respectively. The blue area represents the area where no plastic damage has occurred, the red area represents the area where shear damage has occurred, and the purple area represents the area where stretching and shearing damages have occurred. As shown in Figures 13 and 14, the plastic area under the static load occurs around the roadway, and the plastic area under dynamic action expands along the coal seam in the horizontal direction with a striped distribution.

Under the static load, the area of the plastic zone in the range of 5–15 m is insignificantly reduced, but the plastic area within the coal pillars always runs through the entire coal pillars with the widening of the coal pillars. Therefore,

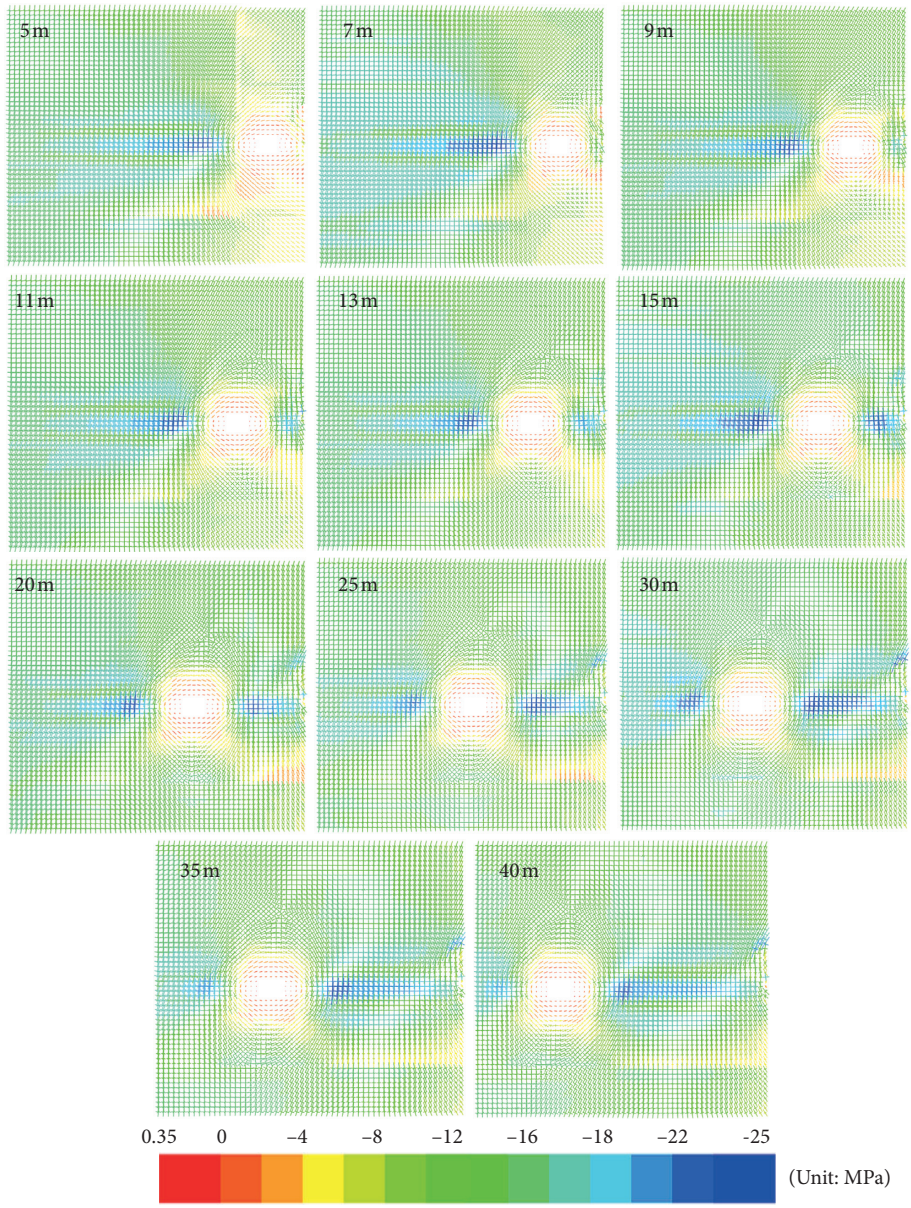

Figure 11: Cloud diagram of the maximum principal stress tensor of different coal pillar widths under the Northridge seismic wave.

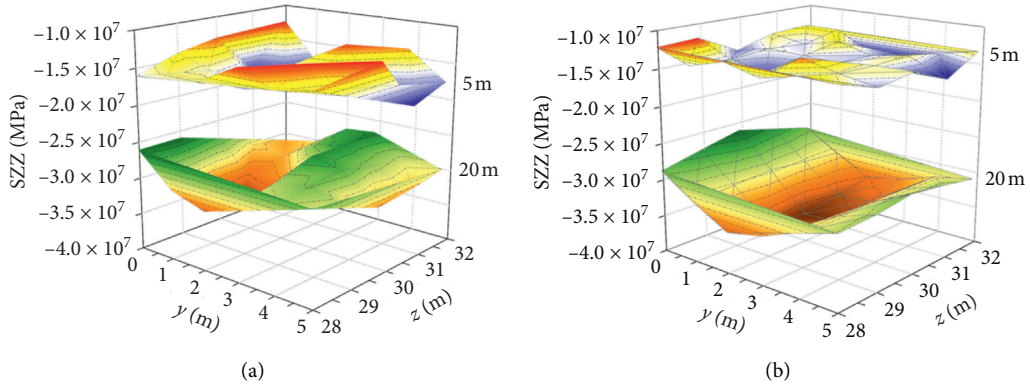

Figure 12: Continued.

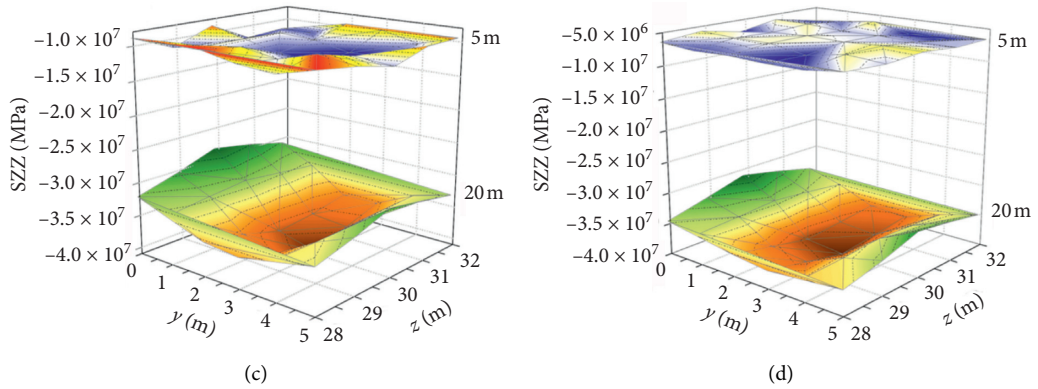

Figure 12: Cloud diagram of the comparison of the vertical stress under 5 and 20 m wide coal pillar under the Loma seismic wave: in (a), (b), (c), and (d), vertical section distances to the goafs are 0.5, 1.5, 2.5, and 3.5 m, respectively.

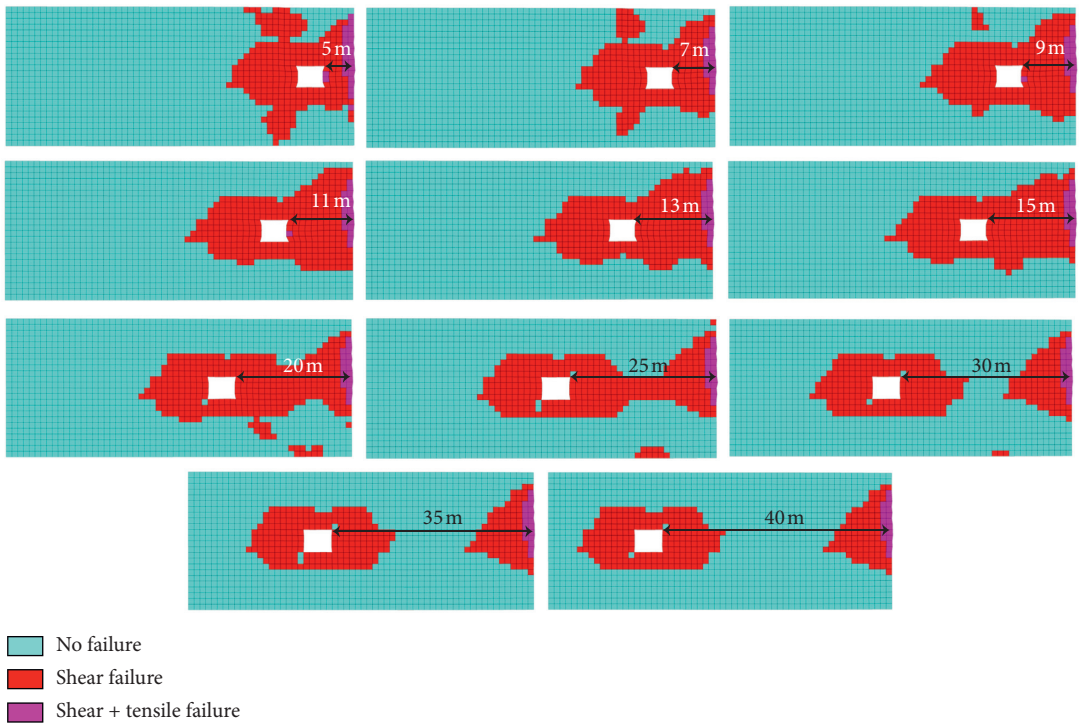

Figure 13: Distribution of roadways and coal pillar plastic zone under the static load.

increasing the width of the coal column from 5 m to 15 m does not reduce the plastic damage, which is affected by the goaf. When the width of the coal pillar increases to 20 m, the plastic area within the coal pillar is gradually reduced. For the coal mining, the coal pillar without plastic damage has higher carrying capacity than that with plastic damage and is relatively safe for coal mining. Wide coal pillars are often used for coal mining in the past.

The distribution of plastic areas under the influence of seismic waves in a single roadway not affected by the goaf is shown in the no gob of Figure 14. A certain range of shear plastic failure areas occur around the roadway, the range of which increases with the continuous occurrence of the earthquake. The distribution of plastic regions under the action of Kobe seismic waves is different from that of static load. With increased width of the coal pillar, the length of the plastic area does not decrease significantly. This finding implies that the plastic area expands with the low strength of the coal seam with the continuous seismic movement, whereas the coal column, which plays a supporting role, completely causes plastic damage. As mentioned earlier, the amount of deformation of the coal pillar where plastic damage occurs gradually increases as the earthquake continues. After the plastic damage occurs, the carrying capacity of the coal pillar is greatly reduced. At this point, the risk can only be reduced by increasing the width of the coal pillar or by strengthening the support of the coal pillar. The coal pillars under the frequent or the continuous

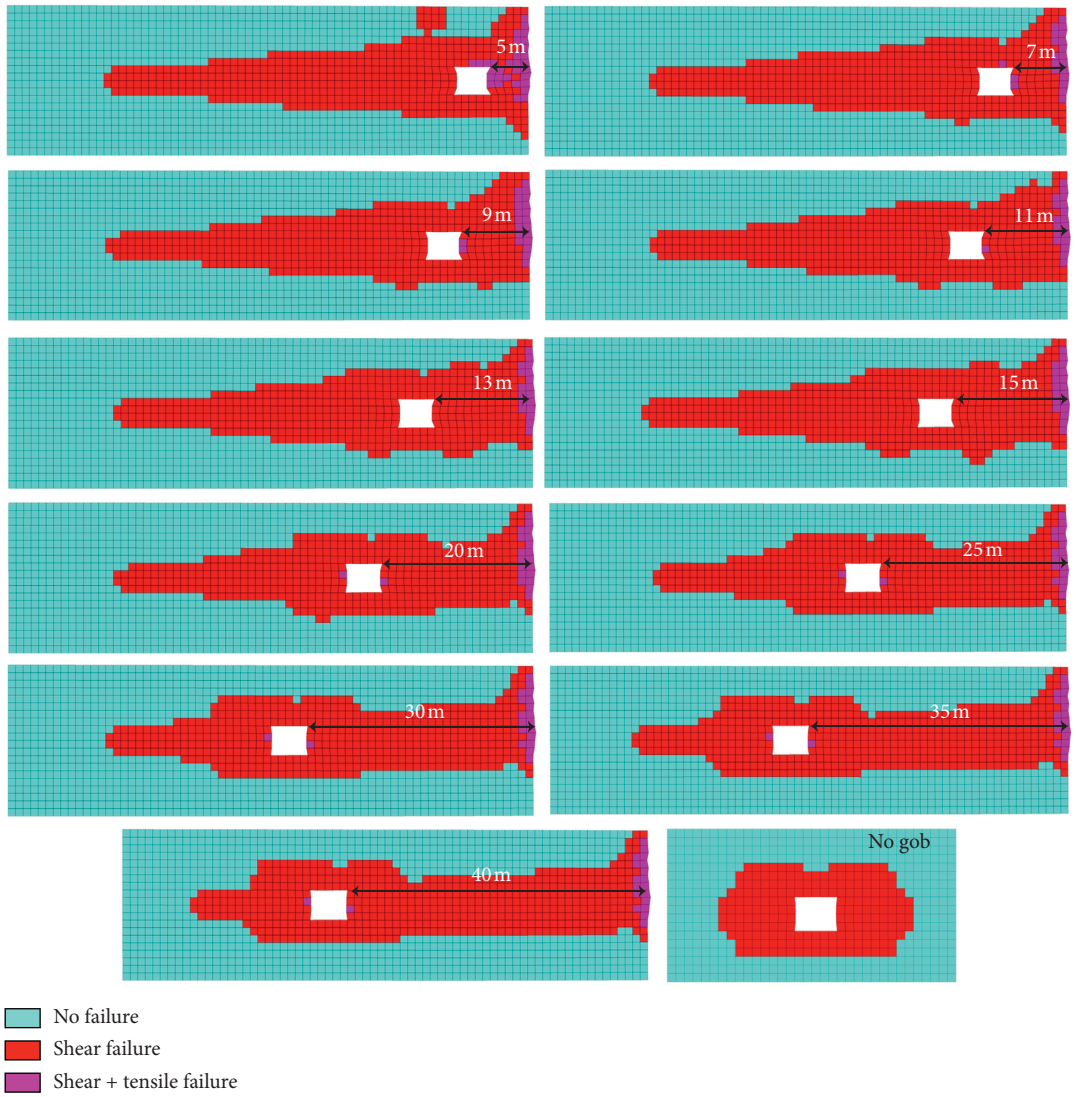

Figure 14: Distribution of roadways and the coal pillar plastic zone under the Kobe seismic wave.

dynamic action have a large area of plastic damage. At this time, the width of the coal pillar should be increased to ensure safety.

7. Conclusions

The seismic response analysis of coal pillars and roadways of adjacent goafs was conducted using the numerical method by utilizing the return airway of the 7435 working face in the Kongzhuang Coal Mine as a case study. The goaf was established using a different bulk model from the past, which was more in line with the actual situation of coal mining. Under the FEM and the DEM, the seismic response analysis was performed on coal pillars and roadways under different coal pillar widths and four seismic waves. This numerical method can be used to determine the width of coal pillars in gob-side entry driving.

The results show that the effect of the bulk medium on the surrounding continuous medium was simply verified because of the effect of the dispersal contact stress, which led to the nonuniform distribution of stress with the continuous medium part of the bulk body and was confirmed in subsequent calculations. For coal pillars and roadways in adjacent goafs that were subject to frequent or sustained dynamic load, a great difference between the static load and a single roadway not affected by the goaf was observed. The deformation of coal pillars and roadways increased with the continuous dynamic load. Narrow coal pillars showed this characteristic, and this trend was reflected in the coal pillar deformation. The stress concentration in the coal pillar tended to weaken compared with the static load with the continuous earthquake motion, and the high-stress area gradually spread to the top and the floors of the coal pillar. The range of plastic areas in roadways and coal pillars gradually expanded along the direction of weak coal seams as the earthquake motion continued. For the coal pillars and roadways in the adjacent goafs that were subject to frequent or sustained dynamic loads, the width of the coal pillar was increased to ensure the stability of roadways and coal pillars, and the width of the coal pillar should be calculated and determined according to the geological background and site.

Data Availability

All data, models, or code generated or used during the study are available in a repository or online in accordance with funder data retention policies.

Conflicts of Interest

The authors declare that they have no conflicts of interest.

Acknowledgments

This research was funded by the National Natural Science Foundation of China (nos. 11872300 and 11572244), Natural Science Foundation of Shaanxi Province of China (2021JQ-463 and 2021JZ-47), and the Youth Innovation Team of Shaanxi Universities.

References

[1] S. Tanimura, K. Mimura, T. Nonaka, and W. Zhu, "Dynamic failure of structures due to the great Hanshin-Awaji earthquake," *International Journal of Impact Engineering*, vol. 24, no. 6-7, pp. 583–596, 2000.

[2] W. L. Wang, T. T. Wang, J. J. Su, C. H. Lin, C. R. Seng, and T. H. Huang, "Assessment of damage in mountain tunnels due to the Taiwan Chi-Chi earthquake," *Tunnelling And Underground Space Technology*, vol. 16, no. 3, pp. 133–150, 2001.

[3] Z. Wang, B. Gao, Y. Jiang, and S. Yuan, "Investigation and assessment on mountain tunnels and geotechnical damage after the Wenchuan earthquake," *Science in China Series E: Technological Sciences*, vol. 52, no. 2, pp. 546–558, 2009.

[4] S. M. Hsiung, W. Blake, A. H. Chowdhury, and T. J. Williams, "Effects of mining-induced seismic events on a deep underground mine," *Pure and Applied Geophysics*, vol. 139, no. 3, pp. 741–762, 1992.

[5] W. Kuhnt, P. Knoll, H. Grosser, and H.-J. Behrens, "Seismological models for mining-induced seismic events," *Seismicity in Mines*, vol. 129, no. 3, pp. 513–521, 1989.

[6] J. A. Vallejos and S. D. McKinnon, "Correlations between mining and seismicity for re-entry protocol development," *International Journal of Rock Mechanics and Mining Sciences*, vol. 48, no. 4, pp. 616–625, 2011.

[7] W. Cai, L. Dou, G. Si, and Y. Hu, "Fault-induced coal burst mechanism under mining-induced static and dynamic stresses," *Engineering*, 2020.

[8] S. J. Gibowicz, "Seismicity induced by mining: recent research," *Advances in Geophysics*, vol. 51, pp. 1–53, 2009.

[9] J.-Q. Kang, J.-B. Zhu, and J. Zhao, "A review of mechanisms of induced earthquakes: from a view of rock mechanics," *Geomechanics and Geophysics for Geo-Energy and Geo-Resources*, vol. 5, no. 2, pp. 171–196, 2019.

[10] Coal Mines Planning and Design Institute, "The damage Kailuan coal mine roadway project in Tangshan earthquake," *Seismic Engineering and Engineering Vibration*, no. 1, pp. 67–76, 1982.

[11] Y. Zeng, "Viscoelastic stress-triggering of the 1999 hector mine earthquake by the 1992 landers earthquake," *Geophysical Research Letters*, vol. 28, no. 15, pp. 3007–3010, 2001.

[12] T. Li, M. F. Cai, and M. Cai, "A review of mining-induced seismicity in China," *International Journal of Rock Mechanics and Mining Sciences*, vol. 44, no. 8, pp. 1149–1171, 2007.

[13] W. Yu, B. Pan, F. Zhang, S. Yao, and F. Liu, "Deformation characteristics and determination of optimum supporting time of alteration rock mass in deep mine," *KSCE Journal of Civil Engineering*, vol. 23, no. 11, pp. 4921–4932, 2019.

[14] Y. Li, Y. Yang, and B. Jiang, "Prediction of coal and gas outbursts by a novel model based on multisource information fusion," *Energy Exploration & Exploitation*, vol. 38, no. 5, pp. 1320–1348, 2020.

[15] P. Konicek and P. Waclawik, "Stress changes and seismicity monitoring of hard coal longwall mining in high rockburst risk areas," *Tunnelling and Underground Space Technology*, vol. 81, pp. 237–251, 2018.

[16] M. V. Kurlenya, M. N. Tsupov, and A. V. Savchenko, "Influence of the bachatsky earthquake on methane emission in roadways in coal mines," *Journal of Mining Science*, vol. 55, no. 5, pp. 695–700, 2019.

[17] P. Konicek and J. Schreiber, "Heavy rockbursts due to longwall mining near protective pillars: a case study," *International Journal of Mining Science and Technology*, vol. 28, no. 5, pp. 799–805, 2018.

[18] C. Srinivasan, S. K. Arora, and R. K. Yaji, "Use of mining and seismological parameters as premonitors of rockbursts," *International Journal of Rock Mechanics and Mining Sciences*, vol. 34, no. 6, pp. 1001–1008, 1997.

[19] T.-H. Ma, C.-A. Tang, S.-B. Tang et al., "Rockburst mechanism and prediction based on microseismic monitoring," *International Journal of Rock Mechanics and Mining Sciences*, vol. 110, pp. 177–188, 2018.

[20] X.-S. He, S.-Y. Li, K. Pan et al., "Mining seismicity, gas outburst and the significance of their relationship in the study of physics of earthquake source," *Acta Seismologica Sinica*, vol. 20, no. 3, pp. 332–347, 2007.

[21] J. Wang, J. Jiang, G. Li, and H. Hu, "Exploration and numerical analysis of failure characteristic of coal pillar under great mining height longwall influence," *Geotechnical and Geological Engineering*, vol. 34, no. 2, pp. 689–702, 2016.

[22] X. Li, Y. Zhao, W. He, L. Li, and F. He, "Study on coal pillar width and surrounding rock control of gob-side entry in extra-thick coal seam," *Geotechnical and Geological Engineering*, vol. 38, no. 6, pp. 6855–6868, 2020.

[23] Y. Zhang, Z. Wan, F. Li et al., "Stability of coal pillar in gob-side entry driving under unstable overlying strata and its coupling support control technique," *International Journal of Mining Science and Technology*, vol. 23, no. 2, pp. 193–199, 2013.

[24] J. Yang, S. Cao, and X. Li, "Failure laws of narrow pillar and asymmetric control technique of gob-side entry driving in island coal face," *International Journal of Mining Science and Technology*, vol. 23, no. 2, pp. 267–272, 2013.

[25] N. Zhang, X. Li, and J. Zhou, "Supporting of gob-side entries driving head-on adjacent advancing coal face with a reserved narrow pillar," *Mining Science and Technology*, CRC Press, Boca Raton, FL, USA, 2004.

[26] Y. Xu, H. Li, G. Guo, and X. Liu, "Stability analysis of hyperbolic coal pillars with peeling and high temperature effects," *Energy Exploration & Exploitation*, vol. 38, no. 5, pp. 1574–1588, 2020.

[27] J. Liu, C. Liu, and X. Li, "Determination of fracture location of double-sided directional fracturing pressure relief for hard roof of large upper goaf-side coal pillars," *Energy Exploration & Exploitation*, vol. 38, no. 1, pp. 111–136, 2020.

[28] G.-L. Feng, X.-T. Feng, B.-R. Chen, Y.-X. Xiao, and Y. Yu, "A microseismic method for dynamic warning of rockburst

development processes in tunnels," *Rock Mechanics and Rock Engineering*, vol. 48, no. 5, pp. 2061–2076, 2015.

[29] G.-I. Feng, B.-R. Chen, Q. Jiang, Y.-X. Xiao, W.-J. Niu, and P.-X. Li, "Excavation-induced microseismicity and rockburst occurrence: similarities and differences between deep parallel tunnels with alternating soft-hard strata," *Journal of Central South University*, vol. 28, no. 2, pp. 582–594, 2021.

[30] G.-L. Feng, S.-T. Feng, Y.-X. Xiao et al., "Characteristic microseismicity during the development process of intermittent rockburst in a deep railway tunnel," *International Journal of Rock Mechanics And Mining Sciences*, vol. 124, 2019.

[31] X. Li and Y. Chai, "Determination of pillar width to improve mining safety in a deep burst-prone coal mine," *Safety Science*, vol. 113, pp. 244–256, 2019.

[32] Y. Zhao, H. Wang, S. Liu, Z. Mu, and Z. Lu, "Dynamic failure risk of coal pillar formed by irregular shape longwall face: a case study," *International Journal of Mining Science and Technology*, vol. 28, no. 5, pp. 775–781, 2018.

[33] S.-L. Wang, S.-P. Hao, Y. Chen, J.-B. Bai, X.-Y. Wang, and Y. Xu, "Numerical investigation of coal pillar failure under simultaneous static and dynamic loading," *International Journal of Rock Mechanics and Mining Sciences*, vol. 84, pp. 59–68, 2016.

[34] T. Wang, C. Yang, X. Yan et al., "Dynamic response of underground gas storage salt cavern under seismic loads," *Tunnelling and Underground Space Technology*, vol. 43, pp. 241–252, 2014.

[35] W. Yu and K. Li, "Deformation mechanism and control technology of surrounding rock in the deep-buried large-span chamber," *Geofluids*, vol. 2020, Article ID 8881319, 22 pages, 2020.

[36] W. Yu, W. Yu, G. Wu, B. An, and P. Wang, "Experimental study on the brittle-ductile response of a heterogeneous soft coal rock mass under multifactor coupling," *Geofluids*, vol. 2019, Article ID 5316149, 15 pages, 2019.

[37] T. Han, J. Shi, and X. Cao, "Fracturing and damage to sandstone under coupling effects of chemical corrosion and freeze-thaw cycles," *Rock Mechanics and Rock Engineering*, vol. 49, no. 11, pp. 4245–4255, 2016.

[38] B. Xia, J. Jia, B. Yu, X. Zhang, and X. Li, "Coupling effects of coal pillars of thick coal seams in large-space stopes and hard stratum on mine pressure," *International Journal of Mining Science and Technology*, vol. 27, no. 6, pp. 965–972, 2017.

[39] Q. Bai, S. Tu, F. Wang, and C. Zhang, "Field and numerical investigations of gateroad system failure induced by hard roofs in a longwall top coal caving face," *International Journal of Coal Geology*, vol. 173, pp. 176–199, 2017.

[40] L. Jiang, P. Zhang, L. Chen et al., "Numerical approach for goaf-side entry layout and yield pillar design in fractured ground conditions," *Rock Mechanics and Rock Engineering*, vol. 50, no. 11, pp. 3049–3071, 2017.

[41] Q. Sun and D. Dias, "Significance of Rayleigh damping in nonlinear numerical seismic analysis of tunnels," *Soil Dynamics and Earthquake Engineering*, vol. 115, pp. 489–494, 2018.

[42] J. M. Mayoral and F. A. Flores, "Effects of soil cracking on the seismic response of soil-structure systems," *Soil Dynamics and Earthquake Engineering*, vol. 30, no. 6, pp. 509–523, 2010.

[43] J. M. Mayoral, S. Tepalcapa, A. Roman-de la Sancha, C. S. El Mohtar, and R. Rivas, "Ground subsidence and its implication on building seismic performance," *Soil Dynamics and Earthquake Engineering*, vol. 126, Article ID 105766, 2019.

[44] M. Wang, "Simulation of compression test on gangue by PFC3D," *Chinese Journal of Rock Mechanics and Engineering*, vol. 32, pp. 1351–1357, 2013.

[45] M. Bai, F. S. Kendorski, and D. J. Van Roosendaal, *Chinese and North American High-Extraction Underground Coal Mining Strata Behavior and Water Protection Experience and Guidelines*, West Virginia University, Morgantown, WV, USA, 1995.

[46] Pacific Earthquake Engineering Research Center, http://peer.berkeley.edu/peer_ground_motion_database/.

[47] Earthquake Software for Signal Processing of Strong-Motion Data, http://www.seismosoft.com.

Hindawi
Advances in Civil Engineering
Volume 2021, Article ID 5533828, 13 pages
https://doi.org/10.1155/2021/5533828

Research Article

The Method of Determining Excavation Damaged Zone by Acoustic Test and the Application in Engineering Cases

Qian-Cheng Sun,[1,2] **Hao-Sen Guo**,[1,3] **Zhi-Hua Xu**,[1] **Yue Liu**,[1] **and Xiao Xu**[1]

[1]*Key Laboratory of Geological Hazards on Three Gorges Reservoir Area (China Three Gorges University), Ministry of Education, Yichang 443002, China*
[2]*State Key Laboratory of Geomechanics and Geotechnical Engineering, Institute of Rock and Soil Mechanics, Chinese Academy of Sciences, Wuhan, Hubei 430071, China*
[3]*East China Jiaotong University, Nanchang 330000, China*

Correspondence should be addressed to Hao-Sen Guo; 3048@ecjtu.edu.cn and Zhi-Hua Xu; zhihuabest@163.com

Received 24 January 2021; Accepted 27 April 2021; Published 29 May 2021

Academic Editor: Robert Černý

It is very important to accurately determine the depth of excavation damaged zone for underground engineering excavation and surrounding rock stability evaluation, and it can be measured by acoustic test, but there is no quantitative method for analysis of the results, and it relies heavily on the experience of engineers, which leads to the low reliability of the results and also limits the application of the acoustic method. According to substantial field test data and the feedback of surrounding rock support parameters, the boundary method is proposed to determine the depth of excavation damaged zone in surrounding rock based on the relation between the ultrasonic velocity of measured point and the background wave velocity of rock mass. When the method is applied to the columnar jointed rock mass of Baihetan and the deep-buried hard rock of Jinping, the excavation damaged zone was well judged. The results in the Baihetan project show that the proposed method of determining excavation damage zone by the acoustic test can well demonstrate the anisotropy characteristics of the columnar jointed rock mass, and the damage evolution characteristics of jointed rock mass at the same position can also be obtained accurately. Moreover, the method also can accurately reveal the damage evolution process of the deep-buried hard rock under the condition of high ground stress, which proved the applicability of this method in jointed or nonjointed rock masses.

1. Introduction

With the intensification of energy utilization activities such as mining, geothermal development, and hydropower station construction, the stability of rock engineering is a common challenge faced by engineers and researchers. As early as the 1970s, foreign scholars as Kelsall put forward the importance of excavation damaged zone (EDZ) in construction of underground caverns [1]. Scholars have also studied the relationship between the depth of excavation damaged zone and its influencing factors, such as the buried depth, the section shape of caverns, the excavation and blasting method, the initial stress state, the mechanical properties of the rock mass, and the supporting state of the surrounding rock [2–6]. The depth of EDZ and damage degree of surrounding rock are the basis of support parameter design and can play an early warning role in engineering disasters such as rock burst and spalling [7, 8]. Therefore, it is very important to accurately determine the depth of EDZ for underground engineering excavation and surrounding rock stability evaluation.

Although many scholars have obtained the theoretical calculation formula of excavation damaged zone depth according to the results of field test and indoor test, it has great limitations due to the influence of complex engineering factors in the application [9, 10]. The field measured EDZ depth does not make any theoretical assumptions, and the test results can be more widely accepted. Generally, GPR method [11], seismic wave, multipoint displacement meter [12], and microseism and

acoustic emission [13] are used to detect the depth of fracture zone in surrounding rock. However, these methods are complicated, costly, and difficult to conduct.

Generally, the excavation damaged zone consists of two parts. The observed interconnected macrofractures are referred to as the highly damaged zone, and the minor damaged zone is partially connected to isolated damage and is even invisible [14]. It is essential, for construction safety, to determine the depth of excavation damaged zone in rock masses around a tunnel. As a new testing method, drilling test technologies, including acoustic testing, digital borehole televiewers, are now widely used in field testing. During such tests, a borehole in local zones of rock masses is used to deduce changes in the internal properties of rock masses by analysing the test indexes of internal rock masses far from the free face. For example, by applying panoramic digital borehole televiewers, Li et al. [15] investigated the evolution of the EDZ in rock masses in deeply buried tunnels at the Jinping II Hydropower Station (Sichuan Province, China) during construction using tunnel boring machines (TBMs). On this basis, the changing characteristics of new cracks, primary fractures, and lithology during the excavation and support process of surrounding rocks were revealed. Moreover, by using testing technologies including acoustic wave technology over holes and sliding micrometers, the deformation conditions and rockburst risk, when excavating deeply buried parallel cavities in Jinping II Hydropower Station, were explored. Moreover, the formation and evolution mechanism of rockbursts were also discussed [16]. By applying acoustic testing technology, Martino and Chandler [17] evaluated the scope of EDZ in rocks surrounding deeply buried underground cavities. Guo et al. [18] explored the fracturing and evolutionary characteristics of EDZ in rocks surrounding Jinping's underground laboratory under the effect of excavation by employing DBT. By utilising the borehole testing method, a new understanding of the changes to the interior of rock masses during engineering activities can be obtained. Scholars have made a lot of meaningful exploration on the EDZ depth test by using acoustic testing method, but the current research results do not provide a clear judgment method based on the results of acoustic test. When the acoustic test is used in the field to determine the depth of excavation damage zone, it almost depends on the experience judgment of engineers, which leads to the low reliability of the results.

In order to increase the operability of the acoustic testing method in the field and improve the reliability of the EDZ test results, the boundary method, based on a large number of field measured data and the feedback of surrounding rock support parameters, is proposed to determine the depth of EDZ in surrounding rock, and the applicability of the proposed method is verified by comparing with the digital borehole televiewers test results.

2. Method of Determining the Depth of EDZ by Acoustic Testing

2.1. Introduction to Acoustic Testing. Acoustic testing is to excite the ultrasonic wave to propagate in the rock mass medium, and the propagation speed of the wave depends on the integrity of the rock mass. The wave velocity of intact rock mass is generally high, but it decreases relatively in the loose zone where the stress drops and the fracture expands. Therefore, there is an obvious change of wave velocity in rock mass with different damage degree. In highly damaged zone, there are visible cracks in the rock mass, which can be obtained by borehole television test. In minor damaged zones, although there are no visible fissures, the propagation of sonic wave velocity in this area still drops significantly compared with that of the original rock mass. Moreover, there is obvious uncertainty in the excavation disturbed zone, part of which becomes the original rock zone as the elastic deformation recovers, while the other part of rock mass produces damage during stress dissipation (a crest in the curve due to stress adjustment) and becomes part of the excavation damaged zone (minor or highly damaged zone). The curve of wave velocity at different lengths of drilling from the surface of surrounding rock can be obtained by using the propagation characteristics of ultrasonic wave, and then the EDZ depth of surrounding rock can be inferred according to the variation curve (V-L curve) and relevant geological data (Figure 1).

The principle of acoustic testing is that the signal of transmitting transducer propagates in rock mass, and the time difference between two receiving transducers is used to estimate the propagation velocity of ultrasonic wave in rock mass. At present, the commonly used acoustic testing methods are single borehole acoustic test and cross hole acoustic test. The single borehole acoustic test method refers to measuring of the wave velocity of surrounding rock in a borehole by moving the transducers synchronously and sequentially. Most of the single hole acoustic testing equipment is a double-band acoustic transducer, which mainly consists of one transmitting transducer and two receiving transducers, as shown in Figure 2(a). The cross hole acoustic test method means that the receiving and transmitting transducers are respectively arranged in two measuring holes, and the receiving and transmitting transducers have the same initial depth and move synchronously with the same spacing to measure the wave velocity of rock strata or surrounding rock between the two holes, as shown in Figure 2(b).

For the single hole acoustic test method, the transmitter can be placed near or far away from the orifice according to the test environment. When testing the EDZ depth of surrounding rock, it is suggested that the transducer close to the orifice can be set as the receiving transducer. The measured wave velocity is the average wave velocity of rock mass between two receiving transducers. When drawing the V-L curve, the position of the wave velocity is the drilling length corresponding to the middle position of the two transducers. The distance between measuring points depends entirely on the moving distance of the testing equipment. Table 1 demonstrates four typical V-L curves according to the results of practical engineering test.

The initial wave velocity of type (a) is low and gradually increases with the borehole length and then tends to be stable, which indicates that the rock mass near the orifice causes plastic failure. The damage degree decreases with the increase of borehole length, and the integrity of the original

rock section is good. The characteristics of type (b) are that the wave velocity near the borehole opening is relatively low. With the increase of length, the wave velocity at a certain position will even exceed that of the original rock section then decrease and then tend to be stable. In this kind of rock mass, the fracture is serious at the borehole position, and there is local stress concentration. The stress is relatively balanced with the increase of borehole length and the wave velocity is stable in the undisturbed original rock section. The characteristics of type (c) are that with the increase of borehole depth, multiple wave peaks appear on the curve, and the rock mass in this region is in the stress adjustment stage. After the adjustment, the rock mass is fractured, leading to a decrease in wave velocity. The wave velocity at local position, where the stress has not dissipated well, is still relatively high, and the rock mass in the undisturbed area gradually tends to be stable with the increase of length. The wave velocity of type (d) curve basically does not change with the change of borehole length, which indicates that the rock mass falls off directly after cracking, and there is no obvious damage area in the surrounding rock, and it can be considered that the surrounding rock in the test area has no plastic failure, and this type of curve is very rare in practical engineering.

2.2. Drilling Layout and Monitoring Frequency. The most intuitive way to determine the damage area by in situ testing is to conduct the test in predrilled hole before the tunnel excavation. The borehole should be arranged in the corresponding position where excavation damage is likely to occur. A large number of engineering practices and studies show that most of the cavity failure occurs at a small angle or approximately parallel to the direction of the maximum principal stress. For large deep caverns, with the occurrence of new cracks or original cracks opening in the excavation of caverns, the layout of boreholes should also be adjusted according to the excavation of caverns.

The layout of boreholes for acoustic testing needs to take equipment requirements into account. The outside diameter of the acoustic transducer is small, and the test process needs to ensure sufficient coupling between the probe and the rock mass, so the aperture of the test hole should not be too large. A test borehole diameter that is too small will affect the continuous testing process of the probe in the borehole and further affect the accurate acquisition of test data. Generally, the test borehole diameter should not be less than 60 mm. The borehole shall be kept within the range of 1~5° downward inclinations for manual operation, and the borehole axis shall be perpendicular to the section of the test sidewall. On the other hand, when using the cross hole acoustic test method, the two holes should have good parallelism. The test hole spacing should be determined according to the resolution of the instrument and the excitation energy and ensure that the ultrasonic signal can be well received, and the hole inclination measurement and hole spacing correction should be carried out before the test.

All kinds of auxiliary small tunnels (such as anchoring holes and drainage corridors) are often distributed around large caverns. Therefore, the layout of the test hole can choose preset hole or temporary hole. Preset hole means that the auxiliary tunnel can be used to set observation holes before the excavation of the test area (Figure 3 ①), and the whole process of surrounding rock damage evolution before and after excavation can be observed. Temporary hole refers to drilling from the excavated area (Figure 3 ②). In this way, the damage evolution process of surrounding rock after excavation and unloading can be tested.

The main purpose of EDZ testing is to monitor the extent of surrounding rock damage caused by excavation. When surrounding rock damage and stress unloading may occur in the observation hole, continuous observation should be made until the change process stops. Generally speaking, the stage of relatively severe development of surrounding rock cracking occurs during the redistribution of surrounding rock stress; that is, continuous excavation and unloading activities will lead to severe evolution of surrounding rock damage. Therefore, when construction activity occurs near the test hole, it should be observed closely. A large number of in situ test results showed that the damage area of deep-buried hard rock is distributed in the scope of 1-time excavated chamber diameter, so the acoustic test shall be continuously observed during the construction of the double chamber diameter. For example, the chamber diameter of Jinping underground laboratory is 14 m, and using drilling and blasting method to dig 3 m at a time, continuous observation is required during the construction within the excavation activity range of 5 times away from the preset hole, as shown in Figure 3(a).

2.3. Method of Determining the Depth of EDZ. According to a large number of field test data, combining with the results of support construction, the boundary method is proposed to determine the depth of EDZ in surrounding rock. It is a method to judge the critical point of surrounding rock EDZ depth based on the variation curve of rock wave velocity with drilling length (*V-L* curve), according to the relation between wave velocity of measured point and the background wave velocity of rock mass. To be specific, it is necessary to determine the background wave velocity of rock mass first. The background wave velocity of a single lithologic rock mass should be the average value of the stable wave velocity far away from the orifice, while for composite lithologic rock mass, it should be the average value of the stable wave velocity of the rock mass in same lithologic region as the excavation damage zone (Figure 3). If the background wave velocity cannot be determined by *V-L* curve, the average value of undisturbed rock mass should be used instead, which can be found in the report of hydrogeological investigation before the excavation of the cavern. Then a parallel *X* axis background wave velocity representative line, a reference line to determine the extent of the damage, is drawn on the V-P curve according to the wave velocity far away from the excavation affected area. Finally, when the wave velocity of three consecutive points (points *a*, *b*, and *c* in Figure 4) near the orifice is smaller than the background wave velocity and these points show an upward trend, the

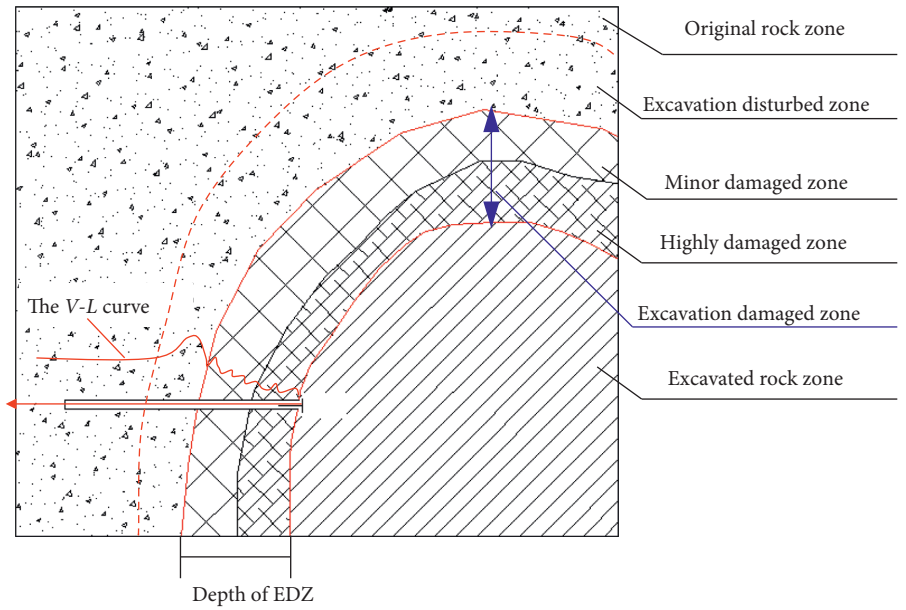

Figure 1: Principle of determining the depth of EDZ by acoustic testing.

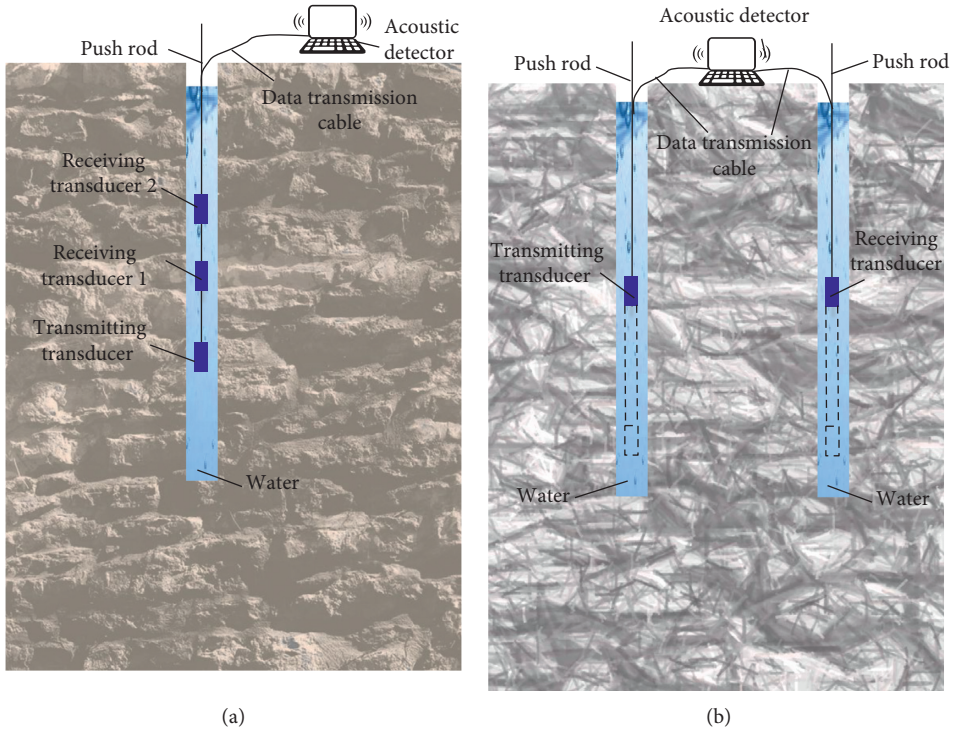

(a) (b)

Figure 2: Principle of determining the depth of EDZ by acoustic testing. (a) Single hole acoustic test. (b) Cross hole acoustic test.

EDZ depth boundary is the closest measured point above the background wave velocity representative line (point d in Figure 4).

It is worth noting that when the EDZ depth of surrounding rock is tested by a double receiver device, if the emission transducer is placed near the orifice, the acoustic wave of rock mass within the full length range of the device cannot be accurately tested. This is because the energy dissipation of acoustic signals released by the transmitter near the orifice is faster, the rock mass at the orifice is broken, and the acoustic signals entering the rock mass are even weaker. If the damage zone of the surrounding rock is small, the moving distance of the test equipment should be small, and generally no more than 10 cm. If three points lower than the intrinsic wave velocity cannot be found by using the boundary method, the test position of all points

Table 1: Typical *V*-*L* curves according to the results of practical engineering test.

No	Curve	Description
(a)	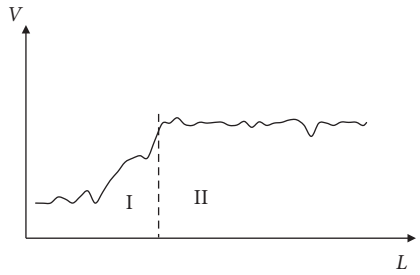	The wave velocity *V* of rock mass near the orifice is very small. With the increase of hole length *L*, the wave velocity of rock mass increases rapidly, and then the growth rate slows down and gradually tends to be stable.
(b)	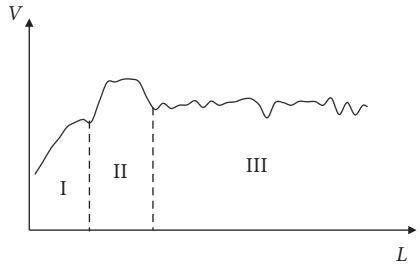	The wave velocity of rock mass can be divided into three distinct stages. Stage I is relatively low near the orifice. With the increase of hole length *L*, the wave velocity in stage II increases and then decreases within a certain range, and then the wave velocity gradually tends to be stable in stage III.
(c)	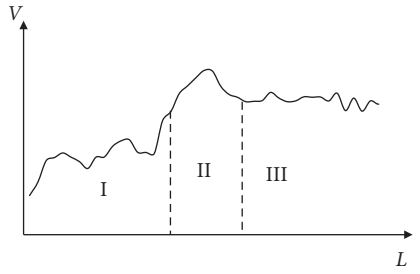	The wave velocity of rock mass also can be divided into three stages: stage I is near the orifice, and there are many wave peaks and troughs; the maximum wave peak appears in stage II, and stage III is that after the last wave peak far away from the orifice. The rock wave velocity gradually decreases and tends to be stable.
(d)	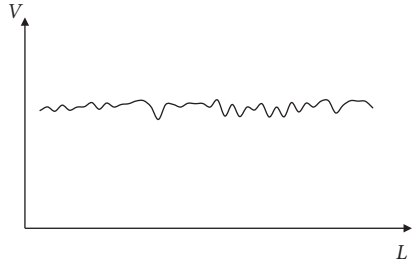	There is no obvious change of wave velocity.

near the orifice closest to the representative line of the background wave velocity can be determined as the damage depth boundary (Figure 5).

3. Application in Engineering Cases

3.1. Application in Baihetan Engineering Project

3.1.1. Introduction of the Engineering. Baihetan Hydropower Station is located on the border between Ningnan County in Sichuan Province and Qiaojia County in Yunnan Province on the lower reaches of the Jinsha River in China. According to the lithology of formations exposed during excavation, basalt of the Emeishan formation in the Permian system (P2β) is mainly found at the dam site, in which developed columnar jointed basalt appears in P2β32 and P2β33 layers. The special structure of columnar jointed rock masses mainly appears as an abnormal development of joint fissures, in which not only intercolumnar joints making up the columnar body appear, but also intracolumnar vertical blind joint planes and intracolumnar horizontal and inclined joint planes are found. The statistical results pertaining to nearly 300 columnar joint planes within the elevation of 630~660 m of the dam foundation at the left bank showed that the proportions of columnar joints with triangular, quadrangular, pentagonal, and hexagonal sections are about 11.76%, 29.41%, 32.35%, and 26.47%, respectively. The average length of the sides of these polygons is about 13.6 cm in which the total number of polygons whose length of side is in the range of 10~20 cm accounted for more than 80% overall. Columnar jointed basalts are intensively developed and the columnar joints are cut by a quantity of low-dip structural

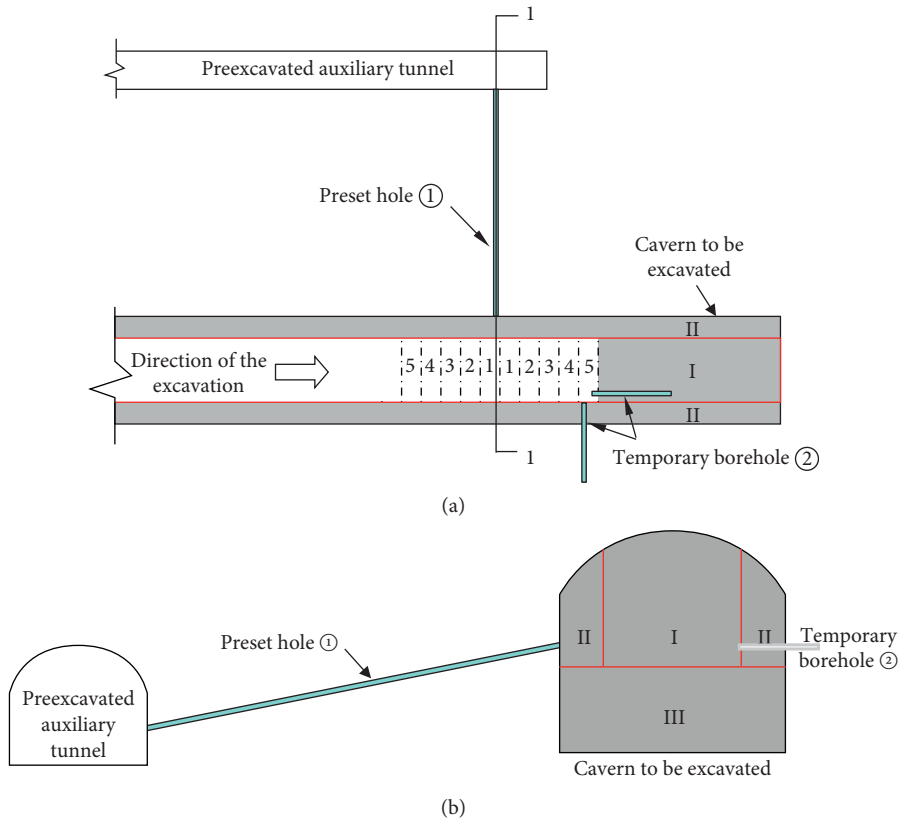

Figure 3: Layout of the test hole for acoustic testing. (a) Plane view and (b) section view of 1-1.

planes and dislocation zones. As a result, except for some zones influenced by tectonics, the inclinations of axes of columnar jointed basalts are all between 60° and 85°.

In the experimental cavern, there are three types of drilling holes with the same diameter in the side wall, which are 45° updipping, 45° horizontal, and 45° downward as shown in Figure 6.

3.1.2. Excavation Damaged Zone of the Jointed Rock Mass from Different Boreholes. In the columnar jointed rock mass cavern, the highly damaged zones in rock mass measured by boreholes with different angles on the left wall are almost the same, while the excavation damaged zones determined by acoustic wave tests vary from each other (Figure 7), and their evolution rules are also different, which is mainly caused by the different relative positions of the primary jointed surface and the borehole. The greater the angle of intersection between the borehole and joint surface, the greater the amplitude of change of acoustic wave propagation path, and the more the number of joints across the borehole per unit length, the more energy loss of acoustic wave in the propagation process. The microfractures in the column expand or break through after the formation of the hole, so that when the boreholes from different angles cross the columnar jointed rock mass, the number of fissures in the drilling wall per unit length is obviously different. This is an important reason that the wave velocities of the original rock mass differ greatly from each other by drilling tests from different angles.

E4 refers to the boreholes at the left spandrel of the diversion tunnel on the left bank of Baihetan Hydropower Station. The evolution of HDZ and EDZ in borehole E4 during different excavation stages was monitored in real time. According to the initial data from boreholes, there were six primary through-going fractures and a block dropping event in the borehole, with the length of HDZ and EDZ being 1.9 m and 2.4 m. After the working face passed 4 m from the measurement point, new fractures appeared at distances of 0.7 m and 2.0 m and a block dropped at 0.9 m along the borehole. Moreover, the fracture at 1.9 m extended from 25.1 mm to 86.6 mm in width. When the working face was 9 m from the measurement borehole, new fractures appeared at 0.6 m and 1.6 m and a block dropped at 1.1 m within the borehole. Moreover, the fracture at 1.9 m further extended from 86.6 mm to 131.2 mm in width. The fracture at 2.0 m was connected with other fractures and the length of the fracture zone increased to 2.1 m, and the length of excavation damaged zone increased to 2.8 m as well (Figure 8).

3.2. Application in Jinping Deep Underground Laboratory

3.2.1. Introduction of the Engineering. Jinping Deep Underground Laboratory (CJPL-II) is situated in the geomorphological slope between Sichuan Basin and Qinghai-Tibet

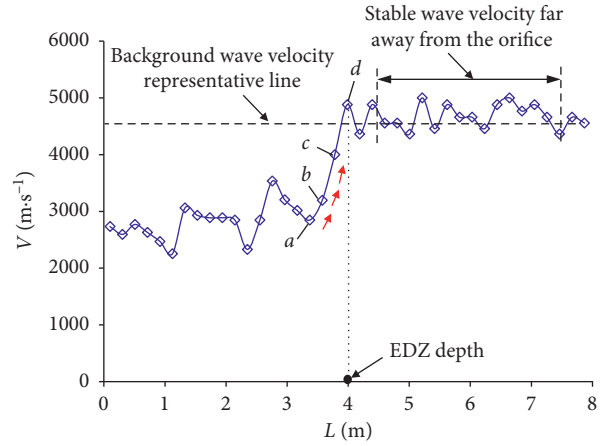

Figure 4: The proposed boundary method.

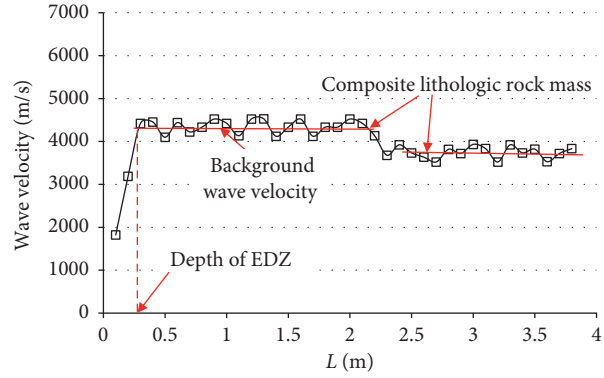

Figure 5: Boundary method used in composite lithologic rock mass.

Plateau. It is located in Jinping Mountain at the lower reaches of Yalong River and the junction of Muli, Yanyuan and Mianning counties, Sichuan, The cliff of Jinping Mountain stands precipitously, and the ridge is mostly in the shape of sharp edge, and the ridge on both sides of the main ridge is in the shape of comb, and the maximum relative height difference exceeds 3000 m (Figure 9).

Jinping Deep Underground Laboratory II phase (CJPL-II) Rock Mechanics Underground Laboratory buried 2375 m belongs to the ultradeep underground laboratory. According to the functional design requirements of the second phase of Jinping Deep Underground Laboratory, combined with geological conditions, existing caves arrangement and construction conditions, the underground laboratory consists of four staggered traffic holes, each hole is 130 m long, with two test holes of 65 m in length, forming an overall pattern of 4 holes with 9 chambers, as shown in Figure 10. The axis direction of test holes is parallel to the auxiliary guide hole of Jinping, and the axis azimuth is N58°W, and the excavation process for 1#~8# test hole, gate shaped with section of 14×14 m, can be divided into three steps, including upper middle drift excavation (Step I), upper expansion excavation (Step II), and bottom excavation (Step III). While the 9-1# test hole is a 5 m circular chamber with full section excavation, the main supporting methods are bolt and shotcrete. The lithology of test grotto #2, #3, and #4 in the engineering area changed significantly.

3.2.2. Excavation Damaged Zone of the Jointed Rock Mass from Different Boreholes. C-04 is a preset drill hole before the excavation of 6# test grotto (Figure 11). The lithology is gray marble. The drill hole is shown in Figure 10. On April 1, 2015, the acoustic wave velocity of C-04 hole and the initial borehole camera data were measured before excavation. The original rock wave velocity of the gray marble was measured to be 5800 km/s, except that it decreased slightly in the region where the original fracture was located, and the wave velocity of the rock mass in the whole section was stable. The excavation of 6# test grotto began in May 2015, and the damaged area gradually emerged and evolved during the excavation stage. On August 25, 2015, when the upper expansion excavation was 8 m away from the measuring hole, the borehole camera and acoustic test within 4 m of the surrounding rock were carried out in situ. The results of borehole photography showed that several new cracks have been added in the hole, and the original cracks have opened locally, forming a 2.1 m highly damaged zone. According to the "boundary method" proposed in this paper, the depth of excavation damaged zone by acoustic test was about 3.1 m (Figure 12).

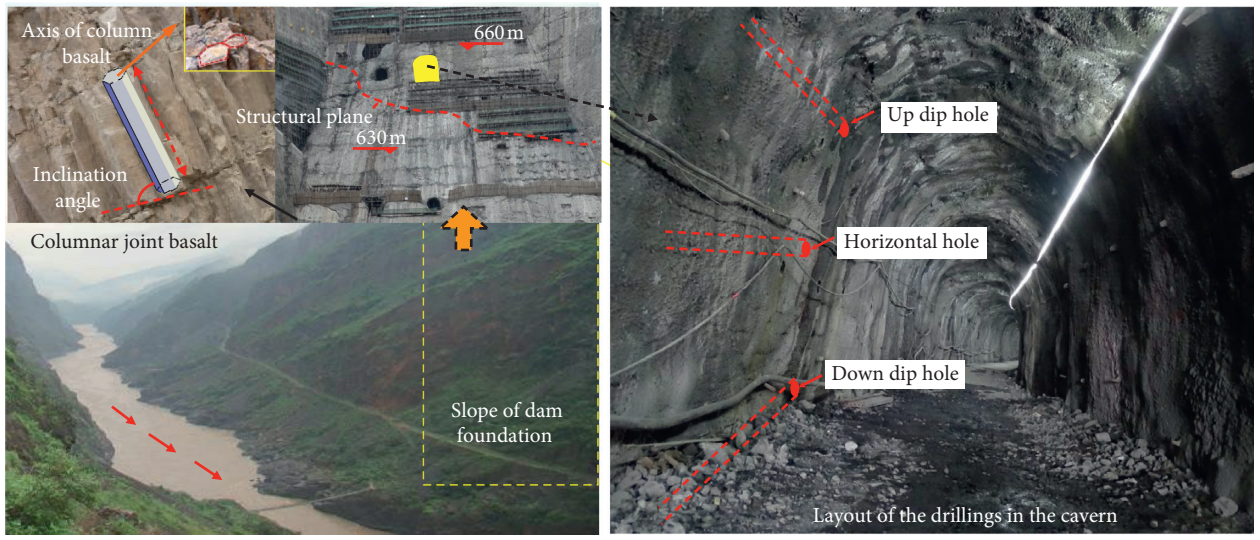

(a) (b)

Figure 6: Columnar joint basalt on the slope of dam foundation in Baihetan.

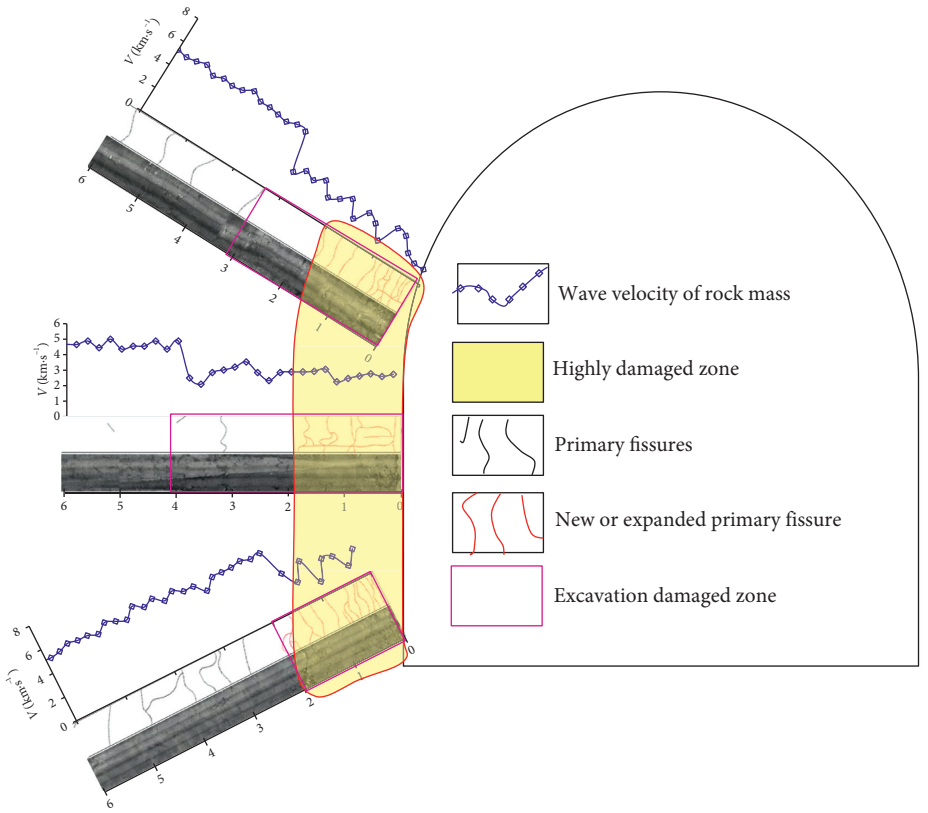

Figure 7: Test results of boreholes at different angles in jointed rock mass.

C-02 is a preset drill hole before the excavation of 2# test grotto. The lithology is black-streaked fine-grained marble. The drilling is shown in Figure 11. On April 1, 2015, the acoustic wave velocity of C-02 and the initial borehole camera data were measured before excavation. The original rock wave velocity was 6000 km/s, which indicated that, compared with gray marble in C-04, the black-streaked fine-grained marble in C-02 has higher strength and better rock integrity. On September 18, 2015, when the bottom excavation was 4 m away from the measuring drilling, the borehole camera and acoustic test within 4 m of the surrounding rock were carried out in situ. The results of borehole photography showed that several new cracks have been added in the hole, and the original cracks have opened

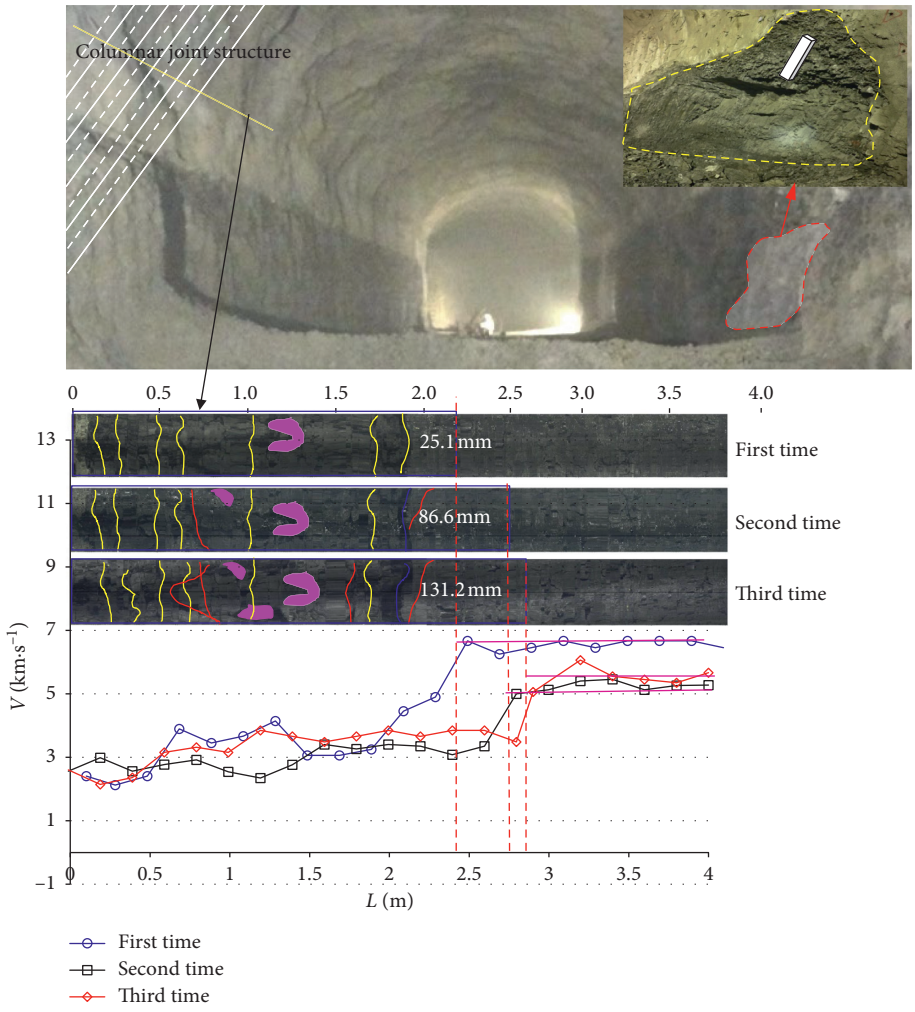

Figure 8: Test results of E4 in jointed rock mass.

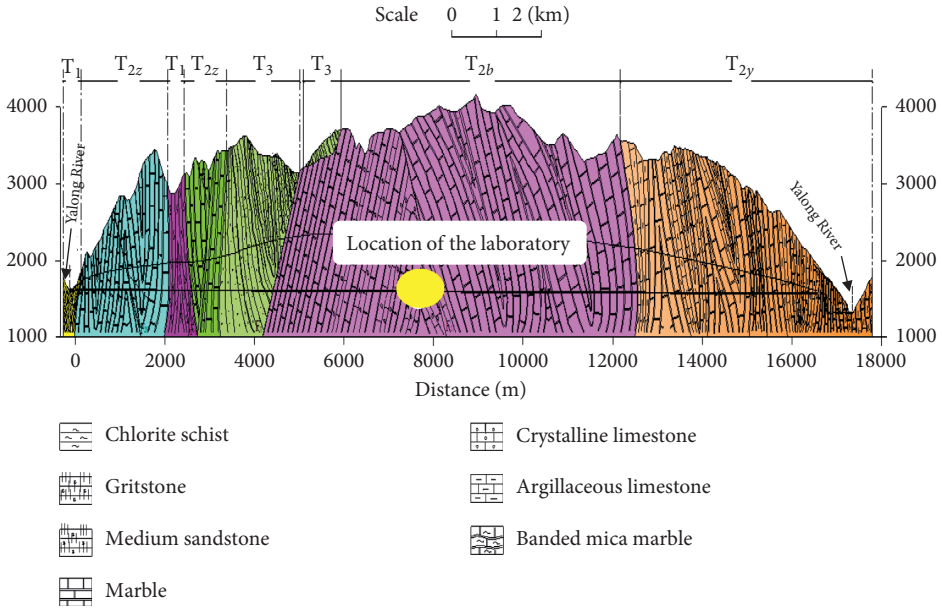

Figure 9: Location of Jinping deep underground laboratory.

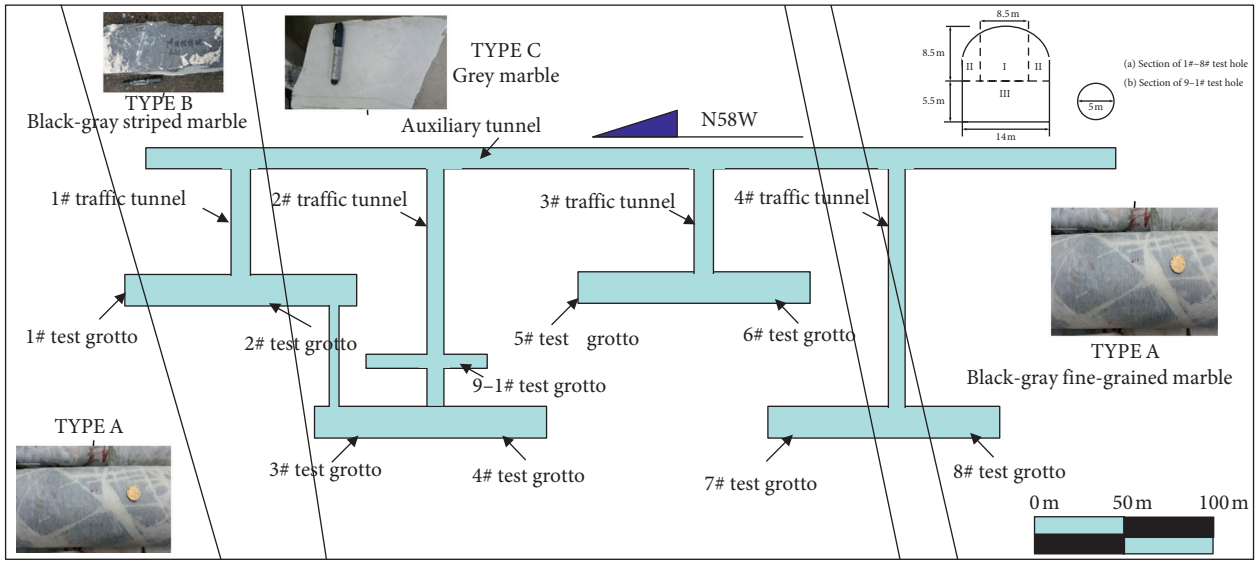

Figure 10: Layout of Jinping deep underground laboratory.

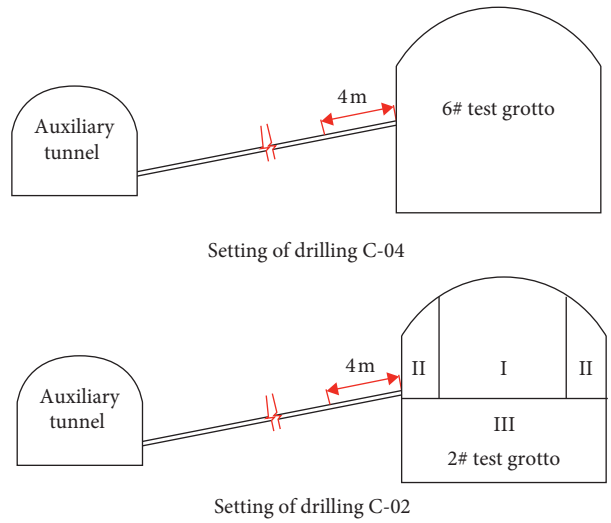

Figure 11: Layout of C-02 and C-04.

locally, forming a 1.1 m highly damaged zone. According to the "boundary method" proposed in this paper, the depth of excavation damaged zone by acoustic test was about 1.6 m, as shown in Figure 13.

4. Discussion

Because of its simple operation and high test accuracy, acoustic test is superior to other test methods, so it occupies the mainstream position of current test methods to determine the depth of EDZ in surrounding rock mass.

However, in practical engineering, the acoustic wave velocity of surrounding rock is not only affected by the damage of surrounding rock, but also by the inhomogeneity of lithology and fault structure, etc., so it would be more complex, which increases the difficulty in determining the EDZ depth of rock mass to some extent. In addition, the deformation and fracture of rock mass are generally the results of progressive damage degradation and continuous accumulation process from the initial microdefects to the final fracture failure, which is also the result of the continuous expansion and penetration of internal microdefects. Sometimes the proposed method is not applicable in zonal fractured rock masses (Figure 14). In zonal fractured rock masses, determining of EDZ depth requires combining testing purposes. For example, if it is used for surrounding rock bolting; the nature of the rock mass and the length of partition should be taken into consideration.

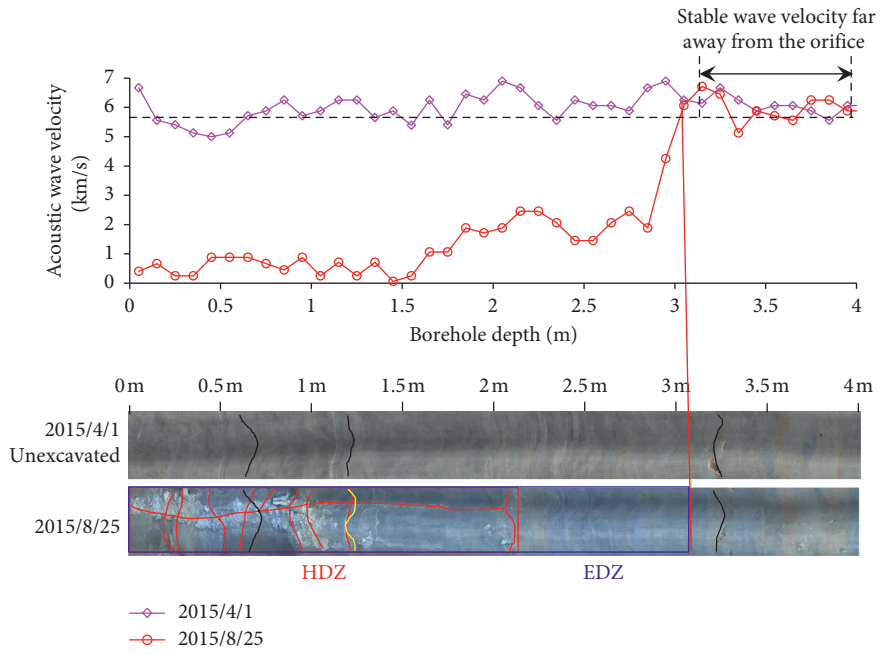

Figure 12: Test results of C-04 in 6# test grotto.

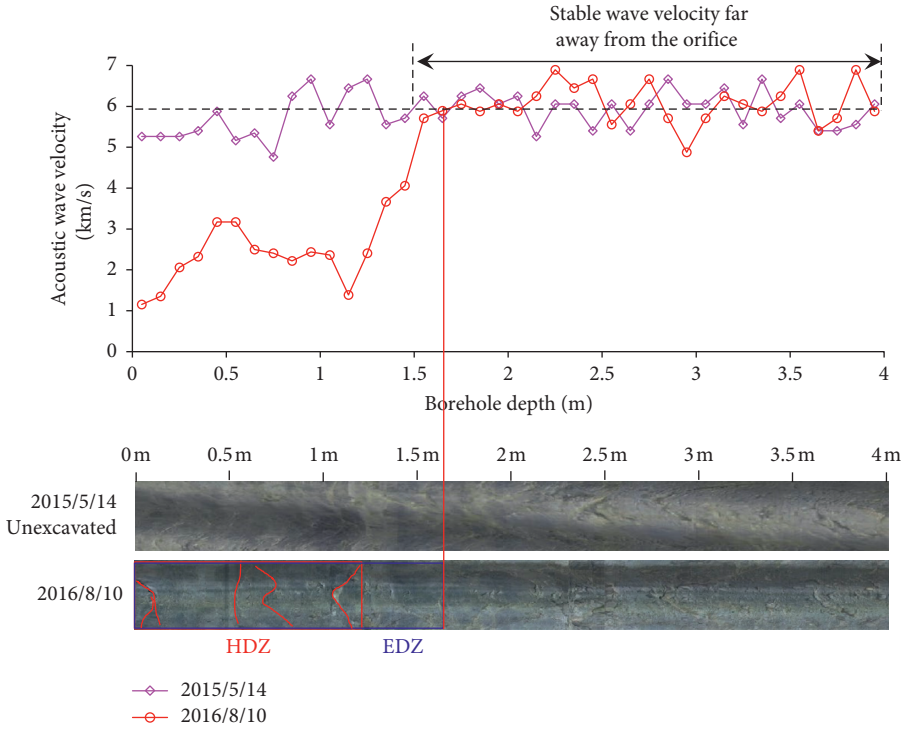

Figure 13: Test results of C-02 in 2# test grotto.

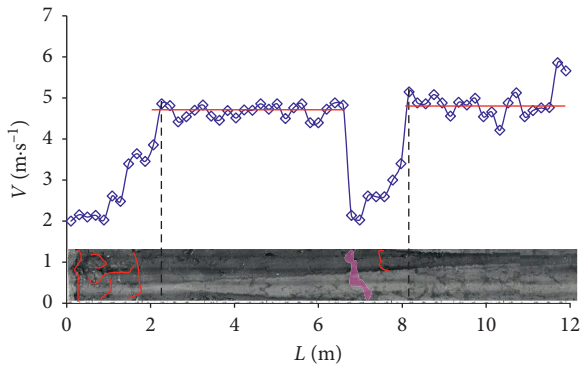

Figure 14: Acoustic test in zonal fractured rock masses.

5. Conclusions

The accurate determination of excavation damaged zone depth directly affects the reasonable selection of supporting parameters after excavation of surrounding rock. On the basis of previous studies, the commonly used acoustic testing method is demonstrated in this work, and the method of determining excavation damage zone by acoustic testing is proposed. The main conclusions drawn as follows.

(1) For jointed rock mass, the anisotropy is the main factor affecting the propagation law of acoustic wave. The depth of excavation damaged zone obtained by acoustic wave represents the damage degree of rock mass affected by excavation in this direction. The damage evolution of rock mass at the same position after excavation obtained by acoustic test is consistent with the fracture evolution of borehole television, but the acoustic wave test results can better reflect the influenced area under excavation.

(2) For deep-buried hard rock, the damage evolution characteristics of rock mass are obviously correlated with lithology. Although the background wave velocity of different hard rocks varies significantly, the depth of excavation damaged zone obtained by acoustic wave test can also reflect the differences in the evolution process.

(3) The proposed method is based on the basic law of rock damage evolution and the propagation characteristics of acoustic waves in rock media of different states. The acoustic wave testing method is simple and easy to operate, and the proposed method for analysing test results is highly operable and reliable in both preset and newly arranged drilling holes.

Data Availability

The data used to support the findings of this study are available from the corresponding author upon request.

Conflicts of Interest

The authors declare no conflicts of interest.

Acknowledgments

This research was funded by the National Natural Science Foundation of China (grant no. 51909136), the Open Research Fund of Key Laboratory of State Key Laboratory of Geomechanics and Geotechnical Engineering (grant no. Z018012), and the Open Research Fund of Key Laboratory of Geological Hazards on Three Gorges Reservoir Area (China Three Gorges University), Ministry of Education (grant no. 2020KDZ03). The authors gratefully acknowledge the support by Young Talents Development Plan of Hubei Province. The authors appreciate the value added through discussion of the work with Zhibin Yao and Professor Shaojun Li.

References

[1] P. C. Kelsall, J. B. Case, and C. R. Chabannes, "Evaluation of excavation-induced changes in rock permeability," *International Journal of Rock Mechanics and Mining Sciences & Geomechanics Abstracts*, vol. 21, no. 3, pp. 123–135, 1984.

[2] R. Pusch and R. Stanfors, "The zone of disturbance around blasted tunnels at depth," *International Journal of Rock Mechanics and Mining Sciences & Geomechanics Abstracts*, vol. 29, no. 5, pp. 447–456, 1992.

[3] T. Sato, T. Kikuchi, and K. Sugihara, "In-situ experiments on an excavation disturbed zone induced by mechanical excavation in Neogene sedimentary rock at Tono mine, central Japan," *Engineering Geology*, vol. 56, no. 1-2, pp. 97–108, 2000.

[4] X. Lai, F. H. Ren, Y. P. Wu, and M. F. Cai, "Comprehensive assessment on dynamic roof instability under fractured rock mass conditions in the excavation disturbed zone," *International Journal of Minerals, Metallurgy and Materials*, vol. 16, no. 1, pp. 12–18, 2009.

[5] A. T. Jakubick and T. Franz, "Vacuum testing of the permeability of the excavation damaged zone," *Rock Mechanics and Rock Engineering*, vol. 26, no. 2, pp. 165–182, 1993.

[6] Z. Hou, "Mechanical and hydraulic behavior of rock salt in the excavation disturbed zone around underground facilities," *International Journal of Rock Mechanics and Mining Sciences*, vol. 40, no. 5, pp. 725–738, 2003.

[7] G. L. Feng, X. T. Feng, B. R. Chen et al., "Characteristics of microseismicity during breakthrough in deep tunnels: case study of Jinping-II hydropower station in China," *International Journal of Geomechanics*, vol. 20, Article ID 04019163, 2020.

[8] G.-L. Feng, X.-T. Feng, B.-R. Chen, Y.-X. Xiao, and Z.-N. Zhao, "Effects of structural planes on the microseismicity associated with rockburst development processes in deep tunnels of the Jinping-II Hydropower Station, China," *Tunnelling and Underground Space Technology*, vol. 84, pp. 273–280, 2019.

[9] S. Kwon, C. S. Lee, S. J. Cho, S. W. Jeon, and W. J. Cho, "An investigation of the excavation damaged zone at the KAERI underground research tunnel," *Tunnelling and Underground Space Technology*, vol. 24, no. 1, pp. 1–13, 2009.

[10] I. Vazaios, N. Vlachopoulos, and M. S. Diederichs, "Assessing fracturing mechanisms and evolution of excavation damaged zone of tunnels in interlocked rock masses at high stresses using a finite-discrete element approach," *Journal of Rock Mechanics and Geotechnical Engineering*, vol. 11, no. 4, pp. 701–722, 2019.

[11] R. S. Read, "20 years of excavation response studies at AECL's underground research laboratory," *International Journal of*

Rock Mechanics and Mining Sciences, vol. 41, no. 8, pp. 1251–1275, 2004.

[12] D. P. Jansen, S. R. Carlson, R. P. Young, and D. A. Hutchins, "Ultrasonic imaging and acoustic emission monitoring of thermally induced microcracks in Lac du Bonnet granite," *Journal of Geophysical Research: Solid Earth*, vol. 98, no. B12, pp. 22231–22243, 1993.

[13] S. R. Carlson and R. P. Young, "Acoustic emission and ultrasonic velocity study of excavation-induced microcrack damage at the underground research laboratory," *International Journal of Rock Mechanics and Mining Sciences & Geomechanics Abstracts*, vol. 30, no. 7, pp. 901–907, 1993.

[14] M. A. Perras and M. S. Diederichs, "Predicting excavation damage zone depths in brittle rocks," *Journal of Rock Mechanics and Geotechnical Engineering*, vol. 8, no. 1, pp. 60–74, 2016.

[15] S. Li, X.-T. Feng, Z. Li, C. Zhang, and B. Chen, "Evolution of fractures in the excavation damaged zone of a deeply buried tunnel during TBM construction," *International Journal of Rock Mechanics and Mining Sciences*, vol. 55, pp. 125–138, 2012.

[16] S. Li, X.-T. Feng, Z. Li, B. Chen, C. Zhang, and H. Zhou, "In situ monitoring of rockburst nucleation and evolution in the deeply buried tunnels of Jinping II hydropower station," *Engineering Geology*, vol. 137-138, pp. 85–96, 2012.

[17] J. B. Martino and N. A. Chandler, "Excavation-induced damage studies at the underground research laboratory," *International Journal of Rock Mechanics and Mining Sciences*, vol. 41, no. 8, pp. 1413–1426, 2004.

[18] H.-S. Guo, X.-T. Feng, S.-J. Li, C.-X. Yang, and Z.-B. Yao, "Evaluation of the integrity of deep rock masses using results of digital borehole televiewers," *Rock Mechanics and Rock Engineering*, vol. 50, no. 6, pp. 1371–1382, 2017.

Hindawi
Advances in Civil Engineering
Volume 2021, Article ID 9939144, 9 pages
https://doi.org/10.1155/2021/9939144

Research Article

A Simple Three-Dimensional Failure Criterion for Jointed Rock Masses under True Triaxial Compression

Yaohui Gao,[1] **Chunsheng Zhang**,[1] **Zhaofeng Wang**,[2,3] **and Jun Chen**[1]

[1]*PowerChina Huadong Engineering Corporation Limited, Hangzhou 310014, Zhejiang, China*
[2]*State Key Laboratory of Geomechanics and Geotechnical Engineering, Institute of Rock and Soil Mechanics Chinese Academy of Sciences, Wuhan 430071, China*
[3]*University of Chinese Academy of Sciences, Beijing 100049, China*

Correspondence should be addressed to Zhaofeng Wang; zfwang@whrsm.ac.cn

Received 1 April 2021; Accepted 17 May 2021; Published 27 May 2021

Academic Editor: Dongsheng Huang

The joint configuration and the intermediate principal stress have a significant influence on the strength of rock masses in underground engineering. A simple three-dimensional failure criterion is developed in this study to predict the true triaxial strength of jointed rock masses. The proposed failure criterion in the deviatoric and meridian planes adopts the elliptic and hyperbolic forms to approximate the Willam–Warnke and Mohr–Coulomb failure criterion, respectively. The four parameters in the proposed failure criterion have close relationships with the cohesion and the internal friction angle and can be linked with the joint inclination angle using a cosine function. Two suits of true triaxial strength data are collected to validate the correctness of the proposed failure criterion. Compared with other failure criteria, the proposed failure criterion is more reasonable and acceptable to describe the strength of jointed rock masses.

1. Introduction

Rock mass strength is an extremely important parameter in predicting the stability of geoengineering such as rock slopes, dam foundation, and deeply buried tunnels [1]. Due to the existing joints, rock mass strength is anisotropic [2–8]. In addition, true triaxial stress state ($\sigma_1 > \sigma_2 > \sigma_3$) is more universal with the increasing depth of engineering. The influence of σ_2 on the compressive strength of jointed rock masses has been investigated extensively in the experimental tests [9–14]. Therefore, establishing a strength criterion considering both the joint and σ_2 dependency is essential for better designing the layout and construction of underground engineering.

A large number of research papers are concentrated on rock strength. Among others, the Mohr–Coulomb failure criterion [15] and the Hoek–Brown failure criterion [16] are most widely used because of their simplicities. However, these two failure criteria ignore the σ_2 effect. Based on the true triaxial strength data, the authors in [17–21] have proposed the three-dimensional failure criteria which can describe the variation in the rock strength with increasing σ_2 very well. There are also some popular true triaxial failure criteria [22–24]. However, these failure criteria are applicable for intact rock and do not consider the joint effect.

To develop a failure criterion considering the joint effect under true triaxial compression, Tiwari and Rao [14] introduced the joint effect into the generalized von Mises theory [20]. In addition, enormous research studies [25–27] have extended the Hoek–Brown failure criterion into the three-dimensional form to predict rock mass strength. Moreover, Singh and Singh and Zhang et al. [28, 29] established a modified Mohr–Coulomb criterion for the polyaxial strength of rock masses, and Rafiai [30] proposed an empirical criterion for rock mass strength under multiaxial state on the basis of a comprehensive experimental database. Based on the research in [7, 10, 30], the modified nonlinear criteria are presented to determine the strength of rock masses.

Most of the abovementioned failure criteria can only consider the effect of the joint or σ_2 on the prediction of rock mass strength. In addition, some aforementioned failure surfaces in three-dimensional principal stress space are not absolutely continuous, which could present difficulties in numerical calculations. To overcome these problems, the true triaxial failure criterion proposed in this paper adopts the modified Willam–Warnke yield criterion and hyperbolic function in the deviatoric and meridian planes, respectively. Moreover, the adopted hyperbolic function takes the Mohr–Coulomb criterion as the asymptote in the meridian plane. To valid the correctness of the developed failure criterion, it is employed to fit two suits of true triaxial strength data of rock masses.

2. A Failure Criterion for Jointed Rock Masses

Within this paper, tensile stress is considered positive and compressive stress is negative. A general form of a failure criterion suggested in [31] can be expressed in a quadratic function:

$$F(\tau_{\text{oct}}, \sigma_{\text{oct}}, \theta_\sigma) = \alpha {\sigma_{\text{oct}}}^2 + \beta\sigma_{\text{oct}} + \gamma + \overline{\sigma_+}^2 = 0, \quad (1)$$

where $\overline{\sigma_+} = \tau_{\text{oct}}/g(\theta_\sigma)$; θ_σ is the Lode angle ($\theta_\sigma = 1/3\cos^{-1}(3\sqrt{3}\,J_3/2J_2^{3/2})$), where J_2 ($J_2 = 1/6[(\sigma_1-\sigma_2)^2(\sigma_2-\sigma_3)^2+(\sigma_3-\sigma_1)^2]$) and J_3 ($J_3 = (\sigma_1-\sigma_{\text{oct}})(\sigma_2-\sigma_{\text{oct}})(\sigma_3-\sigma_{\text{oct}})$) are the second and third invariants of the deviatoric stress tensor, respectively; τ_{oct} and σ_{oct} are the octahedral shear and normal stresses ($\tau_{\text{oct}} = 1/3\sqrt{(\sigma_1-\sigma_2)^2+(\sigma_2-\sigma_3)^2+(\sigma_3-\sigma_1)^2}$ and $\sigma_{\text{oct}} = (\sigma_1+\sigma_2+\sigma_3)/3$); and α, β, and γ are material constants. First, the dependency of τ_{oct} on θ_σ in the deviatoric plane perpendicular to the hydrostatic axis is determined; namely, $g(\theta_\sigma)$ is obtained. Then, the influence of σ_{oct} on $\overline{\sigma_+}$ can be investigated in the meridian plane.

2.1. True Triaxial Failure Criterion in the Deviatoric Plane. The failure curve in the deviatoric plane displays the following significant characteristics of rock failure: (i) continuous, smooth, and convex; (ii) a closed curve or vertex; and (iii) symmetric with respect to three principal stress axes. For this purpose, an elliptical form developed in [32] is adopted here to express the relationship between $g(\theta_\sigma)$ and θ_σ:

$$g(\theta_\sigma) = \frac{R + (2K-1)\sqrt{2R\cos\theta_\sigma + 5K^2 - 4K}}{2R\cos\theta_\sigma + (1-2K)^2}, \quad (2)$$

where $R = 2(1-K^2)\cos\theta_\sigma$; K is the ratio ($K = \tau_{\text{oct},ae}/\tau_{\text{oct},ac}$) between the strength ($\tau_{\text{oct},ae}$) for axisymmetric extension and the strength ($\tau_{\text{oct},ac}$) for axisymmetric compression; $0^\circ \le \theta_\sigma \le 60^\circ$ and $\theta_\sigma = 0^\circ$ ($g(\theta_\sigma) = K$) for axisymmetric extension; and $\theta_\sigma = 60^\circ$ $g(\theta_\sigma) = 1$ for axisymmetric compression.

It is notable that $g(\theta_\sigma)$ in (2) unconditionally satisfies the abovementioned properties of a failure criterion in the deviatoric plane for the range $0.5 \le K \le 1$. Therefore, taking θ_σ as the independent variable, $g(\theta_\sigma)$ is only a function of K.

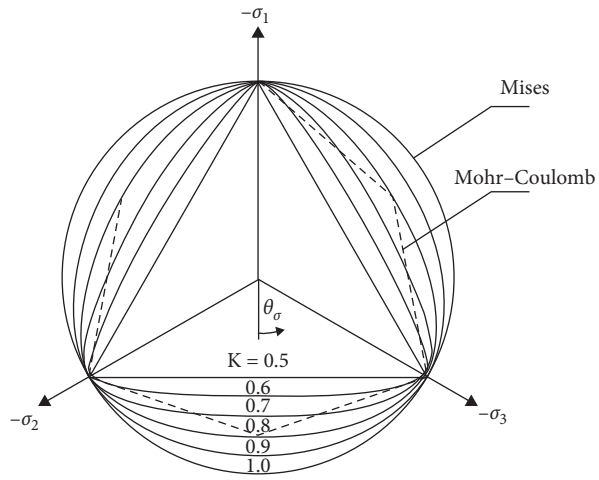

Figure 1: The Willam–Warnke failure criterion in the deviatoric plane with different K values.

Figure 1 shows that the shapes of the failure curves in the deviatoric plane changes with K. More specifically, as K varies from 0.5 to 1, failure surfaces gradually change from a triangle to a circle. It can be seen that the Willam–Warnke failure criterion is more appropriate than the Mohr–Coulomb failure criterion, and the Willam–Warnke criterion can change into the Mises criterion when $K = 1$. Here, to present the joint effect on the failure function in the deviatoric plane, the parameter K depends on both the joint inclination angle β and σ_{oct}, namely, $K = K(\sigma_{\text{oct}}, \beta)$. If K is constant at different σ_{oct}, $g(\theta_\sigma)$ is only a function of β. Thus, the joint inclination angle β can describe the influence of the joint on the failure surfaces in the deviatoric plane.

2.2. True Triaxial Failure Criterion in the Meridian Plane. As pointed out by equation (1), once $g(\theta_\sigma)$ is determined using equation (2), a true triaxial failure criterion can be obtained if the relationship between $\overline{\sigma_+}$ and σ_{oct} is known. Here, a hyperbolic function (as shown in Figure 2) is adopted because of its simplicity and continuity to present the failure criterion in the meridian plane. Thus, equation (1) can be defined by

$$F(\tau_{\text{oct}}, \sigma_{\text{oct}}, \theta_\sigma) = \left(\frac{\sigma_{\text{oct}} - d}{a}\right)^2 - \left(\frac{\overline{\sigma_+}}{b}\right)^2 - 1 = 0, \quad (3)$$

where a, b, and d are material constants. Figure 3 exhibits a typical failure surface of the proposed criterion in the principal stress space.

2.3. Determination of the Parameters in the Failure Criterion. Generally, equation (3) has four parameters: K, a, b, and d. As mentioned above, K can be determined by the strength ratio under axisymmetric extension and compression at different β and σ_{oct} and be given by

$$K = \frac{\tau_{oct,ae}(\sigma_{oct}, \beta)}{\tau_{oct,ac}(\sigma_{oct}, \beta)}. \quad (4)$$

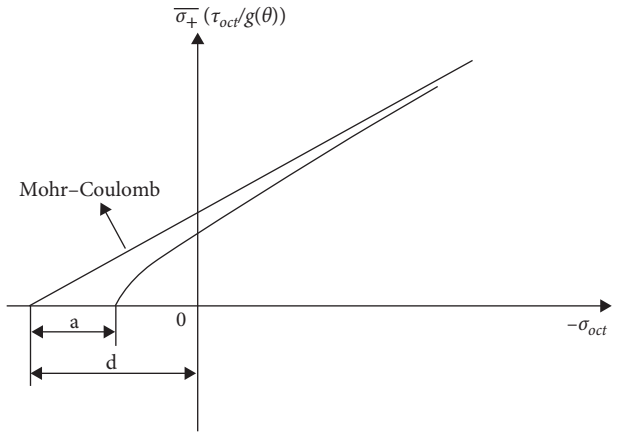

FIGURE 2: The hyperbolic function to approximate the Mohr–Coulomb failure criterion for axisymmetric compression in the meridian plane.

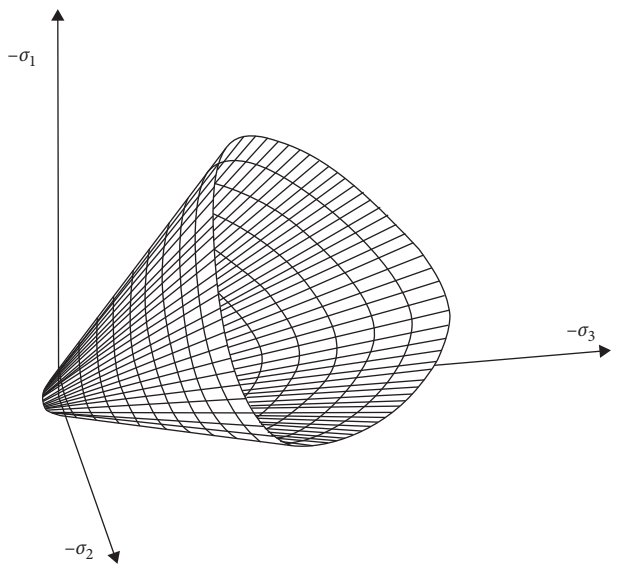

FIGURE 3: The typical failure surface in the principal stress space.

To determine the values of the other parameters, the hyperbolic function in equation (3) approximates the Mohr–Coulomb failure criterion for axisymmetric compression ($g(\theta_\sigma = 60^\circ) = 1$) in the meridian plane (as shown in Figure 2). The Mohr–Coulomb failure criterion at $\theta_\sigma = 60^\circ$ can be expressed by

$$F(\tau_{\text{oct}}, \sigma_{\text{oct}}, \theta_\sigma) = \overline{\sigma_+} + \frac{2\sqrt{2}\sin\varphi}{3-\sin\varphi}\sigma_{\text{oct}} - \frac{2\sqrt{2}c\cos\varphi}{3-\sin\varphi} = 0, \tag{5}$$

where c and φ are the cohesion force and internal friction angle. Taking the Mohr–Coulomb line as the hyperbolic asymptote, the parameters a, b, and d are then obtained as follows:

$$\frac{b}{a} = \frac{2\sqrt{2}\sin\varphi}{3-\sin\varphi}, \qquad d = c\cot\varphi. \tag{6}$$

The parameter a can be fitted by a series of simple experimental tests under axisymmetric compression. As the parameter a tends to be 0, equation (3) is getting closer to the Mohr–Coulomb failure surfaces in the meridian plane. In addition, $g(\theta_\sigma)_{MC}$ in equation (5) is given by

$$g(\theta_\sigma)_{MC} = \frac{3-\sin\varphi}{2\sqrt{3}\cos((\theta_\sigma - \pi)/6) - 2\sin\varphi\sin((\theta_\sigma - \pi)/6)}. \tag{7}$$

Thus, the strength ratio K_{MC} under axisymmetric extension and compression can be calculated using the Mohr–Coulomb failure criterion.

$$K_{MC} = g(\theta_\sigma = 0^\circ)_{MC} = \frac{3-\sin\varphi}{3+\sin\varphi}. \tag{8}$$

If equation (4) is simply substituted by equation (8), four unknown parameters (K, a, b, and d) in equation (3) become three (a, c, and φ) using equations (6) and (8). It is noted that the joint inclination angle β affects the unknown parameters ($a(\beta)$, $c(\beta)$, and $\varphi(\beta)$).

3. Validation of the Proposed Failure Criterion

The validity of the proposed failure criterion in this study is discussed using two following examples. The prediction accuracy is also analyzed and compared with other strength criteria.

3.1. Example 1. The true triaxial strength data for the first example are derived from the experimental results of [9]. This test was conducted on jointed marble which contains a natural joint plane with a rectangular prismatic size ($50 \times 50 \times 100\ \text{mm}^3$). Table 1 lists the derived test data.

The proposed failure criterion is used to model these selected strength data, and the calculated results are also listed in Table 1. Figure 4 presents the comparisons of the predicted strength $\sigma_{1\text{cal}}$ with the experimental data $\sigma_{1\text{exp}}$. The reference line ($\sigma_{1\text{cal}} = \sigma_{1\text{exp}}$) is also demonstrated in Figure 4 to exhibit the calculation accuracy. All of the data points are concentrated around the reference line, which indicates that the predictions by the proposed failure criterion are generally consistent with the experimental data.

The linear Mogi–Coulomb failure criterion [17] was adopted in [9] to fit the test data and is defined by

$$\tau_{\text{oct}} = \frac{2\sqrt{2}}{3}c\cos\varphi + \frac{2\sqrt{2}}{3}\sin\varphi\sigma_{m,2}, \qquad \sigma_{m,2} = \frac{\sigma_1 + \sigma_3}{2}, \tag{9}$$

where $\sigma_{m,2}$ is the effective mean stress. Here, the fitting results by these two failure criteria are compared in Figure 5, and the relationship between $\sigma_{1\text{cal}}$ and $\sigma_{1\text{exp}}$ can be expressed by

$$\sigma_{1\text{cal}} = 1.0049\sigma_{1\text{exp}}\ (R2 = 0.9042), \qquad \sigma_{1\text{cal}} = 1.0059\sigma_{1\ \text{exp}}\ (R2 = 0.9189), \tag{10}$$

Table 1: True triaxial compression strength of experimental and predicted results of jointed marble (data from [9]; here, compressive stress is considered positive).

σ_3 (MPa)	σ_2 (MPa)	σ_{1exp} (MPa), test data at joint inclination angle β (°)						σ_{1cal} (MPa), calculated data at joint inclination angle β (°)					
		0	20	40	60	80	90	0	20	40	60	80	90
0	0	158.59	100.79	73.76	77.57	112.21	141.07	146.23	110.16	81.81	84.31	118.00	144.63
10	60	279.94	296.43	272.40	240.12	242.96	258.62	276.72	254.21	220.28	202.30	224.88	240.92
30	60	332.25	361.55	330.96	305.12	338.63	357.16	354.39	339.66	319.75	307.68	300.75	304.06
30	90	409.76	387.18	363.12	337.69	311.01	297.24	395.24	384.82	363.43	337.62	330.11	331.26
30	120	377.51	366.23	350.79	333.50	316.97	309.78	427.12	421.00	397.62	357.13	350.11	349.71
K	–	–	–	–	–	–	0.7196	0.7221	0.7011	0.6651	0.7084	0.7272	
a	–	–	–	–	–	–	22.64	23.38	5.58	12.21	23.07	25.38	
b	–	–	–	–	–	–	17.98	19.34	4.84	10.37	17.15	17.24	
d	–	–	–	–	–	–	40.96	30.27	17.54	20.26	38.97	55.32	

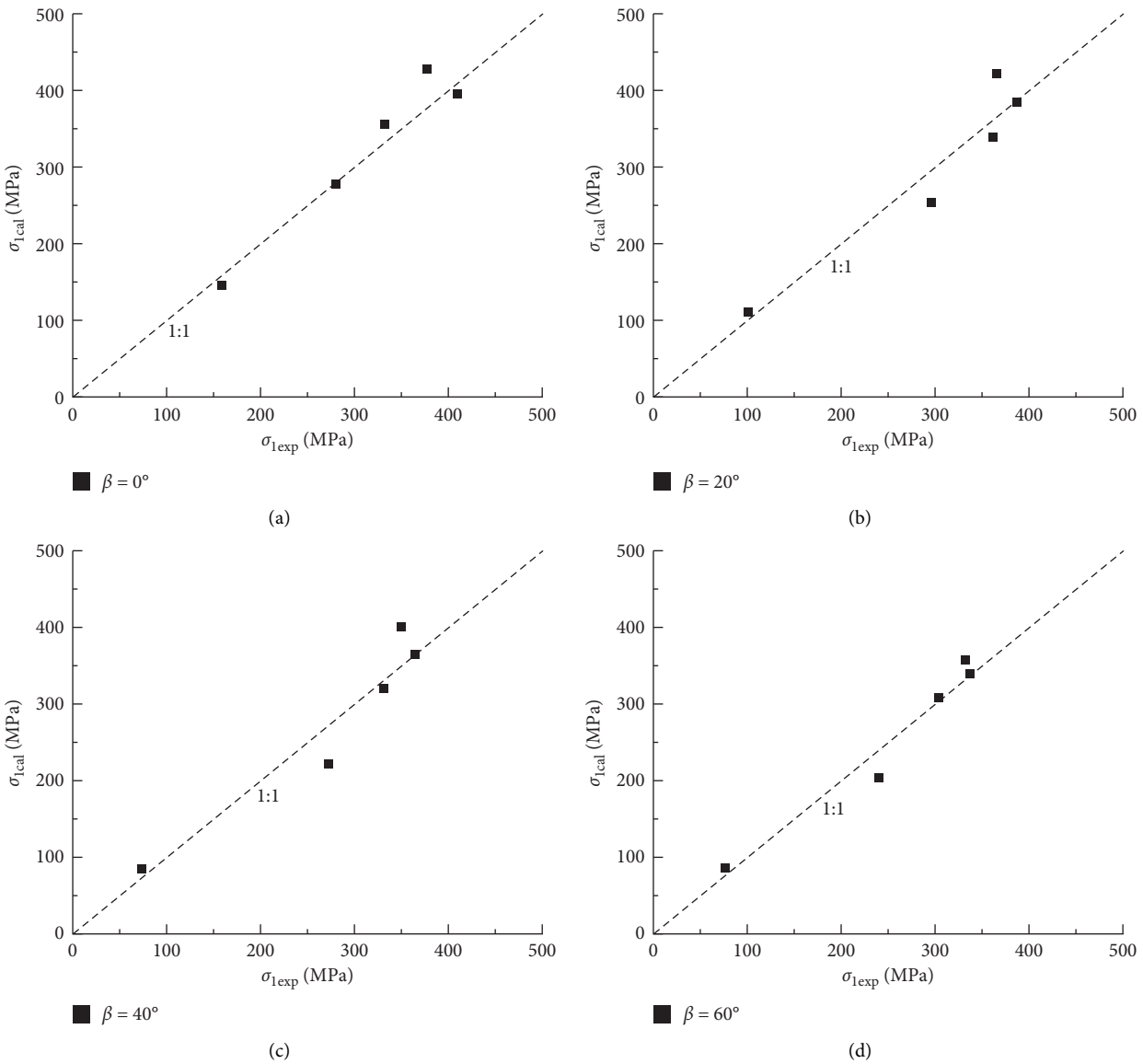

Figure 4: Continued.

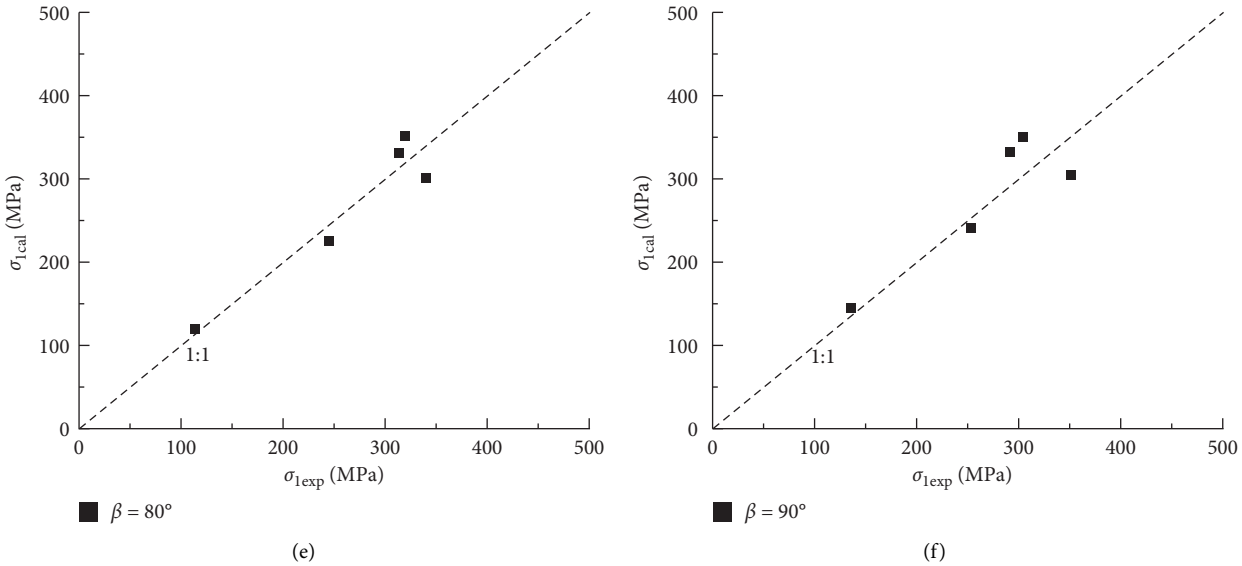

Figure 4: The comparison results of the calculated and experimental strength of jointed marble for different joint inclination angles: (a–f) $\beta = 0^{\circ}$, 20°, 40°, 60°, 80°, and 90°.

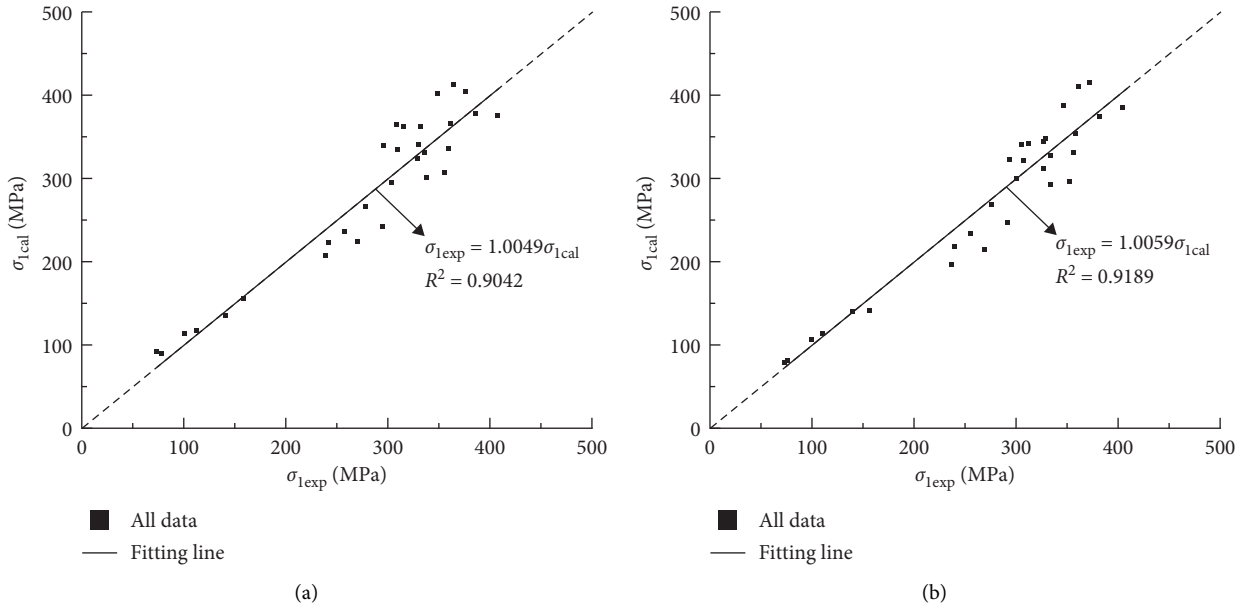

Figure 5: The fitting results of all the experimental strength of jointed marble: (a) the linear Mogi–Coulomb failure criterion and (b) the proposed failure criterion.

where equation (10) refers to the fitting results by the linear Mogi–Coulomb and proposed failure criteria, respectively. Table 2 also shows the percentage error in predicting strength data of jointed marble. Obviously, the proposed failure criterion has higher accuracy than the Mogi–Coulomb criterion. Therefore, the proposed failure criterion is reasonable and applicable to predict the true triaxial strength of jointed rock masses.

3.2. Example 2. The strength data for example 2 are collected from the test results of [14]. This series of true triaxial tests

Table 2: Percentage error in predicting strength data of jointed marble.

σ_3 (MPa)	σ_2 (MPa)	Percentage error in predicting strength data at joint inclination angle β (°)					
		0	20	40	60	80	90
0	0	7.79	9.30	10.91	8.69	5.16	2.52
10	60	1.15	14.24	19.13	15.75	7.44	6.84
30	60	6.66	6.05	3.39	0.84	11.19	14.87
30	90	3.54	0.61	0.08	0.02	6.14	11.45
30	120	13.14	14.95	13.35	7.09	10.46	12.89
Average of this paper		6.46	9.03	9.37	6.48	8.08	9.71
Average of the Mogi–Coulomb criterion [17]		4.88	10.43	11.80	8.52	9.17	11.57

Table 3: True triaxial compression strength of experimental and predicted results of rock mass models (data from [14]; here, compressive stress is considered positive).

σ_3 (MPa)	σ_2 (MPa)	σ_{1exp} (MPa), test data at joint inclination angle β (°)						$_{1cal}$ (MPa), calculated data at joint inclination angle β (°)					
		0	20	40	60	80	90	0	20	40	60	80	90
0.31	0.31	6.81	4.23	2.92	1.84	4.91	7.28	6.81	4.35	2.96	1.87	5.08	7.04
0.31	0.59	7.78	5.01	5.32	2.85	6.76	8.68	7.42	5.05	3.85	2.27	5.71	7.66
0.31	0.95	7.65	6.05	7.34	3.67	7.69	8.34	7.87	5.78	4.89	2.64	6.39	8.11
0.31	1.22	9.32	7.41	7.96	4.24	8.27	7.33	8.09	6.26	5.62	2.86	6.84	8.35
0.31	1.62	9.32	8.68	8.54	7.53	8.54	9.18	8.33	6.90	6.67	3.09	7.44	8.59
0.78	0.78	9.76	7.23	6.26	3.54	7.73	9.54	9.76	6.99	6.18	3.47	7.39	10.05
0.78	1.22	10.6	9.01	9.38	4.99	8.59	10.65	10.68	8.08	7.59	4.10	8.36	10.99
0.78	2.24	11.45	10.6	11.91	7.66	10.86	11.97	11.67	10.03	10.52	5.08	10.13	12.00
1.22	1.22	12.51	9.32	9.13	4.93	9.36	13.13	12.52	9.45	9.18	4.96	9.55	12.87
K	_	_	_	_	_	_		0.6109	0.7475	0.8433	0.8309	0.7666	0.6085
a	_	_	_	_	_	_		0.001191	0.001393	0.001269	0.001199	0.001474	0.002107
b	_	_	_	_	_	_		0.001073	0.001193	0.001185	0.000753	0.001179	0.001917
d	_	_	_	_	_	_		0.9252	0.5677	0.1452	0.3420	0.9118	0.9330

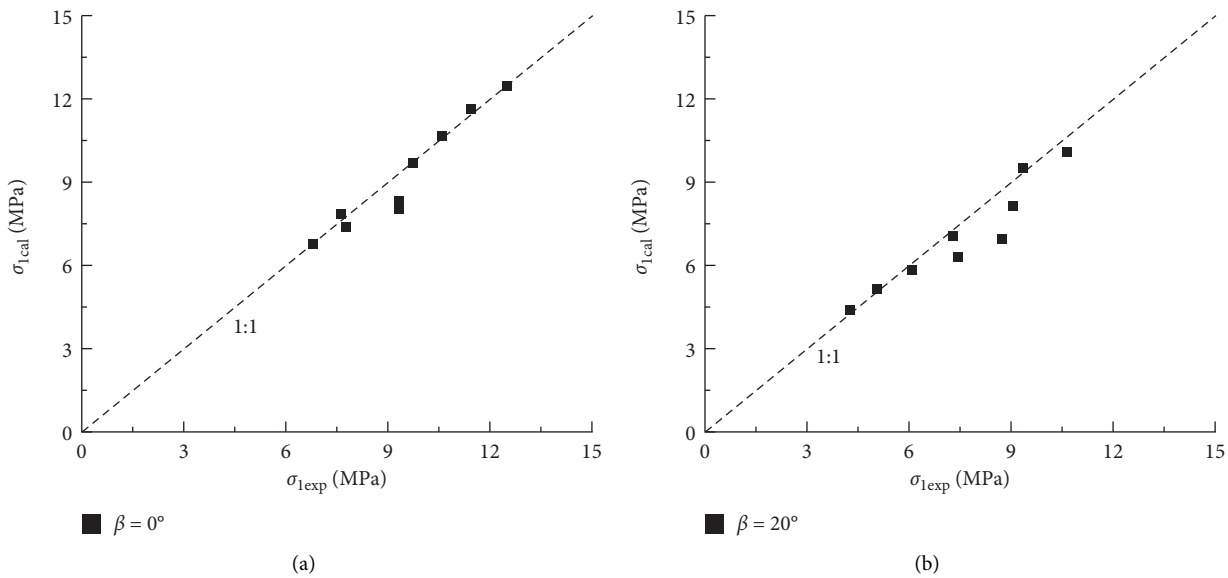

Figure 6: Continued.

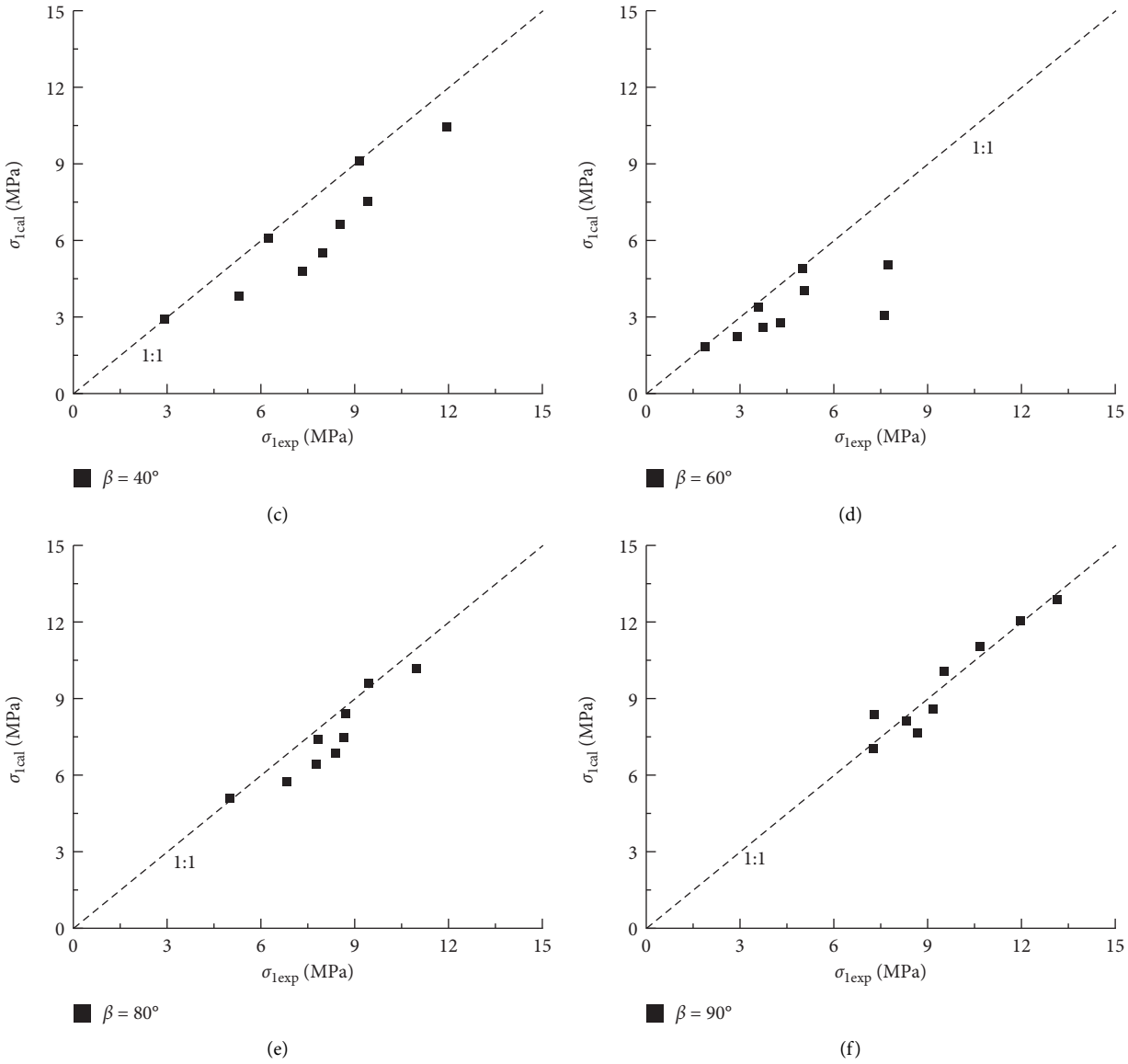

Figure 6: The comparison results of the calculated and experimental strength of jointed blocky mass for different joint inclination angles: (a–f) $\beta = 0^{\circ}$, 20°, 40°, 60°, 80°, and 90°.

were carried out on rock mass models with different joint inclination angles, which is made using similar material and contains three joint sets. Table 3 summarizes the strength data of both experimental and calculated results.

Figure 6 shows the comparison results of the calculated and experimental strength of jointed blocky mass. The data points except the joint inclination 60° are almost around the reference line. Thus, Figure 7 gives the fitting results of all the data and the data except the joint inclination 60°, and the relationship between σ_{1cal} and σ_{1exp} can be given by

$$\begin{aligned} \sigma_{1cal} &= 0.9247\sigma_{1exp}\,(\mathrm{R2} = 0.8738), \\ \sigma_{1cal} &= 0.9400\sigma_{1exp}\,(\mathrm{R2} = 0.9907), \end{aligned} \tag{11}$$

where equation (11) refers to the fitting results using all data and all data except the joint inclination 60°, respectively. In addition, two similar relationships suggested in [10, 28] are defined as follows:

$$\begin{aligned} \sigma_{1cal} &= 1.0150\sigma_{1exp}\,(R2 = 0.9383), \\ \sigma_{1cal} &= 1.0706\sigma_{1exp}\,(R2 = 0.8268). \end{aligned} \tag{12}$$

Table 3 also exhibits the percentage error in predicting strength data of rock mass models using these three strength criteria. Generally, compared with the modified Mohr–Coulomb failure criterion [28] and the empirical strength criterion [10], the proposed failure criterion in this

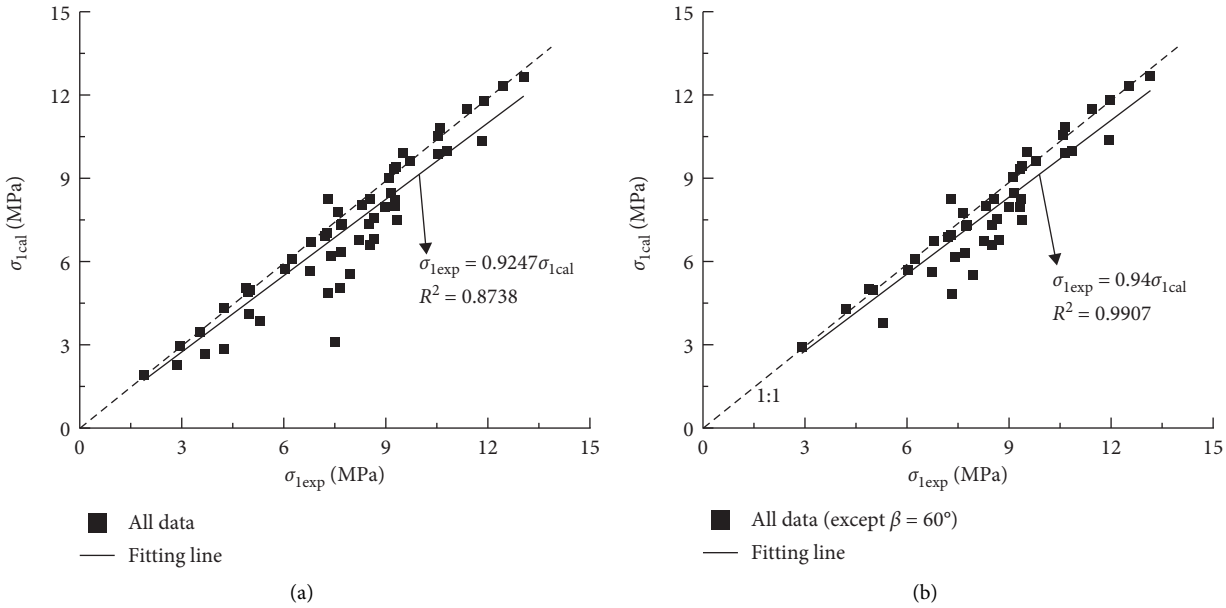

Figure 7: The fitting results of all the experimental strength of jointed blocky mass: (a) all the data and (b) all the data except $\beta = 60°$.

Table 4: Percentage error in predicting strength data of rock mass models.

σ_3 (MPa)	σ_2 (MPa)	Percentage error in predicting strength data at joint inclination angle β (°)					
		0	20	40	60	80	90
0.31	0.31	0.06	2.90	1.52	1.77	3.52	3.35
0.31	0.59	4.62	0.77	27.55	20.33	15.56	11.79
0.31	0.95	2.83	4.42	33.43	28.01	16.94	2.72
0.31	1.22	13.15	15.50	29.41	32.63	17.32	13.89
0.31	1.62	10.59	20.49	21.95	58.92	12.89	6.40
0.78	0.78	0.01	3.35	1.35	2.01	4.41	5.35
0.78	1.22	0.75	10.35	19.07	17.79	2.68	3.19
0.78	2.24	1.88	5.42	11.68	33.63	6.73	0.25
1.22	1.22	0.05	1.44	0.56	0.68	2.00	1.97
Average of this paper		3.77	7.18	16.28	21.75	9.12	5.43
Average of [14]		8.70	11.30	15.30	49.60	13.30	11.80
Average of [10]		17.80	8.36	15.60	29.70	7.70	12.50

study has higher correlation coefficient and smaller average percentage error, as shown in Table 4, which indicates that the proposed failure criterion is acceptable.

4. Conclusions

To investigate the influence of the joint orientation and σ_2 on the strength characteristics of jointed rock masses, a three-dimensional failure criterion is developed and is validated by two examples of true triaxial test results. Some important conclusions can be drawn as follows:

(1) The proposed failure criterion in the deviatoric plane adopts the elliptic form based on the Willam–Warnke failure criterion. The joint effect is considered by only one parameter, strength ratio K.

(2) The proposed failure criterion in the meridian plane uses the hyperbolic function to approximate the Mohr–Coulomb failure criterion so that the parameters can be linked with the cohesion and the internal friction angle.

(3) The proposed failure criterion in the presented study can achieve small percentage error and high correlation coefficient to predict the true triaxial strength data in two examples.

Data Availability

The data used to support the findings of this study are available from the corresponding author upon request.

Conflicts of Interest

The authors declare that they have no conflicts of interest.

Acknowledgments

The authors sincerely acknowledge the financial support from the National Natural Science Foundation of China under grant nos. 51621006 and 51839003. The authors also express their gratitude for the support from the Key Laboratory of Ministry of Education on Safe Mining of Deep Metal Mines, Northeastern University.

References

[1] G. F. Liu, Q. Jiang, G. L. Feng, D. F. Chen, B. R. Chen, and Z. N. Zhao, "Microseismicity-based method for the dynamic estimation of the potential rockburst scale during tunnel excavation," *Bulletin of Engineering Geology and the Environment*, vol. 80, no. 4, pp. 3605–3628, 2021.

[2] L. R. Alejano, J. Arzúa, N. Bozorgzadeh, and J. P. Harrison, "Triaxial strength and deformability of intact and increasingly

jointed granite samples," *International Journal of Rock Mechanics and Mining Sciences*, vol. 95, pp. 87–103, 2017.

[3] H. H. Einstein and R. C. Hirschfeld, "Model studies on mechanics of jointed rock," *Journal of the Soil Mechanics and Foundations Division*, vol. 99, no. 3, pp. 229–248, 1973.

[4] X. Hao, Y. Wei, K. Yang et al., "Anisotropy of crack initiation strength and damage strength of coal reservoirs," *Petroleum Exploration and Development*, vol. 48, no. 1, pp. 243–255, 2021.

[5] P. H. S. W. Kulatilake, J. Liang, and H. Gao, "Experimental and numerical simulations of jointed rock block strength under uniaxial loading," *Journal of Engineering Mechanics*, vol. 127, no. 12, pp. 1240–1247, 2001.

[6] M. H. B. Nasseri, K. S. Rao, and T. Ramamurthy, "Anisotropic strength and deformational behavior of himalayan schists," *International Journal of Rock Mechanics and Mining Sciences*, vol. 40, no. 1, pp. 3–23, 2003.

[7] O. Saeidi, V. Rasouli, R. G. Vaneghi, R. Gholami, and S. R. Torabi, "A modified failure criterion for transversely isotropic rocks," *Geoscience Frontiers*, vol. 5, no. 2, pp. 215–225, 2014.

[8] M. Singh, K. S. Rao, and T. Ramamurthy, "Strength and deformational behaviour of a jointed rock mass," *Rock Mechanics and Rock Engineering*, vol. 35, no. 1, pp. 45–64, 2002.

[9] Y. Gao, X.-T. Feng, Z. Wang, and X. Zhang, "Strength and failure characteristics of jointed marble under true triaxial compression," *Bulletin of Engineering Geology and the Environment*, vol. 905, no. 3, pp. 891–905, 2020.

[10] X. Liu, Q. Liu, Y. Kang, and Y. Pan, "Improved nonlinear strength criterion for jointed rock masses subject to complex stress states," *International Journal of Geomechanics*, vol. 18, no. 3, Article ID 04017164, 2018.

[11] P. Kapang, C. Walsri, T. Sriapai, and K. Fuenkajorn, "Shear strengths of sandstone fractures under true triaxial stresses," *Journal of Structural Geology*, vol. 48, pp. 57–71, 2013.

[12] M. A. Kwàsniewski and K. Mogi, "Effect of the intermediate principal stress on the failure of a foliated anisotropic rock," in *Proceedings of the Third International Conference on Mechanics of Jointed and Faulted Rock*, H. P. Rossmanith, Ed., Rotterdam, Netherlands, April 1990.

[13] G. Reik and M. Zacas, "Strength and deformation characteristics of jointed media in true triaxial compression," *International Journal of Rock Mechanics and Mining Sciences & Geomechanics Abstracts*, vol. 15, no. 6, pp. 295–303, 1978.

[14] R. P. Tiwari and K. S. Rao, "Response of an anisotropic rock mass under polyaxial stress state," *Journal of Materials in Civil Engineering*, vol. 19, no. 5, pp. 393–403, 2007.

[15] J. F. Labuz and A. Zang, "Mohr-coulomb failure criterion," *Rock Mechanics and Rock Engineering*, vol. 45, no. 6, pp. 975–979, 2012.

[16] E. Hoek and E. T. Brown, "Empirical strength criterion for rock masses," *Journal of Geotechnical Engineering*, vol. 106, no. GT9, pp. 1013–1035, 1980.

[17] A. Al-Ajmi and R. W. Zimmerman, "Relation between the mogi and the coulomb failure criteria," *International Journal of Rock Mechanics and Mining Sciences*, vol. 42, no. 3, pp. 431–439, 2005.

[18] C. Chang and B. Haimson, "A failure criterion for rocks based on true triaxial testing," *Rock Mechanics and Rock Engineering*, vol. 45, no. 6, pp. 1007–1010, 2012.

[19] X. Ma, J. W. Rudnicki, and B. C. Haimson, "The application of a matsuoka–nakai–lade–duncan failure criterion to two porous sandstones," *International Journal of Rock Mechanics and Mining Sciences*, vol. 92, pp. 9–18, 2017.

[20] K. Mogi, "Fracture and flow of rocks under high triaxial compression," *Journal of Geophysical Research*, vol. 76, no. 5, pp. 1255–1269, 1971.

[21] X.-T. Feng, R. Kong, C. Yang et al., "A three-dimensional failure criterion for hard rocks under true triaxial compression," *Rock Mechanics and Rock Engineering*, vol. 53, no. 12, pp. 103–111, 2019.

[22] D. C. Drucker and W. Prager, "Soil mechanics and plastic analysis or limit design," *Quarterly of Applied Mathematics*, vol. 10, no. 2, pp. 157–165, 1952.

[23] P. V. Lade and J. M. Duncan, "Elastoplastic stress-strain theory for cohesionless soil," *Journal of the Geotechnical Engineering Division*, vol. 101, no. 10, pp. 1037–1053, 1975.

[24] G. A. Wiebols and N. G. W. Cook, "An energy criterion for the strength of rock in polyaxial compression," *International Journal of Rock Mechanics and Mining Sciences & Geomechanics Abstracts*, vol. 5, no. 6, pp. 529–549, 1968.

[25] H. Jiang and J. Zhao, "A simple three-dimensional failure criterion for rocks based on the hoek-brown criterion," *Rock Mechanics and Rock Engineering*, vol. 48, no. 5, pp. 1807–1819, 2015.

[26] N. Melkoumian, S. D. Priest, and S. P. Hunt, "Further development of the three-dimensional Hoek-Brown yield criterion," *Rock Mechanics and Rock Engineering*, vol. 42, no. 6, pp. 835–847, 2009.

[27] L. Zhang and H. Zhu, "Three-dimensional hoek-brown strength criterion for rocks," *Journal of Geotechnical and Geoenvironmental Engineering*, vol. 133, no. 9, pp. 1128–1135, 2007.

[28] M. Singh and B. Singh, "Modified mohr-coulomb criterion for non-linear triaxial and polyaxial strength of jointed rocks," *International Journal of Rock Mechanics and Mining Sciences*, vol. 51, pp. 43–52, 2012.

[29] Q. Zhang, S. Wang, X. Ge, and H. Wang, "Modified Mohr-Coulomb strength criterion considering rock mass intrinsic material strength factorization," *Mining Science and Technology (China)*, vol. 20, no. 5, pp. 701–706, 2010.

[30] H. Rafiai, "New empirical polyaxial criterion for rock strength," *International Journal of Rock Mechanics and Mining Sciences*, vol. 48, no. 6, pp. 922–931, 2011.

[31] O. C. Zienkiewicz and G. N. Pande, "Some useful forms of isotropic yield surfaces for soil and rock mechanics," in *Finite Elements in Gemechanics*, G. Godehus, Ed., Wiley, New York, NY, USA, 1977.

[32] K. J. Willam and E. P. Warnke, "Constitutive model for the triaxial behaviour of concrete," in *Proceedings of the Presented at the Seminar on Concrete Structures Subjected to Triaxial Stresses*, pp. 1–30, ISMES, Bergamo, Italy, June 1975.

Hindawi
Advances in Civil Engineering
Volume 2021, Article ID 9997924, 10 pages
https://doi.org/10.1155/2021/9997924

Research Article

Analysis of Damage Mechanism of Tunnel Lining Structure under the Coupling Action of Active Fault

Guotao Yang[1], **Sujian Ma**[2], **Liang Zhang**[2], **Xinrong Tan**[3], **Rui Tang**[4] and **Yang Liu**[5]

[1]*China State Railway Group Co., Ltd., Beijing 100844, China*
[2]*Department of Civil Engineering, Southwest Jiaotong University, Chengdu 610031, China*
[3]*China Railway Eryuan Engineering Group Co., Ltd., Chengdu 610031, China*
[4]*Sichuan Highway Planning, Survey, Design and Research Institute Ltd., Chengdu 610041, China*
[5]*Zhongke (Hunan) Advanced Rail Transit Research Institute Co., Ltd., Zhuzhou 412000, China*

Correspondence should be addressed to Liang Zhang; zhangliangdpme@my.swjtu.edu.cn

Received 8 March 2021; Accepted 6 May 2021; Published 20 May 2021

Academic Editor: Guang-Liang Feng

To reveal the failure mechanism of tunnel structure under active fault movement, based on the pseudostatic elastoplastic finite element method, the failure modes of the tunnel lining are studied under different movement ratios of strike-slip faults and thrust faults with 45° dip angle by using numerical simulation. The results show that the range of significant lining failure section can be determined according to any direction of the coupling fault movement decomposition direction, and the damage effect is determined by the overall movement amount of the coupling fault. The significant damage area of the lining under the action of the coupling fault is the same as the area of deformation, which mainly manifests as tensile failure. Compressive failure occurs in the boundary area between the fracture zone and the hanging wall and foot wall. The plastic strain is the largest in the area where the arch waist and the arch bottom intersect. The development of tunnel lining plastic zone under coupling fault is from arch top and arch bottom to both sides of the arch waist. The development of the plastic zone under active fault is mainly determined by the form of fault with a large ratio. The research results can provide a reference for the design and safety evaluation of tunnel crossing active faults.

1. Introduction

The underground structure has better antivibration performance under the pressure of surrounding rock, but related studies have shown [1–4] that the tunnel structure that crosses an active fault will cause more catastrophic damage under the movement of the active fault and even cause the structure to collapse [5–7], which will cause considerable economic losses. In the construction of tunnel engineering, relevant codes stipulate the fault section based on the principle of avoidance. However, the direction of the tunnel route nowadays is more inclined to its demand for traffic function, resulting in increasing section tunnels inevitably crossing the active fault zone [8, 9].

At present, domestic and foreign experts and scholars have achieved some meaningful results in the study of tunnels through active faults. Chen [10] established the surface fracture zone length caused by fault movement in the Taiwan area, the east and west of China, Japan, and India. Two statistical regression formulas for fracture length and magnitude were established to estimate the length of the surface fracture zone through the magnitude and estimate the magnitude through the length of the surface fracture. Wells and Coppersmith [11] collected 244 relatively complete seismic records for statistical analysis and established the relationship between the magnitude and surface, underground fracture length, and surface movement worldwide. Cole and Lade [12] gave a simplified model for predicting the shape and distribution of ground fractures caused by bedrock movement through sand box test and theoretical analysis and summarized three key factors that have an impact: soil thickness, dilatancy angle, and fault dip.

Bransby et al. [13, 14] simulated normal and inverse faults with a fault dip of 60° through centrifuge tests, considering the effect of changing the load on the upper part of the soil layer and changing the position of the rigid foundation on the fracture of the soil layer. Lin et al. [15, 17] simulated the deformation and failure characteristics of tunnels under thrust fault movement through the designed fault test device, studied the influence of relevant parameters on the tunnel structure, and verified the experimental conclusions by numerical simulation. Sabagh and Ghalandarzadeh [18] used a series of finite element numerical models to evaluate the behavior of tunnel and reverse fault intersections. The numerical simulation results of 60° reverse fault in free field mode and tunnel mode are verified by centrifugal test. An et al. [19] proposed a two-level design method of fault dislocation and established a three-dimensional finite element model to estimate the tunnel response under fault dislocation. Zhang et al. [20] established a three-dimensional geomechanical model with faults, used the regional inversion method to obtain the regional stress field distribution under the fault condition, and used the mathematical statistics method to obtain the initial stress field of Daxiangling tunnel. Taking the inclined shaft of Muzhailing highway tunnel as the engineering background, Tao et al. [21] evaluate the supporting effect of carbonaceous slate and the deformation of surrounding rock through model test.

The above research results are of great significance to the construction of tunnels crossing active faults, but also face some complex problems. For example, the preliminary work of statistical data is complicated, and the data is numerous, the mechanism of fault fracture is more complicated, the dispersion of test results is large, the numerical simulation has limitations, etc. Current research needs to be further in depth for guiding engineering practice and seismic design. On the basis of summarizing previous studies, this paper uses a pseudostatic elastic-plastic finite element analysis method based on a domestic tunnel project and estimates the structural damage of the lining from the deformation mechanism, the maximum principal stress distribution and the development of the plastic zone through a large number of calculations, and the failure mechanism of the lining under the complex coupling action of the fault is revealed.

2. Three-Dimensional Finite Element Numerical Model Establishment and Parameter Selection

Relying on an actual tunnel in China, based on the three-dimensional finite element software ABAQUS, this paper established a three-dimensional finite element model of the fracture zone with a 45° dip angle with different strike-slip and thrust ratios. According to the survey data in the preconstruction period, the width of the model fracture zone is 40 m and 180 m before and after the fracture zone is taken to establish a tunnel calculation model for coupling active fault. The cross-sectional shape of the tunnel is drawn with a five-centered circle similar to the actual project. The maximum inner diameter is 10 m, the height is 7 m, the lining wall thickness is 0.5 m, and the tunnel buried depth is 28 m. The domestic tunnel construction empirical practice believes that when the transverse section size is 5–10 times the tunnel section size, the artificial boundary has little effect on the calculation results [22]. Therefore, the cross section size of the model is 70 m, which is 10 times the height of the tunnel and 7 times the width. The model size is 400 m × 70 m × 70 m, and the model calculation diagram is shown in Figure 1.

As shown in Figure 1, the *abcd* segment is the hanging wall area of the active fault, and the *efgh* segment is the foot wall area of the active fault. The fault movement is realized by applying constraint boundary conditions and applying displacement load boundary conditions. This calculation model simulates the failure of the lining under different fault displacements and different ratios of the two displacements. The coupling fault displacement is dominated by thrust faults, and the maximum displacement is 4.0 m. Considering the most unfavorable effects, the calculation model sets a lower movement rate, and each analysis step movement is 0.1 m; that is, the simulated movement rate is 0.1 m/s, which gives the surrounding rock sufficient deformation and maximizes the damage of the tunnel lining [15, 16, 23]. To explore the damage mechanism of the tunnel lining structure under the coupling action of active faults, the constitutive relationship of the lining in the calculation model adopts the concrete structure damage constitutive, the lining material is C55 concrete, and the stress–strain relationship is defined in accordance with the code [24], as is shown in Table 1. The hanging wall and foot walls of the active fault and the fracture zone adopt the Mohr–Coulomb constitutive relationship. The reason for the fault movement along the slip surface of the fracture zone is that the fracture zone has low strength and is easy to damage. Therefore, the calculation model appropriately reduces the strength of the fracture zone according to a safety factor of 0.8. The specific calculation parameters are shown in Table 2. The model design considers the material properties and differences between the lining and the surrounding rock and defines the contact between the two as friction, and the friction parameter is 0.4 [25].

The model calculation is carried out in three steps. The initial ground stress is applied to the unexcavated rock and soil, so that it will not deform under the action of gravity, which simulates the rock and soil under long-term consolidation. After the initial ground stress is balanced, the tunnel excavation and the construction of the lining are simulated. The surrounding rock pressures all act on the lining and the lining will no longer be disturbed by deformation. After the lining and surrounding rock reach the state of balance, displacement loads are applied to the strike-slip direction (*Y*-direction) and thrust direction (*Z*-direction) of the hanging wall of the active fault to realize the coupling and movement of the active fault. The boundary conditions of the foot wall remain unchanged, and the load boundary conditions are shown in Figure 2.

Both the soil element and the lining element of the calculation model adopt hexahedral elements. The mesh is densely divided into the fracture zone and the rock mass

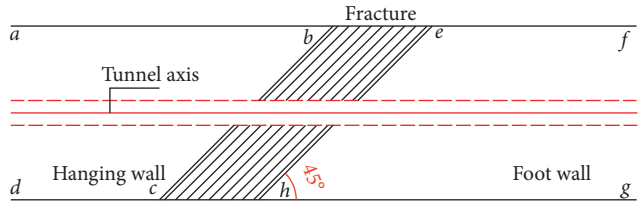

Figure 1: Schematic diagram of the calculation model for dip angle 45°.

Table 1: Material parameters of tunnel lining.

Model	Density (kg/m^3)	Elastic modulus (MPa)	Poisson's ratio	Compressive yield stress (MPa)	Tensile yield stress (MPa)
Lining	2400	2.648×10^4	0.167	32.5	2.64

Table 2: Material parameters of surrounding rock and fault.

Model	Density (kg/m^3)	Elastic modulus (MPa)	Poisson's ratio	Internal friction angle (°)	Cohesion (kPa)
Fault	2300	1.6×10^3	0.4	28	0.1×10^3
Surrounding rock	2400	3.5×10^3	0.32	35	0.4×10^3

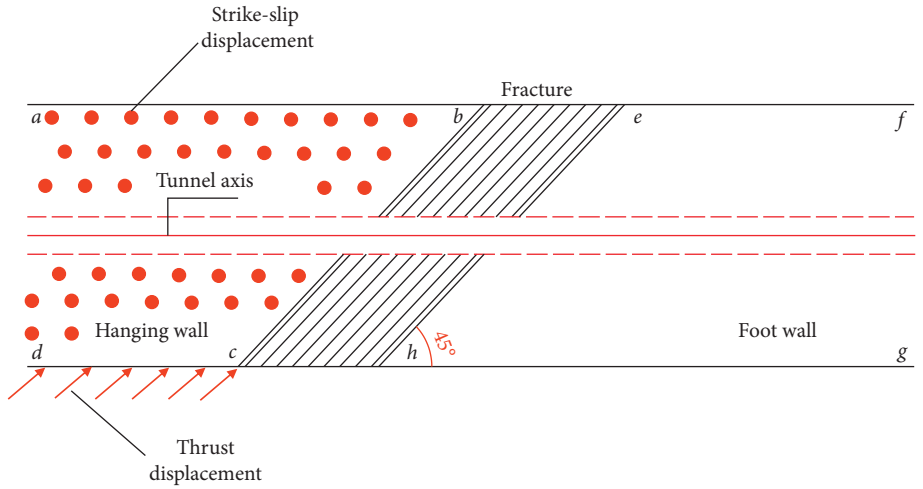

Figure 2: Schematic diagram of the coupling fault displacement load distribution.

around the tunnel lining, and the soil mesh is sparse near the boundary, which ensures the accuracy and reliability of the calculation results and the efficiency of the calculation. The mesh is shown in Figure 3.

3. Safety Analysis of Tunnel Lining with Different Movement Amounts under the Coupling Action of Active Faults

Under strike-slip fault movement, the hanging wall and foot wall move horizontally along the fracture surface. The stress source of fault movement is the shearing action on both sides. The movement surface is smooth, and the shearing effect is obvious [26]. Thrust faults are forward faults with a large displacement distance, showing strong compression [27]. Because the fault movement of the calculation model is dominated by thrust faults, this paper selects the tunnel lining arch vault measurement points under different movements with the ratio of strike-slip fault to thrust fault at 1 : 2 for safety analysis.

Fault movement is divided into stick-slip movement and creeping movement. Stick-slip movement is a kind of rapid fracture motion, and creeping movement is a slow movement that occurs over time. Studies have shown that the slow movement of the fault gives the soil a sufficient deformation process, and the failure form is larger than the stick-slip movement [28]. To explore the influence of the movement amount on the tunnel lining under the coupling action of active faults, this paper takes the lining response when the continuous movement amount of the thrust fault in the coupling fault is 0.1 m, 0.2 m, 0.3 m, 0.4 m, 0.5 m, and 0.6 m. And the failure mechanism of the tunnel lining under different displacements of the coupling fault is revealed through the longitudinal displacement distribution of the lining along the tunnel, the distribution of the maximum

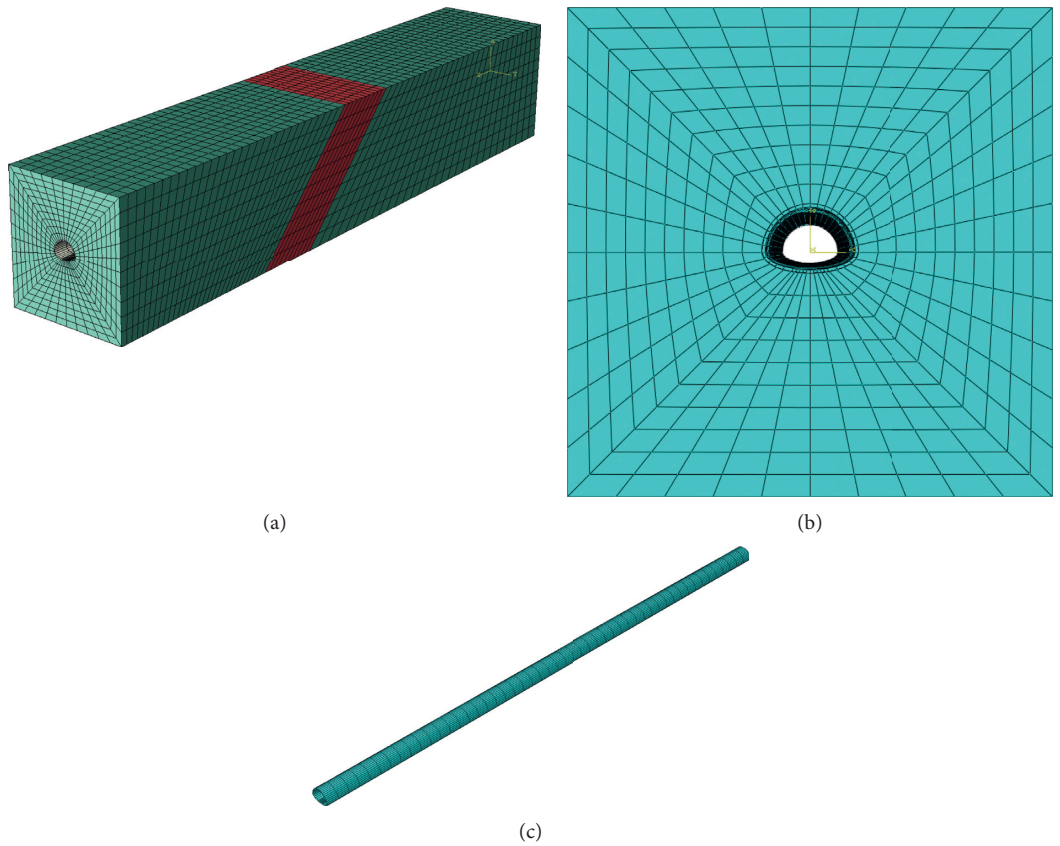

(a) (b) (c)

Figure 3: The meshing diagram of calculation model. (a) The meshing diagram of the overall calculation model. (b) The meshing diagram of the transverse section of the calculation model. (c) The meshing diagram of tunnel lining.

principal stress, and the distribution of the development range of the plastic zone.

3.1. Displacement Response Analysis of Tunnel Lining with Different Movement Amounts under the Coupling Active Fault. Since the coupling fault displacement load is applied in the *Y*-direction and the *Z*-direction, the *Y*-direction and *Z*-direction tunnel lining vault displacement distribution is taken for analysis. Figure 4(a) is the deformation cloud diagram of lining when the fault displacement is 0.4 m, and Figure 4(b) shows the *Y*-direction displacement distribution curve of the lining under different displacements when the coupling ratio between strike-slip fault and thrust fault is 1 : 2, and Figure 4(c) is the *Z*-direction displacement distribution curve of the lining.

Comprehensive analysis of Figure 4 shows that the coupling fault movement drives the lining in the hanging wall area to move in the same form in the strike-slip direction and the thrust direction. The movement platform appears along the lining displacement curve in the longitudinal direction of the tunnel, and the range of the platform is roughly the same as that of the hanging wall of the fault. The coupling fault is 1 : 2 moving in the *Y*- and *Z*-directions, and the lining displacement response is roughly 1 : 2, and the projection of the lining displacement value in the two directions is consistent with the displacement load value. The shape of the lining displacement curve in two directions under the coupling fault movement is "S"-shaped distribution, and the deformation shows a steep drop in the projection area at the bottom of the fracture zone along the longitudinal direction. Since the dip angle of the fracture zone is 45°, the fault projection area is within the range of 110 m~220 m. With the increase of the movement amount of the active fault, the curved platform continues to rise, the slope of the curve in the steep decline section gradually increases, but the range and location of the platform does not change significantly. The steep drop section of the *Y*-direction curve is roughly within the range of 140~200 m, and the steep drop section of the *Z*-direction curve is roughly within the range of 140~200 m. Therefore, the significant damage area of the lining under the coupling active fault is roughly located in the fracture zone. With the increase of the movement of the active fault, the damage range does not change significantly, but the damage effect increased significantly. The significant deformation section of the lining can be judged according to the displacement curve of the projection direction of the coupling fault motion.

3.2. Stress Response Analysis of Tunnel Lining with Different Movement Amounts under the Coupling Active Fault. Since the tunnel lining material is C55 concrete, the maximum principal stress is used as the lining stress response analysis index to study the structural damage mechanism of

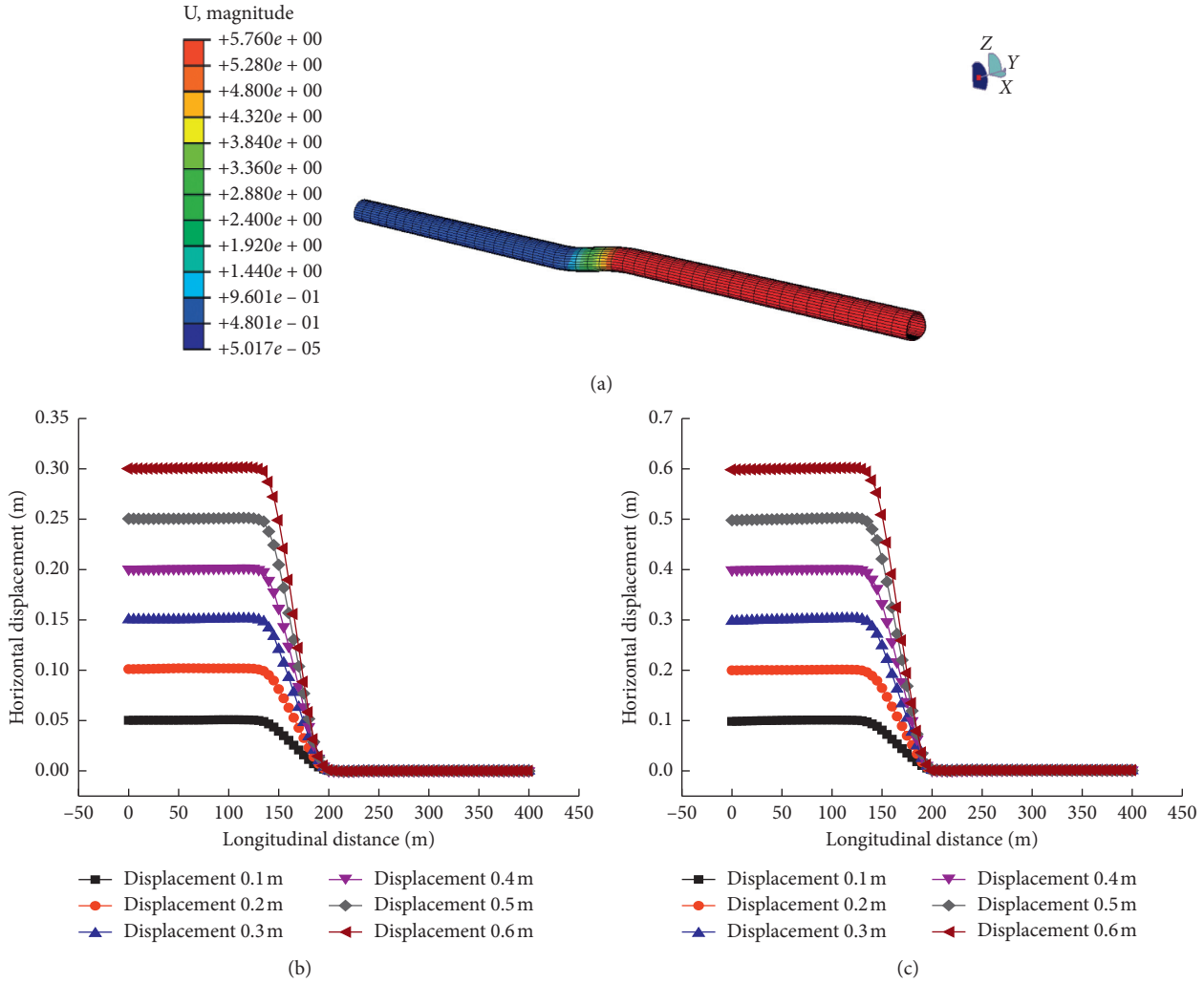

Figure 4: Displacement diagram in different directions under coupling fault. (a) The deformation cloud diagram of lining when the fault displacement is 0.4 m. (b) *Y*-direction displacement curve of lining with different movement amounts in the coupling ratio of 1 : 2. (c) *Z*-direction displacement curve of lining with different movement amounts in the coupling ratio of 1 : 2.

the lining. According to the calculation results, the maximum principal stress distribution curve of the lining with different movements under the coupling fault action is shown in Figure 5.

From a comprehensive analysis of Figure 5, it can be seen that the maximum principal stress curve of the lining under the dip angle of 45° coupling fault movement is symmetrically distributed along the longitudinal direction of the tunnel with the axis of symmetry approximately 140 m. The shape of the distribution curve of the maximum principal stress of the lining under different displacements is roughly similar. When the thrust direction of the coupling fault is misaligned by 0.1 m, the maximum principal stress of the hanging wall is larger than other displacements. The maximum principal stress is the tensile stress before 140 m along the longitudinal direction of the tunnel, and the stress value gradually increases with the longitudinal distance. The maximum tensile stress appears near 140 m, and the compressive stress appears near 200 m in the longitudinal direction of the tunnel, and the lining begins to undergo compression failure. The maximum principal stress of the lining in the foot wall area is basically 0. The foot wall lining of the coupling fault movement shows obvious tensile failure, and the significant increase area of the maximum principal stress is located at the location of the fracture zone. Compression failure occurs at the contact position of the foot wall and the fracture zone, and the tensile failure range of the lining is roughly consistent with the position of the steep drop of the lining displacement curve. Therefore, it can be inferred that the significant damage area of the lining under the action of the coupling fault is the same as the significant area of displacement deformation, which is roughly located near the fracture zone and mainly manifests as tensile failure.

3.3. Analysis of the Development of the Plastic Zone of the Tunnel Lining under the Coupling Effect of Active Faults with Different Displacements. The real-time monitoring method of tunnel lining and the analysis and processing of deformation data have important practical significance for ensuring the stability of the tunnel [29–31]. As one of the important

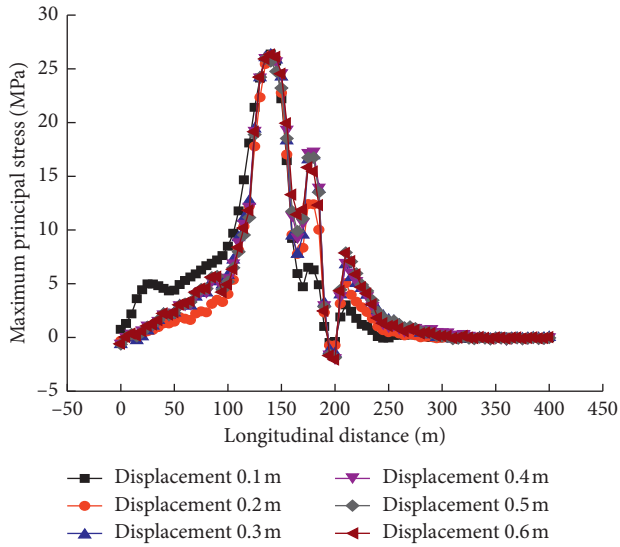

Figure 5: Maximum principal stress distribution curve of the lining with different displacements under coupling fault action.

indicators of lining structure damage, the plastic zone plays an essential role in the monitoring of tunnel construction. Figure 6 is the cloud diagram of the development of the plastic zone of tunnel lining with different displacements under the coupling fault action.

Comprehensive analysis of Figure 6 shows that, at the beginning of the coupling fault, the plastic zone is distributed on the lining vault and the arch bottom, and the distribution range is roughly concentrated on the vault at the intersection of the hanging wall and the fracture zone and the arch bottom at the intersection of the foot wall and the fracture zone. As the amount of coupling fault movement increases, the plastic zone at the top and bottom of the arch continues to expand and connect with both sides of the arch waist. When the coupling fault is displaced for a certain distance, the position of the plastic zone of the tunnel lining changes from the top and bottom of the arch to both sides of the arch waist. The development range of the plastic zone is concentrated in the fracture zone, and the plastic zone on both sides of the arch waist increases with the increase of the active fault movement amount. The cloud diagram of the development of the plastic zone scatters from the center to the surroundings in a discord shape, and the plastic strain is the largest in the area where the arch waist and the arch bottom intersect. The development law of the plastic zone of tunnel lining under coupling fault movement is similar to that of tunnel lining under thrust fault movement. Therefore, the development of plastic zone under active fault movement is mainly determined by the form of fault movement with larger ratio.

4. Safety Analysis of Tunnel Lining with Different Displacement Ratios under the Coupling Action of Active Faults

To explore the influence of different movement ratios on the tunnel lining under the coupling action of active faults, three different ratios of strike-slip and thrust movement ratios of 1 : 1, 1 : 2, and 1 : 3 are taken in this paper, to study the response of the lining when the continuous displacement of the thrust fault is 1.4 m in the coupling fault. And the failure mechanism of the tunnel lining under the different displacements of the coupling fault is revealed through the longitudinal displacement distribution of the lining along the tunnel, the distribution of the maximum principal stress, and the distribution of the development range of the plastic zone.

4.1. Displacement Response Analysis of Tunnel Lining with Different Movement Ratios under the Coupling Active Fault. Coupling active faults are a combination of strike-slip faults and thrust faults. Therefore, it is necessary to study the *Y*- and *Z*-direction lining displacement curves separately. The ratio of strike-slip movement and thrust movement of the 45° fracture zone is 1 : 1, 1 : 2, and 1 : 3, as shown in Figure 7.

It can be seen from Figure 7(a) that since the movement of the active fault is dominated by the thrust fault, the data of different movement ratios of the strike-slip fault and the thrust fault under the coupling fault under 1.4 m of the thrust fault movement are selected for analysis. Therefore, the *Y*-direction lining displacement curve has a movement platform, and the range of the platform is roughly the same as the bottom of the fault hanging wall. With the change of the coupling fault movement ratio, the platform height of the *Y*-direction lining displacement curve gradually decreases, and the platform range does not change significantly. The lining displacement value is roughly the same as the *Y*-direction displacement load applied value, the lining and the hanging wall do the same form of movement. The *Y*-direction lining displacement curve is distributed in an "S" shape, and there is a steep drop in the projection area at the bottom of the fracture zone along the longitudinal direction. With the increase of the movement ratio, the dip angle of the steep-descent section increases continuously, and the damage effect increases significantly, while the significant

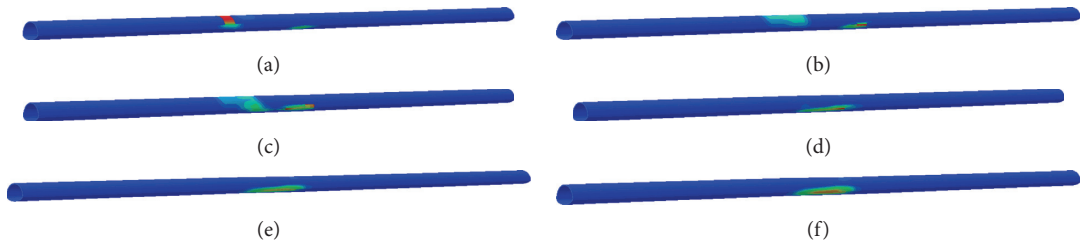

Figure 6: The cloud diagram of the development range of the plastic zone of tunnel lining with different displacements under the coupling fault action. (a) The cloud diagram of plastic zone of 0.1 m tunnel lining with coupling fault movement. (b) The cloud diagram of plastic zone of 0.2 m tunnel lining with coupling fault movement. (c) The cloud diagram of plastic zone of 0.3 m tunnel lining with coupling fault movement. (d) The cloud diagram of plastic zone of 0.4 m tunnel lining with coupling fault movement. (e) The cloud diagram of plastic zone of 0.5 m tunnel lining with coupling fault movement. (f) The cloud diagram of plastic zone of 0.6 m tunnel lining with coupling fault movement.

damage range is roughly concentrated in the same range of the fracture zone.

It can be seen from Figure 7(b) that the coupling fault Z-direction bears a vertical displacement load of 1.4 m, and the lining displacement curve shows a movement platform along the longitudinal direction of the tunnel. The range of the platform is the same as the bottom of the hanging wall of the fault, and the displacement curve shows an "S"-shaped distribution of the same shape. The Z-direction displacement curve shows a steep drop in the fracture zone along the longitudinal direction of the tunnel, and the significant damage area of the lining at 45° dip angle of the fracture zone is approximately 140 m~200 m. Therefore, the significant damage area of the lining under the coupling active fault movement is roughly located in the fracture zone, and the two directions are the same. With the increase of the movement ratio, the damage effect becomes more obvious while the damage range is basically unchanged. The range of the significant damage section of the lining can be determined according to any direction of the coupling fault movement decomposition direction, and the damage effect needs to be determined by the overall movement of the coupling fault.

4.2. Response Analysis of Tunnel Lining Stress with Different Movement Ratios under the Coupling Active Fault. To explore the influence of the stress distribution on the tunnel lining under different movement ratios of strike-slip and thrust faults, the maximum principal stress distribution along the longitudinal length of the tunnel is calculated according to the calculation results, as shown in Figure 8.

Comprehensive analysis of Figure 8 shows that the maximum principal stress curve of the lining under different movement ratios of the 45° dip angle coupling fault is symmetrically distributed along the longitudinal direction of the tunnel with the axis of symmetry approximately 140 m. The shape of the maximum principal stress distribution curve of the lining under different displacement ratios is roughly similar, and the maximum principal stress distribution curve shows a trend of first increasing and then decreasing as a whole. The stress increase area along the longitudinal length of the tunnel is roughly located near the fracture zone. The maximum principal stress continues to increase before 140 m, and the maximum appears at 140 m, which is a tensile stress, and the lining shows tensile failure. Compressive stress occurs in the lining at the boundary between the fracture zone and the hanging wall and foot wall, and compression failure occurs. The maximum principal stress of the lining in the foot wall is basically zero. The lining tensile stress distribution area under the coupling fault movement is wide, so the lining mainly shows tensile failure. The significant tensile failure range of the lining is roughly consistent with the position of the steep drop of the lining displacement curve, showing a consistent change law.

4.3. Analysis of the Development of the Plastic Zone of the Tunnel Lining under the Coupling Effect of Active Faults with Different Movement Ratios. In order to explore the influence of the development of the plastic zone on the tunnel lining under different movement ratios of the coupling active fault, according to the calculation results, the cloud diagram of the development range of the plastic zone of the lining under different movement ratios when the coupling fault is displaced at a 45° angle of 1.4 m is obtained, as shown in Figure 9.

Comprehensive analysis of Figure 9 shows that the distribution of the plastic zone under different ratios of the coupling faults is roughly concentrated in the middle of the fracture zone. When the coupling fault movement ratio is 1 : 1, the plastic zone is concentrated in the arch bottom and waist area of the tunnel lining, and the arch bottom is mainly distributed, and the plastic strain value is discord shape and scatters to the surroundings. With the increase of the movement ratio, the position of the plastic zone of the lining begins to expand from the arch bottom to both sides of the arch waist, and the range increases accordingly. The development law of the plastic zone area under different proportions of movement is similar to the development law of tunnel lining under thrust fault. Therefore, it can be inferred that the development of lining plastic zone is related to the fault movement formed in the dominant direction in the coupling fault, and the development law is affected by the development law of the lining plastic zone under its sole action. The lining plastic zone is roughly concentrated in the fracture zone, which is consistent with the tensile stress

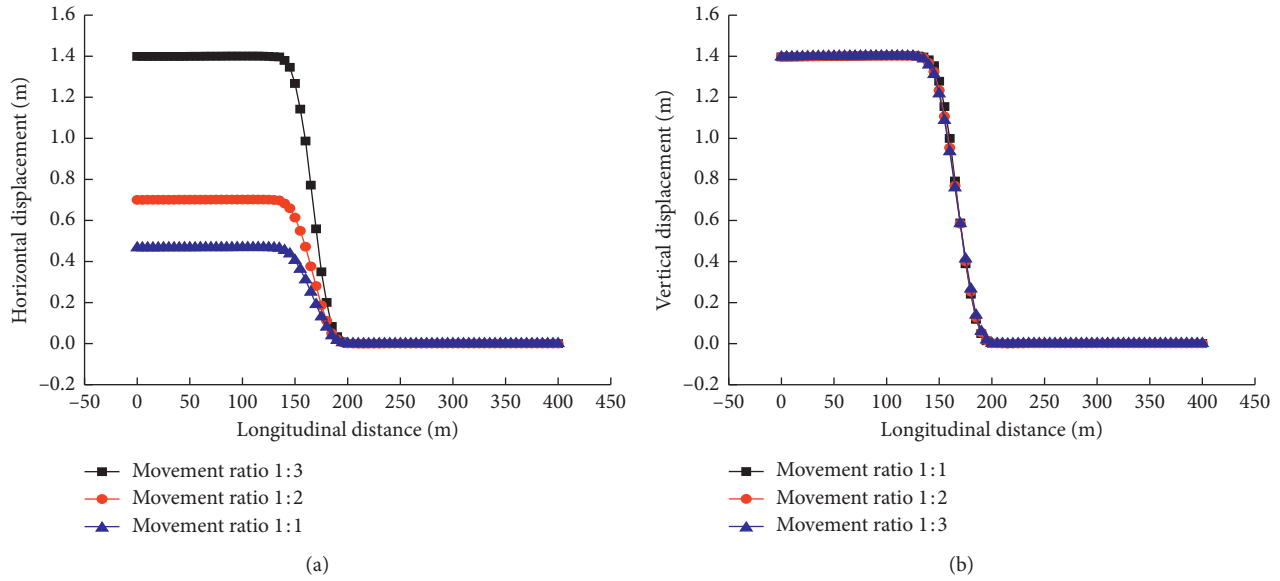

Figure 7: Displacement curves of tunnel lining with different movement ratios of 45°dip angle under coupling fault. (a) *Y*-direction lining displacement curve with different movement ratios under coupling fault. (b) *Z*-direction lining displacement curve with different movement ratios under coupling fault.

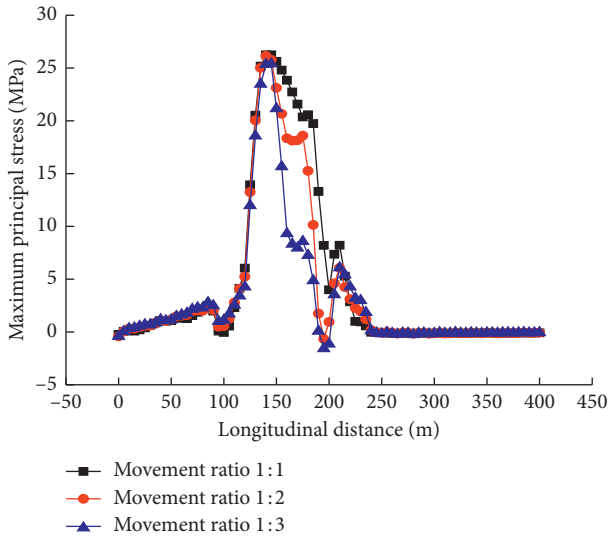

Figure 8: Maximum principal stress distribution curve of the lining with different movement ratios under the coupling fault.

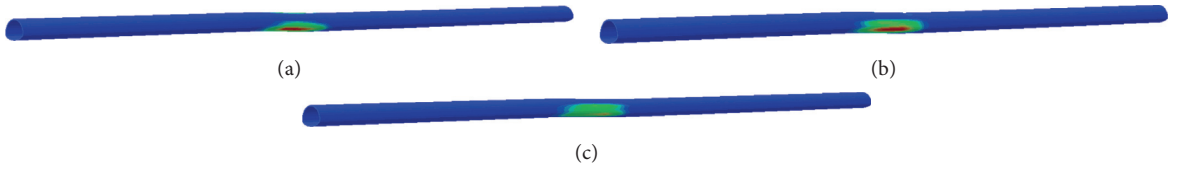

Figure 9: The cloud diagram development range of the plastic zone of the lining with different ratios of 1.4 m at the 45° dip angle. (a) The cloud diagram of plastic zone of 1.4 m tunnel lining with a ratio of 1 : 1. (b) The cloud diagram of plastic zone of 1.4 m tunnel lining with a ratio of 1 : 2. (c) The cloud diagram of plastic zone of 1.4 m tunnel lining with a ratio of 1 : 3.

distribution area of the maximum principal stress of the lining along the longitudinal direction of the tunnel.

5. Conclusion

This paper establishes a three-dimensional finite element tunnel model under the coupling movement of strike-slip and thrust faults, discusses the displacement, stress distribution, and plastic zone development of the tunnel lining under different movements and different movement ratios of the coupling faults, and reveals the damage mechanism of the lining under the active fault movement, and the conclusions are as follows:

(1) The coupling fault movement drives the lining in the hanging wall area to move in the same form in the strike-slip direction and the thrust direction. The significant damage area of the lining under the coupling active fault movement is roughly located in the fracture zone. With the increase of the movement amount of the active fault, the damage effect increases significantly. The range of the significant damage section of the lining can be determined according to any direction of the coupling fault movement decomposition direction, and the damage effect needs to be determined by the overall movement of the coupling fault.

(2) The tunnel lining of the coupling fault movement shows obvious tensile failure. The significant growth area of the maximum principal stress is located at the fracture zone, and compression failure occurs at the contact position of the foot wall and the fracture zone. The lining mainly shows tensile failure, and the significant tensile damage range of the lining is roughly consistent with the position of the steep drop of the lining displacement curve. It can be inferred that the significant damage area of the lining under the action of the coupling fault is the same as the significant displacement change area, which are roughly located near the fault zone and mainly manifested as tensile failure.

(3) At the beginning of the coupling fault, the plastic zone is distributed on the lining vault and the arch bottom. With the increase in the amount of coupling fault movement, the plastic zone at the top and bottom of the arch continues to expand and connect on both sides of the arch waist. The plastic strain is the largest in the area where the arch waist and the arch bottom intersect. The development of plastic zone under active fault movement is mainly determined by the form of fault movement with larger ratio.

Data Availability

The data used to support the findings of this study are available from the corresponding author upon request.

Conflicts of Interest

The authors declare that they have no conflicts of interest regarding the publication of this paper.

Acknowledgments

This study was supported in part by the Science and Technology Research and Development Plan of China National Railway Corporation Limited (no. K2019G009); National Natural Science Fund Project (no. 52078426); National Key Research and Development Plan (no. 2018YFE0207100); Sichuan Provincial Science and Technology Support Project (nos. 2020YJ0253, 2020YFSY0060, 2019JDRC0133, and 2019JDRC0134); China Railway Eryuan Engineering Group Co., Ltd. Scientific Research Project (KYY2019034(19-22) and KYY2019070(19-20)); and China National Railway Group Co., Ltd. Scientific Research Project (nos. SY2016G003 and N2020T004).

References

[1] P. Geng, C. He, and Q. X. Yan, "The current situation and prospect of seismic analysis methods for tunnel structure," *China Civil Engineering Journal*, vol. 46, no. S1, pp. 262–268, 2013.

[2] Y. S. Shen, L. Z. Tang, and P. F. Zhou, "Research on anti-seismic technology of railway tunnel structure crossing soft and hard interface in strong earthquake area," *Railway Standard Design*, vol. 62, no. 10, pp. 123–129, 2018.

[3] L. M. Qu, X. M. Ding, G. Kouroussis, and C. J. Zheng, "Dynamic interaction of soil and end-bearing piles in sloping ground: numerical simulation and analytical solution," *Computer and Geotechnics*, vol. 134, 2021.

[4] J. M. Zhou, Y. Cheng, S. W. Zou, Y. Zhou, and K. Huang, "Research on tunnel mechanical characteristics under fault movement and earthquake," *Railway Standard Design*, vol. 63, no. 11, pp. 138–144, 2019.

[5] Y. Zhang, *Research on Damage and Cracking of Tunnel Lining under Fault Creeping and Fault Action and Flexible Connection Anti-fault Measures*, Southwest Jiaotong University, Chengdu, China, 2016.

[6] Y. Zhao, E. D. Guo, Z. Liu, and L. Gao, "Damage analysis of urban metro tunnel under strike-slip fault," *Rock and Soil Mechanics*, vol. 35, no. S2, pp. 467–473, 2014.

[7] Y. Zhao, *Seismic Response Analysis of Subway Tunnel in Active Fault area*, Institute of Engineering Mechanics, China Earthquake Administration, Harbin, China, 2014.

[8] P. Geng, Y. He, C. He, Q. L. Quan, and Q. X. Yan, "Study on the reasonable seismic fortification length of the tunnel crossing the fracture zone," *Chinese Journal of Rock Mechanics and Engineering*, vol. 33, no. 2, pp. 358–365, 2014.

[9] C. L. Xin, *Research on the Mechanism of Ground Motion Damage and Anti-seismic Measures for Tunnels Crossing faults*, Southwest Jiaotong University, Chengdu, China, 2015.

[10] D. S. Chen, "The empirical relationship between the length of the surface rupture caused by an earthquake and the magnitude of the earthquake," *North China Earthquake Sciences*, vol. 2, no. 2, pp. 26–32, 1984.

[11] D. L. Wells and K. J. Coppersmith, "New empirical relationships among magnitude, rupture length, rupture width, rupture area, and surface displacement," *Bulletin of the*

Seismological Society of America, vol. 84, no. 4, pp. 974–1002, 1994.

[12] D. A. Cole and P. V. Lade, "Influence zones in alluvium over dip-slip faults," *Journal of Geotechnical Engineering*, vol. 110, no. 5, pp. 599–615, 1984.

[13] M. F. Bransby, M. C. R. Davies, A. El Nahas, and S. Nagaoka, "Centrifuge modelling of reverse fault-foundation interaction," *Bulletin of Earthquake Engineering*, vol. 6, no. 4, pp. 607–628, 2008.

[14] M. F. Bransby, M. C. R. Davies, and A. E. Nahas, "Centrifuge modelling of normal fault-foundation interaction," *Bulletin of Earthquake Engineering*, vol. 6, no. 4, pp. 585–605, 2008.

[15] M.-L. Lin, C.-F. Chung, F.-S. Jeng, and T.-C. Yao, "The deformation of overburden soil induced by thrust faulting and its impact on underground tunnels," *Engineering Geology*, vol. 92, no. 3/4, pp. 110–132, 2007.

[16] M. L. Lin, F.-S. Jeng, T. H. Huang et al., "A study on the damage degree of shield tunnels submerged in overburden soil during the thrust fault offset," in *Proceedings of the PVP 2006 ASME Pressure Vessels and Piping Division Conference*, Vancouver, BC, Canada, July, 2006.

[17] M. L. Lin and F. S. Jeng, "Response of soil and a submerged tunnel during a thrust fault offset based on model experiment and numerical analysis," in *Proceedings of ASME Pressure Vessels and Piping Division Conference*, Denver, CO, USA, July 2005.

[18] M.. Sabagh and A.. Ghalandarzadeh, "Numerical modelings of continuous shallow tunnels subject to reverse faulting and its verification through a centrifuge," *Computers and Geotechnics*, vol. 12, pp. 1873–7633, 2020.

[19] S. An, L. J. Tao, X. C. Han, and Y. Zhang, "Application of two-level design method on subway tunnel crossing active fault: a case study on Urumqi subway tunnel intersected by reverse fault dislocation," *Bulletin of Engineering Geology and the Environment*, vol. 3, pp. 1435–9529, 2021.

[20] Z. Zhang, R. Gong, H. Zhang, Q. Lan, and X. Tang, "Initial ground stress field regression analysis and application in an extra-long tunnel in the western mountainous area of China," *Bulletin of Engineering Geology and the Environment*, 2021.

[21] Z. G. Tao, S. L. Ren, G. Li, H. T. Xu, S. L. Luo, and M. C. He, "Model test on support scheme for carbonaceous slate tunnel in high geostress zone at high depth," *Journal of Mountain Science*, vol. 3, no. 18, pp. 1672–6316, 2021.

[22] W. Zhang, *Research on Seismic Response and Damping Measures of Large-Diameter Shield Tunnel Structure*, Institute of Rock and Soil Mechanics, Chinese Academy of Sciences, Wuhan, China, 2009.

[23] Z. Y. Chen and Y. Zhao, "Analysis of tunnel response caused by active reverse fault movement," in *Proceedings of the 2019 National Engineering Geology Annual Conference*, pp. 113–118, The Geological Society of China: Editorial Office of Journal of Engineering Geology, Beijing, China, 2019.

[24] GB 50010-2010, *Code for Design of Concrete Structures*, China Architecture & Building Press, Beijing, China, 2015.

[25] H. Huo, *Seismic Design and Analysis of Rectangular Undergroundstructures*, pp. 23–28, School of Civil Engineering, Purdue University, West Lafayette, IN, USA, 2005.

[26] J. W. Xu, "On the main problems of strike-slip fault," *Frontiers of Earth Science*, vol. 2, no. 2, pp. 125–136, 1995.

[27] H. L. Song, C. H. Zhang, and G. H. Wang, *Structural Geology*, Geological Publishing House, Beijing, China, 2013.

[28] X. Z. Liu, X. L. Wang, and L. L. Lin, "Model experimental study on influence of normal fault with 60° dip angle stick-slip movement on mountain tunnel," *Chinese Civil Engineering Journal*, vol. 47, no. 2, pp. 121–128, 2014.

[29] Q. Fang, W. Su, D. L. Zhang, and F. C. Yu, "Research on deformation characteristics of tunnel surrounding rock based on field monitoring data," *Chinese Journal of Rock Mechanics and Engineering*, vol. 35, no. 9, pp. 1884–1897, 2016.

[30] G. L. Liu, *Research on Key Technologies and Analysis and Forecast Methods of Metro Tunnel Deformation Monitoring*, Wuhan University, Wuhan, China, 2013.

[31] W. B. Ma and J. F. Chai, "Development status of disease detection, monitoring, evaluation and treatment technology of operating railway tunnel," *Tunnel Construction*, vol. 39, no. 10, pp. 1553–1562, 2019.

Hindawi
Advances in Civil Engineering
Volume 2021, Article ID 6643263, 8 pages
https://doi.org/10.1155/2021/6643263

Research Article

A Strain Rate-Dependent Damage Evolution Model for Concrete Based on Experimental Results

Peng Wan,[1] Xiaoyan Lei,[1] Bin Xu ,[2] and Hui Song[2]

[1]*Engineering Research Center of Railway Environmental Vibration and Noise, Ministry of Education, Nanchang 330013, China*
[2]*Jiangxi Provincial Key Laboratory of Hydraulic & Civil Engineering Infrastructure Security, Nanchang Institute of Technology, Nanchang 330099, China*

Correspondence should be addressed to Bin Xu; 2003992786@nit.edu.cn

Received 29 December 2020; Revised 26 February 2021; Accepted 27 March 2021; Published 19 May 2021

Academic Editor: Guang-Liang Feng

There are various definitions of damage variables from the existing damage models. The calculated damage value by the current methods still could not well correspond to the actual damage value. Therefore, it is necessary to establish a damage evolution model corresponding to the actual damage evolution. In this paper, a strain rate-sensitive isotropic damage model for plain concrete is proposed to describe its nonlinear behavior. Cyclic uniaxial compression tests were conducted on concrete samples at three strain rates of $10^{-3}s^{-1}$, $10^{-4}s^{-1}$, and $10^{-5}s^{-1}$, respectively, and ultrasonic wave measurements were made at specified strain values during the loading progress. A damage variable was defined using the secant and initial moduli, and concrete damage evolution was then studied using the experimental results of the cyclic uniaxial compression tests conducted at the different strain rates. A viscoelastic stress-strain relationship, which considered the proposed damage evolution model, was presented according to the principles of irreversible thermodynamics. The model results agreed well with the experiment and indicated that the proposed damage evolution model can accurately characterize the development of macroscopic mechanical weakening of concrete. A damage-coupled viscoelastic constitutive relationship of concrete was recommended. It was concluded that the model could not only characterize the stress-strain response of materials under one-dimensional compressive load but also truly reflect the degradation law of the macromechanical properties of materials. The proposed damage model will advance the understanding of the failure process of concrete materials.

1. Introduction

Concrete is a heterogeneous and discontinuous multiphase composite material. Shrinkage and bleeding can occur in concrete during concrete hardening due to the nonuniformity of material constituents and lead to inevitable development of excessive microcracking and microdefects. The microcracks and microdefects dispersed in the material will gradually expand, evolve, converge, penetrate, and eventually form macrocracks, which will lead to failure under the action of external loads. Studying the damage evolution process will help deepen the understanding of the deterioration of macromechanical properties of concrete.

The internal microcracking and debonding between cement paste and aggregates are the main reasons for the nonlinear behavior of concrete materials. The occurrence and development of damage are considered as the process of damage evolution and appropriate damage variables are regarded as the internal variables in the constitutive relationships that describe the physical and mechanical properties. The authors in [1–3] assumed the damage of material is isotropic and proposed an elastic constitutive equation of isotropic damage. However, [4] recommended adopting different order tensors to describe the anisotropic damage and proposed a model of anisotropic elastic damage. Brünig and Michalski [5] established a model of anisotropic damage for concrete according to irreversible thermodynamics. However, these elastic damage models could not characterize the irreversible behavior of materials.

Researchers have treated irreversible deformations as plastic and proposed elastoplastic damage constitutive equations. A constitutive model for nonlinear characteristics of concrete was recommended by [6]. Oñate et al. [7] proposed a local constitutive model to analyze the failure of solid materials. Zheng et al. [8] obtained a new plastic damage model with two damage variables for concrete crack failure. Jefferson et al. [9] suggested a new comprehensive 3D plastic damage contact model. Feng et al. [10] adopted the elastoplastic damage energy release rates as the driving force of damage. These plastic damage models are used to describe the irreversible behavior of concrete on the basis of yield surface theory and nonassociated flow rules to characterize the occurrence of inelastic deformations. However, there is no clear yield point in the stress-strain curve for concrete under low triaxial stress conditions. An isotropic model for creep damage in concrete under uniaxial compression was proposed by [11]. Pedersen et al. [12] presented a rate-independent viscoelastic and viscoplastic constitutive relationship for the dynamical behavior of concrete. All the models above are based on the phenomenological approaches of field theory methods. This macroapproach is based on continuum mechanics and continuum thermodynamics and determines phenomenologically the material constitutive equations and damage evolution using the thermodynamic theorems and internal variable theory. The method does not need to derive the theoretical relationships between macroscopic quantities directly from the microscopic mechanisms and requires only that the established model be consistent with the actual behavior.

Many researchers utilized the mesoscopic approaches to analyze the damage of concrete. These methods are based on the individual mechanical behavior and interaction of the microscopic material components [13, 14]. Kassner et al. [15] proposed that the mechanics of microcracks in material is based on a multiscale mechanical model and studied the brittle-ductile material behavior at a mesoscale. Contrafatto et al. [16] established a mesoscale model to analyze the nonlinear behavior of concrete with a randomly assigned distribution of phases. These mesoscopic models could describe the physical processes behind damage variables and damage evolution and clearly explain the mechanism of concrete crack initiation. However, the mechanics of heterogeneous microscopic materials requires many simplifying assumptions for transition to macroscopic homogeneous materials. The understanding of the microscopic composition is insufficient because microscopic damage mechanisms are very complicated, and, consequently, it is difficult to obtain their mechanical parameters.

There are various definitions of damage variables used in the existing damage models. On the other hand, the damage evolution models are always established from experience; some are based on a macroscopic perspective and some on a microscopic viewpoint. In fact, damage values calculated by the models based on these two approaches do not agree well with the actual damage values. Therefore, it is necessary to establish a damage evolution model corresponding to the actual damage evolution. In this paper, the damage variable of the material is defined as the ratio of the decrease in the elastic modulus of concrete to the initial elastic modulus. The experimental damage evolution values were quantified and the corresponding damage evolution model was established based on experimental damage data. Finally, the rationality of the proposed viscoelastic damage constitutive model of concrete was verified by the uniaxial cyclic compression test results.

2. Experiments

2.1. Materials and Mix Proportion. The concrete specimens used were 150 mm cubes. The concrete mix proportion is shown in Table 1. A Grade 42.5 ordinary Portland cement, supplied by HaiLuo Cement Co. Ltd., Anhui Province, China, was used in the experiments as the binder. The fine aggregate was desalinated sea sand, the coarse aggregate was crushed stone, and the size of aggregates was kept below 17.5 mm. Ordinary tap water was used. Mixtures were cast in identical plastic molds. To remove entrapped air, the fresh concrete mix was vibrated on a vibrating table after having been poured into the molds. The cast specimen was kept under laboratory conditions for 24 h and then demolded. They were then cured in a laboratory room at 20°C and relative humidity of 95% for 28 days.

2.2. Test Setup. A cyclic uniaxial compression test was conducted in a microprocessor-controlled electrohydraulic servo universal testing machine WAW-2000 produced by Shanghai Bairuo Testing Instrument Co., Ltd. The vertical displacement was measured by two linear variable displacement transducers (1# and 2# LVDT), and the loading rate was set to control by displacement. Nine specimens were divided into three groups and loaded under three strain rates ($10^{-5}s^{-1}$, $10^{-4}s^{-1}$, and $10^{-3}s^{-1}$). The test setup was schematically shown in Figure 1.

Ultrasonic testing was used to detect cracking and deterioration in concrete during the cyclic compression loading experiments. As the ultrasonic wave velocity in concrete is much faster than in the air, the ultrasonic velocity of concrete contains small cracks that would be reduced compared with the initial velocity. Hence, the microcracks nucleation in concrete can be detected by the reduction in ultrasonic velocity [17]. The unloading started at preselected points and the ultrasonic measurements were taken when the compression displacement reached the preselected unloading points. Two ultrasonic probes were arranged vertically in the direction of loading and Vaseline was used as a coupling agent between the probes and concrete to reduce the loss of acoustic energy. Ultrasonic experimental equipment supplied by Beijing Zhibo was adopted.

2.3. Experimental Results. The stress-strain relationships of concrete under cyclic compression load with different strain rates are illustrated in Figure 2. The overall characteristics of the cyclic compression experimental results can be summarized as follows.

A single loading and unloading cycle generally contains two distinct paths: the unloading path and the reloading

Table 1: Mix proportion of concrete samples.

Cement type	Quantity of concrete materials per cubic meter (kg/m^3)				Water/cement ratio
	Cement	Sand	Crushed stone	Water	
PO42.5	451	558	1186	185	0.41

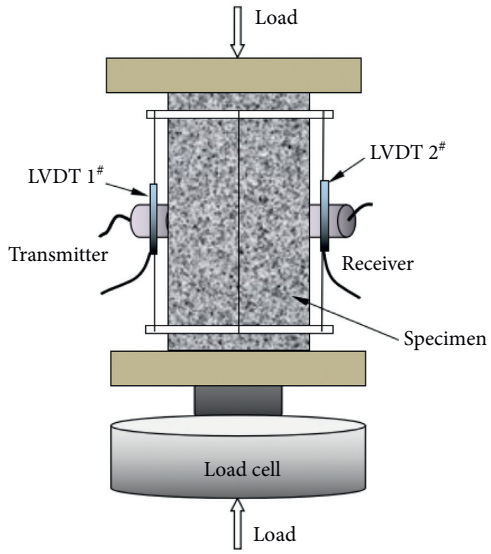

Figure 1: Schematic diagram of a cyclic uniaxial compression test.

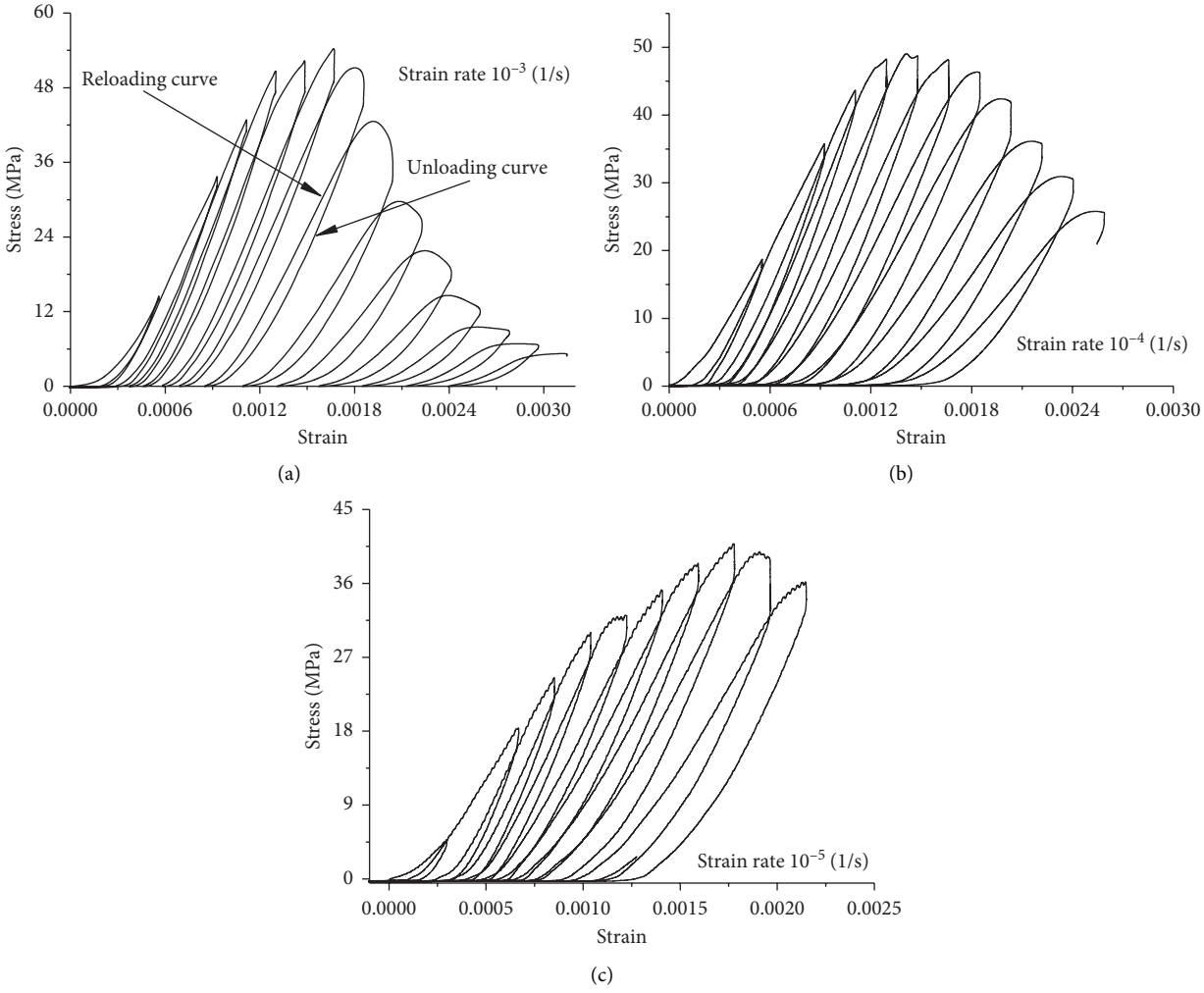

Figure 2: Stress-strain curves of concrete under cyclic compression loading with different strain rates: (a) strain rate of 10^{-3} s^{-1}; (b) strain rate of 10^{-4} s^{-1}; (c) strain rate of 10^{-5} s^{-1}.

path. As presented in Figure 2, concrete stiffness gradually reduced due to the cumulative effect of internal damage of the material caused by the increased number of load cycles.

The stiffness of the unloading curve was significantly less than the stiffness of the reloading curve. This interesting result indicates that some of the internal microdefects of the material closed during the unloading process.

The loading curve can be divided into two stages during the reloading progress. The stress-strain curve was almost linear before reaching the unloading strain. When the value of strain exceeds the unloading point strain, the stress-strain curve exhibited a nonlinear shape. This result may be explained by the fact that the loading process did not cause new damage before the former unloading point. When the strain was greater than the strain at the unloading point, the stress-strain curve showed nonlinearity due to new damage nucleation.

The relative ultrasonic wave velocity results of concrete subjected to compression loading process with different strain rates are presented in Figure 3. From Figure 3, some of the main characteristics of concrete behavior under cyclic compression loading can be deduced as follows.

During the initial stage of experimental loading, the ultrasonic velocity had no obvious change or only a partial increase due to the internal microdefects closing. These findings corroborate the results of the cyclic compression experiments, which show that the unloading paths were almost overlapping with the loading paths.

As the load increased, the ultrasonic propagation velocity started to decrease slowly as the microcracks at the interface between aggregates and cement mortar began to expand gradually. When the load was close to the peak strength, the ultrasonic wave velocity dropped sharply, indicating that the internal cracks in concrete had spread from the interface cracks between aggregates and mortar to the interior of mortar. The material exhibited obvious nonlinear characteristics at this stage and hysteretic energy dissipation was found more and more evident in Figure 2.

When the load was further increased, the cracks became interconnected and obvious macroscopic cracks could be observed on the outer surface of the concrete (Figure 4). The ultrasonic propagation velocity was significantly reduced due to the instability of the crack propagation and it was difficult to detect any ultrasonic wave velocity change in the later stage.

Taken together, these results suggest that there is a relationship between the ultrasonic velocity and the hysteretic energy dissipation. More obvious hysteretic energy dissipation means that more energy was consumed to create more cracks, which in turn would lead to a longer time required for an ultrasonic frequency wave pulse to travel through a concrete sample. Hence, a reduction in ultrasonic velocity will be observed when concrete cracks.

3. Damage Evolution in Concrete under Cyclic Compression

It can be seen from the stress-strain curves obtained in the concrete cyclic loading experiments that the stiffness of the material degenerates due to the development of microvoids and defects as the deformations increase. Therefore, a damage factor, D, was defined as the relative attenuation of the elastic modulus of concrete under cyclic compressive loading:

$$D = 1 - \frac{\widetilde{E}}{E}, \tag{1}$$

where $\widetilde{E}$ is the elastic modulus of the damaged material and E is the initial elastic modulus.

The modulus of material can be calculated from the ultrasonic wave velocity if the material is homogeneous, isotropic, and elastic. Obviously, concrete does not satisfy these physical requirements [18, 19]. In this paper, the secant modulus was considered as the elastic modulus of damaged material. Equation (1) was used to quantify the experimental results of damage versus strain under three strain rates, which reflected the actual degradation of material stiffness during loading. The calculation results are shown in Figure 5.

The damage evolution curves shown in Figure 5 indicate that the entire damage evolution process in concrete can be divided into three stages. During the initial stage of loading,

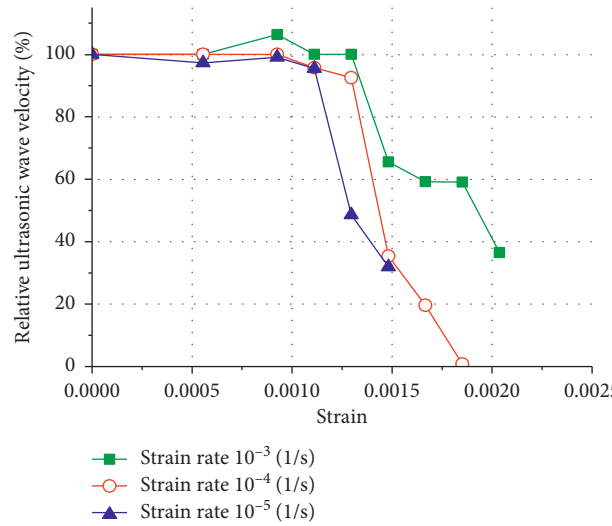

Figure 3: Relative ultrasonic wave velocity of concrete samples subject to the cyclic compressive loading process.

Figure 4: Macroscopic cracks on the outer surface of the concrete.

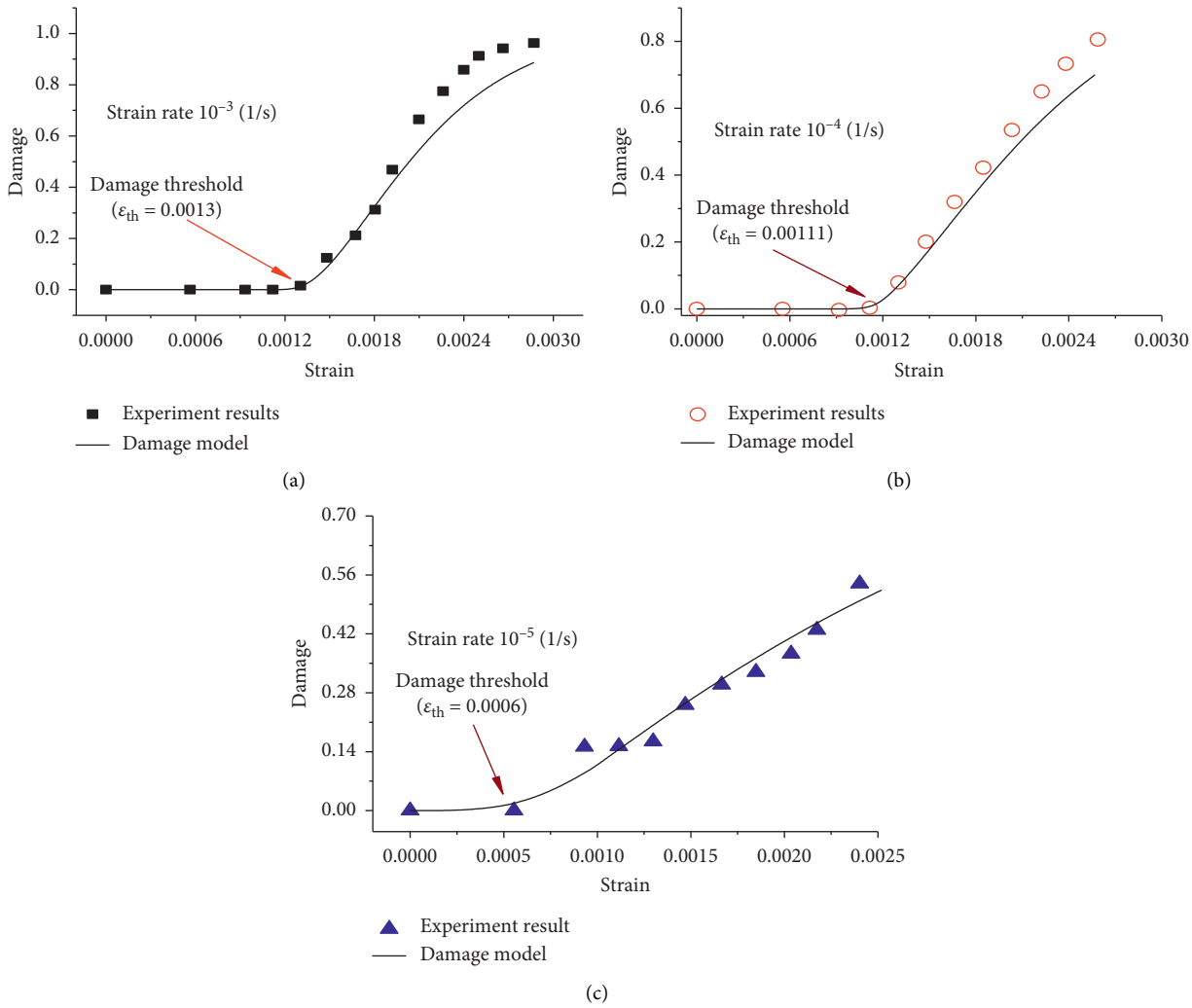

Figure 5: Experimental and model results of damage evolution in concrete under different strain rates.

the initial microcracks between aggregates and cement mortar remained relatively stable and some microcracks closed under loading, which can lead to an increase in density. During this stage, the modulus of material hardly decreased or even increased compared to the initial modulus. The degree of damage can be considered as 0 at this stage; obviously, a damage threshold existed in the damage evolution process. With the increase in load, the internal damage began to increase and the modulus of material began to decrease slowly, mainly due to the gradual increase of cracks in the transition zones between mortar and aggregates. When the loading increased further, the rate of modulus decline began to accelerate and the damage of material began to increase rapidly. This happened mainly due to microcracks in the transition zone nucleated and expanded into the mortar. At the stage of residual strength, microcracks are formed due to the interconnection of microcracks in the interfacial zone between aggregates and mortar. At this stage, the specimen cracked and then the attenuation of modulus of elasticity became gentle and damage stabilized.

It can be seen from Figure 5 that a damage threshold existed in the damage evolution process, which increased with the increase in strain ratio. When the strain ratio was small, the microcracks in the material had enough time to coalesce and propagate. On the other hand, the damage threshold increased with the increase in strain ratio due to the internal microcracks not having enough time to propagate and evolve. Therefore, damage evolution in concrete was related not only to the material rheology but also to the strain rates. This conclusion is consistent with literature [20]. Therefore, the strain-rate dependence should be considered when establishing a damage evolution model.

The damage evolution model for concrete assumed in

this study is as follows:

$$D = \begin{cases} 0, & \varepsilon \le \varepsilon_{\text{th}}, \\ 1 - \exp\left(-\left(\dfrac{\varepsilon - \varepsilon_{th}}{\varepsilon_u}\right)\right), & \varepsilon > \varepsilon_{\text{th}}, \end{cases} \quad (2)$$

$$m = \alpha\left(\frac{\dot{\varepsilon}}{\dot{\varepsilon}_0}\right)^{\beta},$$

where ε_{th} is the damage threshold value, ε_u is the undetermined parameter, $\dot{\varepsilon}_0$ is the reference strain rate which was taken as $1\ s^{-1}$, and m is the shape factor.

By substituting the parameter values listed in Table 2 into equation (2), the damage evolution results can be obtained, as shown in Figure 5. The results of the damage evolution model agreed well with the experimental damage results of modulus attenuation.

4. Model Validation

The experimental results of cyclic the uniaxial compression test of concrete show that some irrecoverable deformation existed after unloading. Song et al. [21] regarded this kind of irrecoverable deformations as viscous conformation. Therefore, the total strain of concrete during compression can be divided into elastic strain and vicious strain as follows:

$$\varepsilon = \varepsilon_e + \varepsilon_v, \quad (3)$$

where ε_e is elastic strain and ε_v is the viscous strain.

Internal variables were introduced to characterize the development of viscous properties. The uniaxial compression experiment was a quasi-static compression process at room temperature, which can be considered as an isothermal. Based on the theory of irreversible thermodynamics, the Helmholtz free energy density function can be expressed as follows:

$$\Phi = \Phi(\varepsilon, D, \xi). \quad (4)$$

Considering the Helmholtz free energy density function of materials as consisting of elastic and irreversible viscous components, equation (4) can be written as follows:

$$\Phi = \Phi_e(\varepsilon_e, D) + \Phi_v(\varepsilon_v, \xi). \quad (5)$$

Based on Lemaitre's equivalent strain principle,

$$\varepsilon_e = \frac{\overline{\sigma}}{E} = \frac{\sigma}{(1-D)E}, \quad (6)$$

where $\overline{\sigma}$ is the effective stress, σ is the nominal stress of the material, and E is the elastic modulus of intact material. Therefore, the elastic part of the free energy density function can be expressed as follows:

$$\Phi_e = \frac{1}{2\rho}(1-D)E\varepsilon_e^2, \quad (7)$$

where ρ is the density of concrete.

Table 2: Parameters of damage evolution model.

Strain rate (s^{-1})	α	β	ε_u	ε_{th}
10^{-3}	2.268	0.05809	0.0009	0.0013
10^{-4}	2.268	0.05809	0.0013	0.0011
10^{-5}	2.268	0.05809	0.0024	0.0006

The stress-strain relationship can be obtained from the thermodynamic governing equation as follows:

$$\sigma = \rho\frac{\partial \Phi_e}{\partial \varepsilon_e} = (1-D)E\varepsilon_e = (1-D)E(\varepsilon - \varepsilon_v). \quad (8)$$

According to the nonlinear iterative solutions of internal variables evolution equations [22],

$$\varepsilon_e = \varepsilon - \varepsilon_v = E\int_{-\infty}^{t} Exp\left(-\frac{t-\tau}{\tau_m}\right)\dot{\varepsilon}(\tau)d\tau, \quad (9)$$

where τ_m is the material relaxation time.

The viscoelastic constitutive model with damage can be obtained by substituting equation (9) into equation (8) as follows:

$$\sigma = (1-D)E\int_{-\infty}^{t} Exp\left(-\frac{t-\tau}{\tau_m}\right)\dot{\varepsilon}(\tau)d\tau\ . \quad (10)$$

The parameters of the damage evolution model are shown in Table 2. Sima et al. [22] proposed that the envelope of the stress-strain curve of concrete under cyclic compression is essentially consistent with that under uniaxial compression. Therefore, to verify the applicability of the model, the envelope of cyclic compression load curves was fitted by the least-squares method according to the established model. The parameters of the viscoelastic constitutive model obtained by the fitting are shown in Table 3.

The curve fitting results demonstrate that the relaxation time was correlated with the loading rate and that it decreased with the increase in strain ratio on account of the multiplicity of molecular motion. The large-scale unit of motion will not respond to a high strain ratio, while the small-scale unit of motion can be activated by a high strain rate, which would lead to a small relaxation time. On the contrary, under a low strain ratio, the large-scale unit of motion and the small-scale unit of motion have sufficient time response; thus, the relaxation time is longer. The curve fitting results are shown in Figure 6.

Figure 6 shows that the viscoelastic constitutive model with damage was in good agreement with the experimental results. In the present study, the R-square of model calculation results and test results is 0.9018, 0.7573, and 0.9313, respectively. Therefore, the proposed model can well characterize the stress-strain response behavior of concrete under uniaxial compression. The previously proposed constitutive models with damage were only required to coincide with the actual stress-strain curves for the verification of their adaptability. However, damage models often do not capture the actual material stiffness degradation. The model proposed in this paper not only

Table 3: Concrete mechanical parameters under uniaxial loading obtained by curve fitting.

Strain rate (s^{-1})	E (GPa)	$\tau_m(s)$
10^{-3}	36.00	1.048×10^5
10^{-4}	31.47	1.907×10^6
10^{-5}	32.55	2.797×10^6

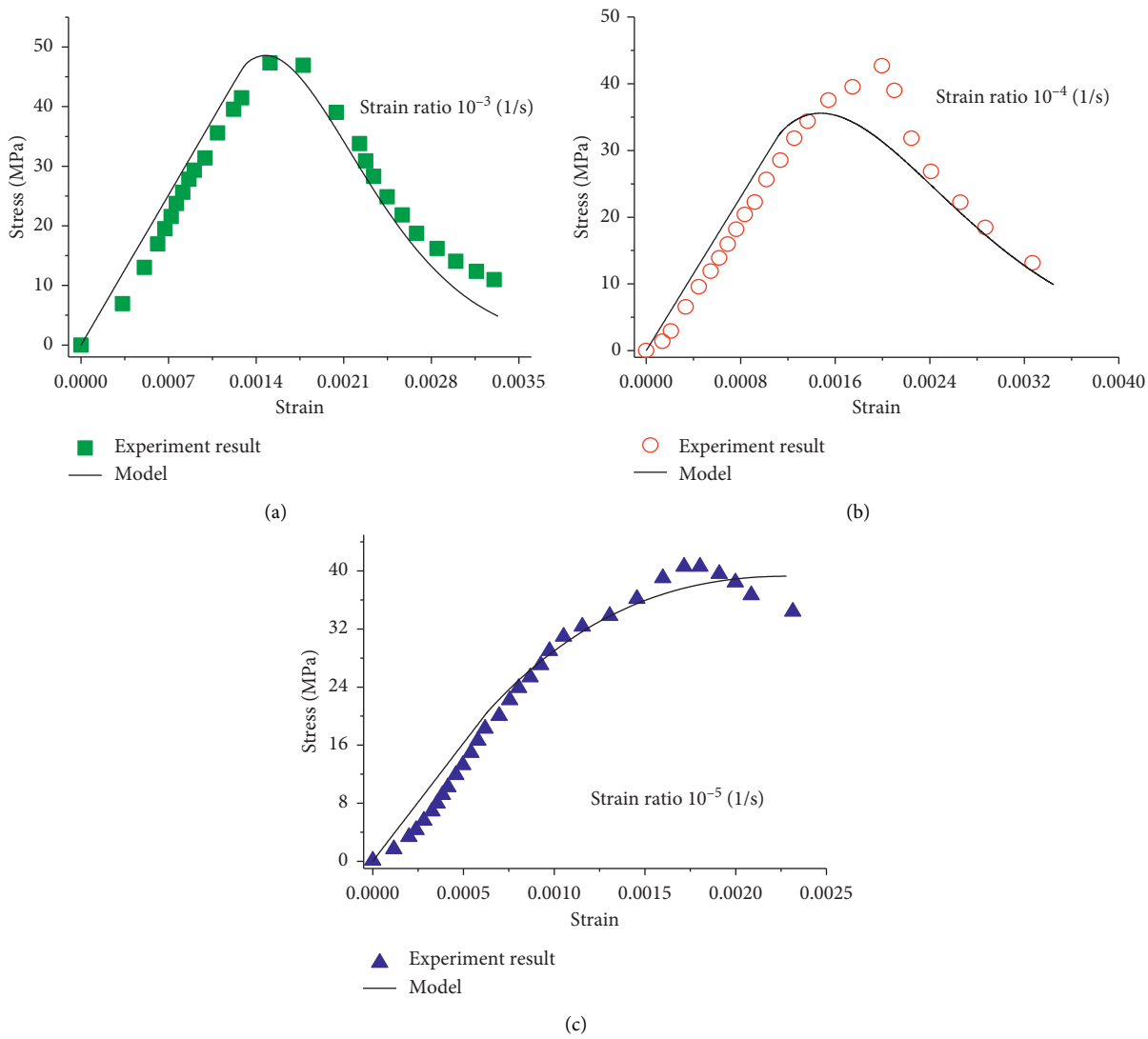

Figure 6: Experimental and model stress-strain curves of concrete under different strain rates.

reflects the rheological degradation of material stiffness but can also characterize the stress-strain response behavior of concrete. The proposed model can characterize the stress-strain response of concrete under quasi-static loading. The proposed model in the present study was not suitable for the strain response behavior of concrete under dynamic loading. Our findings suggested that the strength, stiffness, and damage evolution of concrete were related to the loading rate. Therefore, the dynamic mechanical response behavior of concrete needs to be further studied.

5. Conclusions

The quantitative experimental results of damage evolution in concrete subjected to cyclic uniaxial compression loads were obtained. The results showed that there existed a damage threshold related to the strain ratio. The damage evolution model was established, which was consistent with the quantitative damage experimental results. A viscoelastic constitutive relationship with damage was recommended for concrete. The analyses showed that the model can not only

characterize the stress-strain response of materials under one-dimensional compressive loads but also reflect accurately the degradation of the macromechanical properties.

Data Availability

The data used to support the findings of this study are included within the article.

Conflicts of Interest

The authors declare that there are no conflicts of interest regarding the publication of this paper.

Acknowledgments

This work was financially supported by the Education Department of Jiangxi Province Science and Technology Project (Grant no. GJJ180957), the National Innovation and Entrepreneurship Training Program for College Students (Grant no. 201611319007), the Funding Program for Major Disciplines Academic and Technical Leaders of Jiangxi Provincial in 2017 (Grant no. 20172BCB22022), the Key Science and Technology Research Project in Jiangxi Province Department of Education (Grant nos. GJJ151096 and GJJ14755), and the National Natural Science Foundation of China (Grant no. 51569016).

References

[1] J. Mazars and G. Pijaudier-Cabot, "Continuum damage theory-application to concrete," *Journal of Engineering Mechanics*, vol. 115, no. 2, pp. 345–365, 1989.

[2] J. Mazars, "A description of micro-and macroscale damage of concrete structures," *Engineering Fracture Mechanics*, vol. 25, no. 5-6, pp. 729–737, 1986.

[3] J. Mazars, F. Hamon, and S. Grange, "A new 3D damage model for concrete under monotonic, cyclic and dynamic loadings," *Materials and Structures*, vol. 48, no. 11, pp. 3779–3793, 2015.

[4] F. Supartono and F. Sidoroff, "Anisotropic damage modeling for brittle elastic- materials," *Archives of Mechanics*, vol. 37, no. 4-5, pp. 521–534, 1985.

[5] M. Brünig and A. Michalski, "A stress-state-dependent continuum damage model for concrete based on irreversible thermodynamics," *International Journal of Plasticity*, vol. 90, pp. 31–43, 2017.

[6] J. Lubliner, J. Oliver, S. Oller, and E. Oñate, "A plastic-damage model for concrete," *International Journal of Solids and Structures*, vol. 25, no. 3, pp. 299–326, 1989.

[7] E. Oñate, F. Zárate, J. Miquel et al., "A local constitutive model for the discrete element method. Application to geomaterials and concrete," *Computational Particle Mechanics*, vol. 2, no. 2, pp. 139–160, 2015.

[8] F. Zheng, Z. Wu, C. Gu, T. Bao, and J. Hu, "A plastic damage model for concrete structure cracks with two damage variables," *Science China Technological Sciences*, vol. 55, no. 11, pp. 2971–2980, 2012.

[9] A. D. Jefferson, I. C. Mihai, R. Tenchev, W. F. Alnaas, G. Cole, and P. Lyons, "A plastic-damage-contact constitutive model for concrete with smoothed evolution functions," *Computers & Structures*, vol. 169, pp. 40–56, 2016.

[10] D. C. Feng, X. D. Ren, and J. Li, "Softened damage-plasticity model for analysis of cracked reinforced concrete structures," *Journal of Structural Engineering*, vol. 144, no. 6, p. 04018044, 2018.

[11] C. Mazzotti and M. Savoia, "Nonlinear creep damage model for concrete under uniaxial compression," *Journal of Engineering Mechanics*, vol. 129, no. 9, pp. 1065–1075, 2003.

[12] R. R. Pedersen, A. Simone, and L. J. Sluys, "An analysis of dynamic fracture in concrete with a continuum visco-elastic visco-plastic damage model," *Engineering Fracture Mechanics*, vol. 75, no. 13, pp. 3782–3805, 2008.

[13] E. A. Rodrigues, O. L. Manzoli, L. A. G. Bitencourt Jr, and T. N. Bittencourt, "2D mesoscale model for concrete based on the use of interface element with a high aspect ratio," *International Journal of Solids and Structures*, vol. 94-95, pp. 112–124, 2016.

[14] P. Wriggers and S. O. Moftah, "Mesoscale models for concrete: homogenisation and damage behaviour," *Finite Elements in Analysis and Design*, vol. 42, no. 7, pp. 623–636, 2006.

[15] M. E. Kassner, S. Nemat-Nasser, Z. Suo et al., "New directions in mechanics," *Mechanics of Materials*, vol. 37, no. 2-3, pp. 231–259, 2005.

[16] L. Contrafatto, M. Cuomo, and L. Greco, "Meso-scale simulation of concrete multiaxial behaviour," *European Journal of Environmental and Civil Engineering*, vol. 21, no. 7-8, pp. 896–911, 2017.

[17] H. Y. Qasrawi and I. A. Marie, "The use of USPV to anticipate failure in concrete under compression," *Cement and Concrete Research*, vol. 33, no. 12, pp. 2017–2021, 2003.

[18] A. M. Neville, *Properties of Concrete*, Longman, London, 1995.

[19] R. E. Philleo, "Comparison of results of three methods for determining young's modulus of elasticity of concrete," *Journal Proceedings*, vol. 51, no. 1, pp. 461–470, 1955.

[20] S. Li and J. G. Ning, "Dynamic constitutive relationship of concrete subjected to shock loading," *Engineering Mechanics*, vol. 22, no. 2, pp. 116–119, 2005, in Chinese.

[21] H. Song, J. Chen, C. Qian, Y. Lv, and Y. Cao, "Rate-Dependent characteristic of relaxation time of concrete," *Acta Mechanica Solida Sinica*, vol. 32, no. 1, pp. 69–80, 2019.

[22] J. F. Sima, P. Roca, and C. Molins, "Cyclic constitutive model for concrete," *Engineering Structures*, vol. 30, no. 3, pp. 695–706, 2008.

Hindawi
Advances in Civil Engineering
Volume 2021, Article ID 5590448, 8 pages
https://doi.org/10.1155/2021/5590448

Research Article

Effect of Superficial Scratch Damage on Tension Properties of Carbon/Epoxy Plain Weave Laminates

Miaomiao Duan,[1,2] **Zhufeng Yue**,[1] **and Qianguang Song**[3,4]

[1]*School of Mechanics, Civil Engineering and Architecture, Northwestern Polytechnical University, Xi'an 710129, China*
[2]*School of Urban Planning and Municipal Engineering, Xi'an Polytechnic University, Xi'an 710048, China*
[3]*Beijing Institute of Structure and Environment Engineering, Beijing 100076, China*
[4]*Tianjin Aerospace Reliability Technology Co., Ltd., Tianjin 300462, China*

Correspondence should be addressed to Miaomiao Duan; mmduan@xpu.edu.cn

Received 5 February 2021; Revised 12 March 2021; Accepted 20 March 2021; Published 1 April 2021

Academic Editor: Guang-Liang Feng

The effect of scratch damage on the tension properties of carbon fiber plain weave laminates has been studied in detail using digital image correlation (DIC) and acoustic emission (AE). A range of scratch lengths was machined onto different laminates. The bearing capacity of the laminates was then compared with that of unaltered samples. The strain field distributions near the scratches were measured and analyzed as a function of scratch length with DIC. Initiation and propagation of damage were monitored during the tensile tests using AE. Failure sites and morphologies were observed and analyzed. The results show that superficial scratches have little effect on the strength of plain weave laminates when the scratch length is less than 80% of the specimen width. Scratches affect the distribution of strain near the scratch but not far away from the scratch or at the back face of the sample. Not all samples broke from the scratch site but instead broke from the free edge of the sample or close to the gripping region.

1. Introduction

Composite materials are increasingly used for many important applications in industry, especially in aerospace. This is due to their significantly higher strength, stiffness, and versatile design. Despite these desirable properties, composite structures are susceptible to defects during both manufacturing and in service. This includes the creation of phenomena such as holes, notches, delamination, and scratches. These defects will inevitably affect the structural integrity and structural load-bearing capability of the materials [1–4]. Several studies of damage to composites have focused on the response and performance of composite structures that have been subjected to low- or high-velocity impact [5–8].

Superficial cracks and/or scratches in composite materials may occur, for example, from concrete or other runway debris during aircraft takeoffs and landings. Scratches can also occur via routine ground maintenance operations such as winter deicing operations or mechanical accidents such as tool-drops or abrasion from a sharp object. Scratches can cut into the fibers of some of the plies, which can in turn induce high interlaminar stress and stress concentration. This type of damage can eventually degrade static strength and fatigue strength of the composite structure, making the laminates with scratches more vulnerable to failure under an external load.

Plain weave laminates composed of interlocking fibers and a polymer matrix generally exhibit superior overall performance and are less sensitive to damage than traditional laminated composite materials. For this reason, a deeper understanding of the effects of scratch damage on plain weave laminates is important for the designing of safer structural materials for the aerospace industry, especially when considering the range of possible service conditions. Recently, several research groups have reported studies

regarding the scratch-resistant behavior of composite materials from a tribology perspective, i.e., determining best practices for reducing the wear potential and for protecting the subsurface condition [9–12].

There are significantly fewer studies published regarding the effects of scratches on the mechanical properties of weave laminates. There is a report of the effect of scratches reaching different depths on the delamination of a laminated composite under tensile loading, using experimental and numerical analysis techniques [13]. The results indicated that the scratch tip location and depth are dominant factors for tension load capacity and that scratches can result in undesirable bending and torsional deformations, leading to additional delamination. The influence of different stacking sequences on the failure mode of composite laminates with scratches under tensile loading has also been investigated [14]. Bora et al. studied the effect of scratch resistance on fiber orientation for polymer composites and presented the scratch resistance of polyetherimide composites as a function of scratch hardness, penetration depth, and the coefficient of friction [15]. Size effects in quasi-isotropic carbon/epoxy laminates with the through-thickness center-notches have also been reported [16]. In particular, they used 3-D CT to examine damage ahead of the crack tips and then compared their samples with those of open-hole laminates using the same material, the same stacking sequence, and the same overall dimensions. The discrete ply modeling method has been used to conduct a computational study on notched tensile tests, which analyzed the influence of dimensions, notch shape, and the stacking sequence [17].

All of these previous studies focused on the effect of deep scratches or gouges on the mechanical properties of composite laminates. Here, we present a detailed analysis of the tensile properties of carbon fiber plain weave laminates exposed to more superficial scratches. Our goal is to characterize the effect of different scratch lengths on the mechanical properties of plain weave laminates. The mechanical properties under investigation in this work are tensile strength, distribution of strain, and identification of failure modes.

2. Materials and Methods

2.1. Materials. The material used in these experiments was a composite consisting of a thermoset epoxy resin reinforced with carbon fiber braids (T700GCSC-12K-50C, Toray Industries, characteristics are listed in Table 1). E_1 and E_2 are the elasticity moduli in the fiber direction and the transverse direction, respectively, and G_{12} and G_{23} are the shear moduli in-plane and out of the plane, respectively. The term ϑ_{12} is Poisson's ratio.

Six layers of bidirectional plain weave carbon fabric $[0/90]_6$ were stacked together. The samples (length = 250 mm and width = 25 mm) were cut from plain weave plates using a waterjet cutting machine. The geometry and dimensions of the specimens used for this study are illustrated in Figure 1. Different scratch lengths (5, 10, 15, 20, and 25 mm) were machined using a CNC (computer numerical control) milling machine at the center of the sample. The scratch depth for all specimens was 0.4 mm which is approximately 15% of the test sample thickness. This depth is relatively shallow compared with most of studies on scratches so is called superficial scratch in this paper. The 25 mm scratch length was evident throughout the width of the specimen. To ensure reproducibility of the results, five specimens were tested under the same conditions.

Table 1: Properties of T700SC-12K-50C

E_1/GPa	E_2/GPa	ϑ_{12}	G_{12}/MPa	G_{23}/MPa
55.8	54.9	0.0538	4200	3700

Note. E_1 and E_2 are the elasticity moduli in the fiber direction and in the transverse direction, respectively, and G_{12} and G_{23} are the shear moduli in-plane and out of plane, respectively, and the term ϑ_{12} is Poisson's ratio.

2.2. Methods. DIC is a full-field optical technique that measures displacements on the surface of an object that has been subjected to mechanical, thermal, or various environmental loadings. For these samples, the strain is evaluated via differentiation of the displacement fields. The DIC technique has been widely proven as an advanced and direct technique for measuring full-field strain or displacement [18–20]. In this work, DIC was used to capture surface displacements and evaluate strain in scratched laminate specimens under tensile load.

The AE signals were recorded by using two AE sensors with an optimum frequency range of 100–750 kHz. A 40 dB preamplifier was used to monitor damage progression. The AE sensors were mounted at both ends of the gauge section on the back face of the sample. This positioning allows for DIC monitoring on the scratched face. Before each test, the pencil lead break method was used several times to calibrate the AE sensors according to the ASTM E976-10 standard. The contact surface of the sensor was covered with silicon grease to create good acoustical coupling between the AE sensors and the sample face.

Tensile tests on plain weave laminates were conducted according to ASTM Standard D3039 [21] as shown in Figure 2(a). An Instron 8801 fatigue testing system with a load cell capacity of 100 kN was used to apply a constant displacement to the sample at a speed of 2 mm/min. The tensile load during the test was measured using the load cell. DIC measurements were used to determine the full-field strains at different points in the loading regime, by tracking random speckle patterns on the scratched specimens. Three strain gauges were mounted at points A, B, and C (Figure 2(c)) on the scratched back face and two AE sensors were mounted on the back face of the sample to monitor damage initiation and propagation.

3. Results and Discussion

3.1. Tensile Strength. Representative force-displacement curves of the scratched samples are shown in Figure 3. The curves show an almost linear response up to the point of final failure. Small load drops were observed in some tests at 70–80% of the final failure load, but they are not obvious.

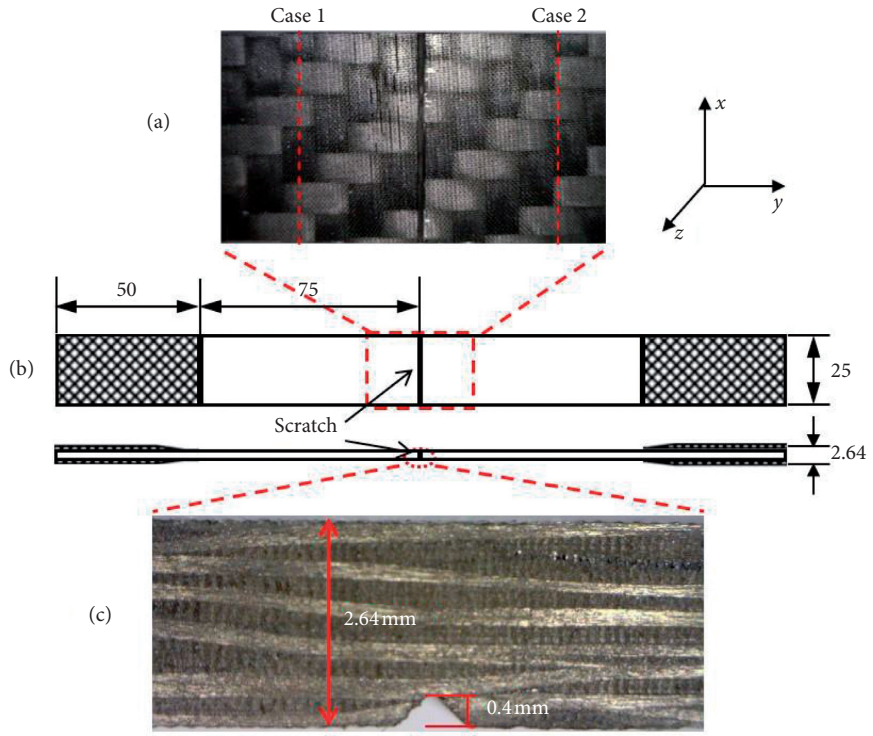

Figure 1: Geometry and dimensions of a representative sample with a 25 mm scratch length.

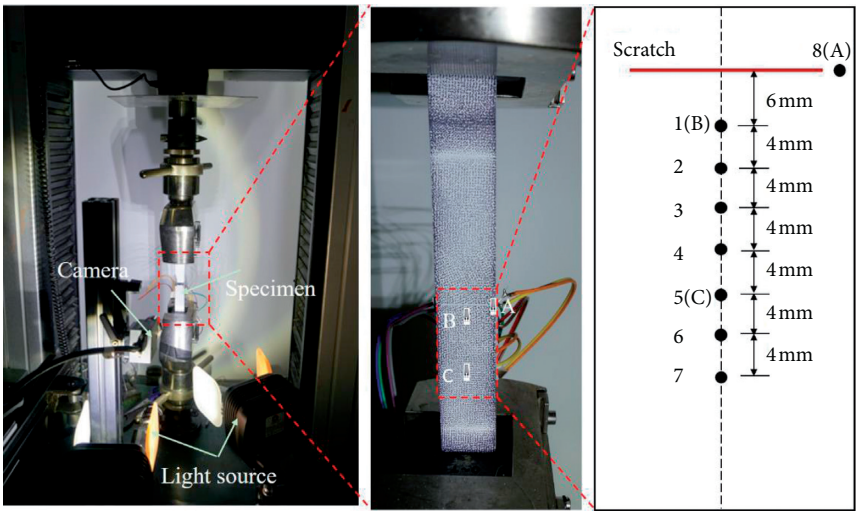

Figure 2: (a) Experimental setup for tensile tests. (b) Photo of the scratched sample. Points A, B, and C denote the locations of the strain gauges on the back face of the sample. (c) Points 1–8 denote the locations of strain evaluated using DIC.

This phenomenon indicates that some fiber breakage occurred in the sample, but they still maintained a bearing capacity. The final failure of all samples was catastrophic and the loads dropped immediately. The failure loads of all specimens are shown in Table 2 and compared with an undamaged sample. In Table 2, W is the width of the sample and CV refers to the coefficient of variation. From Table 2, it could be noted that samples with 5 mm, 10 mm, and 15 mm scratch lengths had an insignificant effect on failure loads. However, longer scratch lengths (20 mm and 25 mm) degraded the tensile strength by 5.4% and 9.75%, respectively, compared with the undamaged sample. This meant that the scratch length could be too small to affect the bearing capacity of the structure. However, if the scratch length was longer than 80% of the specimen width, the scratched materials, in particular the first layer of the sample, resulted in a significant reduction in the bearing capacity of the structure. From Table 2, it was also noted that under the

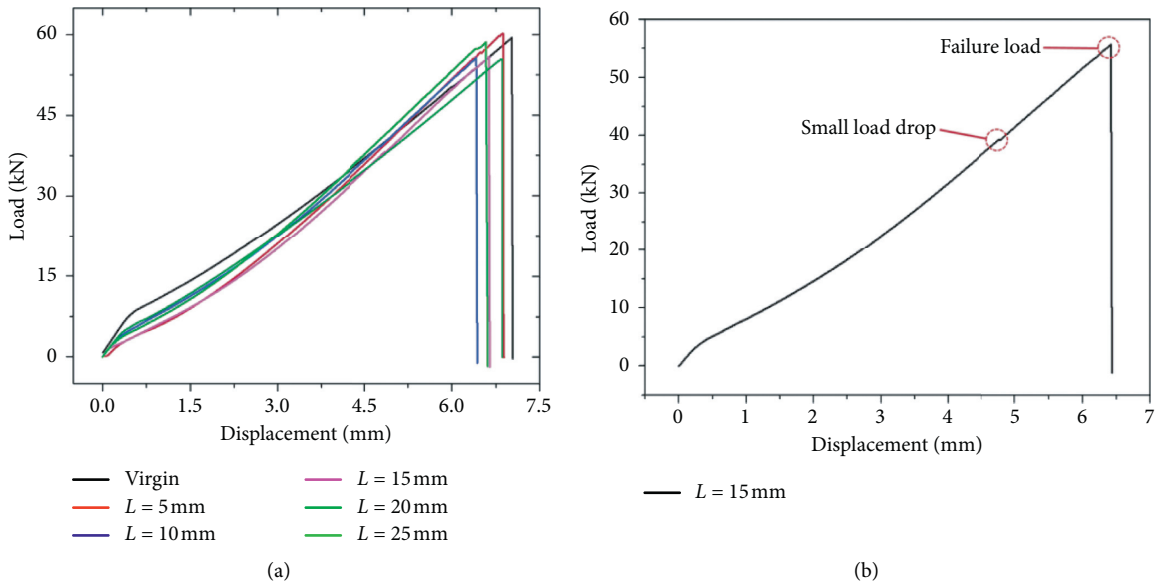

Figure 3: Load-displacement curves.

Table 2: Bearing capacity loads compared between different scratch lengths and virgin specimen.

Specimen	Average failure load (kN)	CV (%)	Load reduction (%)
Virgin	59.28	10.88	—
$L = 5$ mm (20% W)	57.66	10.23	2.83
$L = 10$ mm (40% W)	58.48	4.93	1.35
$L = 15$ mm (60% W)	59.17	6.60	0.19
$L = 20$ mm (80% W)	56.08	3.82	5.40
$L = 25$ mm (100% W)	53.50	10.70	9.75

same conditions, the variation coefficient of the failure load was relatively large. There were two reasons for this observation. Firstly, one of the characteristics of these composite materials was their larger dispersion. Secondly, the scratch position (Figure 1(a)) of plain weave laminates might play a significant role in controlling the bearing capacity of the sample. For case 1, the scratch cuts more warp yarn, which could result in a lower bearing capacity. However, for case 2, the scratch was laid in the intersection between the warp and weft yarns, which effectively cuts less warp yarn and therefore had less influence on the bearing capacity.

3.2. Normal Strain Distribution. Figures 4–6 show DIC results in terms of engineering strain plots ε_{yy} (loading direction) at the location points 1–8 that are previously indicated in Figure 2(c). The same trend in strain distribution of samples with 5 mm, 10 mm, and 15 mm and 20 mm scratch lengths was observed; therefore, further discussion has been made using the results on samples with 15 mm and 25 mm scratch lengths. From Figure 4(a), it was noted that high axial strain concentration occurred at the scratch tip (point 8), especially at the later loading stage. In Figure 4, longitudinal strain at different points shows different trends during the tensile process. At the initial loading stage, the strain at all points increased linearly until the load was increased to 25 kN, followed by a drop at point 1. The closer the point was to the scratch, the earlier the strain decreased, while at points farther away from the scratch, the strain always increased as the load was increased. This phenomenon could be explained as follows: as only part of the fiber in the first layer was cut off, when the load was relatively small, the strain was uniform in distribution. As the load was increased, the scratch was pulled apart and the scratch width became larger. As a free boundary, the material at the scratch showed large interlaminar stress, which resulted in delamination between the first and second layers, causing the strain in the vicinity of the scratch to decrease. With increasing load, the delamination process gradually extended from the scratch to both ends of the sample, and the strain at other points was correspondingly decreased. Surface scratches make the strain near the scratch decrease with the increase in load at the later loading stage, and the strain at the scratch tip increases rapidly with the increase in load due to the existence of the high strain concentration phenomenon. It could be concluded that scratch only affects the distribution of strain near the scratch but does not affect strain far away from the scratch. The affected range was

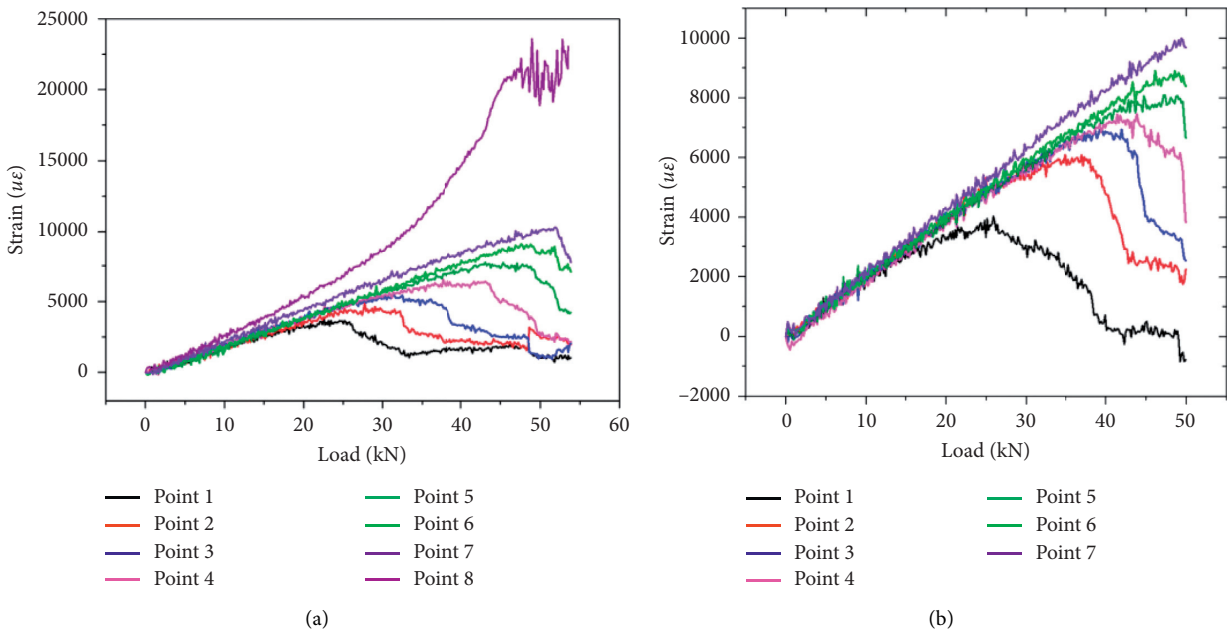

Figure 4: Strain-load curves of specimen with (a) $L = 15$ mm and (b) $L = 25$ mm.

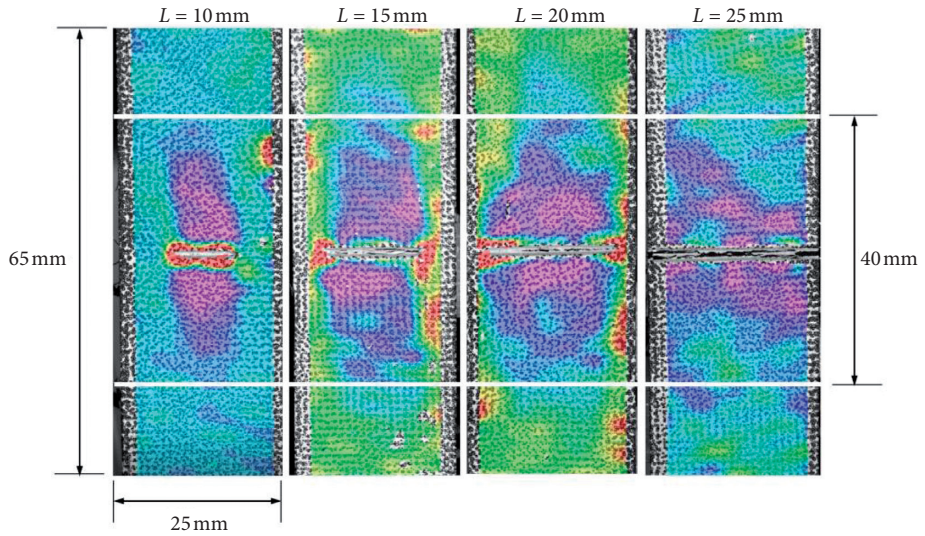

Figure 5: The strain fields under failure load.

about 40 mm (Figure 5) which is 16% of the test sample length. Figure 5 shows that different scratch lengths had an insignificant effect on the affected range of strain in the plain weave laminates.

The strain fields ε_{yy} obtained using the DIC technique at different applied tensile load levels are shown in Figure 6. The results showed high localized strain closer to scratch. Strain concentration occurred around the scratch for samples with a scratch length through the width (25 mm), but the strain concentration of other samples occurred at both ends of the scratch. Figure 6 also highlights the fact that with increased load, the affected range of the scratch on strain distribution was increased gradually.

A comparison of strain values between the gauges on the back face of the samples ($L = 15$ mm) with the DIC results on the scratch face is shown in Figure 7. The position of points 1, 5, and 8 should show results similar to the strain gauges (Figure 2(c)). Figure 7 shows that the strain stayed almost the same for the initial loading stage until the load reached 25 kN except point 8. After this load value, points 1 and 8 in the vicinity of the scratch could be distinguished from the other points due to damage. The strain of point 8 is higher than that of other points after 8 kN, especially at the later loading stage. Because point 8 is located at the tip of the scratch, there is a large strain concentration phenomenon which becomes more and more obvious with the increase in load. The conclusion could be drawn that the scratch only affected

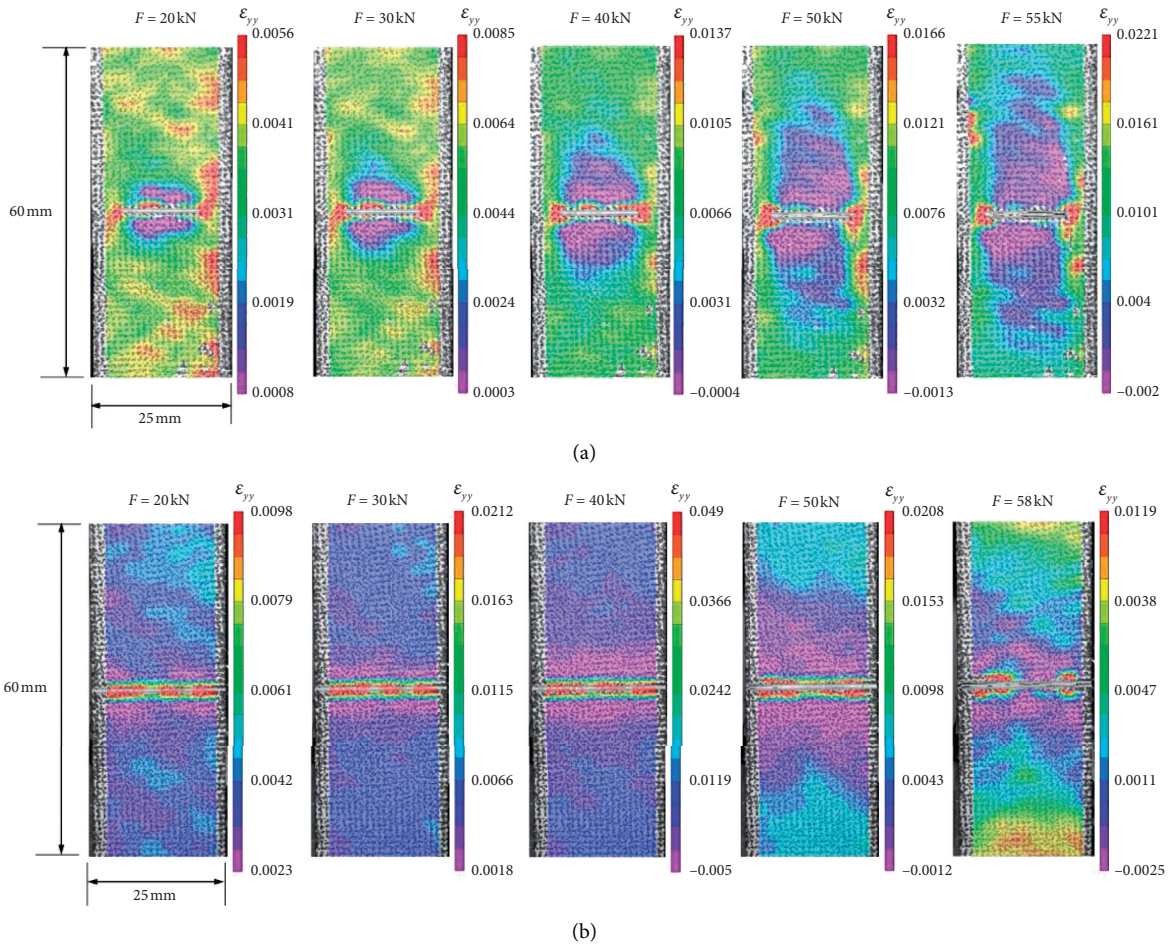

Figure 6: Strain fields ε_{yy} obtained using the DIC technique during testing: (a) $L = 15$ mm and (b) $L = 25$ mm.

the distribution of the strain near the scratch (about 40 mm) but did not affect the strain far away from the scratch (point 5) and at the back face (points A, B, and C).

3.3. Failure Mechanisms. Figure 8 shows the load-time and AE cumulative energy-time curves for the $L = 25$ mm sample. According to Figure 8, the AE cumulative energy curve could be divided into three regions. In region I, at the initial damage stage (0–170 s), the corresponding load was 0–25 kN. At the beginning of the loading, the AE signal was generated. The cumulative energy was relatively low, and it barely increased with an increase in the load. There was slight damage to the sample, but the damage expanded slowly. Due to the high preparation temperature of the composite material and the mismatch between the thermal expansion coefficient of the fiber and the matrix, thermal stress was generated when the sample was cooled to room temperature after preparation, resulting in microcracks in the matrix. AE signals at this stage were mainly generated when microcracks expanded in the matrix and the interface.

In region II, interfacial damage between the fiber and the matrix (170–235 s) was observed, and the corresponding load was 25–34 kN. The AE cumulative energy increased gradually as the load was increased, which indicated that the macrocracks in the matrix expanded steadily and delamination was initiated at the scratch, accompanied by some fiber breakage. However, the sample still had a load-bearing capacity, which was as per the DIC results. In region III, i.e., the fiber breakage stage (235–340 s), the corresponding load was 34–48 kN. The AE cumulative energy increased rapidly and reached a maximum, which indicated that more fibers started to break until the sample was completely failed.

From the experimental results, it was found that not all samples broke from the scratch site. Failure sites were classified as follows: (a) scratch location, (b) gauge length (except for scratch location), and (c) grip section, as illustrated in Figure 9. Figure 10 helps to explain the reasoning for the failure sites. In Figure 10, the black boxes denote the locations of strain concentration. From Figure 10, it could be noted that when the sample has broken, strain concentration might occur at the scratch site, the free edge of the sample, and close to the gripping region, corresponding to all three failure sites. Localized strain concentration determined the failure onset of the entire sample.

Figure 11 shows failure morphology of scratch specimen. The fracture was disorganized, and a large amount of fiber breakage and delamination was observed. A large number of

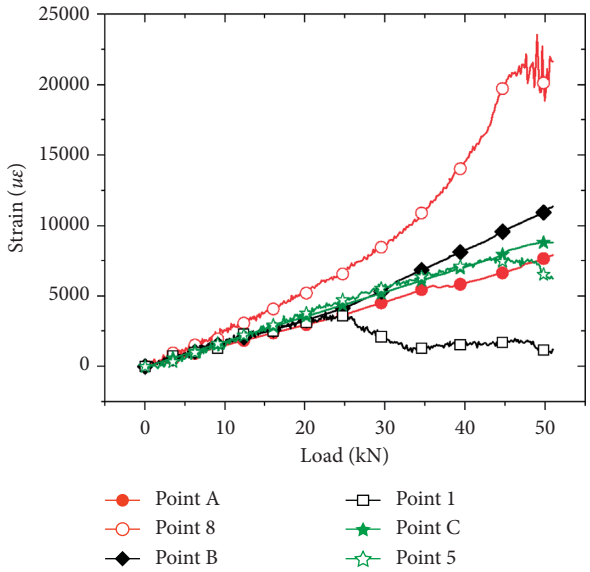

Figure 7: Comparison of strain values between gauge measurements and DIC results.

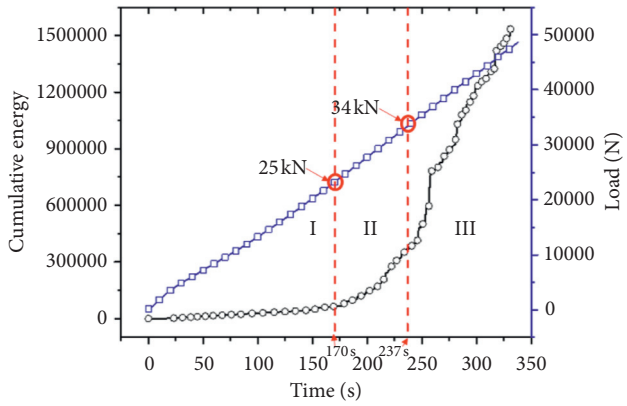

Figure 8: Load-time and AE cumulative energy-time curves for specimen ($L = 25$ mm).

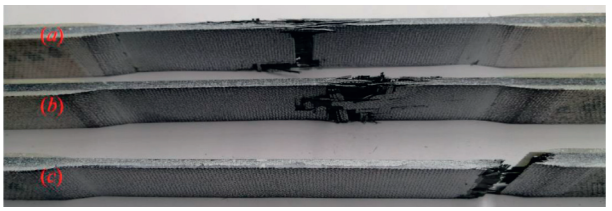

Figure 9: Failure sites of scratched samples.

fiber bundles were detached from the plain weave laminate, and the resin fell off the surface. This was because the tensile strength of the fiber bundles was greater than the binding power between the fibers and the resin; therefore, the fibers and the resin were separated from the plain weave laminate. The scratch rendered the first weave layer unrestrained in the loading direction, resulting in a lowered bearing capacity.

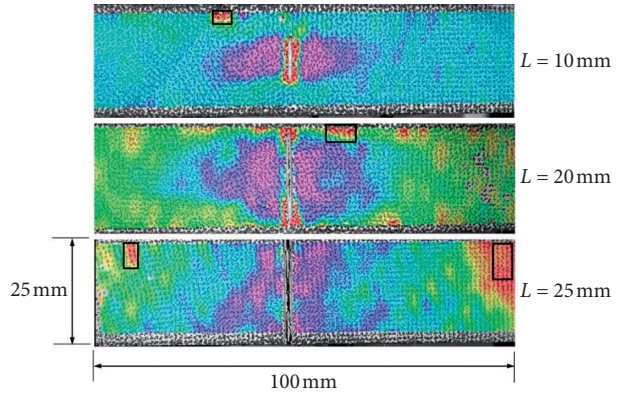

Figure 10: Strain fields ε_{yy} of scratched samples under failure load.

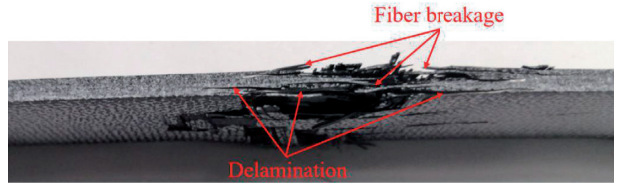

Figure 11: Fracture morphology of a representative scratched sample.

This made the fiber prone to separation, tearing, and rapid failure. When the fiber in the first weave layer failed, the crack expanded rapidly along the fiber direction, eventually causing delamination.

4. Conclusions

In this study, the experimental tensile load investigations of carbon/epoxy plain weave laminates with different scratch lengths were presented and discussed. The normal strain distribution around the scratches was measured, and the fracture site and morphology were observed. Several conclusions could be drawn from these experiments:

(1) The effect of superficial scratches was insignificant in terms of tensile strength when the scratch length was small. Relatively lower tensile strengths were observed in the samples when the scratch length was more than 80% of the sample width. This was attributed to the first layer of the samples having almost no bearing capacity.

(2) Superficial scratches make the strain near the scratch decrease with the increase in load at the later loading stage, and the strain at the scratch tip increases rapidly with the increase in load. Scratching was also found to only affect strain distribution near scratch, with an effective range being 16% of the test sample length. The strain far away from scratch and at the back face was unaffected. Different scratch lengths had no significant effect on the affected range of strain in plain weave laminates.

(3) The failure mechanisms of plain weave laminates with superficial scratches were characterized by fiber breakage, leading to delamination. The failure site of some samples was not at the scratch site because localized strain concentration might have occurred at the scratch site, the free edge of the sample, or close to the gripping region.

Data Availability

The data used to support the findings of this study are included within the article.

Conflicts of Interest

The authors declare no potential conflicts of interest with respect to the research, authorship, and/or publication of this article.

Acknowledgments

This work was supported by the Natural Science Foundation of Shaanxi Province (No. 2017JM5018).

References

[1] J. Awerbuch and M. S. Madhukar, "Notched strength of composite laminates: predictions and experiments," *Journal of Reinforced Plastics and Composites*, vol. 4, pp. 153–159, 1985.

[2] F. K. Chang and K. Y. Chang, "A progressive damage model for laminated composites containing stress concentrations," *Journal of Composite Materials*, vol. 2, no. 21, pp. 834–855, 1987.

[3] R. F. El-Hajjar and D. R. Petersen, "Gaussian function characterization of unnotched tension behavior in a carbon/epoxy composite containing localized fiber waviness," *Composite Structures*, vol. 93, no. 9, pp. 2400–2408, 2011.

[4] C. Soutis and J. Lee, "Scaling effects in notched carbon fibre/epoxy composites loaded in compression," *Journal of Materials Science*, vol. 43, no. 20, pp. 6593–6598, 2008.

[5] S. Long, X. Yao, and X. Zhang, "Delamination prediction in composite laminates under low-velocity impact," *Composite Structures*, vol. 132, pp. 290–298, 2015.

[6] H. R. Wang, S. C. Long, X. Q. Zhang, and X. H. Yao, "Study on the delamination behavior of thick composite laminates under low-energy impact," *Composite Structures*, vol. 184, pp. 461–473, 2018.

[7] H. Tuo, Z. Lu, X. Ma, C. Zhang, and S. Chen, "An experimental and numerical investigation on low-velocity impact damage and compression-after-impact behavior of composite laminates," *Composites Part B: Engineering*, vol. 167, pp. 329–341, 2019.

[8] C. T. Key and C. S. Alexander, "Numerical and experimental evaluations of a glass-epoxy composite material under high velocity oblique impacts," *International Journal of Impact Engineering*, vol. 137, pp. 1–10, 2020.

[9] V. Bharathi, M. Ramachandra, and S. Srinivas, "Influence of fly ash content in aluminium matrix composite produced by stir-squeeze casting on the scratching abrasion resistance, hardness and density levels," *Materials Today: Proceedings*, vol. 4, no. 8, pp. 7397–7405, 2017.

[10] R. D. K. Misra, R. Hadal, and S. J. Duncan, "Surface damage behavior during scratch deformation of mineral reinforced polymer composites," *Acta Materialia*, vol. 52, no. 14, pp. 4363–4376, 2004.

[11] Y. N. Liang, S. Z. Li, R. H. Zhang, and S. Li, "Effect of fiber orientation on a graphite fiber composite in single pendulum scratching," *Wear*, vol. 198, no. 1-2, pp. 122–128, 1996.

[12] Z. Zhang, I. A. Alhafez, and H. M. Urbassek, "Scratching an Al/Si interface: molecular dynamics study of a composite material," *Tribology Letters*, vol. 66, pp. 85–96, 2018.

[13] S. Seyedmohammad and F. E. Rani, "Effects of scratch damage on progressive failure of laminated carbon fiber/epoxy composites," *International Journal of Mechanical Sciences*, vol. 67, pp. 70–77, 2013.

[14] R. P. Derek, F. E. Rani, and A. K. Bashar, "On the tension strength of carbon/epoxy composites in the presence of deep scratches," *Engineering Fracture Mechanics*, vol. 90, pp. 30–40, 2012.

[15] M. O. Bora, O. Çoban, T. Sinmazcelik, and V. Gunay, "Effect of fiber orientation on scratch resistance in unidirectional carbon-fiber-reinforced polymer matrix composites," *Journal of Reinforced Plastics and Composites*, vol. 29, no. 10, pp. 1476–1490, 2010.

[16] X. Xu, M. R. Wisnom, Y. Mahadik, and S. R. Hallett, "An experimental investigation into size effects in quasi-isotropic carbon/epoxy laminates with sharp and blunt notches," *Composites Science and Technology*, vol. 100, pp. 220–227, 2014.

[17] J. Serra, C. Bouvet, B. Castanié, and C. Petiot, "Experimental and numerical analysis of carbon fiber reinforced polymer notched coupons under tensile loading," *Composite Structures*, vol. 181, pp. 145–157, 2017.

[18] J. Cuadra, P. A. Vanniamparambil, K. Hazeli, I. Bartoli, and A. Kontsos, "Damage quantification in polymer composites using a hybrid NDT approach," *Composites Science and Technology*, vol. 83, pp. 11–21, 2013.

[19] M. A. Caminero, S. Pavlopoulou, M. Lopez-Pedrosa, B. G. Nicolaisson, C. Pinna, and C. Soutis, "Analysis of adhesively bonded repairs in composites: damage detection and prognosis," *Composite Structures*, vol. 95, pp. 500–517, 2013.

[20] J. J. Andrew, V. Arumugam, D. J. Bull, and H. N. Dhakal, "Residual strength and damage characterization of repaired glass/epoxy composite laminates using A.E. and D.I.C." *Composite Structures*, vol. 152, pp. 124–139, 2016.

[21] ASTM D3039, *Standard Test Method for Tensile Properties of Polymer Matrix Composite Materials*, ASTM International, West Conshohocken, PA, USA, 2007.